Genetic and Chemical Intervention of the BfrB:Bfd Interaction Dysregulate Iron Homeostasis in *Pseudomonas aeruginosa* and Affect its Broader Metabolism

By
Achala Punchi Hewage

Submitted to the graduate degree program in Department of Chemistry and the Graduate Faculty of the University of Kansas in partial fulfillment of the requirements for the degree of Doctor of Philosophy.

Advisor: Mario Rivera, PhD.

Chair: Heather Desaire, PhD.

Susan M. Lunte, PhD.

Robert C. Dunn, PhD.

Josephine Chandler, PhD.

Lynn Hancock, PhD.

Date Defended: 24 March 2020

The dissertation committee for Achala Punchi Hewage certifies that this is the approved version of the following dissertation:

Genetic and Chemical Intervention of the BfrB:Bfd Interaction Dysregulate Iron Homeostasis in *Pseudomonas aeruginosa* and Affect its Broader Metabolism

_____

Advisor: Mario Rivera, PhD.

_____

Chair: Heather Desaire, PhD.

Date Approved: 12 May 2020

Abstract

Pseudomonas aeruginosa is a Gram-negative opportunistic pathogen that is accountable for multiple types of infections, including pneumonia, wound, burn, and urinary tract infections. *P. aeruginosa* is an emerging threat in the hospital environments and preferentially found in comorbid illnesses. Current treatments for the *P. aeruginosa* infections recommend the use of combination therapy, a β-lactam with an aminoglycoside or a fluoroquinolone. Also, resistance to such procedures is rapidly emerging. Moreover, *P. aeruginosa* has been given critical priority for anti-infective development in the 2017 World Health Organization (WHO) report on prioritizing pathogens to guide the discovery of new antibiotics.

Iron metabolism in bacteria has gained much more attention as a potential target for antibiotic development. Regulation of iron homeostasis is crucial for cells to have enough iron for growth while avoiding iron-induced toxicity. Iron homeostasis involves iron uptake, storage, and mobilization. Two iron storage molecules co-exist in *P. aeruginosa*, FtnA, and BfrB. Previous *in-vitro* studies established the importance of the bacterioferritin associated ferredoxin (Bfd) in iron mobilization from BfrB. The X-ray crystallographic structure and biochemical characterization of the BfrB:Bfd complex identified the hot spot residues of the interaction. The residues E81, E85, and L68 in BfrB, and M1, Y2, and L5 in Bfd majorly contribute to the binding energy. Mutating E81 and L68 to alanine completely inhibited iron mobilization from BfrB. The insights gathered from these *in-vitro* studies were used in this work to interrogate the importance of the BfrB:Bfd interaction in *P. aeruginosa* cells.

In this work, *P. aeruginosa*, wild type (PAO1), Δ*bfd*, *bfrB*(E81A/L68A), and Δ*bfrB* cells were used to study the significances of the BfrB:Bfd interaction *in P. aeruginosa* cells. A Native-PAGE method was optimized to image iron in BfrB in *P. aeruginosa* lysates. This advanced technique allowed us to identify BfrB as the main iron storage protein of *P. aeruginosa*. The same method was used to image iron storage in BfrB and its subsequent mobilization in *P. aeruginosa* cells (wild type, Δ*bfd*, and *bfrB*(E81A/L68A)). The intact BfrB:Bfd interaction capable wild type cells showed maximum accumulation of iron during the early stationary phase, and iron mobilization from BfrB during the late stationary phase. In contrast, the

Δ*bfd* and *bfrB*(E81A/L68A) mutants demonstrated irreversible accumulation of iron in BfrB. Due to the irreversible flux of iron into BfrB, the Δ*bfd* and *bfrB*(E81A/L68A) mutants developed low cytosolic free iron levels and a high total iron to free iron ratio. The consequences of the genetic blockade of the BfrB:Bfd interaction was further investigated by comparing the expression proteomes of the wild type and Δ*bfd* mutant cells. The iron homeostasis dysregulation affected the iron-dependent and independent metabolic processes in the Δ*bfd* mutant cells. Proteins involved in the TCA cycle, amino acid biosynthesis, oxidative stress regulation, and respiratory chain were under-represented in the Δ*bfd* mutant cells. On the other hand, proteins involved in the iron acquisition systems (pyoverdine, pyochelin, Heme iron acquisition), sulfur assimilation, quorum sensing were over-represented in the Δ*bfd* mutant cells. These findings show that iron homeostasis dysregulation can affect the broader metabolism of *P. aeruginosa* cells.

The chemical intervention of the BfrB:Bfd interaction in *P.aeruginosa* cells was carried out with small molecule inhibitors, analogs of 4-aminoisoindoline-1,3-dione. These analogs acted on their target, BfrB in *P. aeruginosa* cells. Moreover, the analogs elicited a concentration-dependent growth retardation, and a pyoverdine hyper-production as a result of cytosolic iron deprivation. Analog-treated cells experienced an irreversible accumulation of iron in BfrB and high total iron content in the treated cells. Hence, the developed 4-aminoisoindoline-1,3-dione derivatives were potent to dysregulate iron homeostasis in *P. aeruginosa* cells.

The BfrB:Bfd inhibitors also potentiated the activity of fluoroquinolones in *P. aeruginosa* (PA01), and in two cystic fibrosis isolates, MR3B and MR60. The growth impairment of the cystic fibrosis and urinary tract clinical isolates of *P. aeruginosa*, and *Acinetobacter baumannii* (AB5075) demonstrate the potential widespread application of the developed 4-aminoisoindoline-1,3-dione derivatives in blocking the BfrB:Bfd interaction. These findings strongly support the suitability of inhibiting the BfrB:Bfd interaction as a novel target in anti-infective development.

Acknowledgments

I offer my heartiest gratitude to my Ph.D. advisor Prof. Mario Rivera for the support and guidance given to me throughout my research. You made me realize the excitement behind the research, and these five years had been an invaluable life experience for me. You guided me in every possible aspect to become a better scientist. You have been a great motivation, and I am fortunate to have an advisor like you. I would also like to thank Dr. Huili Yao in our group for the tremendous help and guidance given by her for my projects, I am lucky to have her in my team.

I would also like to extend my deepest gratitude to all our collaborators, especially Dr. Richard Bunce and his group at Oklahoma State University for coming up with synthesis strategies and synthesizing the designed analogs that allowed me to complete the *in-cell* studies; Dr. Josephine Chandler and her group at the University of Kansas for preparing the *P. aeruginosa* mutants that helped me develop iron imaging techniques and complete proteomics study; Dr. Scott Lovell at the University of Kansas, Structural Biology Facility for solving the protein X-ray crystallography structures; Dr. Allen Reitz at the Fox Chase Chemical Diversity Center for proving us the fragment library and the guidance given on the Medicinal Chemistry aspects; Dr. Jessie Guidry at the LSU Health Science Proteomics Facility for acquiring the proteomics data and Dr. Fabrizio Donnarumma at LSU Proteomics Facility for providing me useful insights in proteomics data analysis.

I also would like to thank the past Rivera group members, Dr. Yang Wang, and Dr. Kate Eshelman, for their valuable support and guidance. I appreciate all the help and courage given by the present group members Dr. Huili Yao, Dr. Anabel Soldano, Leo Fontenot, Aisha Cook, Suliat Alli, and Nimesha Rajapaksha.

I appreciate the support given by my Ph.D. dissertation committee for all their valuable comments and time. I am deeply grateful to Dr. Heather Desaire for agreeing to be the chair of my dissertation committee. My heartfelt gratitude is offered to the University of Kansas and the Department of Chemistry

for providing me this opportunity to pursue my graduate studies in the United States. I want to thank all the lectures, especially to Dr. M. P. Deeyamulla, Department of Chemistry, the University of Kelaniya in Sri Lanka. My sincere gratitude goes to all my teachers at Girls' High School, Kandy, Sri Lanka.

I want to thank my loving husband, Thilanga, for the support he gave me during the hard times. My heartiest gratitude goes to mother and father and brother for their support and encouraging words. I am fortunate to have a family like you.

Table of Contents

Table of Figures

Chapter 1 : Introduction

1.1 Urgent need for novel antibiotic development

Antibiotics help people all around the world to prevent and treat infections. Antibiotics have played an important part in achieving major advances in medicine and surgery. In developing countries, antibiotics have lowered the morbidity and mortality caused by poverty related and food borne infections. Penicillin was the first modern era antibiotic discovery by Alexander Fleming in 1928. It was used against bacterial infections as a prescribed drug in 1940. From 1940-1960 was the golden era for antibiotic discovery, which involved two streams of origin, natural products and synthetic antimicrobials. Penicillins, aminoglycosides, cephalosporins and tetracyclines are some of the main classes of antibiotic natural products discovered during this time period. The activity of these model natural products was further enhanced by semi-synthetic approaches, forming subsequent generations that are currently in use. The historical synthetic antimicrobial compounds that have been in use since the 1930s are the sulfa drugs. The next group of synthetic antibiotics are the fluoroquinolones. Fluoroquinolones were developed after the accidental discovery of nalixidic acid in 1962 which was a by-product of chloroquine [1]. This was the starting point for the synthesis of a library of quinolones, including the ones currently in use. Norfloxacin was the first "fluoroquinolone", where the C-6 position contains a fluorine [1]. Novel antibiotics, linezolid (2000), daptomycin (2003) and retapamulin (2007) were discovered nearly 40 years after the discovery of quinolones but these chemical classes of antibiotics, oxazolidinones, acid lipopeptides, and pleuromutilins were first reported in 1978, 1987 and 1952, respectively [2]. The evolution of the above discussed antibiotics were just improvements, variations or just repurposing the use of the existing main classes of antibiotics [1, 3]. Unfortunately, in last two decades fewer new classes of antibiotics have been developed and prescribed [3]. In addition to the dwindling discovery rate of novel antibiotics, an antibiotic resistant crisis has exerted a large impact on bacterial infections, making them a serious threat to public health.

The antibiotic resistance for penicillin started around 1950s, arising a clinical problem. As a solution, β-lactam antibiotics were discovered and deployed. In the same decade methicillin resistant

Staphylococcus aureus was identified [4]. To treat the methicillin resistant *S. aureus*, vancomycin was developed in 1972. For a while no antibiotic resistance was seen for vancomycin until resistant coagulase-negative staphylococci was found in 1978 and in 1983. To treat vancomycin-resistant enterococci and methicillin-resistant *Staphylococcus aureus*, synercid and daptomycin antibiotics were introduced. The β-lactam class of antibiotics is a good example to illustrate the challenges presented by resistance development: About 1000 β-lactamases that would inactivate the β-lactam antibiotics had been identified by 2010, a 10 fold increase since 1990 [5]. Carbapenem resistance in Enterobacteriacea has increased from 0 % in 2000 to 1.4 % 2010, with the most rapid increase recorded in *Klebsiella* spp [6].

Antibiotic resistance can occur due to biochemical and physiological mechanisms. The resistance due to genomic mutations in microbes has been extensively studied. The mutated strains get a competitive advantage from the selection pressure of the antibiotics. Sublethal concentrations of antibiotic allow stepwise selection of resistance. When mutations leading to resistance occur in the bacterial chromosomes some of these mutations could have occurred in transmissible elements within the bacterial genome. Hence, these mutations can be transmitted between species, spreading the resistance traits. Antibiotic resistance can be enhanced due to various factors such as, overuse, excessive prescribing and excessive use in agriculture. Thus, antibiotic misuse adds selective pressure for the survivability of pathogens [7], and the resulting antibiotic resistant bacterial infections require the use of highly effective broad-spectrum antibiotics for treatment.

Gram-negative pathogens in the ESKAPE group (***E****nterococcus faecium*, ***S****taphylococcus aureus*, ***K****lebsiella pneumoniae*, ***A****cinetobacter baumanii*, ***P****seudomonas aeruginosa* and **E**nterobacter species) have emphasized the challenges associated with treating antibiotic resistant infections [8]. To exacerbate these challenges, there hasn't been an improvement in developing an antibiotic to treat Gram-negative bacteria for decades. Even though the use of polymixins (*e.g*. colistin) was avoided due to toxicity 40 years after they were discovered, in past years polymixins have been used mainly to treat gram-negative resistant infections [8]. Recently, resistant genes for "last resort" antibiotics (carbapenems and colistin) have been

discovered. These resistant strain infections are predicted to be untreatable with currently available antibiotics [9].

Clearly, there is a need for continuous cycling of new antibiotics discovery and development as the genes in the global resistome can be transferred at different frequencies, driving resistance to each generation of newly introduced antibiotics.

1.2 Targets engaged by existing commercial antibiotics

In the current antibiotic arena, there are five clinically validated antibiotic targets:

(1) Peptidoglycan (an essential structural component of the bacterial cell wall) biosynthesis inhibitors are represented by both β-lactams and vancomycin type glycopeptides. β-lactams (penicillins, carabapenems and cephalosporins) bind to the penicillin binding proteins (transpeptidases) and inhibit the cross linking of peptidoglycan. Glycopeptide antibiotics (e.g vancomycin) can bind to the peptidoglycan (PG) units, inhibiting transglycosylase and transpeptidase activity, and preventing the PG maturation,

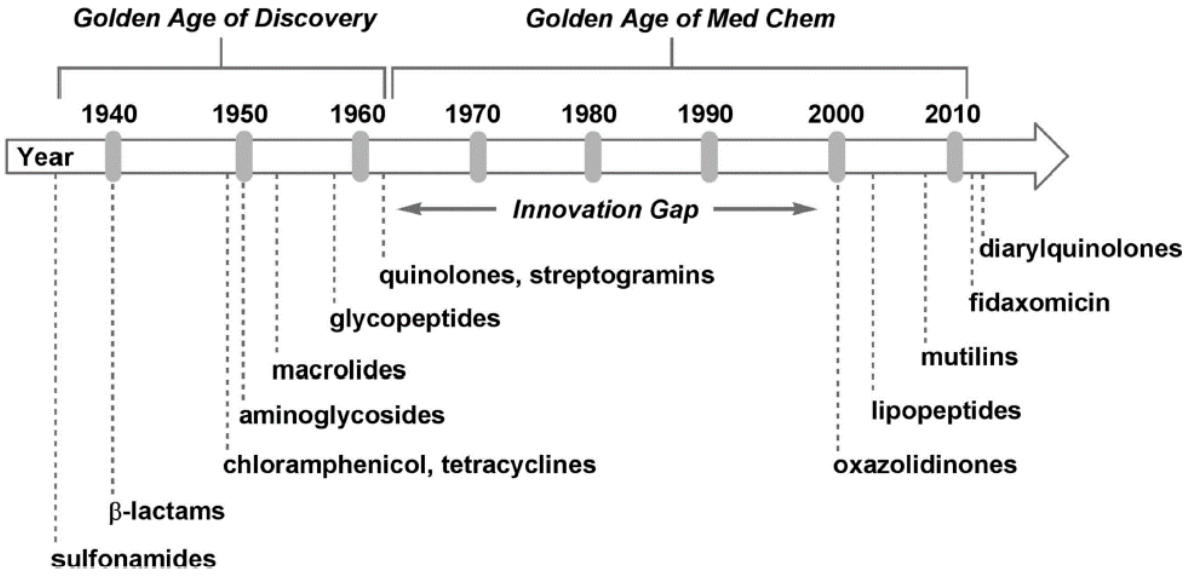

Figure 1-1: The timeline of antibiotic discovery. The Golden age of discovery (1940-1960), golden age of medicinal chemistry (1960-present), innovation gap (1962-2000) are indicated together with the timeline for innovating different classes of antibiotics (Figure reprinted by permission from Springer Nature, The Journal of Antibiotics, Ref. 8, 2014).

lowering the cellular mechanical strength. β-lactams are used to treat both Gram-negative and Gram-positive infections, whereas the glycopeptides are only used to treat Gram-positive bacteria [10].

(2) Protein synthesis inhibitors target 50S or 30S subunits of ribosomes. The 50S ribosomal subunit inhibitors, such as macrolide, lincosamide, amphenicol (*e.g.*, chloramphenicol) and oxazolidinone (*e.g.*, linezolid) classes of antibiotics block initiation of translation or inhibit the peptidyl transferase reaction by translocating peptidyl tRNAs. Tetracycline and aminocyclitol classes of antibiotics target the 30S subunit of the ribosome. Aminoglycosides encourage protein mistranslation by adding unsuitable amino acids into the elongating peptides [11].

(3) DNA replication inhibitors target DNA replication and transcription in bacterial cells by inhibiting DNA gyrase and RNA polymerase. Fluoroquinolones target DNA topoisomerase II (gyrase) and IV. The gyrase subunit A nicks double stranded DNA and subunit B introduces negative supercoils, in order to lower the positive supercoiling of DNA prior to DNA replication and transcription. Once the negative supercoils are introduced, DNA is re-annealed by gyrase subunit A. Fluoroquinolones bind to the subunit A of gyrase and the fluoroquinolone bound DNA strands are unable reanneal, resulting in cell death [12]. Rifamycins bind to the DNA bound-RNA polymerase subunit at the actively transcribing state. Rifamycins are bactericidal for Gram-positive and bacteriostatic to Gram-negative bacteria.

(4) Folate biosynthesis inhibitors have been identified and validated by the clinical use of several drugs. The sulfonamides act as analogs of p-aminobenzoic acid and become a competitive inhibitor of dihydropteroate synthase. Dihydro-folate reductase is the final enzyme of the folate biosynthetic pathway which is inhibited by diaminopyrimidine antibiotics (*e.g.* trimethoprim). Affecting the folate pool in the cell inhibits growth, as the reduced folate is an important co-factor for the biosynthesis of cellular components [13].

(5) Membrane cell disruptors, which affect cell membrane integrity (*e.g.*, daptomycin) will cause membrane depolarization and disturb membrane associated processes such as cell division and cell wall biosynthesis, causing cell death. Daptomycin is delivered in micelles and once it has approached closer to the bacterial membrane it can be inserted into the bilayer. It has been predicted that daptomycin can

oligomerize in the membrane resulting in large pores, which leads to membrane depolarization, potassium efflux and cell death [14]. This is a more recent target and has been common in the clinical setting [8].

1.3 Novel targets in the pipeline for antibiotic development

The expansion in bacterial genomics, transcriptomics, bioinformatics and proteomics have facilitated novel target identification for the advancement of antibiotic development.

Antibiotics are designed based on the essentiality of the target involved in a key bacterial process that is required for the viability of the pathogen during an infection. If a homolog of the projected target is present in human, it's important to identify whether there are adequate differences to suggest the selectivity of the antibiotic on the bacterial target. It is also important that the novel antibiotic target, to be conserved within and between bacterial species, so that the developed drug's effect can be applied to a wide range of bacteria [9].

Multiple possible bacterial targets have been identified recently and one such is the amino acid biosynthesis. Bacterial cells are capable of biosynthesizing the essential amino acids (leucine, lysine, tryptophan, histidine etc.) even though these cannot be synthesized by the human body. In addition, lysine is an important amino acid in bacterial peptidoglycan (cell wall) biosynthesis. Lysine (L,L-diaminopimelate aminotransferase (DapL)), aromatic amino acids and tryptophan biosynthesis pathways afford potential antibiotic targets [15, 16].

Teixobactin, a novel antibiotic that inhibits the cell wall biosynthesis by interacting with the lipid-pyrophosphate-sugar motif of Lipid II (a precursor of peptidoglycan) and Lipid III of wall teichoic acid (Gram-positive bacteria). Possibility of predicted mutations in the structure of Lipid II is very low, therefore, it's prophesied to be free from resistance for Teixobactin [17].

Quorum sensing (QS) is involved in bacterial communication and signaling. Signal molecules are produced to coordinate their behavior in a cell density dependent manner. In Gram-negative bacteria acylhomoserine lactone (AHL) QS system and in Gram-positive bacteria autoinducing peptide (AIP) QS system, and in both autoinducer-2 (AI-2) QS systems are used. The QS system is important for bacterial

biofilm formation, maturation and dispersal. Bacterial biofilms show an altered lifestyle than planktonic cells, and therefore, harder to be treated by antibiotics. Inhibitors of the QS system is a promising to target biofilm formation and making biofilm-entrenched cells susceptible to antibiotics [18].

Two component signal transduction system is involved in monitoring the bacterial external environment and allowing bacteria to adapt for survival. This system has shown to play an important role during infection. Bacterial cell division inhibition is another possible target, as the process involves many protein-protein interactions, such as FtsZ and FtsA. Additionally, isopreniod and fatty acid biosynthesis pathways are also considered to be suitable for antibacterial agent development.

1.4 *Pseudomonas aeruginosa*, an opportunistic pathogen that has developed Multidrug Resistance

In the 2017 World Health Organization report on prioritizing pathogens to guide discovery of new antibiotics, carbapenem resistant *Pseudomonas aeruginosa*, *Acinetobacter baumannii* and, carbapenm and 3rd generation cephalosporin resistant *Enterobacteriaceae* have been categorized as critical priority pathogens [19]. According to the Center for Disease Control and Prevention (CDC 2019) multidrug resistant *Pseudomonas aeruginosa* is categorized as a serious threat. During 2017, in the USA, about 32,600 estimated cases among hospitalized patients were caused by multidrug resistant *P. aeruginosa,* resulting in about 2700 deaths [20, 21].

Pseudomonas aeruginosa infections have gained much more attention in hospital acquired infections, mainly among immunocompromised and critically ill patients. *P. aeruginosa* colonization in the intensive care and burn units, especially in medical devices such as in urinary catheters and endotracheal tubes, have been a serious issue. *P. aeruginosa* form antibiotic and disinfectant tolerance biofilms on biotic and abiotic surfaces. They use swimming, swarming and twitching motilities, and their capability to migrate against a flow, enhance their colonization of surfaces relative to other bacterial species. The biofilm environment helps the development of small colony variants and persister cells, which can tolerate high antibiotic concentrations. Also, the penetration of the antibiotic deeper into the biofilm can be limited. *P. aeruginosa* can adjust metabolism and virulence factor expression accordingly, causing acute and chronic

infections. The outer membrane of *P. aeruginosa* has limited permeability, and the organism is equipped with a variety of efflux pumps limiting the access of the antibiotics into the bacterial cell [22]. In some cases, they are intrinsically resistant to antibiotics which they have never even being exposed to. *P. aeruginosa* can constantly express efflux pumps even in the presence of efflux pump inhibitors by readily generating mutations [23]. These resistant mechanisms are encoded intrinsically in the chromosome and or genetically imported. *P. aeruginosa* expresses antibiotic inactivating enzymes such as AmpC β-lactamases that can degrade multiple β-lactam antibiotics. In addition, target modifications like accumulation of porin mutations and expression of carbapenemases can block the carbapenem import. The resistance mechanisms of some strains of *P. aeruginosa* are affective on major classes of antibiotics such as aminoglycosides, carbapenems, cephalosporins and fluoroquinolones [22]. *P. aeruginosa* cells produce antibacterial effectors and has the capability of growing in competitive environments such as in polymicrobial infections. These features of *P. aeruginosa* require second- or third-line drugs to treat infections, which makes this pathogen prone to further potential resistant development.

1.5 Novel therapeutics in the pipeline for the treatment of *P. aeruginosa* infections

Currently, *P. aeruginosa* infections are treated by broad spectrum antibiotics, such as aminoglycosides or fluoroquinolones, meropenem or imipenem (carbapenems), third generation cephalosporins or Gram-negative selective monobactam, aztreonam and piperacillin, alone or in combination with tazobactam. Polymyxin B and E are given under a life-threatening Gram-negative infection, as these drugs are neurotoxic and nephrotoxic [24].

In addition to the existing antibiotics, novel therapeutic agents are also emerging. KB001 is a high affinity antibody fragment that binds to the PcrV protein, inhibiting the type three secretion system (T3SS). KB001 is in the phase II clinical trials. Inhibiting the type three secretion system, reduces the pathogenicity and toxicity to patients' immune and epithelial cells, and enhance the clearance by antibiotics [25]. A bispecific therapeutic antibody (MEDI-3902), which is also in phase II clinical trials, can recognize PcrV

and the biofilm matrix polysaccharide Psl. The anti-Psl navigate the antibody towards the cell surface where anti-PcrV will inhibit the T3SS [26].

NXL104 is a class of diazabicyclo [3.2.1] octanone capable of inhibiting many serine β-lactamases. The combination of NXL104/ceftazidime is an inhibitor-cephalosporin combination that is in phase II clinical trials. In addition, several novel β-lactamase inhibitor/antibiotic (lactams, piperacillin) combinations are currently being tested [24].

Inhibiting lipopolysaccharide (LPS) biosynthetic or transport enzymes can be lethal or can potentiate penetration of antibiotics into Gram-negative bacterial cells. Currently, protein inhibitors of LpxC (lipid A biosynthesis) and LptD (involved in the LPS transport system from inner to outer membrane) are being studied; the latter is in phase III clinical trials [23].

Bacterial efflux pump inhibitors are another potential lead for therapeutic development. These inhibitors could increase the antibiotic concentrations in the cells and the treatment could be in combination with currently used antibiotics. An example for an efflux inhibitor and an outer membrane permeabilizer is phenylalanine−arginine β-naphthylamide, which hasn't been tested clinically due to its toxicity. This approach has not yet been tested beyond preclinical tests [24, 27, 28].

Iron uptake and disruption of iron homeostasis is another approach for the development of antibacterial compounds. Approaches so far include: (i) reducing host bioavailability of iron by natural or synthetic iron chelators, (ii) inhibition of iron uptake by inhibiting siderophore biosynthesis or internalization, (iii) siderophore-drug conjugates to deliver antibiotics, (iv) iron metabolism inhibitors, and (v) use of iron mimics such as Ga(III).

The FDA approved Ganite®'s [active ingredient $Ga(NO_3)_3$] is used for the treatment of hypercalcemia. In the context of potential antibiotic applications, biological systems are unable to discriminate Fe(III) and Ga(III) because of the similarities in their ionic radii. Therefore, Ga^{3+} can substitute Fe^{3+} in the cell, but lacks redox properties of iron. Therefore, Ga^{3+} can inhibit or retard iron required cellular processes competitively. The gallium-based compounds have shown promising effects against cystic fibrosis and multidrug resistant *P. aeruginosa* in planktonic and biofilm bacterial communities [29-31].

1.6 Bacterial iron homeostasis as a target for antibiotic development

1.6.1 Iron is an essential nutrient

Iron is an essential nutrient for both humans and bacteria. Iron is involved my many biological processes in nature, such as photosynthesis, N_2 fixation, tricarboxylic acid cycle, oxygen transport, DNA biosynthesis etc. Iron utilizing biological functions depend on incorporating iron into proteins as mono- or bi-nuclear iron centers or as heme. Iron exists in two main oxidation states, ferric (Fe^{3+}) and ferrous (Fe^{2+}). In oxygenated environments soluble Fe^{2+} (0.1 M at pH 7.0) converts to insoluble Fe^{3+} (10^{-18} M at pH 7.0) resulting in lower bioavailability than the nutritional requirement of bacterial cells, which is about 10^{-7} to 10^{-5} M [32]. The ability of iron to undergo oxidation and reduction reactions is an important factor for its biological functions. However, the redox cycling of iron can generate free radicals and other strongly oxidizing species, causing damage to the cells. In the cell, hydrogen peroxide is produced in processes related to respiration. Free ferrous ions react with H_2O_2, producing hydroxyl radicals and ferric ions. Ferric

$$Fe^{3+} + O_2^{\cdot -} \rightarrow Fe^{2+} + O_2 \qquad (1)$$

$$Fe^{2+} + H_2O_2 \rightarrow Fe^{3+} + OH^- + OH^{\cdot} \quad \text{(Fenton reaction)} \qquad (2)$$

The net reaction:

$$O_2^{\cdot -} + H_2O_2 \rightarrow O_2 + OH^- + OH^{\cdot} \qquad (3)$$

Figure 1-2: The involvement of the Fenton chemistry in Haber-Weiss reaction is the major mechanism of generating hydroxyl radicals in the cells. (Figure reprinted from Ref. 34., copyright (2000), with permission from Elsevier)

iron reacts with $O_2^{\cdot -}$ producing oxygen and regenerating the ferrous catalyst [33]. As shown in **figure 1-2**, involvement of Fenton chemistry in the Haber-Weiss cycle is a major mechanism for generating hydroxyl radicals in cells [34].

For effective iron homeostasis, bacteria should uptake enough iron to fulfil their nutritional requirements while managing cellular iron levels to avoid iron induced toxicity that could be generated by

Fenton reaction [32]. Iron acquisition and storage in bacteria are controlled by the ferric uptake regulator (*fur*), which controls the bacterial iron metabolism depending on iron availability. Under iron replete conditions, Fe^{2+} bound Fur forms homodimers and interact with Fur box sequence within the target promoters, repressing the expression of iron acquisition genes. This could be direct repression or indirect repression by extra cytoplasmic sigma factors (ECF σ) [35].

Under high intracellular iron levels Fur positively regulates the expression of nonessential iron using proteins, iron storage proteins, carbon metabolizing, respiration and reactive oxygen species detoxifying enzymes by repressing small RNAs (*e.g.,*PrrF1 and PrrF2) [36]. In *Pseudomonas aeruginosa* and in *Mycobacterium tuberculosis fur* has been identified as an essential gene, as the *fur* knockout mutants were not viable [37].

1.6.2 Iron uptake

The concentration of iron under physiological conditions is orders of magnitude below the required level for bacterial growth. In the host, there are multiple ways to restrict iron availability for pathogens. Lactoferrin in the host can reversibly coordinate Fe^{3+} with a higher binding affinity. It scavenges free iron in the blood restricting the iron availability for pathogens. Transferrin is mainly found in secretions and granules of neutrophils; it sequesters iron from mucosal surfaces and release iron from neutrophils at an infection. Even though, the host nutritional immunity exists, bacterial have evolved diverse strategies for iron acquisition.

a) Siderophores

In order to acquire iron from the natural environments or from an infection setting, pathogenic and nonpathogenic bacteria synthesize, secrete and retrieve siderophores, which are high affinity iron chelators ($K_d = 10^{-20}$ to 10^{-52} M). Siderophores could dissolve iron from insoluble salts and extract iron from the host Fe sequestering proteins. Siderophore syntheses is a ribosomal independent process, which utilizes citrate, chorismate, proteogenic and nonproteogenic amino acids. Depending on the nature of the Fe^{3+} coordinating

moieties, siderophores can be categorized into four groups, catecholates, hydroxamates, (α-hydroxy-) carboxylates, phenolates and mixed type [38].

P. aeruginosa produces two major siderophores for Fe^{3+} acquisition, pyoverdine and pyochelin. Pyoverdine is the high affinity siderophore (K_a=10^{32} M^{-1}) and it consists of a peptide chain (amino acids may vary from 6-12), and a chromophore. Iron is coordinated by two hydroxamate and one catecholate moieties. The peptide chain of pyoverdine varies between different Pseudomonas species [39]. The synthesized pyoverdine is secreted from the cell. Once the ferri-pyoverdine complex (PVDI) is formed, it is transported from the outer membrane to the periplasm via FpvA (FpvB receptor also has a minor contribution). In the periplasm iron is reduced and Fe^{2+} is released from the siderophore. It has been found that FpvG acts as a reductase and FpvH, FpvJ, and FpvK are involved as partners. Reduced iron is chelated by FpvC and delivered to the pyoverdine ABC transporter FpvDE for the translocation into the cytoplasm [40].

Pyochelin is the low affinity siderophore secreted by *P. aeruginosa*; its synthesis involves a lower number of genes than that of pyoverdine [39]. Under low iron conditions, pyochelin is first synthesized and secreted, when the iron become extremely low cells start to switch to pyoverdine biosynthesis [41].

b) Heme iron acquisition

P. aeruginosa also utilizes heme-iron. Heme-iron uptake from hemoproteins, such as hemoglobin and hemopoxin, is carried out *via* two systems, Has and Phu. In the Phu system, heme is directly extracted by an outer membrane, TonB-dependent receptor (TBDR). In the Has system, heme is extracted *via* a hemophore and this complex is recognized by HasR, which is another TBDR. Heme is bound by a periplasmic binding protein and transported into the cytoplasm via an ABC transporter. Next, heme is bound by a heme chaperon PhuS and delivered to heme oxygenase (HemO) for the degradation of heme into biliverdin, CO, and Fe^{2+} [39].

c) Ferrous iron transporters

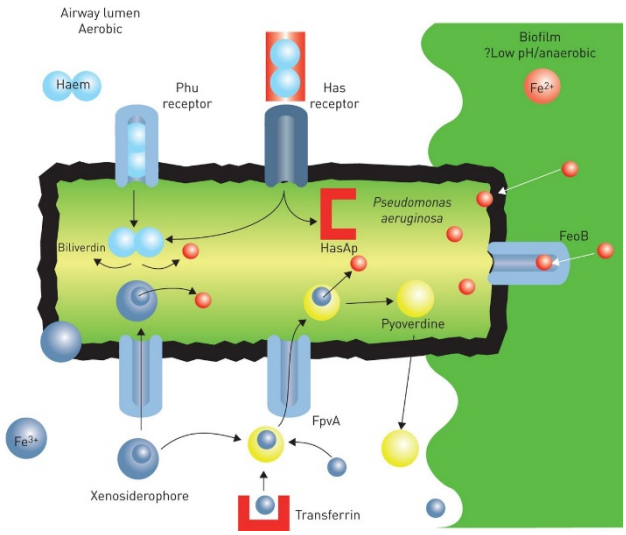

Figure 1-3: A summary of iron uptake systems in *P. aeruginosa*. Heme iron is acquired via Phu and Has systems. Siderophore, pyoverdine captured iron is transported to the periplasm via FpvA, reduced in the periplasm and transported into the cytosol. Feo system transports Fe^{2+} to the cytosol. (Figure reprinted from Ref. 31, with permission from European Respiratory Society)

Ferrous (Fe^{2+}) ion is the favorable form for bacterial utilization. Unlike Fe^{3+}, Fe^{2+} is comparatively soluble and this form can be predominating under anaerobic and low pH environments. Some bacteria have the capability to reduce Fe^{3+} to Fe^{2+} making it more soluble to uptake. Ferrous ions uptake can occur via passive diffusion through outer membrane porins. Iron in the periplasm is transported to the cytoplasm through the FeO system, which in gammaproteobacteria is composed of a permease FeoB and proteins FeoA, and FeoC. In the majority of bacteria (89 %), the Feo system contains FeoA and FeoB [42]. FeoA is a 8.3 kDa cytosolic protein which has a SH3-domain that could activate FeoB. FeoB is a 83 kDa transmembrane protein, where the C-terminal is an integral membrane domain and the N-terminal is a soluble domain. FeoC is a 8.7 kDa cytosolic protein which regulates the transcription of FeoB. A proposed model for FeoB shows that the GTPase activity of FeoB is stimulated by Fe^{2+}. Once the Fe^{2+} is bound to the G-domain, it sends out a signal for GTP binding. GTP binding or GTP hydrolysis will result a conformational change in the protein, opening the pore allowing Fe^{2+} to flow into the cytosol [43-45].

1.6.3 Iron storage molecules

Iron storage proteins act as an iron reservoir, supporting growth when iron supplies are limited. Additionally, they manage cellular iron levels to protect cells from iron induced toxicity. Bacteria can have three types of iron storing proteins, ferritins (Ftn), bacterioferritins (Bfr) and Dps (DNA-binding protein from starved cells). These are composed of 24 (ferritins and bacterioferritins) or 12 (Dps) subunits which are arranged as a sphere, creating a central cavity for iron storage. Ferritins and bacterioferritin are large proteins (about 500 kDa) that can store 2000-3000 iron atoms in their central cavity, whereas Dps can store about 500 iron atoms. All the above types are thought to co-exist in the same bacterium cell [32].

a) Ferritin and Bacterioferritin

Bacteria has two ferritin like molecules, the bacterioferritins (Bfr) and bacterial ferritins (Ftn). Ftns and Bfrs are assembled as nearly spherical hollow structures, which have an outer diameter of ~ 120 Å and an inner diameter of ~ 80 Å [46]. The Bfrs and Ftns are made of 24 subunits, where each subunit exhibits

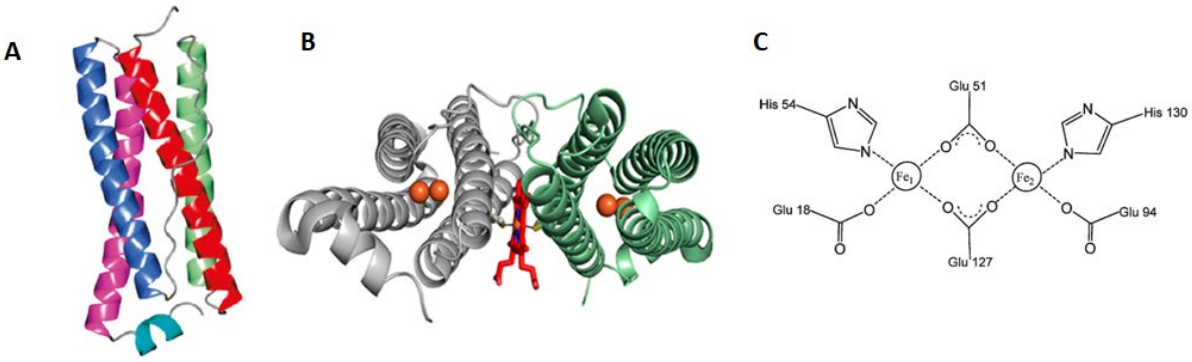

Figure 1-4: A) The classical four- helix fold of ferritins, helix A (red), a long loop connects helix B (green) to C (blue), helix D (magenta) is followed by helix E (Cyan). (B) Subunit dimer of Bfr, heme molecule (Red) between two subunits is coordinated via methionine residues from each subunit. Ferroxidase centers (FCs) are located at the center of each subunit, iron in FCs are shown as orange spheres. (C) A typical symmetrical ferroxidase center of bacterioferritin, Glu51 and Glu127 are bridging ligands, and His54/Glu18 and His130/Glu94 are capping pairs. (Figures are reprinted with permission from: Ref. 47 copyright (2011) American Chemical Society, Ref. 48 (https://doi.org/10.1021/acs.biochem.5b00937, further permissions related to the material excerpted should be directed to the ACS) and Ref. 49 copyright (2010) American Chemical Society)

a four-helix bundle fold as illustrated in **Figure 1-4-A**: two homologous pairs of antiparallel helixes [helices A (red) and D (magenta)]; a long loop connects helix B (green) to helix C (blue) and the helix D is followed by a small α-helix (E helix-cyan) perpendicular to the four-helix bundle [47].

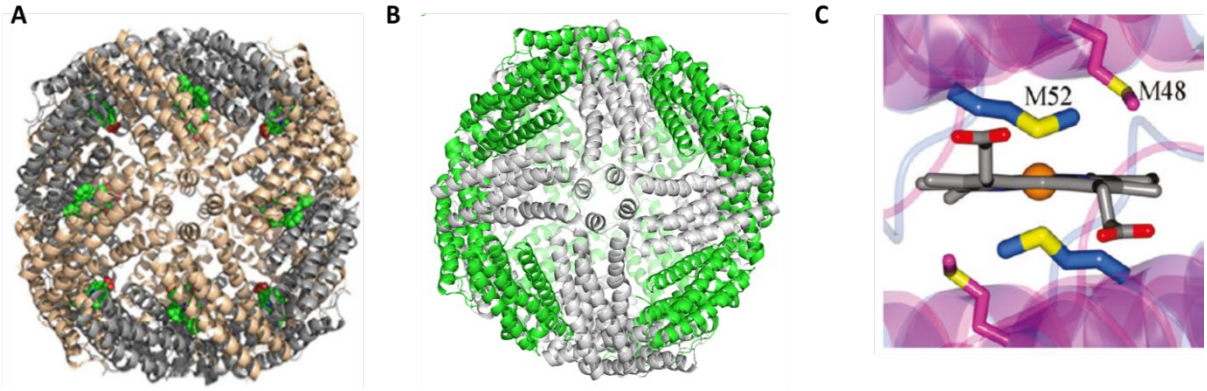

Figure 1-5: Two ferritin like molecules coexist in *P. aeruginosa.* (A) Structure of mineralized BfrB from *Pseudomonas aeruginosa* (PDB ID: 3IS7) and (B) As-Isolated FtnA from *Pseudomonas aeruginosa* (PDB ID: 3R2K). Both assemble into a 24-mer. (C) BfrB can coordinate a heme via M52, in between two subunits where the M48 from FtnA is not. (Figures are reprinted with permission from: Ref. 55 copyright (2013) World Scientific and Ref. 47 copyright (2011) American Chemical Society)

Each four-helix bundle harbors a ferroxidase center (FC). Iron is taken to the proteins as Fe^{2+} and oxidized to Fe^{3+} via a ferroxidation step occurred at the ferroxidase centers. Ferroxidase center residues are highly conserved and have the capability to coordinate two Fe^{2+} ions. In ferritins and bacterioferritins, ferroxidase centers are in the central area of individual subunits as illustrated in **Figure 1-4-B** [48]. Many ferroxidase residues are widely conserved with only few differences. The iron in the FC is shown as orange spheres and the two subunits of Bfr is are colored in grey and green. **Figure 1-4-C** illustrates a symmetrical ferroxidase center of a typical bacterioferritin, which contains two Glu bridging ligands and, Glu and His as capping ligands [46, 49]. Once the Fe^{2+} is bound, it is oxidized to Fe^{3+} by O_2. Next, the oxidized iron is stored as ferrihydrite or ferric phosphate in the core of the protein [32].

Ftn and Bfr proteins in many ways are similar in bacterial and archaeal domains of life. They share the same quaternary structure and have a similar E helix in the C-terminus of their subunits. The most important difference between Ftn and Bfr is the binding of heme in Bfr. A 24-meric protein can bind 12 hemes. The heme iron is located at a two-fold center of symmetry between two subunits, which places the heme molecule toward the inner surface of the protein. As demonstrated in **Figure 1-4-B** and **1-5-C**, the heme iron is coordinated by two methionine residues, one from each of the two-fold related subunits [50]. The formed spherical Bfr and Ftn shells have channels at the symmetry sites (where subunits meet), which allows iron and other small molecules to enter and exit the protein, which are further discussed in section **1.7** [51].

In *P. aeruginosa*, *bfrA* and *bfrB* are the two distinct genes coding for ferritn-like molecules. In global genetic response experiments, *bfrB* was observed to be upregulated in response to high iron conditions, whereas *bfrA* did not respond to different iron conditions [52]. The *bfrA* gene is currently added as *ftnA* in the *P. aeruginosa* genomic database and the gene codes for FtnA, a bacterial ferritin. The conserved heme ligand, M52, is only present in BfrB and not in FtnA [47]. The M48 present in FtnA is too far for the coordination of a heme molecule (**Figure 1-4**). These observations demonstrated that the product of *ftnA* (FtnA) did not evolve a heme binding site. The ferroxidase centers of BfrB coordinate Fe_1 and Fe_2 using two bridging glutamate ligands and by glutamate and histidine capping ligands, which is an arrangement characteristic of ferroxidase centers in Bfrs. In FtnA, Fe_1 and Fe_2 is bridged *via* only one glutamate ligand, which is an arrangement commonly observed in Ftns. The products from *bfrB* and *ftnA* genes encodes for bacterialferritin (Ftn) and a bacterioferritin (Bfr) respectively [46].

1.7 Structure-function relationships in *Pseudomonas aeruginosa* -Bacterioferritin B (*Pa*-BfrB)

Pa-BfrB share similar structural features with other bacterioferritins. BfrB consists of 24 subunits and 12 hemes. Two subunits form a dimer harboring a heme, which is coordinated by Met52 from each subunit (**Figure 1-6-A**) . Heme molecules are buried inside the protein shell, with the heme propionates

extending into the interior cavity where the Fe^{3+} mineral is stored (**Figure 1-6-B**). Ferroxidase centers (FC) are present in the middle of each four-helix bundle [53].

At the FC, Fe1 and Fe2 are coordinated by the residues Glu51 and Glu127 as bridging ligands. The residues Glu18 and His54, Glu94 and His130 act as capping ligands for Fe1 and Fe2, respectively (**Figure 1-6-C**) [49]. X-ray crystal structures from crystals of *Pa*-BfrB soaked in Fe^{2+}solution, suggested possible routes for iron entrance and translocation in the ferroxidase centers [49]. The His 130 of BfrB is flexible and can adopt the "gate open" conformation when the FC is empty, or the "gate closed" conformation when Fe is bound at the di-Fe^{2+}-centers. Once Fe^{2+} is bound to the FCs forming a di-iron center, the bound iron is oxidized by O_2 or H_2O_2 forming a μ-oxo/hydroxo di-Fe (III) moiety, which triggers the rearrangement of His130 to the "gate open" position, allowing the Fe^{3+} to move into the protein interior cavity and be stored as a ferric mineral [49]. The flexibility of the His130 side chain allows internalization of iron and subsequent

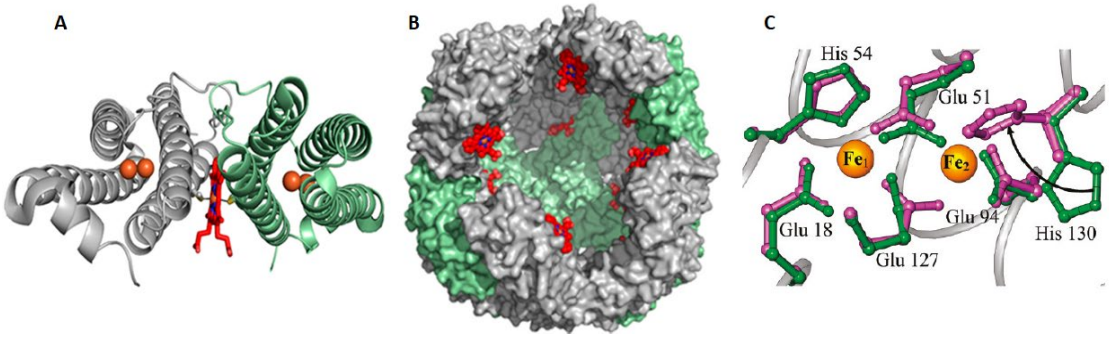

Figure 1-6: (A) Subunit dimer and the coordination of heme (red) by a conserved methionine in each of the subunits. (B) BfrB interior cavity, heme buried inside the protein shell propionates extending into the interior cavity. (C) Overlay of the FCs of *Pa*- BfrB structures, the "gate open" (green) and "gate closed" (magenta). The rotation of His 130 facilitates Fe^{2+} binding to the FC for oxidation to Fe^{3+} and subsequent entry of Fe^{3+} to the interior cavity for storage. (Figures are reprinted with permission from: Ref. 48 (https://doi.org/10.1021/acs.biochem.5b00937, further permissions related to the material excerpted should be directed to the ACS) and Ref. 49 copyright (2010) American Chemical Society)

entry of the ferroxidase iron into BfrB cavity. Once the iron is internalized the FC is ready to start another cycle.

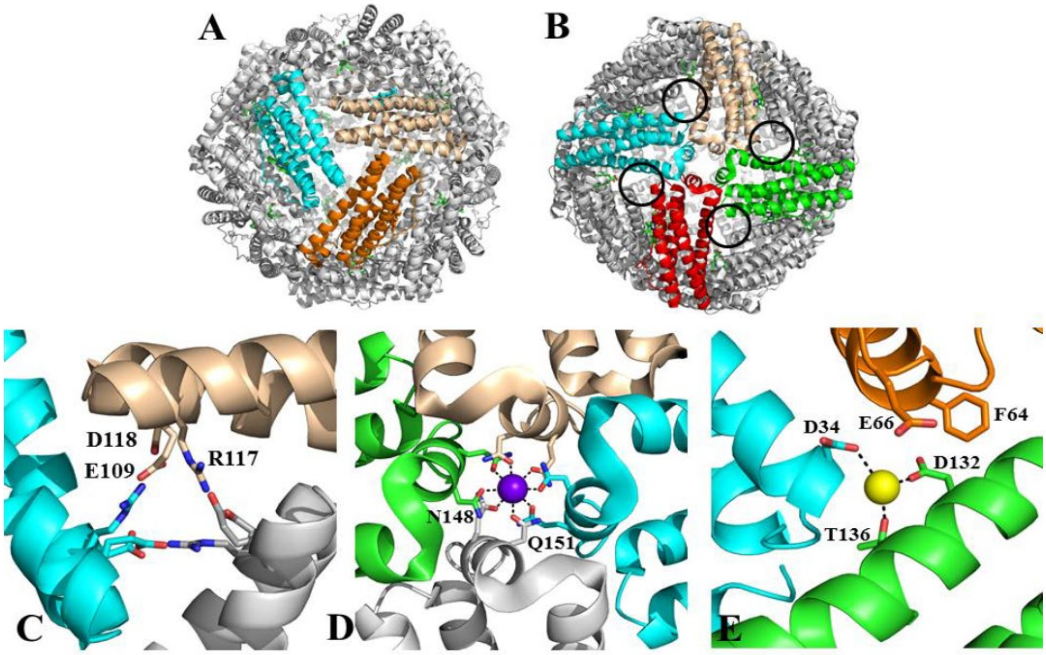

Figure 1-7: A) The view of one of the 3- fold pores and (B) 4- fold pores of BfrB. The B-pores surrounding the 4-fold pore is marked with black circles. (C) The 3- fold pores are lined with alternative positively and negatively charged residues. (D) In the 4-fold pore, a potassium ion is coordinated by the N148 and Q151 residues. (E) View of a B-pore, a sodium ion coordinated by D34, D132 and T136. (Figures are reprinted with permission from Ref. 54 copyright (2015) American Chemical Society)

The protein shell of ferritins separate iron mineral stored in the protein core from the cytosol, which helps to avoid unwanted reactions occurred by iron. In order to traffic iron and small molecules in and out, ferritin shells consist pores (**Figure 1-7-A** and **1-7-B**) [54]. There are eight 3-fold pores and six 4-fold pores in 24-mer ferritins [46]. These channels connect the protein core to the exterior. The 3-fold channels of the bacterioferritins are lined alternatively by positively and negatively charged residues. The **Figure 1-7-C** shows one of the 3-fold pored of *Pa* BfrB viewed from the exterior surface [46, 49, 55].

In *Pa* BfrB three Glu 109 residues form salt bridges with three Arg 117, capping the pore entrance. Residues Asp 118 and Asp 122 are lining the interior of the pore [46, 49]. X-ray crystallographic analysis of Fe-soaked *Pa*-BfrB crystals revealed the presence of sulphate ions (from the crystallization solution) in the middle and the bottom of the 3-fold pores; at the exit into the interior cavity interacting with three iron irons [46, 49]. When iron is storied as Fe^{3+} mineral in BfrB, iron is deposited nearly at a 1:1 ratio with phosphate. Phosphate is an important component for the formation of the BfrB core mineral. The exploration of the 3- fold pores suggest the possibility of trafficking phosphate ions through 3- fold pores to get access to the BfrB interior cavity, where they interact with Fe^{3+} before mineralization [49, 54, 55].

The 4- fold pores in the *Pa* BfrB consist of two layers: Asn 148 outer layer and Gln 151 inner layer. As shown in **Figure 1-7-D**, the 4-fold pore shows binding of a potassium ion (purple sphere) coordinated by four Asn 148 and Gln 151 residues [49]. The presence of the potassium ion is reasonable because the protein storage buffer is 100 mM potassium phosphate. The presence of cations in the 4-fold pore was also observed in two *Azotobacter vinelandii* Bfr structures, where one contains iron and the other contains Ba^{2+} [49]. Even though, iron ions were not observed in 4- fold pores of BfrB, iron ions have been bound at the external perimeter of the 4- fold pore. Therefore, it can be speculated that these sites can work as iron binding sites prior to oxidation at FCs or storing as ferric mineral [49].

In addition to the 3-fold and 4- fold pores bacterial Ftns and Bfrs have B-pores. As shown in **Figure 1-7-E**, the B-pores are located between three subunits at an asymmetric site [46]. The Fe-soaked crystals of C89S/K96C and D34F *Pa* BfrB revealed iron in the B-pores. The B-pores of C89S/K96C BfrB is indistinguishable from wild type BfrB [54]. The Fe-soaked structures show two iron ions: the innermost is coordinated by D132 and the outermost is coordinated by D34 and E66 [54]. The D132F mutant BfrB affected the reactivity of the FCs by lowering the conformational flexibility. Which indicates that the disturbing B-pores reduce the access of iron into the interior of BfrB [46, 54].

1.8 Iron mobilization from bacterioferritinB; insights from *in-vitro* studies

Under high iron conditions the *bfrB* gene is upregulated. Under low iron conditions the genes coding for bacterioferritin-associated ferredoxin (*bfd*) and ferredoxin reductase (*fpr*) are upregulated [56]. It is also noteworthy that the *Pa-bfrB* gene is contiguous to [2Fe-2S] cluster binding bacterioferritin-associated ferredoxin (Bfd). These observations led to the proposal of an electron transfer model for the mobilization of iron from BfrB **(Figure 1-8-A)**, which proposed electron transfer from NADPH to the NADPH dependent flavoprotein *Pa*-Fpr and from *Pa*-Fpr to the [2Fe-2S] cluster of *Pa*-Bfd [55]. The validity of this model has been tested *in-vitro* by mobilizing iron from BfrB in the presence of NADPH, recombinant Fpr, and recombinant Bfd, in the presence of the Fe^{2+} chelator 2'2-bipyridine, which allowed monitoring of Fe^{2+} mobilization from BfrB by following the absorbance (523 nm) of the $[Fe(bipy)_3]^{2+}$ complex (**Figure 1-8-B**) [57]. The addition of NADPH to a mixture of BfrB and Fpr showed negligible iron release (the bottom trace in **Figure 1-8-B**). In contrast, the addition of Bfd promoted fast and complete iron release from BfrB (the top trace in **Figure 1-8-B**) [57]. The participation of the [2Fe-2S] cluster of Bfd in electron transfer has been shown by the spectroscopic observations following the reduced form of the

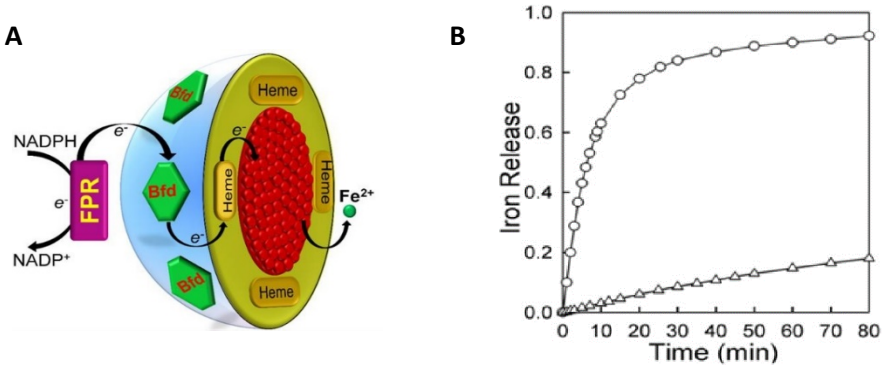

Figure 1-8: A) Electron flow path from NADPH is mediated by FPR, Bfd and heme in BfrB. Electrons delivered from heme reduce the Fe^{3+} mineral, and allow mobilization of Fe^{2+}. B) Iron release *in-vitro* is monitored by the formation of the $[Fe(bipy)_3]^{2+}$complex, (Δ) *Pa*-BfrB and *Pa*-FPR, and (○) *Pa*-BfrB, *Pa*-FPR and *Pa*-Bfd. The absorbance at 523 nm is normalized to the absorbance reading once all the iron in BfrB is mobilized. (Figures are reprinted with permission from: Ref. 55, copyright (2013) World Scientific and Ref. 57 (https://doi.org/10.1021/ja305180n, further permissions related to the material excerpted should be directed to the ACS))

[2Fe-2S] cluster attaining spectral characteristics of oxidized [2Fe-2S] clusters during [57]. These investigations also showed that electrons from Bfd are transferred to the iron core of BfrB *via* the heme.

1.9 Structure of the BfrB:Bfd complex

The co-crystal structure of the BfrB:Bfd complex revealed that 12 Bfd molecules can bind to a 24 mer BfrB (**Figure 1-9-A**) [57].Bfd is bound at the interface of the BfrB subunit dimer right above the heme. The [2Fe-2S] cluster of Bfd is placed approximately 22 Å from the heme iron of BfrB (**Figure 1-9-B**) [57]. The *in vitro* iron release experiments (see above) demonstrated that the electron transfer from the [2Fe-2S] cluster in Bfd to the Fe^{3+} mineral in the interior cavity of BfrB is mediated by heme [53]. The BfrB:Bfd

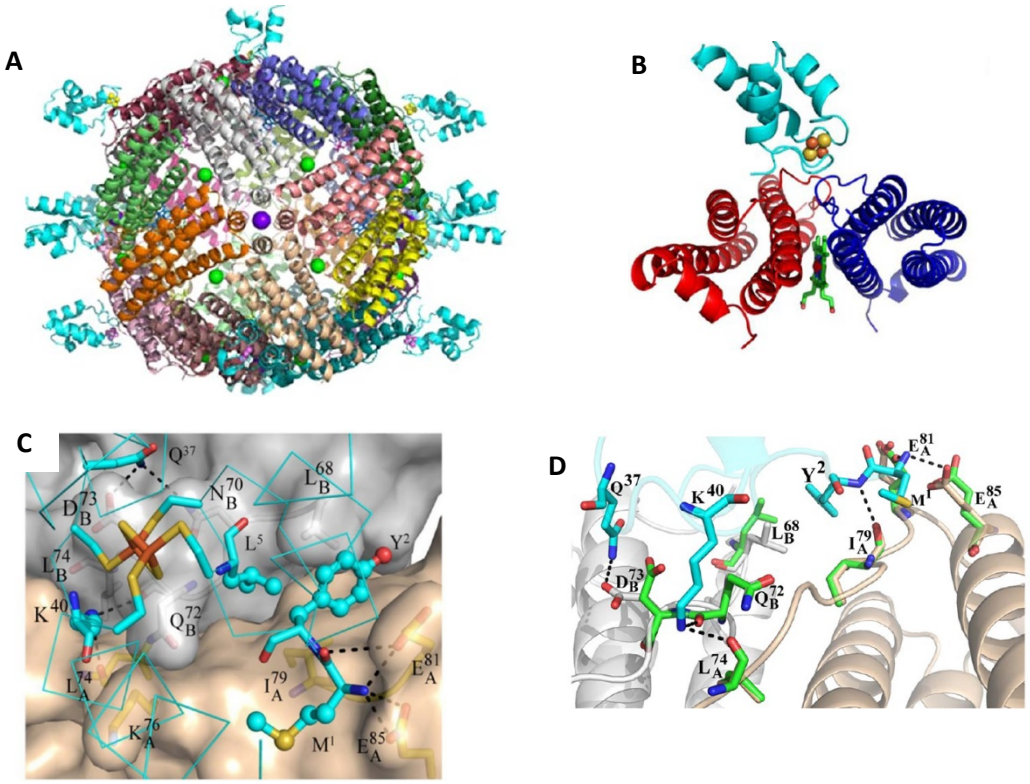

Figure 1-9: The structure of BfrB:Bfd complex. A) In the biological assembly 12 Bfd molecules are bound to a 24 mer BfrB. B) Bfd is bound between two subunits of BfrB (subunit A- **wheat**, subunit B- **grey**) above the heme. C) The BfrB-Bfd interface, Bfd is in cyan and the two subunits of BfrB are in wheat and grey. D) A representation of rearrangement in BfrB upon Bfd binding, Bfd-cyan, side chains of unbound BfrB- green and changes in BfrB, subunit A- wheat and subunit B – grey. (Figures are reprinted with permission from Ref. 57 (https://doi.org/10.1021/ja305180n, further permissions related to the material excerpted should be directed to the ACS))

structure revealed that the edge to edge distance of the [2Fe-2S] in Bfd and heme in BfrB is 15.1 Å. The electron transfer is likely to happen from the S2 of the iron sulfur cluster to vinyl β carbon of heme with the help of Q72 and L71 residues [57]. The stability of the Bfd fold maintained by a phosphate ion, which helps to maintain the integrity of the [2Fe-2S] cluster [57, 58].

The protein-protein interaction interface of the BfrB:Bfd complex is shown in **Figure 1-9-C** [57]. The Bfd protein is shown in cyan and the two subunits of BfrB are shown in grey and wheat. The minor rearrangements in the L68, E81 and E85 of BfrB are crucial to the stability of the complex. The binding of Bfd Y2 and L5 are accommodated by narrowing the cleft formed by E81 and L68 of BfrB. The changes in BfrB residues before binding with Bfd are shown green and, after binding in wheat (subunit A) and grey

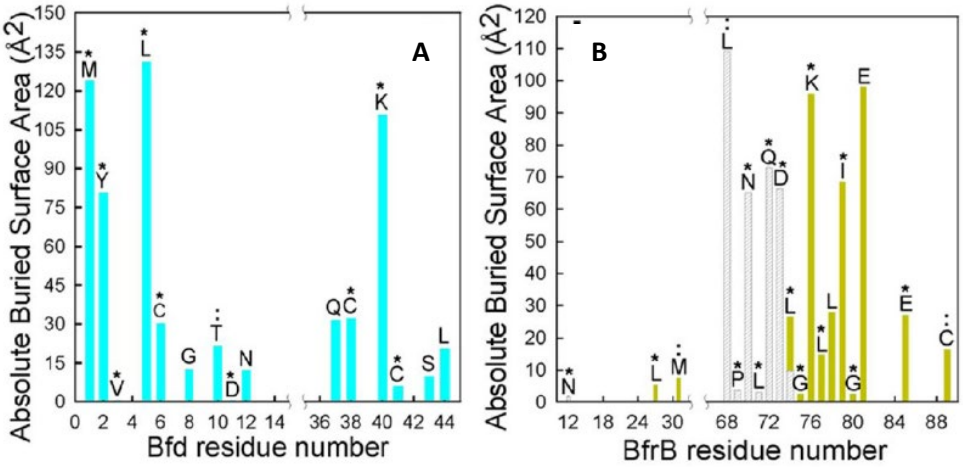

Figure 1-10: Buried surface area per residue at the BfrB:Bfd complex interphase. A) Contributions of Bfd residues- cyan B) Contributions of BfrB residues in subunit A- grey and subunit B- yellow. * Conserved residues, : Conservative replacements. (Figures are reprinted with permission from Ref. 57 (https://doi.org/10.1021/ja305180n, further permissions related to the material excerpted should be directed to the ACS))

(subunit B). The average rmsd of main and side chains of *Pa*-BfrB subunits, and the *Pa*-BfrB:Bfd complex is 0.14 and 0.67 Å respectively [57]. The buried surface area at the BfrB:Bfd interface is 607 Å^2. The amino acid residues at the interface and their total buried surface are shown in **Figure 1-10** [57]. The residues Y2,

L5 and K40 in Bfd are the largest contributors to the buried surface of Bfd (**Figure 1-10-A**). The side chains of these residues are wedged in a cleft formed on the surface of BfrB. M1, the fourth residue in Bfd with largest contribution to the buried interface, interacts with BfrB subunit A *via* hydrophobic interactions and H-bonding [57]. The symbols on top of the bars (*) represent conserved residues and the symbols (:) indicate conservative replacements in a number of Gram-negative pathogens. It is important to note that the majority of the amino acid residues at the buried surface of BfrB:Bfd interface are conserved, indicating the biological significance of this interaction in regulating the cytosolic iron in a variety of Gram-negative bacteria.

1.10 Hot-spot residues in the BfrB:Bfd complex

The hot spot residues of a protein-protein interaction contribute the most to the binding energy of the interaction. In order to identify the most important residues for the stability of the BfrB:Bfd complex and to identify the inhibition of iron mobilization from BfrB, the residues L68, E81, E85 and L68/E81 of BfrB, residues Y2, L5 and K40 of Bfd were mutated to alanine [48]. Iron release assays were carried out with the mutated BfrB- L68A, E81A, E85A and L68A/E81A in the presence of wild type Bfd. As shown in **Figure1-11-A** (green, orange and cyan traces), the mutations L68A, E81A and E85A lowered the iron release rates significantly, whereas in the double mutant L68A/E81A iron release is completely abolished [48].

The dissociation constant (K_d) of the wild type BfrB:Bfd complex has been determined to be 3 μM by Surface Plasmon Resonance (SPR) and Isothermal Titration Calorimetry (ITC) techniques [48]. The K_d values for the binding of Bfd to BfrB mutants L68A or E81A were 100-fold and 170-fold weaker than the value corresponding to the interaction of wt BfrB and Bfd, respectively. The dissociation constant for the association between L68A/E81A BfrB and Bfd could not be measured due to the abrogation of the BfrB:Bfd interaction [48]. The Bfd Y2F, K40A and L5A mutations have increased the K_d 3, 2 and 30-fold respectively. Consequently, residues L68, E81 and E85 in BfrB, and residues Y2 and L5 in Bfd were

identified as hot spot residues. The hot spot residues of the BfrB:Bfd interface are conserved in variety of Gram negative bacteria [57].

A

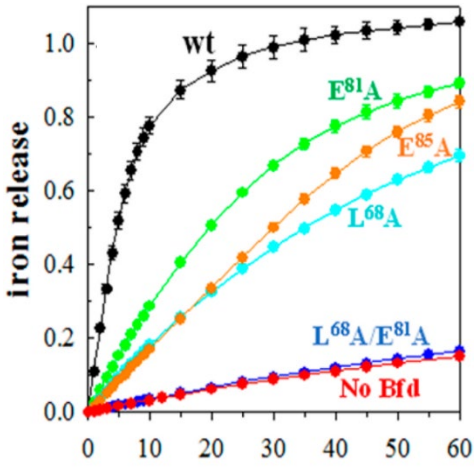

B

protein	K_d (μM) (pH 7.4)
wild type	3.3 ± 0.5
BfrB E81A	258.5 ± 21.5
BfrB L68A	298.5 ± 20.5
BfrB E85A	590 ± 2
BfrB L68A/E81A	not measurable
Bfd Y2F	10.7 ± 0.2
Bfd K40A	7.7 ± 0.5
Bfd L5A	82 ± 2.5

Figure 1-11: Iron mobilization from wild type and mutant BfrB. A) Iron mobilization is retarded in E81A, E85A and L68A. The double mutant L68A/E81A shows negligible amount of iron release, similar to that observed in the absence of Bfd. B) The dissociation constants of mutant BfrB and Bfd. **The dissociation constant of the BfrB:Bfd complex in BfrB L68A/E81A mutant is about 170 fold larger. In Bfd L5A mutant the dissociation constant is about 30-fold larger than the wildtype.** (Figures are reprinted with permission from: Ref. 48 (https://doi.org/10.1021/acs.biochem.5b00937, further permissions related to the material excerpted should be directed to the ACS))

1.11 Research problem and rationale

Iron is an essential nutrient for bacterial growth. Regulation of iron homeostasis is vital because it allows cells to have enough iron for growth while avoiding iron induced toxicity. The iron homeostasis machinery involves iron uptake, storage and mobilization. The essentiality of iron as a nutrient and the tight regulation of iron in the cells suggests iron homeostasis dysregulation as a good candidate for the development of novel antibiotics. To progress toward this goal, it is important to attain detailed understanding of iron homeostasis in the bacterial cells.

P. aeruginosa has two ferritin-like molecules, a bacterioferritin (BfrB) and a bacterial ferritin (FtnA). As will be shown in Chapter 2, BfrB has been identified as the main iron storage protein with the aid of native poly-acrylamide gel electrophoresis. As discussed above, previous *in-vitro* studies have demonstrated the importance of bacterioferritin associated ferredoxin (Bfd) in BfrB iron mobilization. In the absence of Bfd very little or no iron is mobilized from BfrB. Structural insights of the amino acid residues involved in the BfrB:Bfd interaction were gathered from the co-crystal structure of BfrB:Bfd complex, and residues E81, E85 and L68 in BfrB, and M1, Y2 and L5 in Bfd were identified as key amino acids that contribute to most of the binding energy of the complex. The *bfrB* and *bfd* genes are adjacent in the genome of *P. aeruginosa*, and the BfrB:Bfd hot spot residues are conserved in a number of Gram-negative bacteria. This is a very good indication of the biological significance of the BfrB:Bfd interaction in the regulation of bacterial iron in the cytosol. Consequently, disrupting BfrB:Bfd interaction is an appropriate target for novel antibiotic development and it is expected to have a broad impact.

Progressing toward identifying BfrB:Bfd as a new target, the work presented here explores the significance of disrupting the BfrB:Bfd interaction in *P.aeruginosa* cells using genetic and chemical intervention approaches. *P. aeruginosa*, wild type (PAO1) and Δ*bfd*, *bfrB(E81A/L68A)* and Δ*bfrB* mutant cells are used to study the consequences of disrupting BfrB:Bfd interaction *in-cells*. This is carried out by studying iron storage and iron mobilization by imaging iron in BfrB using optimized iron-stained native-PAGE gels and lysates of *P. aeruginosa* cells. In addition, the advantages of having an intact iron homeostasis machinery for the cells will be researched using wild type and Δ*bfd* mutant cells. The differences in the proteome and metabolome under the iron homeostasis dysregulation is explored using quantitative proteomics and bioinformatics. These results are discussed in chapter 2 and 4.

Capitalizing on the knowledge of the hot spot residues in the BfrB:Bfd interaction, our laboratory is developing inhibitors of the BfrB:Bfd interaction using a fragment-based drug discovery approach (FBDD), followed by iterative structure-based design. Initial screening of BfrB against a fragment library identified 6 fragments that are bound to BfrB at the Bfd binding interface. The co-crystal structure of

fragment **1** was used for the structure-based designing of small molecule BfrB:Bfd inhibitor library. The developed analogues are tested *in-vitro* and *in-cell*. In this work, the activity of the developed analogues against *P. aeruginosa* cells is tested, in order to identify the analogues that permeate the cell membrane. This is done by monitoring cell growth in the presence of different analogs at different concentrations. the relative efficacy of each analog was determined by calculating IC_{50} values. Furthermore, the consequences of inhibiting the BfrB:Bfd interaction in the bacterial cell using analogues is also evaluated. The results from these studies indicate that the analogues permeate the Gram-negative cell membrane, retard *P. aeruginosa* cell growth, address their target (BfrB) and inhibit iron mobilization from BfrB. In addition, the possibility of combination therapy is tested for the developed analogues with existing antibiotics. Interestingly, the analogues show an adjuvant effect on the floroquinolone family of commercially available antibiotics. The developed analogues are also tested against *P. aeruginosa* clinical isolates and *Acinetobactor baumannii* stains to rule out any strain specific effects.

The dysregulation of iron homeostasis by inhibiting the BfrB:Bfd interaction offer numerous advantages. First, bacterioferritins are unique to bacteria and the sequence similarity with eukaryotic ferritins are <20 %. Second, the BfrB:Bfd interaction in iron mobilization exists only in bacteria and the hot spot residues in this interaction are conserved in a variety of Gram-negative pathogens. Therefore, analogues designed to inhibit the BfrB:Bfd interaction in *P. aeruginosa* are likely to also inhibit the Bfr:Bfd interaction in other pathogens. In fact, the work presented here begins to explore this idea by demonstrating that analogues designed to inhibit the BfrB:Bfd interaction in P. aeruginosa also affect *Acinetobacter baumannii* cells.

1.12 References

1. Andriole, V.T., *The quinolones: past, present, and future.* Clin Infect Dis, 2005. **41 Suppl 2**: p. S113-9.
2. Silver, L.L., *Challenges of antibacterial discovery.* Clin Microbiol Rev, 2011. **24**(1): p. 71-109.
3. Walsh, C., *Opinion—anti-infectives: Where will new antibiotics come from?* Nature Reviews Microbiology, 2003. **1**(1): p. 65 %@ 1740-1534.
4. Ventola, C.L., *The antibiotic resistance crisis: part 1: causes and threats.* Pharmacy and therapeutics, 2015. **40**(4): p. 277.
5. Davies, J. and D. Davies, *Origins and evolution of antibiotic resistance.* Microbiol Mol Biol Rev, 2010. **74**(3): p. 417-33.
6. Centers for Disease, C. and Prevention, *Vital signs: carbapenem-resistant Enterobacteriaceae.* MMWR Morb Mortal Wkly Rep, 2013. **62**(9): p. 165-70.
7. Laxminarayan, R., et al., *Antibiotic resistance-the need for global solutions.* Lancet Infect Dis, 2013. **13**(12): p. 1057-98.
8. Walsh, C.T. and T.A. Wencewicz, *Prospects for new antibiotics: a molecule-centered perspective.* J Antibiot (Tokyo), 2014. **67**(1): p. 7-22.
9. Fields, F.R., S.W. Lee, and M.J. McConnell, *Using bacterial genomes and essential genes for the development of new antibiotics.* Biochemical pharmacology, 2017. **134**: p. 74-86 %@ 0006-2952.
10. Sarkar, P., et al., *A review on cell wall synthesis inhibitors with an emphasis on glycopeptide antibiotics.* Medchemcomm, 2017. **8**(3): p. 516-533.
11. Kohanski, M.A., D.J. Dwyer, and J.J. Collins, *How antibiotics kill bacteria: from targets to networks.* Nat Rev Microbiol, 2010. **8**(6): p. 423-35.
12. Kapoor, G., S. Saigal, and A. Elongavan, *Action and resistance mechanisms of antibiotics: A guide for clinicians.* J Anaesthesiol Clin Pharmacol, 2017. **33**(3): p. 300-305.
13. Bermingham, A. and J.P. Derrick, *The folic acid biosynthesis pathway in bacteria: evaluation of potential for antibacterial drug discovery.* Bioessays, 2002. **24**(7): p. 637-648 %@ 0265-9247.
14. Robbel, L. and M.A. Marahiel, *Daptomycin, a bacterial lipopeptide synthesized by a nonribosomal machinery.* J Biol Chem, 2010. **285**(36): p. 27501-8.
15. Triassi, A.J., et al., *L,L-diaminopimelate aminotransferase (DapL): a putative target for the development of narrow-spectrum antibacterial compounds.* Front Microbiol, 2014. **5**: p. 509.
16. Mantravadi, P.K., et al., *The Quest for Novel Antimicrobial Compounds: Emerging Trends in Research, Development, and Technologies.* Antibiotics (Basel), 2019. **8**(1).
17. Ling, L.L., et al., *A new antibiotic kills pathogens without detectable resistance.* Nature, 2015. **517**(7535): p. 455 %@ 1476-4687.
18. Brackman, G. and T. Coenye, *Quorum sensing inhibitors as anti-biofilm agents.* Current pharmaceutical design, 2015. **21**(1): p. 5-11 %@ 1381-6128.
19. Organization, W.H., *Prioritization of pathogens to guide discovery, research and development of new antibiotics for drug-resistant bacterial infections, including tuberculosis*. 2017, World Health Organization.
20. CDC, *Antibiotic resistance threats in the United States, 2013*. 2013, US Department of Health and Human Services Atlanta.
21. CDC, *Antibiotic Resistance Threats in the United States, 2019*. 2019: Atlanta, GA:U.S. Department of Health and Human Services, CDC; 2019.
22. Bassetti, M., et al., *How to manage Pseudomonas aeruginosa infections.* Drugs Context, 2018. **7**: p. 212527.
23. Burrows, L.L., *The Therapeutic Pipeline for Pseudomonas aeruginosa Infections.* ACS Infect Dis, 2018. **4**(7): p. 1041-1047.
24. Page, M.G. and J. Heim, *Prospects for the next anti-Pseudomonas drug.* Curr Opin Pharmacol, 2009. **9**(5): p. 558-65.

25. Baer, M., et al., *An engineered human antibody fab fragment specific for Pseudomonas aeruginosa PcrV antigen has potent antibacterial activity.* Infect Immun, 2009. **77**(3): p. 1083-90.
26. Warrener, P., et al., *A novel anti-PcrV antibody providing enhanced protection against Pseudomonas aeruginosa in multiple animal infection models.* Antimicrob Agents Chemother, 2014. **58**(8): p. 4384-91.
27. Sharma, A., V.K. Gupta, and R. Pathania, *Efflux pump inhibitors for bacterial pathogens: From bench to bedside.* Indian J Med Res, 2019. **149**(2): p. 129-145.
28. Lomovskaya, O., et al., *Identification and characterization of inhibitors of multidrug resistance efflux pumps in Pseudomonas aeruginosa: novel agents for combination therapy.* Antimicrob Agents Chemother, 2001. **45**(1): p. 105-16.
29. Bonchi, C., et al., *Repurposing of gallium-based drugs for antibacterial therapy.* Biofactors, 2014. **40**(3): p. 303-12.
30. Ballouche, M., P. Cornelis, and C. Baysse, *Iron metabolism: a promising target for antibacterial strategies.* Recent Pat Antiinfect Drug Discov, 2009. **4**(3): p. 190-205.
31. Smith, D.J., et al., *Targeting iron uptake to control Pseudomonas aeruginosa infections in cystic fibrosis.* Eur Respir J, 2013. **42**(6): p. 1723-36.
32. Andrews, S.C., A.K. Robinson, and F. Rodriguez-Quinones, *Bacterial iron homeostasis.* FEMS Microbiol Rev, 2003. **27**(2-3): p. 215-37.
33. Winterbourn, C.C., *Toxicity of iron and hydrogen peroxide: the Fenton reaction.* Toxicol Lett, 1995. **82-83**: p. 969-74.
34. Kehrer, J.P., *The Haber-Weiss reaction and mechanisms of toxicity.* Toxicology, 2000. **149**(1): p. 43-50.
35. Cornelis, P., S. Matthijs, and L. Van Oeffelen, *Iron uptake regulation in Pseudomonas aeruginosa.* BioMetals, 2009. **22**(1 %@ 1572-8773): p. 15-22.
36. Vasil, M.L., *How we learnt about iron acquisition in Pseudomonas aeruginosa: a series of very fortunate events.* BioMetals, 2007. **20**(3 %@ 1572-8773): p. 587-601.
37. Pasqua, M., et al., *Ferric Uptake Regulator Fur Is Conditionally Essential in Pseudomonas aeruginosa.* Journal of Bacteriology, 2017. **199**(22): p. e00472-17.
38. Wilson, B.R., et al., *Siderophores in iron metabolism: from mechanism to therapy potential.* Trends in molecular medicine, 2016. **22**(12): p. 1077-1090 %@ 1471-4914.
39. Cornelis, P. and J. Dingemans, *Pseudomonas aeruginosa adapts its iron uptake strategies in function of the type of infections.* Front Cell Infect Microbiol, 2013. **3**: p. 75.
40. Ganne, G., et al., *Iron Release from the Siderophore Pyoverdine in Pseudomonas aeruginosa Involves Three New Actors: FpvC, FpvG, and FpvH.* ACS Chem Biol, 2017. **12**(4): p. 1056-1065.
41. Dumas, Z., A. Ross-Gillespie, and R. Kummerli, *Switching between apparently redundant iron-uptake mechanisms benefits bacteria in changeable environments.* Proc Biol Sci, 2013. **280**(1764): p. 20131055.
42. Lau, C.K., K.D. Krewulak, and H.J. Vogel, *Bacterial ferrous iron transport: the Feo system.* FEMS Microbiol Rev, 2016. **40**(2): p. 273-98.
43. Seyedmohammad, S., et al., *Structural model of FeoB, the iron transporter from Pseudomonas aeruginosa, predicts a cysteine lined, GTP-gated pore.* Biosci Rep, 2016. **36**(2).
44. Cartron, M.L., et al., *Feo–transport of ferrous iron into bacteria.* Biometals, 2006. **19**(2): p. 143-157 %@ 0966-0844.
45. Hantke, K., *Is the bacterial ferrous iron transporter FeoB a living fossil?* Trends in microbiology, 2003. **11**(5): p. 192-195 %@ 0966-842X.
46. Rivera, M., *Bacterioferritin: structure, dynamics, and protein–protein interactions at play in iron storage and mobilization.* Accounts of chemical research, 2017. **50**(2): p. 331-340 %@ 0001-4842.
47. Yao, H., et al., *Two distinct ferritin-like molecules in Pseudomonas aeruginosa: the product of the bfrA gene is a bacterial ferritin (FtnA) and not a bacterioferritin (Bfr).* Biochemistry, 2011. **50**(23): p. 5236-48.

48. Wang, Y., et al., *Characterization of the Bacterioferritin/Bacterioferritin Associated Ferredoxin Protein-Protein Interaction in Solution and Determination of Binding Energy Hot Spots.* Biochemistry, 2015. **54**(40): p. 6162-75.
49. Weeratunga, S.K., et al., *Structural studies of bacterioferritin B from Pseudomonas aeruginosa suggest a gating mechanism for iron uptake via the ferroxidase center.* Biochemistry, 2010. **49**(6): p. 1160-75.
50. Andrews, S.C., *The Ferritin-like superfamily: Evolution of the biological iron storeman from a rubrerythrin-like ancestor.* Biochim Biophys Acta, 2010. **1800**(8): p. 691-705.
51. Arosio, P., L. Elia, and M. Poli, *Ferritin, cellular iron storage and regulation.* IUBMB Life, 2017. **69**(6): p. 414-422.
52. Palma, M., S. Worgall, and L.E. Quadri, *Transcriptome analysis of the Pseudomonas aeruginosa response to iron.* Arch Microbiol, 2003. **180**(5): p. 374-9.
53. Weeratunga, S.K., et al., *Binding of Pseudomonas aeruginosa apobacterioferritin-associated ferredoxin to bacterioferritin B promotes heme mediation of electron delivery and mobilization of core mineral iron.* Biochemistry, 2009. **48**(31): p. 7420-31.
54. Yao, H., et al., *Concerted motions networking pores and distant ferroxidase centers enable bacterioferritin function and iron traffic.* Biochemistry, 2015. **54**(8): p. 1611-27.
55. Rivera, M., *Bacterioferritin: Structure Function and Protein–Protein Interactions*, in *Handbook of Porphyrin Science (Volume 30)*. p. 135-178.
56. Ochsner, U.A., et al., *GeneChip expression analysis of the iron starvation response in Pseudomonas aeruginosa: identification of novel pyoverdine biosynthesis genes.* Mol Microbiol, 2002. **45**(5): p. 1277-87.
57. Yao, H., et al., *The structure of the BfrB-Bfd complex reveals protein-protein interactions enabling iron release from bacterioferritin.* J Am Chem Soc, 2012. **134**(32): p. 13470-81.
58. Wijerathne, H., et al., *Bfd, a New Class of [2Fe-2S] Protein That Functions in Bacterial Iron Homeostasis, Requires a Structural Anion Binding Site.* Biochemistry, 2018. **57**(38): p. 5533-5543.

Chapter 2 : A technique developed to follow iron storage/ mobilization from bacterioferrin in bacterial cells enabled understanding of the crucial role played by the BfrB:Bfd interaction in iron homeostasis

This chapter is based on the publication:

Eshelman, K.*; Yao, H.*; **Punchi Hewage, A. N. D.**; Deay, J. J.; Chandler, J. R.; Rivera, M., "Inhibiting the BfrB:Bfd interaction in Pseudomonas aeruginosa causes irreversible iron accumulation in bacterioferritin and iron deficiency in the bacterial cytosol". Metallomics 2017, 9 (6), 646-659.
*These authors contributed equally

2.1 Introduction

2.1.1 Iron is an essential nutrient for bacteria

Iron is essential for metabolic processes and key enzymatic reactions in bacteria. Heme and Fe-S clusters are an important feature of cytochromes, aconitase, and fumarase, which are necessary proteins for respiration and tricarboxylic acid cycle (TCA) functionality. In addition, gene regulation and DNA biosynthesis also involve iron-containing proteins. Being an important metal for biological processes, the chemical properties of iron are not in the favor of most of aerobic organisms on the planet [1].

In the beginning of life the atmosphere was anerobic and iron was a friendly element. With the success of photosynthetic organisms, however, presented new challenges to life on the planet; the atmosphere became oxygenic and the major form of iron shifted from the soluble Fe^{2+} (0.1 M at pH 7.0) to the extremely insoluble Fe^{3+} (10^{-18} M at pH 7.0) [1]. In addition, the dioxygen (O_2) and and its one-electron and two-electron reduced species (superoxide and peroxide) cause toxic effects to biological systems in the presence of iron. Due to the poor solubility and potential toxicity of iron, bacteria and other organisms use complex machineries to maintain iron homeostasis. Iron homeostasis involves efficient scavenging of iron from the surrounding and regulating intracellular free iron levels to avoid iron induced toxicity caused by the Fenton reaction, where the ferrous ion and hydrogen peroxide react to produce hydroxyl radicals, which cause significant injuries to living cells [3]. As a way to defend from the threat of iron and oxygen living cells evolved ferritin protein cages for the oxidation of Fe^{2+} and compartmentalization of Fe^{3+} in their

interior cavities where the the insoluble ferric mineral is preventing from rusting in cytosol. When needed iron stored in ferritin-like molecules is mobilized and safely incorporated into metabolism while avoiding the damaging effects of unchecked Fenton reactions.

2.1.2 Two iron storage molecules coexist in the pathogen *Pseudomonas aeruginosa*

Ferritins can be divided in to three subfamilies: heme containing bacterioferritins (Bfrs), canonical ferritins (Ftns) and DNA-binding proteins from starved cells (DPS) [4]. The Bfrs and Ftns are made of 24 subunits and the DPS consists of 12 subunits. Ftns are found in both eukaryotes and prokaryotes, and Bfrs and DPS are restricted to prokaryotes. The ferritin subunits consist of 4-helical bundles. All ferritins contain ferroxidase centers except the FtnL chains are found in eukaryotic ferritins [5].

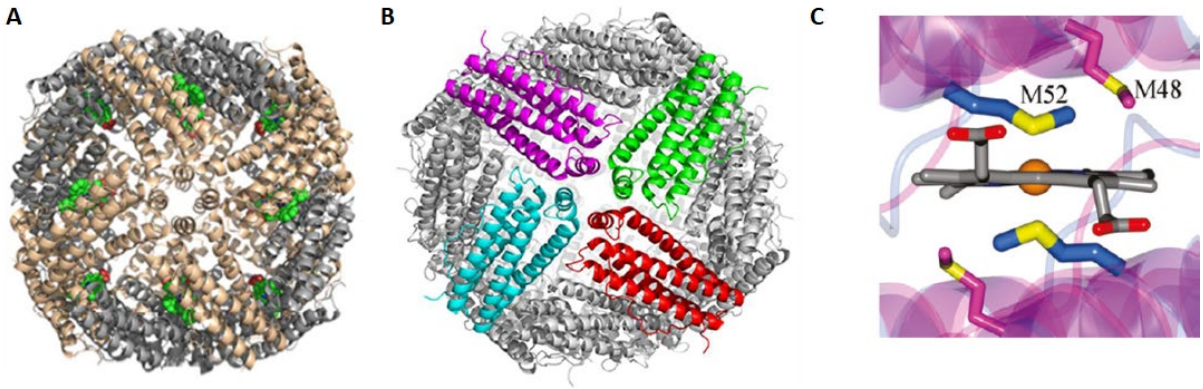

Figure 2-1: Nearly spherical 24-meric structures of (A) BfrB from *Pseudomonas aeruginosa* (PDB ID: 3IS7); the heme molecules are shown in green and (B) FtnA from *Pseudomonas aeruginosa* (PDB ID: 3R2K). (C) Conserved M52 in BfrB coordinates heme, whereas the M48 in the FtnA sequenced cannot. (Figures are reprinted with permission from: Ref. 4 copyright (2013) World Scientific and Ref. 7 copyright (2011) American Chemical Society)

Pseudomonas aeruginosa is a Gram-negative opportunistic pathogen that has been included in the critical priority group for novel anti-microbial development by the World Health Organization because of its intrinsic and acquired antibiotic resistance [6]. Two types of ferritin like molecules coexist in *P. aeruginosa*, a bacterialferritin (FtnA) and a bacterioferritins (BfrB). Both BfrB and FtnA assemble into

nearly spherical 24 meric units (**Figure 2-1-A and 2-1-B**) [4, 7]. Bacterioferritins bind a heme in between two subunit dimers. As shown in **Figure 2-1-C**, in BfrB heme is coordinated *via* two M52 residues from each subunit. In contrast, the M48 in FtnA is not in proximity to a heme to allow coordination [7]. The f*tnA* gene is adjacent to the heme catalase gene *katA*. In the f*tnA* knockout mutant, the catalase activity was reduced by 50 % than the wild type cells. This observation let to the speculation that FtnA transfers iron to the catalase KatA for assembly of the heme cofactor in the enzyme [8].

2.1.3 Iron mobilization from BfrB requires interaction with its cognate partner protein, Bfd

In *P. aeruginosa* the *bfrB* gene is adjacent to the *bfd* gene, which codes for a [2Fe-2S] bacterioferritin-associated ferredoxin. Studies with *E. coli* Bfd have suggested that the function of Bfd can either be as an electron acceptor in the iron uptake process of Bfr or as an electron donor in the iron mobilization from Bfr [9]. Global genetic response studies of *P. aeruginosa* to low Fe conditions showed an increase of the *bfd* expression by 200-fold and the ferredoxin reductase (f*pr*) by 3-fold [10]. These observations led Rivera and coworkers to propose an electron transfer model where electrons from the ferredoxin reductase (Fpr) are passed to the [2Fe-2S] cluster of Bfd which in turn reduces the heme molecules in BfrB. Reduced heme transfers electrons to the Fe^{3+} mineral in the BfrB cavity and thereby enables mobilization of Fe^{2+} (see **Figure 2-2**) [4, 11]. I*n-vitro* investigations carried out with recombinant Bfd, Fpr and BfrB from *P. aeruginosa* provided strong support for the proposed electron transfer model and highlighted the importance of the BfrB:Bfd interaction in mobilization of iron from BfrB [12].

The co-crystal structure of the BfrB:Bfd complex revealed structural details in depth about the interaction. In the X-ray crystal structure, 12 Bfd molecules are bound to a 24- mer BfrB at identical sites. A Bfd molecule is bound right on top of the heme of BfrB at the interface of two subunits. This binding place the Fe-S cluster of Bfd at the right position for electron transfer to the heme in BfrB. **Figure 2-2B** shows the electron transfer path that was predicted by the program Harlem [12]. Electrons are transferred from the S2 of Bfd iron-sulfur cluster to the heme vinyl β carbon (CBB) in BfrB via two nonbonding jumps and, Q72 and L71 of BfrB subunit B [12].

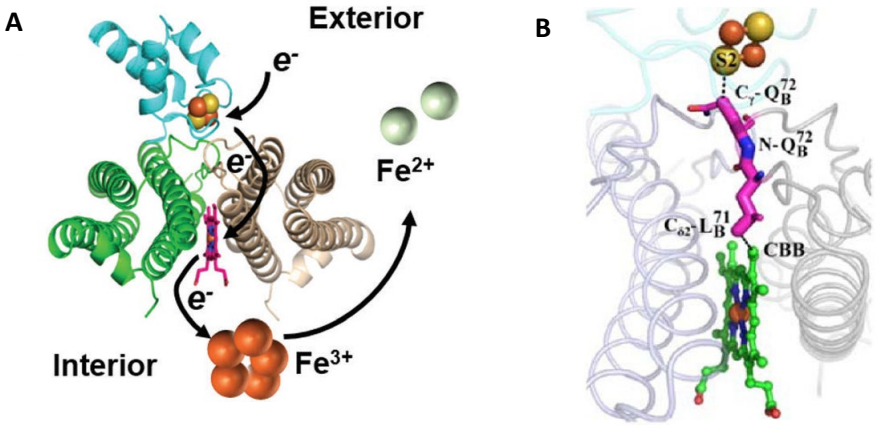

Figure 2-2: A) A heme molecule is bound between two subunits of BfrB, heme is coordinated by conserved Met residues from each subunit. Bfd binds at the interface of the two BfrB subunits. The electron transfer path from the [2Fe-2S] cluster of Bfd to the Fe^{3+} mineral in the protein core is shown by arrows. (B) The electron transfer path from Bfd S2 of [2Fe-2S] cluster to heme vinyl β carbon (CBB) of heme in BfrB. (Figures are reprinted with permission from: Ref. 11 (https://doi.org/10.1021/acs.accounts.6b00514) and Ref. 12 (https://doi.org/10.1021/ja305180n). Further permissions related to the material excerpted should be directed to the ACS)

The BfrB:Bfd interface hot spot residues have been identified by alanine mutagenesis. The residues L68, E81 and E85 of BfrB and Y2, L5 and K40 of Bfd contribute to most of the binding energy (**Figure 2-3**) [13]. The K_d of the BfrB:Bfd interaction is 3 μM. Mutating E81 and L68 to alanine increased the K_d by about 100-fold. The K_d for the double mutant L68A/E81A of BfrB was undetectable as the interaction is disturbed [13]. In addition, the *in-vitro* iron release assays showed that the iron mobilization from BfrB was retarded in the L68A and E81A BfrB mutants, and most importantly the iron mobilization was completely inhibited in the L68A/E81A double mutant of BfrB and it was similar to not having Bfd in the reaction [13]. This is a clear indication that the BfrB:Bfd interaction can be inhibited by mutating L68A/E81A of BfrB.

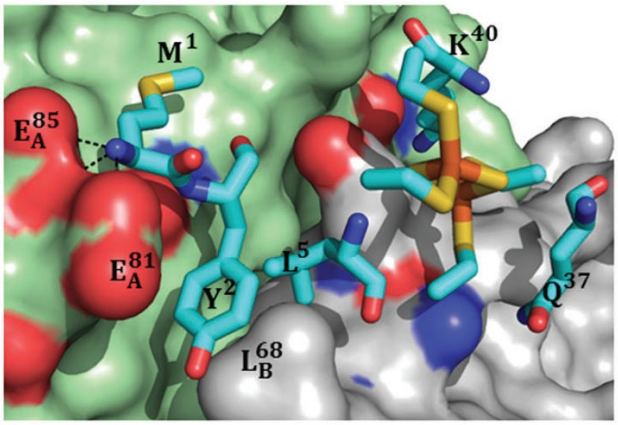

Figure 2-3: The BfrB:Bfd interface. Key residues in Bfd are shown in cyan; BfrB subunit A is in green and BfrB subunit B in grey. The residues L68, E81 and E85 in BfrB and Y2, L5 and K40 in Bfd are the hot spot residues of the BfrB:Bfd interaction. (Figure is reprinted with permission from Ref. 12 (https://doi.org/10.1021/ja305180n). Further permissions related to the material excerpted should be directed to the ACS)

In this study, insights gathered from *in-vitro* experiments on the BfrB:Bfd interaction were used as a guide to explore the contributions of BfrB and the BfrB:Bfd interaction to iron hemostasis in *Pseudomonas aeruginosa* cells. In order to study the importance of BfrB for the *P. aeruginosa* cells, a *bfrB* gene knockout mutant was prepared. To study the significances of the BfrB:Bfd interaction in *P. aeruginosa* cells, (i) a *bfd* gene knockout mutant (*Δbfd*), and (ii) a mutant made by replacing the *bfrB* gene with a L68A/E81A double mutant *bfrB* allele at the native site [*bfrB*(L68A/E81A)] were prepared [2].

2.1.4 Significance of following iron storage and mobilization in *P. aeruginosa* cells

The main goals of the study were to understand: (i) how iron is stored/mobilized during different phases of *P. aeruginosa* cell growth, (ii) how iron storage/ mobilization is handled by the cells under iron replete and deplete conditions, and (iii) how iron storage/mobilization is affect upon genetic intervention directed at blocking the BfrB:Bfd interaction (Δ*bfd* and *bfrB*(L68A/E81A). To accomplish these goals requires a clear view of the fate of iron in BfrB within *P. aeruginosa* cells. In order to analyze the state of iron storage and mobilization, an optimized Native PAGE (Polyacrylamide Gel Electrophoresis) method is

developed. Imaging iron on Native-PAGE gels had been used previous to this study in order to detect iron in recombinant proteins, such as transferrin, lactoferrin and ferredoxin [14]. To this end, the proteins were electrophoretically separated under native conditions and stained with iron specific stains such as FereneS, potassium ferricyanide and 3,5-diaminobenzoic acid and imaged [14-16]. Using Native-PAGE to image iron in the proteins of a bacterial cell lysate is a novel approach. The successful application of this method requires additional optimizations relative to what had been reported previously because of the complexity of the sample and the low signal levels intrinsic to the cell lysate samples. When Native-PAGE is used for the recombinant proteins, the proteins are pure and can be concentrated to improve signal, but this is not practical for the cell lysate samples. The signal of the cell lysate proteins is hard to improve by concentrating. Cell lysates contain a complex mixture of proteins and require additional time and effort to concentrate. In addition, there is always a possibility of sample loss or precipitation while concentrating. Therefore, alternative optimization approaches are used to improve the signal while preventing sample loss.

The cell lysis protocols and gel running conditions were optimized by (i) finding cell lysis conditions to maximize sample yield, (ii) increasing the sample loading volume by increasing the thickness of the gels, and (iii) fine-tuning the voltage and the electrophoresis run times to get sharp bands. Getting sharp and non-distorted Native-PAGE iron stains is one of the central experimental details that is required to determine the importance of BfrB and the BfrB:Bfd interaction in *P. aeruginosa* cells because the relative intensity of the iron stain in the Native-PAGE is to be correlated with the amount of iron present in BfrB within *P. aeruginosa* cells.

The optimized native-PAGE method reported herein allowed us to demonstrate that BfrB and not FtnA acts as the main iron storage protein in *P. aeruginosa*. When the *P. aeruginosa* cells are grown in the presence of 10 μM iron, the wild type cells show maximum iron accumulation in BfrB at about 12-14 h. Stored iron start to mobilize from BfrB during late exponential and early stationary growth phases. As the BfrB:Bfd interaction is functional, wild type cells take advantage of the stored iron in BfrB to gain a growth advantage in the iron limiting media [2]. The optimized native-PAGE method also allowed us to determine

that Tthe *Δbfd* and *bfrB*(L68A/E81A) mutants irreversibly accumulate iron in BfrB, irrespective of the iron levels in the media, and also show retarded growth in low iron media due to the absence of a functional BfrB:Bfd interaction. Irreversible accumulation of iron in BfrB in the *Δbfd* and *bfrB*(L68A/E81A) mutants resulted in low intracellular free iron levels and a low total iron to free iron ratio, which is an indication of iron homeostasis dysregulation upon blockade of the BfrB:Bfd interaction [2].

2.2 Experimental

2.2.1 Media and growth conditions

All chemicals were purchased from Fisher Scientific unless otherwise stated. *Pseudomonas aeruginosa* isolation (PI) media (20 g L^{-1} peptone, 2.99 g L^{-1} $MgCl_2.6H_2O$, 10 g L^{-1} K_2SO_4, 25 mg L^{-1} irgasan (Sigma-Aldrich), and 20 mL L^{-1} glycerol, pH 7.0) was used for the normal bacterial growth experiments. PI media was supplemented with 10 µM iron using a 10 mM stock of $(NH_4)_2Fe(SO_4)_2$ (pH ~2.0) unless otherwise stated. Pre-cultures were grown in 5 mL of PI media at 37 °C at 220 rpm. Cultures were inoculated to an optical density at 600 nm (OD_{600}) of 0.001 for the experiments using the pre-culture.

The following media (1 L) was prepared for the experiments under low iron conditions, 24 g HEPES, 0.93 g $(NH_4)_2SO_4$, 3.245 g succinic acid, 615 mL of 2 mM K_2HPO_4 (Sigma-Aldrich) and 385 mL of 2 mM KH_2PO_4 (Sigma-Aldrich) at pH 7.0. The trace metals were added in the following volumes: 2 mL of 1 M $MgSO_4$, 100 µL of 4 M $CaCl_2$, 10 µL 15 mM ammonium molybdate, 1 mL of 17 mM EDTA, 300 µL of 10 mM $CuSO_4$, 100 µL of 20 mM $Co(NO_3)_2$, 100 µL of 94 mM $Na_2B_4O_7$, and 100 µL of 76 mM ZnSO4 [2].

Experiments under low iron conditions were carried out by growing the *P. aeruginosa* pre-cultures in PI media supplemented with 10, 20, and 30 µM iron and growing for 24 h at 37 ^{0}C.Media recipes have been adapted from [2].

2.2.2 Strains used in the study

Pseudomonas aeruginosa PA01 was purchased from the University of Washington. The PA01 derived stains used in the study are listed in the **Table 2-1** [2].

Table 2-1: *P. aeruginosa* strains used in this study (Reprinted from Ref.2 with permission from the Royal Society of Chemistry)

Strain	Description	Reference
PA01	Wild type strain	[17]
PA01 Δ*bfrB*	An unmarked, in-frame *bfrB* deletion in PA01	[2]
PA01 Δ*bfd*	An unmarked, in-frame *bfd* deletion in PA01	[2]
PA01 *bfrB*(L68A/E81A)	A variant *bfrB* allele at the native *bfrB* locus in PA01 encoding the BfrB L68A/E81A	[2]
PA01Δ*bfrB* *attn7::*P_{lac}*bfrB*	Introduced pUC18-miniTn7T-LAC *bfrB* to PA01 Δ*bfrB* and removed the GentR marker	[2]
PA01 Δ*bfd attn7::*P_{lac}*bfd*	Introduced pUC18-miniTn7T-LAC *bfd* to PA01 Δ*bfd* and removed the GentR marker	[2]

2.2.3 Optimized method for imaging iron stored in BfrB using Native-PAGE

Pre-cultures of *P. aeruginosa* were grown in 5 mL of PI media supplemented with 10 μM iron as presented in media and growth conditions. PI media (5 mL cultures) supplemented with 10 μM iron (or the required concentration) was inoculated to OD_{600} = 0.001 using the pre-culture. Cells were grown at 37 ^{0}C and shaking at 230 rpm. Samples were collected at 6, 8, 10, 12, 24, 36 and 48 h post inoculation. An independent 5 mL culture was used for each time point. Cells were centrifuged for 15 min at 4000 rpm and 4 ^{0}C. Cells were re-suspended in 1 mL of PI media and centrifuged for 10 min at 13300 rpm and 4 ^{0}C and the cell pellets were frozen at -80 ^{0}C.

Cell pellets were thawed and lysed using 300 μL of the lysis buffer (50 mM Tris-base buffer pH 8.0, 10% glycerol, 20 mg/mL lysozyme, 0.2 mg/mL DNAse (Gold Bio), 0.1 M NaCl, 1 mM $MgSO_4$ and

1% Triton-X100 (Sigma)) and incubated at 25 ^{0}C for 90 min and at 37 ^{0}C for 30 min with shaking. Samples were then centrifuged for 10 min at 13,300 rpm and the supernatant was filtered through a 0.45 μm membrane by centrifugation. Supernatant (100 μL) was mixed with 10 μL of the native gel loading dye (0.5 mL 1M Tris-HCl pH 6.8, 5.9 mL water, 0.5 mL glycerol, 0.4 mL β-mercaptoethanol, 0.4 mL 1 % bromophenol blue). The mixed solution (100 μL) was loaded into a 2 mm thick Native gel (4 % stacking gel and 8 % resolving gel). Electrophoresis was carried out at 60 V for 9 h at 4 ^{0}C. Once running is complete, the gel was stained for iron by immersing it for 10 min in the dark in a FereneS solution (0.049 FereneS, 250 μL thioglycolic acid, 2.4 mL glacial acetic acid in 100 mL of water) and photographed [14].

2.3 Results and discussion

2.3.1 Optimization of the gel thickness, gel running conditions and cell lysis to image iron in *P. aeruginosa* cell lysates using Native Page Electrophoresis

P. aeruginosa codes for two ferritin like molecules, BfrB and FtnA. It is therefore important to investigate how the two ferritin-like molecules are involved in iron storage and distribution of iron in the cells. Imaging iron stored in these proteins in the cell lysate could help answer several questions that arise while investigating iron storage / mobilization from ferritin-like molecules in bacterial cells. Since iron storage proteins accumulate a reasonable amount of iron when cells are grown under iron replete conditions, once the proteins are separated on a Native-PAGE it is possible to use colorimetric detection to image the iron. To get a better understanding of the fate of iron in the iron storage proteins, the detection method needs to be sensitive enough to qualitatively indicate the levels of iron present in the protein during different growth phases of the cell. Therefore, the ability to image iron accumulated in iron storage proteins is a crucial step toward understanding iron homeostasis in *P. aeruginosa* cells. As imaging iron accumulated in iron storage proteins in cell lysates is a novel approach, the Native-PAGE method needs optimization to obtain sharp bands with sufficient sensitivity to make accurate conclusions on iron storage and mobilization.

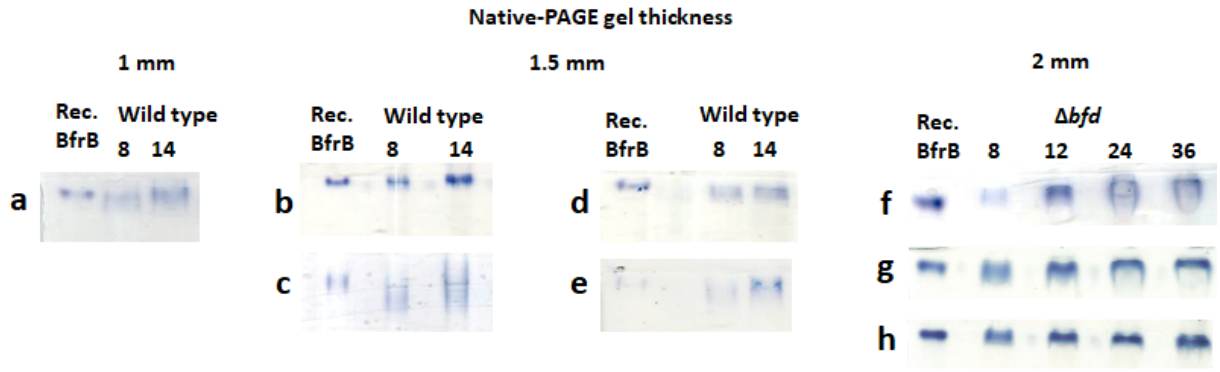

Figure 2-4: Optimization of the Native-PAGE protocol for imaging iron accumulated in bacterioferritin within *P. aeruginosa* cells. (a) Iron stained Native-PAGE, **1 mm thick,** 7 % separating and 5% stacking gel ran at 60 V for 4 h. **1.5 mm thick:** (b) 8 % separating and 4% stacking gel, 60 V for 4 h (c) 8 % separating and 4% stacking gel, 140 V for 2 h (d) 8 % separating and 4% stacking gel, 100 V for 2.15 h, (e) 7 % separating and 4% stacking gel, 100 V 2.15 h. **2 mm thick:** (f) 8 % separating and 4% stacking gel, 60 V for 1 h and 90 V for 8 h, 200 µL lysis buffer, (g) 8 % separating and 4% stacking gel, 60 V for 1 h and 90 V for 8 h,300 µL lysis buffer, loading dye supplemented with 5 % β-mercaptoethanol, (h) 8 % separating and 4% stacking gel, 60 V 9 h, 300 µL lysis buffer, loading dye supplemented with 5 % β-mercaptoethanol .

During the initial stages of my efforts to image iron in cell lysates, 10-20 mL cultures were used, and after harvesting the cells a volume of lysis buffer equal to the cell pellet (~100-200 µL) was used for cell lysis. Once the cells were lysed, lysates were mixed with an equal volume of native gel loading dye (causes a 2-fold dilution of the lysate) and 80 µL of the resultant mixture was loaded on each well. Lysates were electrophoretically separated on a Native-PAGE gel with dimensions of 20×20 cm x 1 mm (thickness) in a PROTEAN II XL electrophoresis system (Bio-Rad). Electrophoresis was carried out for 2 h at 25 mA and then for 6 h at 35 mA. These experiments did no produce the sharp bands required to draw confident conclusions on iron storage/mobilization. This may have been because the cell lysis process was not optimum and the protein in the lysates was diluted excessively prior to loading the gel. Also, the large size of the gels made gel preparation tedious and electrophoresis inefficient due to the large size of the buffer chamber that is needed to run these large gels, which consumed lot of material and running buffer (40 mL

of 8 % poly-acrylamide solution and 3-4 L of native gel running buffer). In order to overcome these issues, it was decided to scale down the size of the Native-PAGE system, such that amini-gel system (10-15 mL 8 % poly-acrylamide solution and 900 mL of native gel running buffer) could be used instead of the large PROTEAN II XL system. Scaling down, however, required improving the sensitivity of detection. Additionally, when scaling down to a mini-gel setup, the cell lysis protocol and the gel running conditions also had to be opitimized in order to improve detection.

In the second wave of experiments *P. aeruginosa* cells were grown in 5 mL cultures of PI media supplemented with 10 µM iron. Cells collected at 8 and 14 h post inoculation were lysed in 140 µL of the lysis buffer indicated in the experimental section. The lysis buffer used with the PROTEAN II XL system was modified to include 10 % glycerol. This allowed lowering the volume of loading dye that is used to mix with the sample while maintaining the required density, thus eliminating the issue of sample dilution prior to loading. In this context, it is important to note that the purpose of the loading dye in Native-PAGE is to increase the density of the sample allowing the sample to sink into the wells while the bromophenol blue dye works as an indicator of electrophoretic mobility at the gel front. Therefore, the modification of increasing glycerol to 10% in the lysis buffer caused significant less sample dilution while loading (~1.1-fold dilution rather than 2-fold). The resultant lysates were separated under using the conditions described below.

An important limitation of using a mini-gel, is the volume of sample that can be loaded per well, which is about 20-25 µL for a typical 1 mm thick gel. As shown in **Figure 2-4a**, when 1 mm thick gels are used (7 % separating and 5% stacking gel, ran at 60 V for 4 h) the iron stain is weak because the small sample volume results in relatively low protein concentrations in the gel. Increasing the gel thickness to 1.5 mm allowed loading of ~40 µL of sample per well and resulted somewhat sharper bands, as illustrated in **Figure 2-4b** (8 % separating and 4% stacking gel, ran at 60 V for 4 h). Next, the gel running voltage and the percentage of separating gel was explored. When the voltage was increased from 60 V to 100 V (**Figure 2-4d**, 8 % separating and 4% stacking gel, 100 V for 2.15 h) and 140 V (**Figure 2-4c**, 8 % separating and

4% stacking gel, 140 V for 2 h) the sharpness of the iron stain deteriorated, resulting in diffuse bands. A similar observation was made when the separating gel percentage was lowered to 7 % from 8 % (**Figure 2-4e**, 7 % separating and 4% stacking gel, 100 V for 2.15 h). Therefore, a low voltage such as 60 V and 8 % separating gel seemed the ideal conditions to get sharp bands.

As there was an improvement in increasing the gel thickness and running the gel at 60 V, next the thickness of the gel was increased to 2 and 3 mm by using custom-made spacers. This allowed to increase the loading volume, which is about 90-100 µL for a 2mm thick gel and about 120 µL for a 3 mm thick gel. Note that this sample volume is more than can be loaded into the PROTEAN II XL gels. Being able to load a larger sample volume is important to get improved signals specially when the amount of iron accumulated in BfrB is low or when cell densities are low. An application of this gained sensitivity will be further discussed in Chapter 3. *P. aeruginosa Δbfd* mutant cells were used to optimize the cell lysis process. Using *Δbfd* mutant allowed to optimize the lysis of highly mucoidal, high cell density samples (36 h-48 h cultures). Also, the improvement of lysis can be visualized from the iron stains of the gels because *Δbfd* mutant cells are unable to mobilize iron from BfrB so the time-dependent iron stains clearly revealed the irreversible accumulation of iron in BfrB. For the initial trials with the 2 mm thick gels, 200 µL of the lysis buffer was used. As shown in **Figure 2-4f** (8 % separating and 4% stacking gel, 60 V 1 h and 90 V 8 h), the iron stain showed a significant improvement compared to stains observed with the 1.5 mm thick gels, but the 24 and 36 h samples suggest less than optimum lysis of the cells. Therefore, the lysis volume was increased to 300 µL and also the sample loading dye was supplemented with 5 % β-mercaptoethanol to eliminate disulfide bonds between BfrB proteins, thus avoiding streakiness in the gels. The resultant gel is shown in **Figure 2-4g** (8 % separating and 4% stacking gel, 60 V 1 h and 90 V 8 h). Clearly, cell lysis has improved, but there is a decrease in the sharpness of the bands, especially in the 24 and 36 h samples. When revising the 1.5 mm thick gel results, it was obvious that the voltage impacts the sharpness of the iron stain (**Figure 2-4c** and **Figure 2-4d**). Therefore, the same samples were ran at a lower voltage (60 V 9 h) and the resultant gel, shown in **Figure 2-4h** (8 % separating and 4% stacking gel, 60 V for 9 h) shows sharp bands. Hence, the

optimum conditions include: 300 µL lysis volume, 2 mm thick gels (12 mL gel volume), 8 % separating and 4% stacking gel, 60 V, 9 h run time at 4 ^{0}C clearly resulted sharp, intense, non-streaky iron stain bands in the Native-PAGE, which allowed to make strong arguments that are further discussed in the subsequent sections.

2.3.2 BfrB is the main iron storage protein in *P. aeruginosa*

Most bacterial genomes code for at least two types of ferritins, bacterial ferritins (Ftn) and bacterioferritins (Bfr). Both assemble into the same quaternary structure and share the identical fold. Ftns and Bfrs function as iron storage proteins as they can oxidize Fe^{2+} at the ferroxidase centers and store it as Fe^{3+} in the interior protein cavity [4]. The reasons for the co-existance of two ferritin-like molecules in bacterial is still not understood and it has led to the suggestion that in different bacteria, the physiological role played by Ftn and Bfr are different [18]. The main iron storage protein in *E. coli* is FtnA whereas in *Salmonella entrica* it is Bfr [19, 20].

In order to identify the main iron storage protein of *P. aeruginosa*, the optimized iron stained native-PAGE protocol described above was used. Cells were grown as explained in the experimental section by supplementing PI media with different iron concentrations (10, 20 and 30 µM) and sampling at 6, 8,12 and 14 h post inoculation. Cells were lysed and loaded into the gel. To identify the corresponding electrophoretic

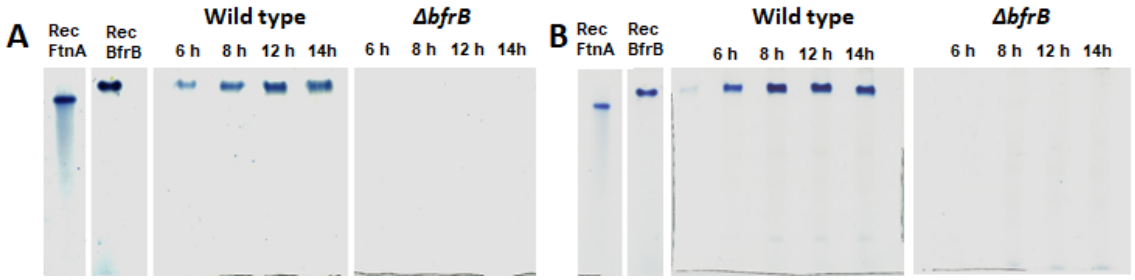

Figure 2-5: Wild type and *ΔbfrB* cells were grown in PI media supplemented with (A) 10 µM and (B) 30 µM iron. Cell lysates were separated on a Native-PAGE and stained with FereneS. Comparing the electrophoretic mobilities it is obvious that BfrB acts as the main iron storage protein in *P. aeruginosa*. In the *ΔbfrB* mutant cells no iron accumulation was detected even when the media was supplemented with 30 µM iron. (Reprinted from Ref.2 with permission from the Royal Society of Chemistry)

migration of the protein, recombinant FtnA and BfrB containing about 400 iron atoms in their interior cavities were used. The migration difference of BfrB and FtnA proteins is clearly noticeable in the native-PAGE shown in **Figure 2-5A**, where the recombinant proteins are termed as Rec FtnA and Rec BfrB. The lanes loaded with lysates from wild type *P. aeruginosa* cells showed an iron stained band that migrated similarly to BfrB, whereas a band corresponding to the migration of FtnA was not detectable in the lysates, even at high iron concentrations (30 μM, **Figure 2-5B**).

In the lysates of *ΔbfrB,* there was no detectable iron accumulation even under iron rich conditions (**Figure 2-5B**). It was assumed that in *ΔbfrB* mutant cells FtnA would compensate for the absence of BfrB. The results from the native-PAGE experiments, however, revealed no iron accumulation in the *ΔbfrB* mutant cells, indicating that FtnA doesn't accumulate iron in *P. aeruginosa* (not detectable by the FreneS stain), even in the absence of BfrB, under the laboratory conditions used in these experiments. These findings agree with the observations that the *bfrB* gene is upregulated in the presence of high iron levels in the environment, whereas expression of the *ftnA* gene does not respond to external high iron levels [21].

2.3.3 Bfd is required to mobilize iron from BfrB in *P. aeruginosa* cells

During the biochemical and structural *in-vitro* studies, BfrB iron was mobilized in the presence of Bfd, Fpr and NADPH. Electrons are transferred from NADPH to FPR and then to the [2Fe-2S] cluster of Bfd. Next, the electrons are transferred to the Fe^{3+} mineral in the central cavity *via* the heme in BfrB. In the absence of Bfd the iron mobilization from BfrB was inhibited *in-vitro* [12].

The co-crystal structure of the BfrB:Bfd protein-protein complex revealed many structural insights on the interaction. The residues L68, E81 and E85 of BfrB and Y2, L5 and K40 of Bfd were identified as the hot spot residues of the interaction [13]. The K_d for the BfrB:Bfd complex was determined to be 3 μM and the mutation of L68A and E81A in BfrB lowered the affinity for Bfd in about 100-fold. The K_d of the double mutant L68A/E81A was not measurable due to the disruption of the BfrB:Bfd interaction. The iron release *in vitro* from the L68A/E81A mutant BfrB showed similar results to those observed in the absence of Bfd, indicating that the L68A/E81A BfrB mutant is incapable of interacting with Bfd [13]. In agreement

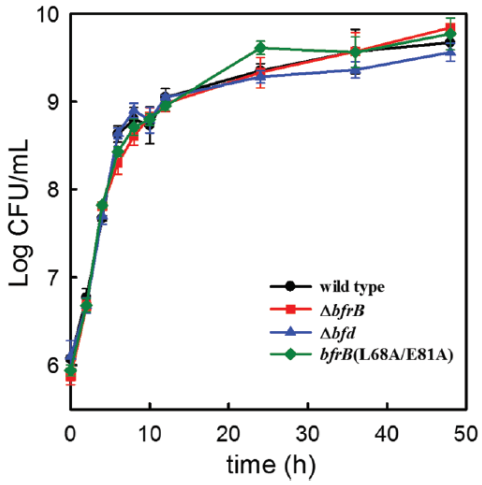

Figure 2-6: The *P. aeruginosa* wild type, *Δbfd*, *bfrB* (L68A/E81A) and *ΔbfrB* mutants grow similarly in the iron sufficient conditions. (Reprinted from Ref.2 with permission from the Royal Society of Chemistry)

with these observations *in vitro*, in *P. aeruginosa* cellsthe BfrB:Bfd interaction was inhibited by, (i) deleting *bfd* gene (*Δbfd*), and (ii) by introducing a L68A/E81A *bfrB* variant allele at the native *bfrB* locus [*bfrB*(L68A/E81A)].

Under iron sufficient conditions (PI media supplemented with 10 µM iron), the wild type and the mutant cells grow similarly (**Figure 2-6**) [2]. Hence, wild type and mutant *P. aeruginosa* cells were grown in the presence of 10 µM iron, and cells were collected at 6, 8, 12, 14, 18, 24, and 36 h post inoculation. The cells were lysed and the lysates were ran on a Native-PAGE, and stained for iron. As shown on **Figure 2-7a** the wild type cells start to accumulate iron in BfrB during the logarithmic growth phase (6 h) and show maximum iron accumulation during the early stationary phase (12 h). Once the iron in the media is depleted (~18 h) the iron accumulated in BfrB is mobilized (18 h and beyond). In the *Δbfd* and *bfrB* (L68A/E81A) mutant cells iron also accumulates in BfrB. However, the accumulated iron is not mobilized from BfrB even under iron deprived conditions (24- 36 h, **Figure 2-7 b** and **Figure 2-7 c**). These observations

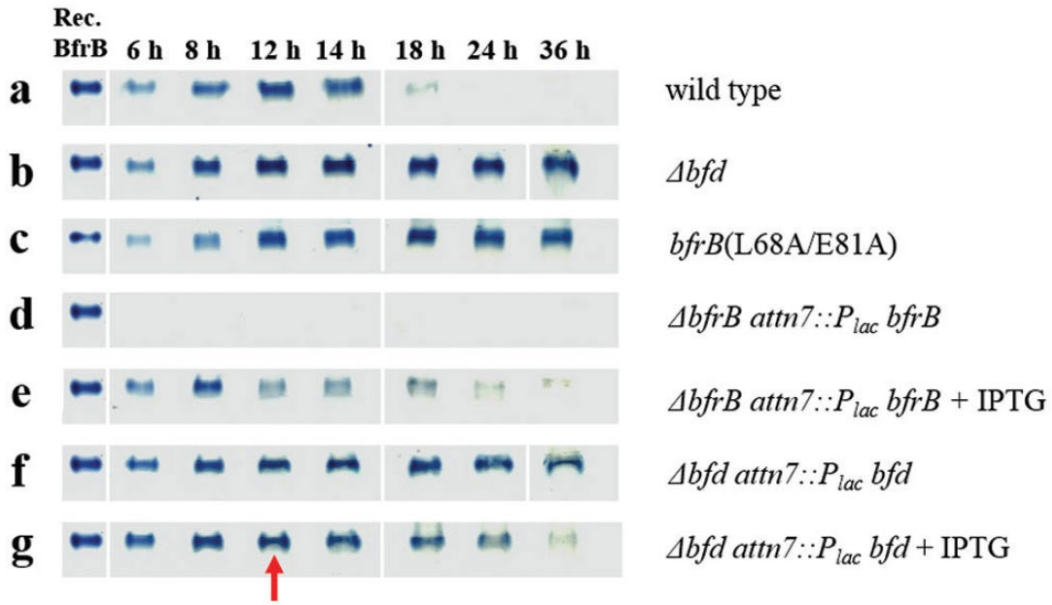

Figure 2-7: *P. aeruginosa* wild type and mutant cells were grown in PI media supplemented with 10 µM iron. Cell lysates at different time points were separated on a Native-PAGE and stained with FreneS. (a) wild type cells accumulate iron in BfrB and then mobilize it when iron in the media is low. (b) *Δbfd*, (c) *bfrB* (L68A/E81A) mutants show irreversible accumulation of iron. (d) *ΔbfrB attn7::*P_{lac} *bfrB* complemented cells don't show iron accumulation in BfrB in the absence of IPTG but (e) accumulate iron in BfrB upon induction of the *bfrB* gene by IPTG (f) The *Δbfd attn7::*P_{lac} *bfd* complemented cells show irreversible accumulation of iron in the absence of IPTG and (g) induction of the bfd gene with IPTG starts the expression of Bfd and mobilization of iron from BfrB. (Reprinted from Ref.2 with permission from the Royal Society of Chemistry)

demonstrate that in *P. aeruginosa* cells the BfrB:Bfd interaction is the only mechanism used to mobilize iron accumulate in BfrB. In addition, as discussed in the previous section *ΔbfrB* mutant cells, don't show any iron accumulation (**Figure 2-5 A, B**).

The *Δbfd* and *ΔbfrB* mutants were complemented with, a *bfd* or a *bfrB* gene expressed from an IPTG inducible *lac* promoter gene installed in the in *P. aeruginosa* chromosome at a neutral *att* site (*ΔbfrB attn7::*P_{lac} *bfrB* and *Δbfd attn7::*P_{lac} *bfd*). As shown in **Figure 2-7d**, there was no iron accumulation in the *ΔbfrB attn7::*P_{lac} *bfrB* in the absence of IPTG. However, adding 1 mM IPTG at the beginning of the growth restored the BfrB. Consequently, the *ΔbfrB attn7::*P_{lac} *bfrB* strain accumulated iron during the exponential

and early stationary growth phases, and mobilized BfrB-iron during late stationary phase, which is very similar to observations made with the wild type cells (**Figure 2-7e**). Small deviations in the iron accumulation pattern may have been caused by the presence of 1 mM IPTG from the beginning of the growth, which might have altered the expression levels of BfrB. The *Δbfd* mutant cells were also complemented with an IPTG-inducible *bfd* gene inserted at an neutral *att* site of the *P. aeruginosa* genome (*Δbfd attn7::*P_{lac} *bfd*). In the absence of IPTG, the cells cannot mobilize iron store in BfrB(**Figure 2-7f**). Addition of 1 mM IPTG (shown by the red arrow) 12 h post inoculation, however, results in the production

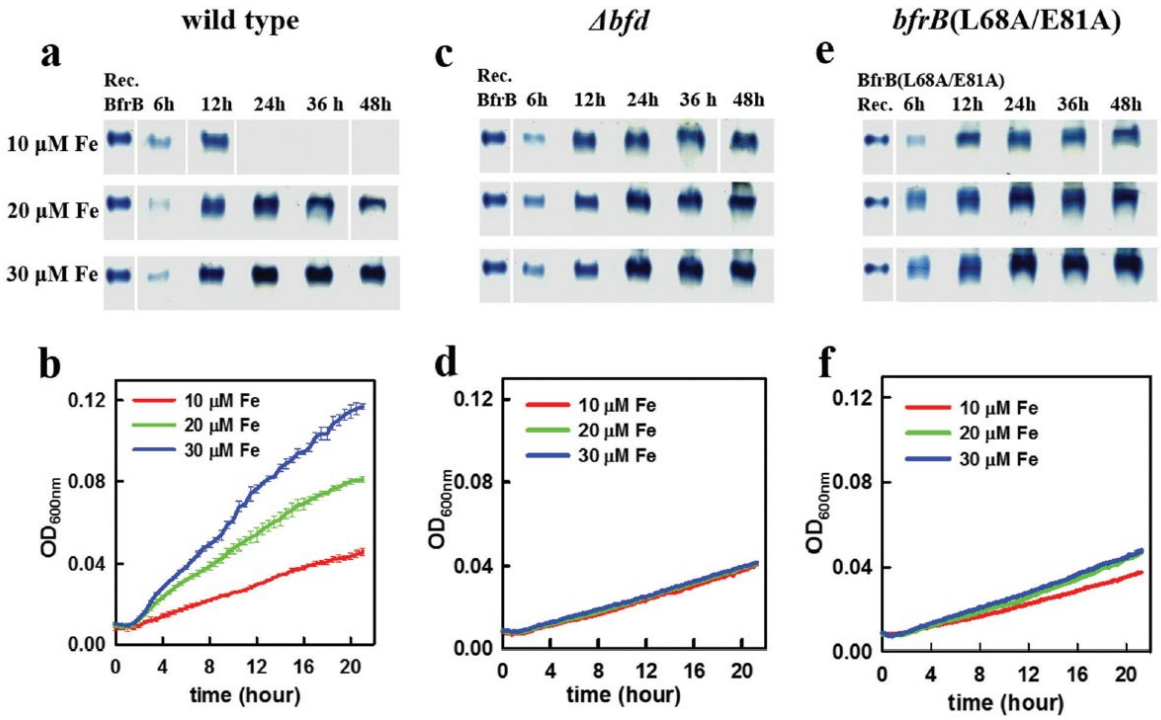

Figure 2-8: *P. aeruginosa* (a) wild type (c) *Δbfd* and (e) *bfrB* (L68A/E81A) cells were grown in the presence of 10, 20 and 30 µM iron, respectively. Lysates were separated on Native-PAGE and stained with FereneS. (b) Wild type cells can take the advantage of the iron stored in BfrB while growing in iron depleted media. The growth rate and the cell density of the cultures is proportional to the amount the concentration of iron supplemented in the first culture. (d) *Δbfd* and (f) *bfrB* (L68A/E81A) cells show impaired growth and the growth rate and cell density is independent of the concentration of supplemented iron. (Figures are reprinted from Ref.2 with permission from the Royal Society of Chemistry)

of Bfd and in the mobilization of iron from BfrB (**Figure 2-g**). The above discussed results clearly demonstrate that the BfrB:Bfd interaction is the only mechanism to mobilize iron from BfrB in *P. aeruginosa* cells.

2.3.4 Iron stored in BfrB promote growth under low iron conditions

Figure 2-7a shows that wild type *P. aeruginosa* cells grown in PI media supplemented with 10 μM iron show maximum iron accumulation at ~12 h, but when the iron in the media starts to deplete iron is mobilized from BfrB (beyond ~18 h). The iron mobilized from BfrB is used fulfill the iron requirement of the cells. Under these conditions, there is no detectable iron in BfrB beyond 24 h, as shown by FereneS stained Native-PAGE (**Figure 2-7a and 2-8a**). As shown in **Figure 2-8a**, when the cells are grown in the presence of 20 or 30 μM iron, there is iron accumulation beyond 24 h and the iron stains are more intense compared to the 10 μM iron supplemented growth. The 20 and 30 μM iron supplemented growths also show iron mobilization from BfrB beyond 24 h of culture, but iron is still detectable in BfrB at 48 h. The insights gathered from the above data were used to test whether *P. aeruginosa* cells can take the advantage of the iron reservoirs in BfrB to grow when transferred into an iron-limiting media. Wildtype *P. aeruginosa* cells were grown in PI media supplemented with 10, 20 and 30 μM iron and cells were collected 24 h post inoculation, centrifuged, washed and transferred to an iron deficient media (< 0.1 μM Fe). The cells suspended in iron deficient media were aliquoted into a 96 well plate and the growth was monitored by measuring $O.D_{600}$. The cell growth in the low iron media was proportional to the concentration of supplemented iron in the first growth, where the wildtype cells that had been grown in 30 μM iron showed the highest cell density when cultured in iron deficient media. The cells grown with a 10 μM iron supplementation had the lowest cell density (**Figure 2-8-b**) [2]. These results show that the wild type cells can use their BfrB iron reserves when facing challenges in growing iron limiting conditions.

Similar experiments were done with *Δbfd* and *bfrB* (L68A/E81A) mutant cells, where they were grown in PI media supplemented with 10, 20 and 30 μM iron. Iron stained Native-PAGE experiments clearly show irreversible accumulation of iron in the mutant cells, with the intensities of the iron stain being

proportional to the concentration of supplemented iron (**Figure 2-8-c and 2-8-e**). However, since the iron stored in BfrB cannot be mobilized in the *Δbfd* and *bfrB* (L68A/E81A) mutant cells, when these are passaged to iron limiting conditions, they show impaired growth. Note that the growth rates of the *Δbfd* and *bfrB* (L68A/E81A) mutant cells are independent from the supplemental iron concentrations and, are significantly lower than the wildtype cells (**Figure 2-8-d, 2-8-f**). In this context, it is important to note that in absence of the BfrB:Bfd interaction the iron stored in BfrB is not usable to the *Δbfd* and *bfrB* (L68A/E81A) mutant cells. The above results demonstrate the classical concept of iron storage proteins, where the protein accumulates iron for the utilization under iron limiting conditions.

2.3.5 Blocking the BfrB:Bfd interaction elicits iron deficiency in *P. aeruginosa* cells

An important characteristic of *P. aeruginosa* cells under iron limiting conditions is the secretion of Fe^{3+}-chelating siderophores such as pyoverdine (Pvd) and pyocheline (Pch). Pyoverdine is the siderophore with the highest affinity for Fe^{3+} and is a green-yellow fluorescent molecule. When excited at 400 nm pyoverdine exhibit fluorescence with emission maximum at 460 nm. An important phenotype that was observed with the *Δbfd* and *bfrB* (L68A/E81A) mutant cells is the hyper production of pyoverdine, compared to the wild type cells. These observations were made when cells were grown in PI media supplemented with 10 μM and the secretion of pyoverdine from the wild type and the *Δbfd, bfrB* (L68A/E81A) and *ΔbfrB* mutants was monitored by fluorescence spectroscopy at different time points post inoculation. Under the above conditions, wild type and the mutants grow similarity reaching stationary phase in ~12 h (**Figure 2-6**) [2]. The fluorescence intensity was normalized to the viable cell count for each time point. As shown in **Figure 2-9a** there wasn't detectable levels of pyoverdine until 24 h post inoculation. During longer culture times such as 36 and 48 h, the *Δbfd* and *bfrB* (L68A/E81A) cells secrete 3-4-fold more pyoverdine than the wildtype cells [2], suggesting acute iron starvation in the *Δbfd, bfrB* (L68A/E81A) cells due to the unidirectional flux of iron into BfrB.

The analysis of iron in the spent media shows that when PI media is supplemented with 10 µM iron, at the end of 20-24 h of growth the media is left with <1 µM iron. Wild type, *Δbfd* and *bfrB* (L68A/E81A) cells utilize iron similarly, whereas the *ΔbfrB* cells utilize iron at a lower rate (**Figure 2-9b**) [2]. The time when iron in the spent media is ~1 µM corresponds with time that the secretion of pyoverdine

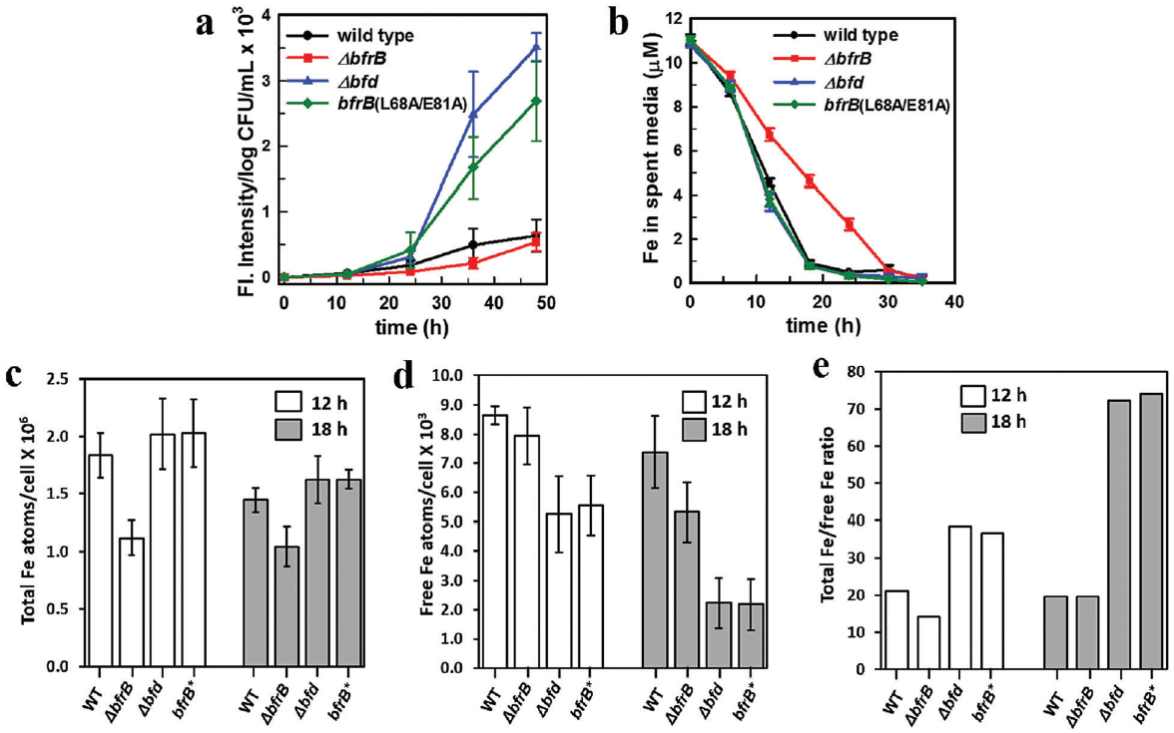

Figure 2-9: The cells were growth in PI media supplemented with 10 µM iron. (a)The amount of pyoverdine secreted by wild type, *Δbfd*, *bfrB* (L68A/E81A) and *ΔbfrB* cells, normalized to the log CFU/mL (b) The iron concentration of the spent media at different time points post inoculation. (c) Total iron levels per cell (d) Free iron atoms per cell and (e) the ratio of total iron to free iron of the wild type, *Δbfd*, *bfrB* (L68A/E81A) and *ΔbfrB* mutant cells at 12 and 18 h post inoculation. (Reprinted from Ref. 2 with permission from the Royal Society of Chemistry)

becomes detectable. The *ΔbfrB* cells take approximately about 30 h to reduce iron levels <1 µM and by this time pyoverdine secretion becomes detectable in *ΔbfrB* cell cultures. Clearly, *P. aeruginosa* cells sense iron starvation and start secreting Fe^{3+} chelating siderophores when the iron levels are about 1 µM [2].

The correlation between the cellular iron levels and the observed phenotypes were investigated by measuring total iron and free intracellular iron in the wild type and mutant cells. Cells were grown in PI media supplemented with 10 μM iron and harvested 12 (early stationary phase) and, 18 h (late stationary phase) post inoculation. The total intracellular iron levels were measured spectroscopically using an iron detection reagent (Ferrozine) after digesting the cells [2, 22]. The levels of free intracellular iron were measured using whole-cell electron paramagnetic resonance (EPR) spectroscopy method after chelating the iron in the cells using a cell membrane permeable iron chelator deferoxamine mesylate (DFO) [2, 23, 24].

The total iron levels in the wild type, *Δbfd* and *bfrB* (L68A/E81A) mutant cells were very similar at 12 and 18 h; these total iron levels don't suggest iron homeostasis dysregulation (**Figure 2-9c**) [2]. However, free iron levels of the *Δbfd* and *bfrB* (L68A/E81A) mutant cells were 60 % and 25 % those in the wild type cells at 12 and 18 h respectively (**Figure 2-9d**) [2]. By 12 h, about 5 μM iron is left in the media and the free iron levels in the *Δbfd* and *bfrB* (L68A/E81A) mutant cells are not severely compromised, but once the media becomes iron depleted (18 h, ~1 μM iron) the unidirectional flow of iron into BfrB exacerbates the depletion of free iron in the cytosol of the mutants. Therefore, the ratios between the total iron and free iron levels for the *Δbfd, bfrB* (L68A/E81A) mutant cells were ~40 at 12 h and ~75 at 18 h. Despite the iron concentration in the media, wildtype cells maintain the total iron to free iron levels ratio around 20 (**Figure 2-9e**) at both 12 and 18 h [2]. This is a clear indication of iron homeostasis dysregulation caused by blocking the BfrB:Bfd interaction which causes the irreversible accumulation of iron in BfrB, which severely depletes the levels of free iron in the cytosol compared to the wild type cells.

As shown schematically in **Figure 2-10b**, the unidirectional flux of iron into BfrB lowers the free iron levels in the cytosol [2]. Once the BfrB:Bfd interaction is disrupted, the equilibrium between Fe^{3+} stored in BfrB and free Fe^{2+} in the cytosol is compromised. Hence, it can be concluded that this equilibrium functions as a buffer to control the free Fe^{2+} levels in the cytosol, which also contribute to the dynamic equilibrium between the apo- form of the master iron uptake regulator (Fur) and the Fe^{2+}-Fur complex. When the cytosolic free iron levels are lower than the K_d of the Fe^{2+}-Fur complex, dissociation of Fe^{2+}-Fur complex derepresses the iron acquisition genes, such as those coding for the biosynthesis of pyoverdin. This was evident in the pyoverdine hyper production phenotype observed with the *Δbfd*and *bfrB* (L68A/E81A) mutant cells where the equilibrium between free cytosolic Fe^{2+} and Fe^{3+} stored in BfrB is severely compromised, which results in significantly depressed cytosolic free Fe^{2+} levels and dysregulated expression of pyoverdine biosynthesis genes [2].

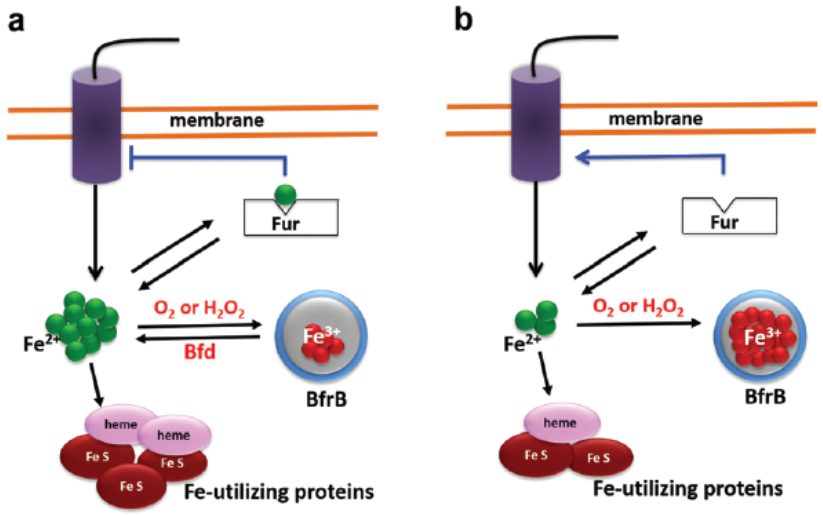

Figure 2-10: There is a dynamic equilibrium between the Fe^{3+} stored in BfrB and the free Fe^{2+} in the cytosol. When the free Fe^{2+} concentration is above or equal to the K_d of the Fe-Fur complex the iron acquisition genes are repressed. As the BfrB:Bfd interaction is disrupted, cytosolic free Fe^{2+} levels drop below the value of the K_d of Fe-Fur complex because of the unidirectional flux of iron into BfrB; when Fur is no longer bound with Fe^{2+} it derepresses iron acquisition genes. (Reprinted from Ref. 2 with permission from the Royal Society of Chemistry)

2.4 Conclusions

The optimized Native-PAGE method developed to image iron in bacterioferritin enabled our team to identify the function of BfrB as the main iron storage protein in *P. aeruginosa*. Imaging iron in BfrB also allowed us to follow iron storage and mobilization during different growth phases of the *P. aeruginosa* cells under different iron concentrations. It also permitted to discover the importance of the BfrB:Bfd interaction in maintaining iron homeostasis in *P. aeruginosa* cells. The *Δbfd* and *bfrB* (L68A/E81A) mutant cells are unable to mobilize iron from BfrB. As a consequence, the mutant cells showed irreversible accumulation of iron in BfrB and impaired growth in the low iron media. Additionally, blocking the BfrB:Bfd interaction caused unidirectional flow of iron into BfrB resulting in low cytosolic free iron levels. The *Δbfd* and *bfrB* (L68A/E81A) mutants had a higher total iron to free iron ratio (~75) 18 h post inoculation, whereas the wild type cells were able to maintain this ratio at ~20 [2]. Once the BfrB:Bfd interaction is blocked, iron stored in BfrB is no longer usable to the cells and the dynamic equilibrium between Fe^{3+} stored in BfrB and free cytosolic Fe^{2+} is disrupted, dysregulating the iron homeostasis of the cell. Also, the *bfr* and *bfd* genes are adjacent in a variety of Gram-negative bacteria, which suggests that the BfrB:Bfd shows extensive importance in iron homeostasis.

2.5 References

1. Andrews, S.C., A.K. Robinson, and F. Rodriguez-Quinones, *Bacterial iron homeostasis.* FEMS Microbiol Rev, 2003. **27**(2-3): p. 215-37.
2. Eshelman, K., et al., *Inhibiting the BfrB:Bfd interaction in Pseudomonas aeruginosa causes irreversible iron accumulation in bacterioferritin and iron deficiency in the bacterial cytosol.* Metallomics, 2017. **9**(6): p. 646-659.
3. Winterbourn, C.C., *Toxicity of iron and hydrogen peroxide: the Fenton reaction.* Toxicol Lett, 1995. **82-83**: p. 969-74.
4. Rivera, M., *Bacterioferritin: Structure Function and Protein–Protein Interactions*, in *Handbook of Porphyrin Science (Volume 30)*. p. 135-178.
5. Andrews, S.C., *The Ferritin-like superfamily: Evolution of the biological iron storeman from a rubrerythrin-like ancestor.* Biochim Biophys Acta, 2010. **1800**(8): p. 691-705.
6. Organization, W.H., *Prioritization of pathogens to guide discovery, research and development of new antibiotics for drug-resistant bacterial infections, including tuberculosis*. 2017, World Health Organization.
7. Yao, H., et al., *Two distinct ferritin-like molecules in Pseudomonas aeruginosa: the product of the bfrA gene is a bacterial ferritin (FtnA) and not a bacterioferritin (Bfr).* Biochemistry, 2011. **50**(23): p. 5236-48.
8. Ma, J.F., et al., *Bacterioferritin A modulates catalase A (KatA) activity and resistance to hydrogen peroxide in Pseudomonas aeruginosa.* J Bacteriol, 1999. **181**(12): p. 3730-42.
9. Garg, R.P., et al., *A [2Fe-2S] protein encoded by an open reading frame upstream of the Escherichia coli bacterioferritin gene.* Biochemistry, 1996. **35**(20): p. 6297-301.
10. Ochsner, U.A., et al., *GeneChip expression analysis of the iron starvation response in Pseudomonas aeruginosa: identification of novel pyoverdine biosynthesis genes.* Mol Microbiol, 2002. **45**(5): p. 1277-87.
11. Rivera, M., *Bacterioferritin: structure, dynamics, and protein–protein interactions at play in iron storage and mobilization.* Accounts of chemical research, 2017. **50**(2): p. 331-340 %@ 0001-4842.
12. Yao, H., et al., *The structure of the BfrB-Bfd complex reveals protein-protein interactions enabling iron release from bacterioferritin.* J Am Chem Soc, 2012. **134**(32): p. 13470-81.
13. Wang, Y., et al., *Characterization of the Bacterioferritin/Bacterioferritin Associated Ferredoxin Protein-Protein Interaction in Solution and Determination of Binding Energy Hot Spots.* Biochemistry, 2015. **54**(40): p. 6162-75.
14. Chung, M.C., *A specific iron stain for iron-binding proteins in polyacrylamide gels: application to transferrin and lactoferrin.* Anal Biochem, 1985. **148**(2): p. 498-502.
15. Kuo, C.F. and I. Fridovich, *A stain for iron-containing proteins sensitive to nanogram levels of iron.* Anal Biochem, 1988. **170**(1): p. 183-5.
16. Leong, L.M., B.H. Tan, and K.K. Ho, *A specific stain for the detection of nonheme iron proteins in polyacrylamide gels.* Anal Biochem, 1992. **207**(2): p. 317-20.
17. Stover, C.K., et al., *Complete genome sequence of Pseudomonas aeruginosa PAO1, an opportunistic pathogen.* Nature, 2000. **406**(6799): p. 959-64.
18. Bradley, J.M., N.E. Le Brun, and G.R. Moore, *Ferritins: furnishing proteins with iron.* J Biol Inorg Chem, 2016. **21**(1): p. 13-28.
19. Abdul-Tehrani, H., et al., *Ferritin mutants of Escherichia coli are iron deficient and growth impaired, and fur mutants are iron deficient.* J Bacteriol, 1999. **181**(5): p. 1415-28.
20. Velayudhan, J., et al., *The role of ferritins in the physiology of Salmonella enterica sv. Typhimurium: a unique role for ferritin B in iron-sulphur cluster repair and virulence.* Mol Microbiol, 2007. **63**(5): p. 1495-507.
21. Palma, M., S. Worgall, and L.E. Quadri, *Transcriptome analysis of the Pseudomonas aeruginosa response to iron.* Arch Microbiol, 2003. **180**(5): p. 374-9.

22. Fish, W.W., *Rapid colorimetric micromethod for the quantitation of complexed iron in biological samples.* Methods Enzymol, 1988. **158**: p. 357-64.
23. Woodmansee, A.N. and J.A. Imlay, *Quantitation of intracellular free iron by electron paramagnetic resonance spectroscopy.* Methods Enzymol, 2002. **349**: p. 3-9.
24. Yan, Y., et al., *Intracellular free iron and its potential role in ultrahigh-pressure-induced inactivation of Escherichia coli.* Appl Environ Microbiol, 2013. **79**(2): p. 722-4.

Chapter 3 : Small molecule inhibitors of the BfrB:Bfd interaction affect the fitness of *P. aeruginosa,* dysregulate iron homeostasis and potentiate fluoroquinolone activity

This chapter is based on the publication:

Punchi Hewage, A. N. D.*; Yao, H.*; Nammalwar, B.; Gnanasekaran, K. K.; Lovell, S.; Bunce, R. A.; Eshelman, K.; Phaniraj, S. M.; Lee, M. M.; Peterson, B. R.; Battaile, K. P.; Reitz, A. B.; Rivera, M., "Small Molecule Inhibitors of the BfrB–Bfd Interaction Decrease *Pseudomonas aeruginosa* Fitness and Potentiate Fluoroquinolone Activity". Journal of the American Chemical Society 2019, 141, 8171-8184.

*These authors contributed equally

3.1 Introduction

Iron is an essential nutrient for prokaryotic and eukaryotic cells. It is the fourth most abundant element on earth. Iron mainly exists in two oxidation states, Fe^{2+} and Fe^{3+}. The soluble Fe^{2+} is abundant in anaerobic or microaerobic aqueous environments. In oxygenated environments, Fe^{3+} is the most abundant oxidation state of iron; the low solubility of Fe^{3+} brings challenges in fulfilling the nutritional requirements of microorganisms with an aerobic lifestyle [1]. In the presence of free iron, dioxygen, and its one-electron and two-electron reduced species (superoxide and peroxide) exert toxic effects on biological systems. Cells regulate iron rigorously to maintain low intracellular free iron levels to protect against the damages caused by oxyradicals [2]. Bacteria have evolved diverse mechanisms to acquire sufficient iron for growth while avoiding iron-induced toxicity.

P. aeruginosa is a Gram-negative opportunistic pathogen and one of the leading causes of hospital-acquired infections. In *P. aeruginosa,* 6 % of the transcribed genes are iron-responsive [3]; this exemplifies the importance of iron for the vital cellular functions, such as respiration, gene regulation, DNA biosynthesis, and the tricarboxylic acid cycle (TCA). In the priority list published by the World Health Organization (WHO) for the development of anti-infectives, carbapenem-resistant *Pseudomonas aeruginosa* and *Acinetobactoer baumannii* have been assigned critical priority [4]. Therefore, numerous efforts with diverse strategies have been put into the development of anti-infectives to kill or disarm *P.*

aeruginosa [5]. In this context, approaches that interfere with the iron homeostasis are considered to have potential for developing anti-infective inventions [3, 6].

3.1.1 Significance of the BfrB:Bfd interaction in iron homeostasis of *P. aeruginosa*

BfrB is the main iron storage protein in *P. aeruginosa* [7]. Iron mobilization from BfrB requires interactions with its cognate partner protein, Bfd. In the BfrB:Bfd complex, 12 Bfd molecules are bound to BfrB; each Bfd molecule binds between two subunits, above each heme molecule [8, 9]. The 12 Bfd binding sites on BfrB are equivalent and independent. The residues M1, Y2, and L5 of Bfd, and L68 and E81 of BfrB contribute the most to the stabilization of the BfrB:Bfd complex [10]. The K_d value of the BfrB:Bfd complex is 3 μM. Mutating L68 or E81 to alanine in BfrB resulted in a 100-fold higher K_d relative

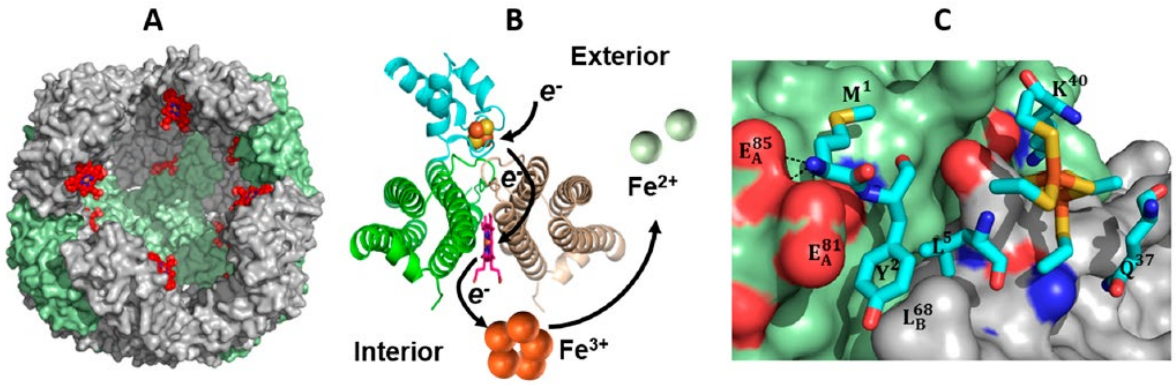

Figure 3-1: (A) *P. aeruginosa* BfrB is assembled from 24 identical subunits with 12 hemes (red), each heme resides between two subunits. The Fe^{3+} mineral is stored in the hollow cavity (80 Å diameter). (B) Heme (red) is bound between two subunits of BfrB (green and grey). Bfd (cyan) binds above the heme of BfrB. Black arrows indicate the electron flow path from the [2Fe-2S] cluster (yellow and orange spheres) of Bfd to the Fe^{3+} mineral in BfrB, thus allowing the mobilization of Fe^{2+}. (C) A view of the BfrB:Bfd interface. Key Bfd residues Y2 and L5 reside on the surface pockets formed by L68 and E81 of BfrB. The [2Fe-2S] is shown in yellow and orange. (Figures are reprinted from Ref. 7 with permission from Royal Society of Chemistry and Ref. 9 (https://pubs.acs.org/doi/10.1021/acs.accounts.6b00514) with permission. Further permissions related to the material excerpted should be directed to the ACS))

to the wild type BfrB:Bfd complex. When both, L68 and E81 are mutated to alanine, the association of the Bfd with BfrB was undetectable [10].

The repercussions of blocking the BfrB:Bfd interaction in *P. aeruginosa* was investigated by deleting the *bfd* gene (*Δbfd*) or by replacing the *bfrB* gene with a L68A/E81A double mutant *bfrB* allele at the *bfrB* native site (*bfrB*(L68A/E81A)) [7]. As discussed in Chapter 2, these two mutants disclosed the importance of the BfrB:Bfd interaction in *P. aeruginosa* cells. In absence of the BfrB:Bfd interaction iron accumulates irreversibly in BfrB. The unidirectional flux of iron into BfrB caused a more significant fraction of iron to be trapped in BfrB, and this trapped iron is not a usable resource to the bacterial cell. Consequently, the *Δbfd* and the *bfrB*(L68A/E81A) mutant cells showed acute iron starvation responses (overproduction of pyoverdine) as a consequence of low free iron levels in the cytosol, despite seemingly normal intracellular ion levels caused by irreversible accumulation of iron in BfrB. The BfrB:Bfd interaction is the only available mechanism to mobilize iron from BfrB [7]. Disruption of the BfrB:Bfd interaction dysregulates iron homeostasis and affects the broader metabolism of *P. aeruginosa.* As discussed in Chapter 4, iron homeostasis dysregulation has significant effects on TCA cycle, amino acid biosynthesis, respiratory cycle, and oxidative stress management in *P. aeruginosa.*

Blocking the BfrB:Bfd interaction appears to be a suitable and novel approach to induce iron homeostasis dysregulation in *P. aeruginosa*. Small-molecule chemical probes that have the potential to inhibit the BfrB:Bfd interaction have been developed in our lab. These chemical probes can be useful in studying bacterial iron homeostasis and recognizing additional weaknesses caused by iron homeostasis dysregulation. Testing the effects of these novel chemical probes on the fitness of *P. aeruginosa* cells is at the center of work presented in this Chapter.

3.1.2 Challenges in developing antimicrobials for Gram-negative bacteria

Discovering anti-infective agents against Gram-negative bacteria is challenging, especially for *P. aeruginosa*, where the hit rates of screening campaigns are 1000-fold lower than hit rates of campaigns against Gram-positive bacteria [11]. One of the primary reasons for a lower hit rate is the limited membrane permeability. Gram-negative bacteria have two membrane cell envelopes. The outer membrane (OM) is comprised of an asymmetric bilayer of lipopolysaccharides (LPS) and phospholipids, which are known to

slow down the uptake of anti-infectives significantly. The presence of LPS in the OM makes Gram-negative bacteria resistant to antibiotics. [12].

The outer membrane permeability of *P. aeruginosa* is about 8 % that of *E. coli* because *P. aeruginosa* outer membrane lacks general diffusion porins such as OmpC and OmpF of *E.coli.* The most abundant porin in *P. aeruginosa* is the outer membrane protein F (OprF) which is highly selective and shows very slow solute diffusion. The diffusion of L-arabinose into *P. aeruginosa* by the OprF porin was 50-fold slower than the OmpF porin in *E. coli.* The other porins, such as OprC, OprD, OprE are relatively expressed in low levels in *P. aeruginosa* [12-14].

Permeating two protective lipid bilayers in Gram-negative bacteria by a drug is quite challenging. Importantly, Lipinski's rule of five is not valid for the antibiotics that require penetration of bacterial membranes because passage through the OM requires different physiochemical rules than the IM and vice versa. Therefore, an acceptable set of rules for antibacterial agents appear to be nonexistent. Richter and co-workers have explored the small molecule accumulation in the Gram-negative cells. According to the results, to be successfully taken by the cells, a molecule must contain an amine, have low globularity, be amphiphilic, and rigid [15].

It is essential to evaluate the effectiveness of inhibitors *vs. P. aeruginosa* cells *in-cell*, in order to select compounds not only exhibiting good affinity for BfrB *in vitro*, but also activity against *P. aeruginosa* cells. Hence, the work presented in this Chapter is directed at evaluating compound activity against *P. aeruginosa*, as well as demonstrating that the inhibitors engage their intended target (BfrB) in the *P. aeruginosa* cytosol.

It is essential to evaluate the effectiveness of inhibitors *vs. P. aeruginosa* cells *in-cell*, in order to select compounds not only exhibiting good affinity for BfrB *in vitro*, but also activity against *P. aeruginosa* cells. Hence, the work presented in this Chapter is directed at evaluating compound activity against *P.*

aeruginosa, as well as demonstrating that the inhibitors engage their intended target (BfrB) in the *P. aeruginosa* cytosol.

3.1.3 Challenges faced in developing protein-protein interaction inhibitors

Protein-protein interactions (PPIs) play a crucial role in cellular processes. PPIs are an attractive target for molecular probe development [16]. Initially, PPIs had been considered inflexible for developing inhibitors because of the highly dynamic and broad interfacial areas. PPIs are stabilized using a large burial of atomic interfaces, which can extend up to thousands of $Å^2$. These interface areas are very large compared to the interaction sites in an enzyme or in a receptor. Also, the PPI interfaces represent diverse and multifaceted binding sites which present significant challenges in finding efficient inhibitors, and the PPI surfaces, which are mostly flat, do not exhibit deep pockets for small molecule binding. In addition, inhibition of PPIs does not offer simple assays to identify activity and potency [17, 18].

More recently, mutating amino acid contacts within the PPI site into alanine revealed that mutation of only certain residues causes significant destabilizing effects on the protein-protein complexes. These residues, which have been found to contribute to most of the binding energy, have been termed “hot-spot” residues in a PPI. Consequently, an inhibitor which makes reasonably strong interactions with the hot-spot residues in a protein will be able to effectively compete with binding partner protein, without having to bind to the entire PPI binding surface [16, 18].

3.1.4 Fragment-Based Drug Discovery Strategy in inhibitor development

Discovering novel molecules for the modulation of biological functions is one of the primaries on drug development. Over the past decade, pharmaceutical industries mainly relied on high-throughput screening (HTS) to identify possible inhibitors for a target. During HTS, a large library of compounds (10^6) is screened against the target. Maintenance of the diversity and the quality of the HTS library is tedious. Some of the molecules in the library may not be druglike, lack thermodynamic solubility, and show relatively lipophilic properties. The molecules in the HTS library may not cover many possible chemical spaces. Even after identifying a hit in HTS, the relative contribution by the different sites of a molecule to

the binding energy of a complex is not clear. This raises difficulties in increasing potency by structure-based development [19].

In the Fragment-Based Drug Discovery (FBDD) strategy, chemical starting points are identified and improved to develop drug-like molecules. Fragment-based methods use a library of about 1000 fragments, which contains weakly binding small molecules with the following properties, (i) < 300 Da molecular weight, (ii) up to three hydrogen bond donors and acceptors, (iii) calculated logP (clogP) of ≤3. When a small molecule (100 μM affinity) binds to a part of the potential drug site (3 nM affinity), even if the affinity for the site is 33,000 times weaker, the small molecule contributes over half of the favorable energy. Even though fragments bind with relatively low affinity, fragments can form high quality-interactions [20]. Hence, fragments are very "atom efficient," as demonstrated by their high ligand efficiency (LE), which is defined as $-\Delta G$ in kcal mol^{-1} divided by the number of heavy atoms (non-hydrogen). The fragment libraries used in the FBDD strategy contain a relatively small number of fragments compared to HTS libraries, because fragments can cover significantly larger chemical space [19]. In addition, since the fragments in a fragment library are less complex than compounds in a traditional HTS library, higher hit rates are achieved screening a fragment library than screening an HTS library comprised of drug-sized molecules (complex molecules result in mismatches with the target due to suboptimal interactions or clashes) [17, 19].

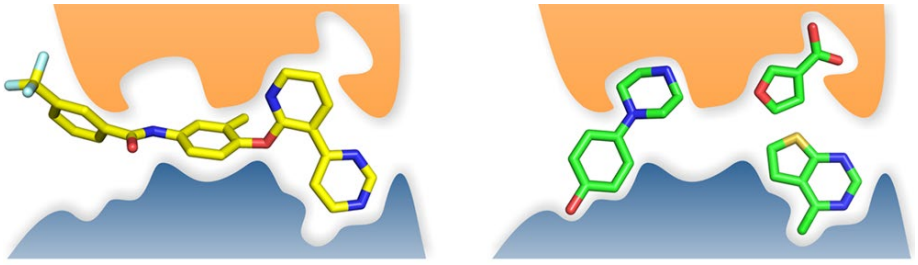

Figure 3-2*:* HTS screen hits bind to the target with numerous suboptimal interactions. Fragments are more ligand efficient and have fewer but optimal interactions. (Figures are reprinted with permission from Ref. 19 copyright (2012) American Chemical Society)

Three stages are involved in a Fragment-Based Drug discovery campaign, (i) library design, (ii) fragment screening (NMR, X-ray crystallography, Mass spectrometry, Surface Plasmon Resonance, *etc.*), and (iii) elaboration of the fragment hits into lead compounds.

3.1.5 Developing small molecule inhibitors of the BfrB:Bfd interaction in *P. aeruginosa*

Chemical probes are a powerful tool to complement the use of genetic techniques. They can be used alone or in combination with synergistic or antagonistic probes. Using the structural information gathered from the BfrB:Bfd co-crystal structure, a small fragment library was designed by focusing on the stabilizing interactions between Y2 and L5 of Bfd, and L68 and E81 in BfrB, the hot region of the BfrB:Bfd complex. Hence, the fragment library was constructed from fragments with chemical properties resembling the aromatic and aliphatic side chains of Tyr and Leu, also having other standard fragment properties (MW<300 Da, total hydrogen bond donors/acceptors <3, and clogP <3). Fragments containing electron-rich and deficient aromatic rings were also added to the library [21].

To identify the fragments that are bound to BfrB at the Bfd site, a Saturation Transfer Difference (STD) NMR assay was developed [21]. The STD NMR assay is suited to screen fragments that bind to large proteins (~440 kDa BfrB). Since the STD NMR strategy detects fragment resonances, the protein resonance assignments are not required. Spin diffusion and saturation transfer from the protein to the ligand are enhanced due to the large rotational correlation time (τ_c) of BfrB. **Figure 3-3** illustrates the STD NMR screening process using fragment **1** (5-hydroxyisoindoline-1,3-dione) as example. The ^{1}H NMR spectrum was acquired for the fragment alone (**Figure 3-3-A**) and for the fragment with BfrB (**Figure 3-3-B**) [21]. The STD spectrum of the fragment with BfrB is used to identify fragments that bind to BfrB. The STD NMR spectrum in **Figure 3-3-C** illustrates the binding of fragment **1** to BfrB [21]. This strategy allowed

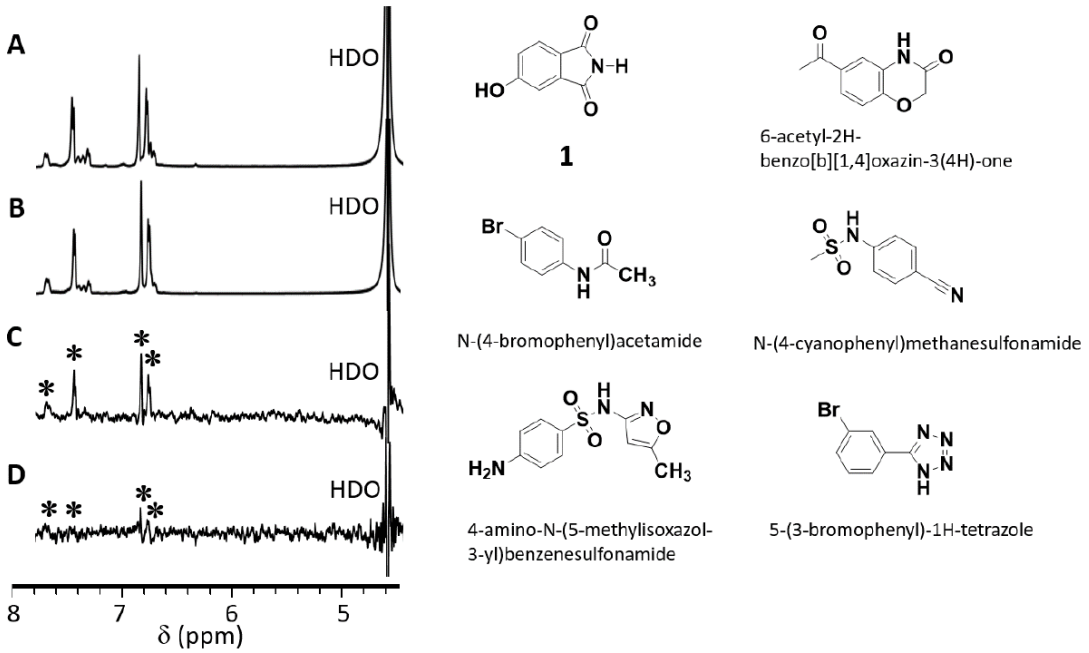

Figure 3-3: The fragment **1** screening process with Saturation Transfer Difference (STD) NMR. (A) ^{1}H NMR spectrum of fragment **1** alone. (B) ^{1}H NMR spectrum of fragment **1** with BfrB. (C) The STD NMR spectrum of a solution that contains fragment **1** and BfrB (fragment **1** binds to BfrB). (D) The STD NMR of a solution with fragment **1**, BfrB and Bfd. Decreased intensity compared to C indicates the displacement of BfrB bound fragment **1** by Bfd. The right panel shows six fragments that are identified to bind BfrB at Bfd binding site. (Figures are reprinted with permission from Ref. 21 (https://pubs.acs.org/doi/10.1021/jacs.9b00394) and further permissions related to the material excerpted should be directed to the ACS)

us to identify 18 fragments that are bound to BfrB. Next, a displacement strategy was employed using Bfd as the competitor to find the fragments that are bound to BfrB at the Bfd binding site. To this end, a STD spectrum of the fragment in the presence of BfrB and Bfd was acquired. The almost disappearance of the STD signal indicates the fragment binding at the Bfd-binding site on BfrB (**Figure 3-3-D**) [21].

Using the developed STD strategy, six fragments (**Figure 3-3** right panel) that bind BfrB at the Bfd binding site were identified [21]. All the six fragments were tested in ligand soaking experiments using BfrB protein crystals. The structure of fragment **1** (5-hydroxyaminoisoindoline-1,3-dione) bound to crystals of C98S/ K96C BfrB helped to uncover structural information on fragment-BfrB binding (**Figure 3-4-B**) [21]. The residues, E81 and L68 of BfrB, and L5 and Y2 of Bfd have a significant contribution to the BfrB:Bfd complex stability (**Figure 3-4-A**) [8, 10]. As illustrated in **Figure 3-4-B**, fragment **1** binds in the same pocket in BfrB, where L5 of Bfd binds [21]. One of the carbonyl oxygens in fragment **1** forms an H-bond with the backbone NH of L_A^{71} and the N-H group of fragment **1** forms another H-bond with the backbone carbonyl oxygen of P_A^{69}. Additional stabilization for binding stems from the H-bonding network linking carbonyl oxygen of fragment **1** and G_A^{67} in BfrB. This structural information permitted branching the fragment from the isoindoline ring carbons C4 or C5 positions to grow the fragment into the cleft formed by the side chains of L68 and E81 of BfrB, where Y2 of Bfd binds.

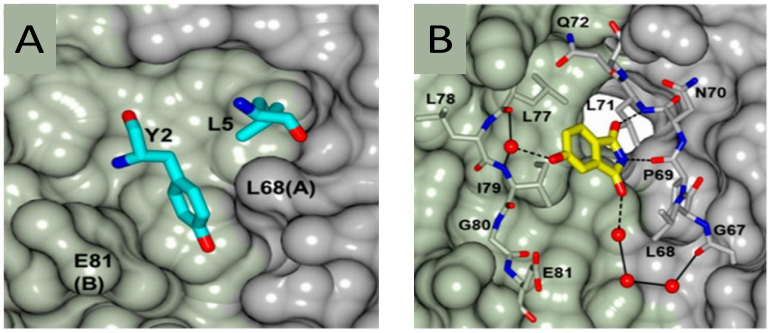

Figure 3-4: (A) The BfrB:Bfd binding interface. BfrB subunit A and B are colored grey and green, respectively. Bfd residues Y2 and L5 (cyan) bind in the pockets of the BfrB surface. (B) Fragment **1** is bound in a pocket near L68, where L5 from Bfd binds (PDB ID: 6NLG). The hydrogen bond interactions between the fragment and BfrB are indicated by a dashed line and the water-mediated contacts are shown in solid lines. (Figures are reprinted with permission from Ref. 21 (https://pubs.acs.org/doi/10.1021/jacs.9b00394) and further permissions related to the material excerpted should be directed to the ACS)

Figure 3-5-A shows a general synthetic approach used in the synthesis of analogs of fragments **1**, **5** and **8** [21]. Ether analogs (**4**) are derived from 5-hydroxyisoindoline-1,3-dione (**1**), amine analogs such as **6**, or amide analogs such as **7** are derived from 5-aminoisoindoline-1,3-dione (**5**); amine analogs such as **9**, or amide analogs such as **10** are derived from 4-aminoisoindoline-1,3-dione (**8**). The active analogs prepared by the reductive amination of fragment **8** are shown in the bottom panel of **Figure 3-5** [21].

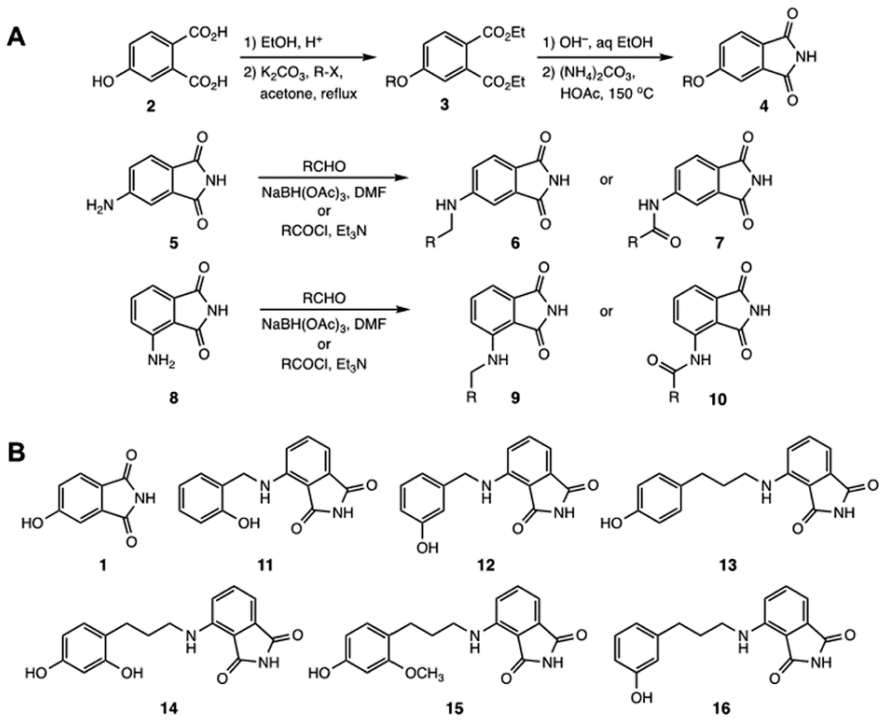

Figure 3-5: (A) Summary of synthetic procedures used in the preparation of analogs from fragments **1**, **5** and **8**.
(Figures are reprinted with permission from Ref. 21 (https://pubs.acs.org/doi/10.1021/jacs.9b00394) and further permissions related to the material excerpted should be directed to the ACS)

The synthesized 4-aminoisoindoline-1,3-dione derivatives were tested *in-vitro* for binding by measuring K_d for binding to BfrB and by soaking BfrB crystals in solutions containing each of the analogs. The analogs were also tested for activity *vs. P. aeruginosa* and for target (BfrB) engagement in the *P. aeruginosa* cytosol. As will be shown below, the 4-aminoisoindoline-1,3-dione derivatives acted on its target, BfrB, blocked iron mobilization from BfrB, elicited bacterial cell growth retardation, and

overproduced pyoverdine [21]. Additionally, the 4-aminoisoindoline-1,3-dione derivatives provoked growth retardation in more than one strain of *P. aeruginosa* and in other Gram-negative bacteria, such as *Acinetonbactor baumannii* (AB5075).

3.2 Experimental

3.2.1 Strains, growth media and conditions

Pseudomonas aeruginosa (PA01) and *Acinetobactor baumannii* (AB5075) were purchased from the University of Washington Genome Center. The *P. aeruginosa* cystic fibrosis lung clinical isolates, MR3B and MR60 were received from the Seattle Children's Research Institute via the Antimicrobial Tools and Resources services offered by the Cystic Fibrosis Foundation. The *P. aeruginosa* urinary tract clinical isolates, JMI U1 (1044308), JMI U2 (1046460), JMI U4 (1050182), and JMI U6 (1044635) were purchased from the JMI Laboratories, North Liberty, IA. All chemicals were purchased from Fisher Scientific (Hampton, NH) unless otherwise stated.

The *P. aeruginosa* (PA01) derived strain *ΔbfrB* with an unmarked deletion of the *bfrB* gene had been prepared previously [7]. *P. aeruginosa* strains were kept on Pseudomonas isolation agar (PIA) (BD Biosciences, CA), and *A. baumannii* (AB5075) was kept on LB agar.

M63 media per liter contained: 13.6 g of KH_2PO_4 (Sigma-Aldrich), 2 g of $(NH_4)_2SO_4$, 2 g of glucose, 4 g of citric acid, 0.25 g of tryptophan (Acros organics), 5 g of nontechnical grade casamino acids (BD scientific), and 0.24 g of $MgSO_4$ (Alfa Aesar), and the pH was adjusted to 7.0 with KOH [22]. M63 media was supplemented with 0.1 % (w/v) hypromellose (HPMC, Sigma-Aldrich) to prevent the analog aggregation and precipitation [23]. Colorimetric analysis of iron in the M63 media revealed ~2 μM iron. A 10 mM iron stock solution was prepared by dissolving 39.2 mg of $(NH_4)_2Fe(SO_4)_2$ in 10 mL of acidic water (pH ≈ 2.0). The media was supplemented with iron using the 10 mM stock solution to reach appropriate concentrations.

Modified M63 media was prepared with small modifications of the above protocol. Modified M63 media contained per liter: 2 g of $(NH_4)_2SO_4$, 13.6 g of KH_2PO_4(Sigma-Aldrich), 2.5 g of glucose, 10% MEM non-essential amino acid solution (*Gibco*®), 4 % MEM amino acid solution (*Gibco*®) and 0.12 g of $MgSO_4$(Alfa Aesar), and the pH was adjusted to 7.0 with KOH. The modified M63 media contained 0.025% (w/v) of hypermellose (HPMC, Sigma-Aldrich). The media was supplemented with 4 μM iron using the 10 mM $(NH_4)_2Fe(SO_4)_2$ stock.

P. aeruginosa pre-cultures were grown in LB media for 12 h at 37 ^{0}C and with shaking at 220 rpm. Cells were collected by centrifugation and washed twice in M63 media before diluting the cells to the desired OD_{600}.

3.2.2 Growth Curves and IC_{50} Determination

P. aeruginosa pre-cultures were grown as described above. Cells were diluted to give an OD_{600} = 0.01. Analog stocks (100 mM) were kept in DMSO. Analog stocks were diluted to 10 or 1mM in DMSO and used in the subsequent steps. The appropriate volumes from the analog stocks (to result in different analog concentrations) were transferred to a glass vial and adjusted to a final volume of 30 μL with DMSO. For the untreated control, 30 μL of DMSO was used. A volume of 1470 μL from the cell suspension was added to each vial containing the 30 μL of analog in DMSO. For the cultures treated with ciprofloxacin, a volume of 11.2 μL from the ciprofloxacin stock (100 μg/mL in sterile water) was mixed with 30 μL of DMSO, and the final volume was adjusted to 1.5 mL using the cell suspension. The resulting concentration of ciprofloxacin in the solution was 0.75 μg/mL, which is the 3x the Minimum Inhibitory Concentration (MIC) for *P. aeruginosa* (PA01) [24]. From the resultant mixtures, a volume of 200 μL was aliquoted to wells of a 96 well plate; the 96 well plate was incubated at 35 ^{0}C, 205 cpm for 13 h in an Epoch 2 microplate spectrophotometer (Biotek Instruments, Inc., Vermont). Each condition was comprised of 5 technical replicates. The OD_{600} was recorded every 15 minutes. The % growth was calculated at 13 h post-inoculation using **equation 1**. The terms used in **equation 1** are as follows: OD_T is the OD_{600} of the analog treated culture, OD_U is the OD_{600} of the untreated culture, and OD_{Cip} is the OD_{600} of the ciprofloxacin treated

culture. The % growth was plotted against *log* [analog (μM)], and the resultant plot was fitted to **equation 2** to calculate IC_{50}. In **equation 2** the term *b* is defined as the slope factor.

$$\text{growth } \% = \frac{OD_T - OD_{Cip}}{OD_U - OD_{Cip}} \times 100 \quad (1)$$

$$\text{growth } \% = OD_{Cip} + \frac{OD_U - OD_{Cip}}{1 + \left(\frac{\log[\text{analog}(\mu M)]}{IC_{50}}\right)^{-b}} \quad (2)$$

3.2.3 Secreted pyoverdine analysis

Experiments were carried out as presented in the growth curves and IC_{50} determination section. At 13 h post-inoculation, the content of each well was serially diluted in phosphate-buffered saline (PBS, pH 7.4) and plated for enumerating viable cells. The 500-fold diluted samples from the previous step were centrifuged, and the supernatants were collected for the pyoverdine measurements. Collected supernatants were analyzed by fluorescence spectrophotometry with excitation at 400 nm and fluorescence emission measured at 455 nm using a Synergy H1 microplate reader. Emission spectra (430-550) nm were collected using a PerkinElmer LS50B spectrophotometer. The pyoverdine fluorescence intensity from the samples was normalized to the Colony Forming Units/mL (CFU/mL) for each sample.

3.2.4 Imaging iron stored in BfrB

P. aeruginosa pre-cultures were prepared as described in the growth conditions. Cells were centrifuged, washed twice, and diluted to OD_{600} = 0.1 in M63 media supplemented with 4 μM iron. A volume of 5 mL from the cell suspension was mixed with 37.5 μL of DMSO and 62.5 μL of 10 mM analog **16** (in DMSO) working solution to result in a 125 μM analog concentration and 2 % DMSO. For the untreated control, 5 mL of cell suspension was mixed with 100 μL of DMSO (resulting 2% DMSO in 5.1 mL). Sample tubes were covered with an air-permeable membrane and incubated at 35 ^{0}C and 120 rpm. Sample tubes were collected at 6, 9, 12, 15, 18, 21, and 24 h post-inoculation. A volume of 100 μL was

withdrawn from each sample and serially diluted for plating and enumerating viable cells. The remaining culture was centrifuged (4000 rpm, 15 min), washed with PBS, and frozen at -20 ^{0}C until analysis.

Cell pellets were lysed by using the optimized protocol (see Chapter 2) with minor modifications [7]. Cell pellets were re-suspended in 300 µL lysis buffer (50 mM Tris pH 8.0, 20% glycerol, 20 mg/mL lysozyme, 0.2 mg/mL DNase, 100 mM NaCl, 10 mM $MgCl_2$, and 1% Triton X). Cell suspensions were exposed to two freeze-thaw cycles in liquid N_2. Samples were incubated with shaking at 25 ^{0}C for 90 min in a rocker, and the lysates were centrifuged at 12500 rpm for 15 min at 4 ^{0}C. A volume of 100 µL from the lysate was mixed with 10 µL of loading dye, and 100 µL from the resultant solution was loaded into a 3 mm thick Native-PAGE (8 % separating gel and 4 % stacking gel). Electroporation was done at 60 V for 7 h at 4 ^{0}C. Gels were stained with FereneS (0.049 g of FereneS, 250 µL of thioglycolic acid, 2.5 mL of acetic acid, and 100 mL of water) for 10 min [25], imaged and then analyzed using ImageJ software.

3.2.5 Analysis of total intracellular iron in analog-treated *P. aeruginosa* cells

P. aeruginosa pre-cultures were grown as described in the media and growth conditions. Cells collected from the pre-cultures were centrifuged, washed twice in M63, and diluted to OD_{600} = 0.1 in M63. For the analysis of total intracellular iron, 5 mL cultures were prepared in M63 media supplemented with 4 µM iron, with analog **16** at 125 µM or with DMSO, as described in **section 3.2.4.** Samples were collected at 12, 15, 21, 24, and 28 h post-inoculation. A volume of 100 µL was withdrawn from the samples for viable cell enumeration. Cells were collected by centrifugation (4000 rpm, 15 min) and washed twice with PBS. The analysis of total intracellular iron was done by following a published protocol, but using FreneS as the colorimetric reagent instead of Ferrozine [26].Cell pellets were mixed with 500 µL of 1:1 (v/v) 1.2 N HCl and 4.5% w/v $KMnO_4$ in water. Suspensions were incubated at 65 ^{0}C for 4 h, and after letting samples come to the room temperature, 500 µL of the iron chelation reagent (6.5 mM Ferene S, 13.1 mM neocuproine, 2 M ascorbic acid, and 5 M ammonium acetate) was added. Samples were incubated at 25 ^{0}C for 30 min, and the absorbance of the Fe^{2+}-FereneS complex was measured at 593 nm (ε =34,500M^{-1} cm^{-1}) using Cary 60 UV-vis spectrophotometer. The total iron levels were reported as Fe atoms per CFU.

3.2.6 Antibiotic and analog combination treatment of *P. aeruginosa*

P. aeruginosa pre-cultures were prepared as described in the media and growth conditions. Cells were diluted to OD_{600} = 0.1 in M63 media supplemented with 4 μM iron. 5 mL from the cell suspension was treated with (i) analog **16** alone, (ii) fluoroquinolones ciprofloxacin (0.25 μg/mL), levofloxacin (0.5 μg/mL), or norfloxacin (0.9 μg/mL) only, (iii) analog **16** and fluoroquinolone in combination. Varying analog **16** concentrations were used (75, 100, and 125 μM) for the treatment. The final DMSO concentration in the samples was 2%. Samples were incubated at 35 ^{0}C and 120 rpm and collected 18 h post-inoculation; viable cells were enumerated by withdrawing 100 μL. A similar set of experiments were carried out with analog **11** and ciprofloxacin. The combination treatment of analog **16** (125 μM) with other antibiotics, tobramycin (5 μg/mL), gentamycin (5 μg/mL), ceftazidime (1 μg/mL), and imipenem (1.5 μg/mL) was done following the same experimental protocol.

3.2.7 Growth of clinical isolates of *P. aeruginosa* and *A. baumannii*

Pre-cultures were grown as indicated above. Cells were collected by centrifugation and washed twice in modified M63. The cell suspension was adjusted to 5×10^5 CFU/mL in the modified M63 media supplemented with 4 μM iron. The 5×10^5 CFU/mL initial cell density is recommended for the susceptibility assays by the Clinical and Laboratory Standards Institute [27]. A 10 mM analog stock was used to deliver the appropriate volumes to make 1 mL of 32, 64, and 128 μM analog concentrations. The total volume of DMSO in the tubes was adjusted to 20 μL. A volume of 980 μL from the cell suspension was added to the analog DMSO mixture. For *P. aeruginosa* growth curves, a volume of 200 μL from the resultant solution was aliquoted into a 96 well plate. For *A. baumannii* growth curves, a volume of 1 mL from the resultant solution was aliquoted into a 48 well plate. Plates were incubated at 35 ^{0}C and 205 cpm. At 22 h (*P. aeruginosa*) or 24 h (*A. baumannii*) post-inoculation viable cells were enumerated by plating. The % growth of the treated samples was calculated relative to the untreated control.

3.2.8 Chrome Azurol S (CAS) assay for siderophore detection in *A. baumannii* cultures

Acinetobactor baumannii cell cultures were treated as in **section 3.2.6**. Cell-free supernatants were collected at 24 h post-inoculation. A volume of 25 µL from the supernatant was mixed with 175 µL from the CAS assay reagent (10 mM hexadecyltrimethyl ammonium bromide- HDTMA, 1 mM $FeCl_3.6H_2O$, 2 mM chrome azurol S–CAS in 145 mM PIPES buffer pH 5.9) [28]. Solutions were incubated at room temperature for 2 h, and absorbance at 630 nm was measured using an Epoch 2microplate spectrophotometer (Biotek Instruments, Inc., Vermont). Percent Siderophore Units (PSU) was calculated using **equation 3** [29].

$$\text{Percent Siderophore Units (psu)} = \frac{(\text{Ar-As}) \times 100}{\text{Ar}} \qquad \textbf{(3)}$$

Where Ar is the absorbance of the reference (CAS solution and un-inoculated broth) and As is the absorbance of the sample (CAS solution and cell-free supernatant of the sample). The PSU was normalized to the CFU/mL of the respective sample.

3.3 Results and Discussion

3.3.1 Structure-based development of fragment binders

Saturation Transfer Difference NMR was able to identify 18 fragments bound to BfrB, and six fragments bound to BfrB at the Bfd-binding site. These six fragments were used in ligand soaking experiments with BfrB protein crystals. The X-ray crystallographic structure of fragment **1** (5-hydroxyaminoisoindoline-1,3-dione) bound to C98S/ K96C BfrB was used to gather structural insights of binding [21].

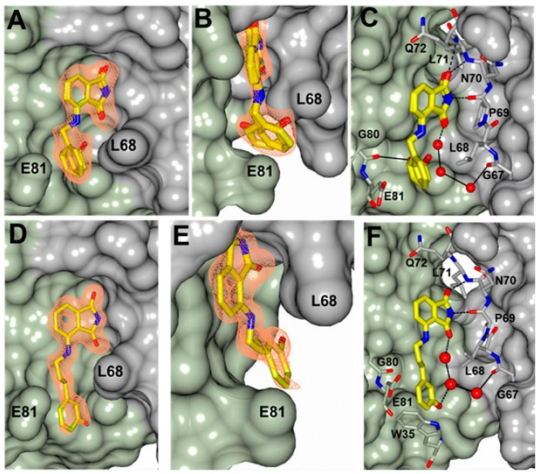

Figure 3-6: X-ray crystallographic structures of analog **11** (PDB ID: 6NLI) and **16** (PDB ID: 6NLN) bound to *P. aeruginosa* BfrB. (A) F_o-F_c omit map contoured at 3σ from analog **11** bound to BfrB, (B) modeled two orientations for the o-hydroxyphenyl ring of analog **11,** (C) contacts of analog **11**; dashed lines illustrate hydrogen bonding and the solid lines illustrate water mediated contacts. (D) F_o-F_c omit map contoured at 3σ from analog **16** bound to BfrB. (E) Same as D, but rotated to illustrate the m-hydroxyphenyl ring in the cleft formed by L68 and E81. (F) Hydrogen bond interactions are indicated by dashed lines and the water mediated contacts are indicated in solid lines. (Figures are reprinted with permission from Ref. 21 (https://pubs.acs.org/doi/10.1021/jacs.9b00394) and further permissions related to the material excerpted should be directed to the ACS)

Fragment **1** is bound to BfrB, where L5 of Bfd binds. A structure-guided approach was used to elaborate fragment **1** into the small cleft formed by the side chains of L68 and E81 of BfrB (where the Y2 of Bfd binds). Analogs that were developed by branching from the isoindoline ring at C4 and C5 positions

of fragment **1** or its analogs **8** and **5** are shown in **Figure 3-5-A** [21]. The X-ray crystallographic structures of BfrB bound analogs were only attained for analogs **11 -16** (**Figures 3-6** and **3-7**). These are the derivatives of 4-aminoisoindoline-1,3-dione (Fragment **8**) with different length carbon linkers, $-(CH_2)-$ and $-(CH_2)_3-$. Analogs **11** and **12** contain a $-(CH_2)-$ linker, and **13-16** contain a $-(CH_2)_3-$ linker (**Figure 3-5-B**)[21]. Fragment branching from the isoindoline ring carbon C4 allowed to engage the cleft formed by L68 and E81 of BfrB.

The isoindoline-1,3-dione moiety is bound identically in all the analog:BfrB structures (**Figure 3-4-B**, **3-6,** and **3-7**) [21]. The benzyl portion of the analogs engage the cleft formed by L_A^{68} and E_B^{81} of BfrB. As illustrated in **Figure 3-6-B**, the X-ray crystallography structures of analog **11** bound to BfrB indicate two possible orientations for the *o*-hydroxyphenyl ring [21]. One orientation points the hydroxyl group toward the base of the cleft and allows to form a hydrogen bond with G_B^{80}. The other orientation points the hydroxyl group toward the solvent which enables packing of the hydroxyphenyl ring and the $-(CH_2)-$ moiety against the side chains of the M_B^{31} and I_B^{79}. Additional stability for the complex is gathered by the H-bonded water network between the carbonyl oxygen of analog **11** and G_A^{67} of BfrB. Analog **12** shows two orientations for the o-hydroxyphenyl ring as well, and a similar set of interactions with BfrB (**Figure 3-7-A and 3-7-B**) [21].

The crystal structure of analog **16** with BfrB illustrates the same pose for isoindoline-1,3-dione. The m-hydroxyphenyl ring and the $-(CH_2)_3-$ linker pack against the E_B^{81} and L_A^{68} of BfrB. There is an additional network of H-bonding from water between the carbonyl oxygen of analog and the carbonyl oxygen of L_A^{68} (**Figure 3-6-F**) [21]. The crystal structures of other $-(CH_2)_3-$ linker analogs with BfrB are shown in **Figure 3-7-C** to **3-7-H** [21]. These analogs show similar interactions with BfrB as of analog **16**.

A fluorescence polarization binding assay was carried out to explore the binding affinities of the analogs with BfrB. Analogs **11-16** bind to BfrB with significantly higher affinity than fragment **8** (**Table 3-1**) [21]. This enhancement in the binding affinity is achieved by branching the fragment from the C4

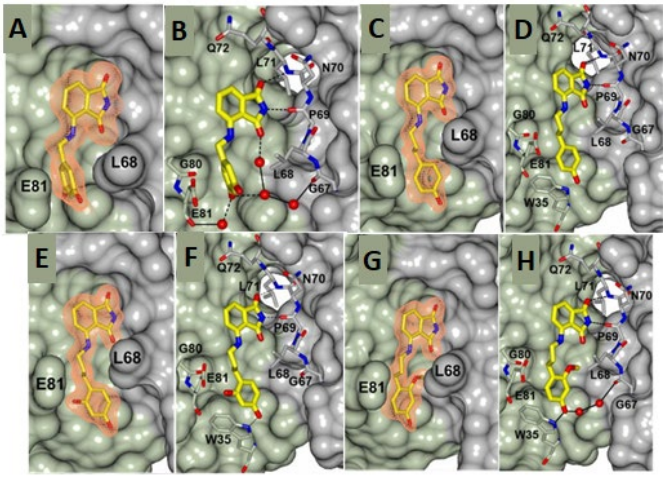

Figure 3-7: X-ray crysllography structures of analogs **12-16**. Orange mesh respresnts the F_o-F_c omit map contoured at 3σ from analog bound at Bfd binding site BfrB. Contacts made by analogs; hydrogen bond interactions are indicared by dashed lines and the water mediated contacts are indicated by the solid lines. Analog **12** (A-B); PDB ID 6NLJ, analog **13** (C-D)); PDB ID 6NLK, analog **14** (E-F)); PDB ID 6NLL and analog **15** (G-H)); PDB ID 6NLM. (Figures are reprinted with permission from Ref. 21 (https://pubs.acs.org/doi/10.1021/jacs.9b00394) and further permissions related to the material excerpted should be directed to the ACS)

position and growing towards the cleft formed by E81 and L68. Besides, the $-(CH_2)-$ linker containing analogs **11** and **12** show 2-5 fold lower binding affinity than the $-(CH_2)_3-$ linker analogs **13-16** [21]. Insights from the in-vitro studies revealed that analogs **11-16** bind to BfrB with a similar association as of the BfrB:Bfd interaction (K_d= 3 μM) and these analogs may be good candidates inhibit the BfrB:Bfd interaction in *P. aeruginosa* cells [10].

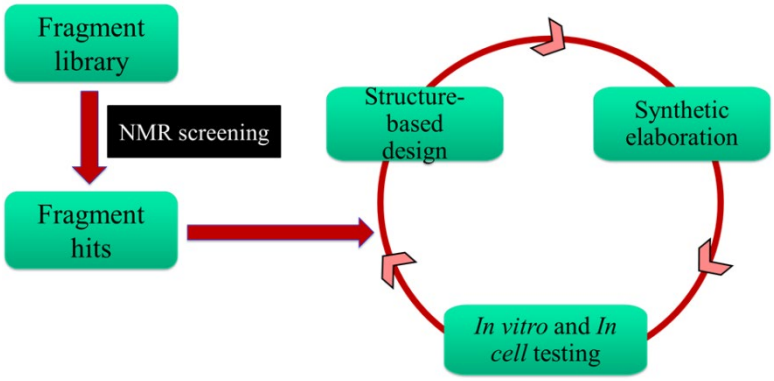

Figure 3-8: Iterative structure-based design workflow. Fragments identified to bind BfrB at the Bfd binding site were eleborated in the structure based design. Selected fragments were grown into analogs by synthetic approaches. Deleoped analogs were screened *in-vitro* by X-ray crystallography and fluoresence polarization. Additionally, in-cell activity and target engagement was studied.

3.3.2 4-aminoisoindoline-1,3-dione derivatives elicit a growth retardation phenotype in *P. aeruginosa* cells

The activity of 4-aminoisoindoline-1,3-dione derivatives was tested using *P. aeruginosa* cells in M63 media. The growth of the cells was monitored by measuring the OD_{600}. At the end of growth, the OD_{600} of each analog concentration (three replicates) was averaged and plotted against time. The resultant growth curves for analog **16** (**Figure 3-9-A**) and **11** (**Figure 3-9-B**) show clear dose-dependent growth retardation when challenged with different analog concentrations. Similarly, the growth curves for analogs **13**, **14,** and **15** were constructed (**Figure 3-10 A**, **B,** and **C,** respectively). Analog **12** was not active in the cells even at concentrations as high as 250 µM (**Figure 3-11**).

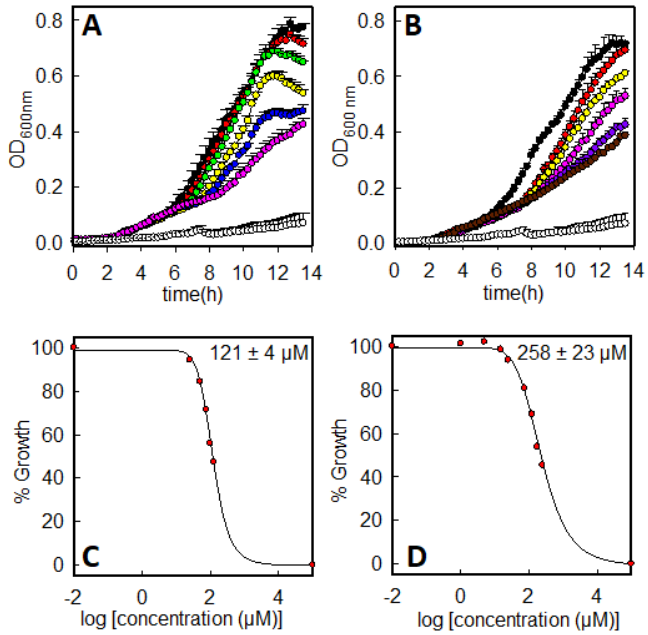

Figure 3-9: Growth curves of *P. aeruginosa* cells, treated with analog **11** and **16** (A) Cells were treated with different concentrations of analog **16**: Untreated control (black), 25 µM (red), 50 µM (green), 75 µM (yellow), 100 µM (blue), 125 µM (magenta) and 0.75 µg/mL of ciprofloxacin (white). (B) *P. aeruginosa* cells were treated with different concentrations of analog **11**: Untreated control (black), 25 µM (red), 75 µM (yellow), 125 µM (magenta), 175 µM (purple), 250 µM (brown) and 0.75 µg/mL of ciprofloxacin (white). The % growth Vs log [concentration (µM)] were fitted to equation **2**, to calculate the coresponding IC_{50} values for (C) analog **16** and (D) analog **11**. (Figures are reprinted with permission from Ref. 21 (https://pubs.acs.org/doi/10.1021/jacs.9b00394) and further permissions related to the material excerpted should be directed to the ACS)

The potency of compounds against *P. aeruginosa* cells was compared by calculating an IC_{50} value for each compound using the OD_{600} after 13 h of growth. The % growth *vs*. log [concentration (µM)] curves were constructed by taking the untreated growth as 100 %, and the growth in the presence of ciprofloxacin at 3x Minimum Inhibitory Concentration (MIC) (0.75 µg/mL) as 0 % (**equation1**). The resultant curves were fitted to **equation 2** to calculate the IC_{50} values. The IC_{50} curves are shown below the corresponding

growth curve for each analog. The IC_{50} values shown in the sub-panel are calculated from three independent experiments. Data for IC_{50} and binding affinity for the analogs **11-16** are summarized in **Table 3-1**.

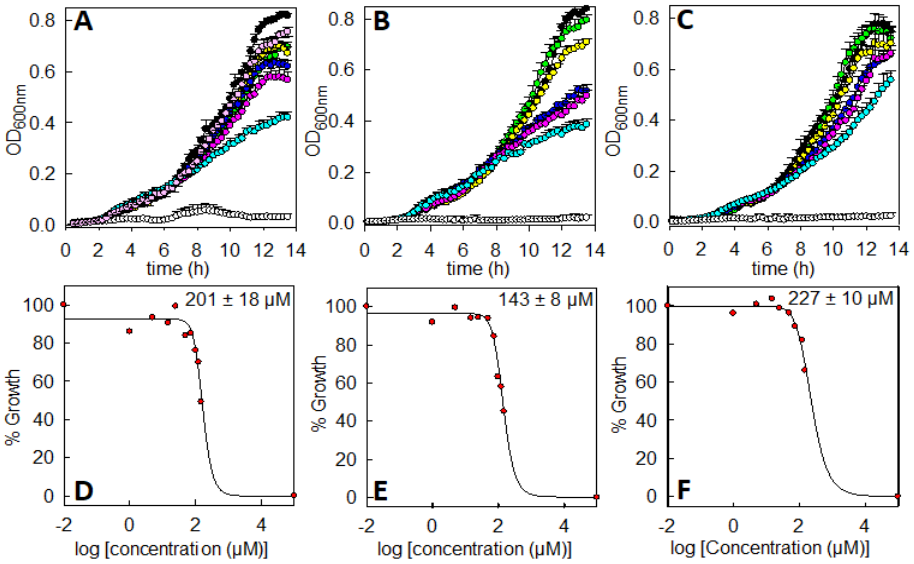

Figure 3-10: Growth curves of *P. aeruginosa* cells treated with analog **13** (A), **14** (B) and **15** (C). The growth curves present: untreated control (black), 15 µM (pink), 50 µM (green), 75 µM (yellow), 100 µM (blue), 125 µM (magenta), 150 µM (cyan) and 0.75 µh/mL ciprofloxacin (white). The bottom panels D, E, F show IC_{50} curves for analogs **13**, **14** and **15** respectively. (Figures are reprinted with permission from Ref. 21 (https://pubs.acs.org/doi/10.1021/jacs.9b00394) and further permissions related to the material excerpted should be directed to the ACS)

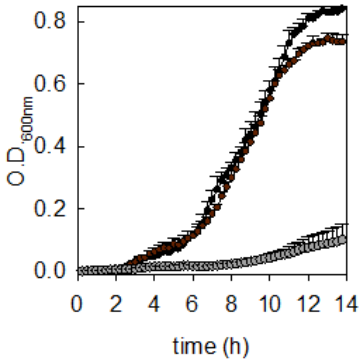

Figure 3-11: Analog **12** unable to elicit *P. aeruginosa* growth impairments. The growth in the presence of analog **12** at 250 µM is presented as brown circles. The black circles correspond to the untreated control and the grey circles correspond to the 0.75 µg/mL ciprofloxacin. (Figure is reprinted with permission from Ref. 21 (https://pubs.acs.org/doi/10.1021/jacs.9b00394) and further permissions related to the material excerpted should be directed to the ACS)

Table 3-1: Binding affinity and IC_{50} of 4-aminoisoindoline-1,3-dione derivatives. (Table is adapted from Ref. 21 (https://pubs.acs.org/doi/10.1021/jacs.9b00394) with permission and further permissions related to the material excerpted should be directed to the ACS)

Analog	Structure	*K_d (μM)	IC_{50} (μM)
8	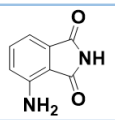	300 ± 50	not active
11	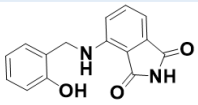	11 ± 1	258 ± 23
12	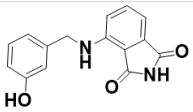	15 ± 2	not active
13	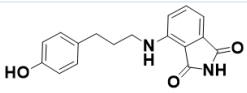	3 ± 1	201 ± 18
14	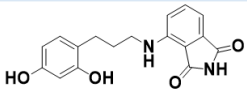	4 ± 2	143 ± 8
15	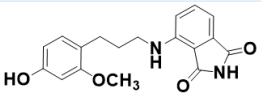	5 ± 2	227 ± 10
16	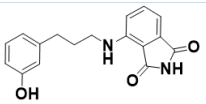	6 ± 1	121 ± 4
KM-05-025	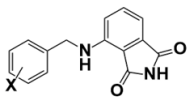	4.07 ± 0.55	32 - 64
KM-05-035		4.52 ± 0.42	32 - 64
JAG-005-030		1.53 ± 0.21	32 - 64
KM-5-66	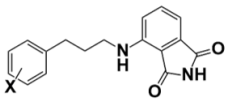	0.35 ± 0.05	~32
JAG-005-006		0.43 ± 0.07	~32

*K_d measurements were done by Dr. Huili Yao - Unpublished data

Measured K_d values are very similar for analog **11** (K_d ~11 μM) and **12** (K_d ~15 μM), but analog **12** failed to elicit a growth retardation phenotype. When comparing the efficacies of analogs with a $-(CH_2)-$ linkers, however, only analog **11** was able to penetrate the cell and elicit a growth retardation phenotype in *P. aeruginosa* cells.

Analog **16** (K_d ~6 μM) elicited the most effective growth retardation against *P. aeruginosa* cells (IC_{50}= 121 μM) among the −$(CH_2)_3$− linker analogs **13-16**. In comparison, the K_d values for analogs with a −$(CH_2)_3$− linker were 2-5-fold lower, and the corresponding *in-cell* activity was higher than that of analogs with a −(CH_2) − linker (**11**and **12)**. These alterations may be due to the efficiency of analog uptake by the cells or their varying stabilities in the cell culture. Further studies are necessary to understand the analog structural characteristics in uptake efficiency by the *P. aeruginosa* cells.

For the subsequent experiments, analog **11** from the −(CH_2)− linker category and analog **16** from the −$(CH_2)_3$− linker group were selected to treat *P. aeruginosa* cells.

3.3.3 4-aminoisoindoline-1,3-dione derivatives act on their target (BfrB) in *P. aeruginosa* cells

Analogs **11** and **13-16** elicited a growth retardation phenotype in *P. aeruginosa* cells. The more potent analogs from each category were chosen to test the selectivity on the target, BfrB, in *P. aeruginosa* cells. *P. aeruginosa* wild type and *ΔbfrB* cells (*bfrB* gene knockout mutant) were tested against different concentrations of analog **11** and **16**. Cells were grown as 5 mL cultures in M63 media supplemented with 4 μM iron, in the presence of different analog concentrations. At 15 h post-inoculation, viable cells were enumerated by plating. The untreated viable cell number was taken as 100 %, and the viable cell counts for the treated samples were normalized relative to the untreated control. The resultant plots in **Figure 3-12** illustrate wild type growth in closed circles and *ΔbfrB* cell growth in open circles. The left and right plots correspond to analog **16** (3-12-A), and **11** (3-12B), respectively. Wild type cells treated with analog **11** or **16**, experienced a monophasic concentration-dependent growth decrease. However, the *ΔbfrB* mutant cells with analog **11** and **16**, underwent a biphasic growth decrease. The *ΔbfrB* mutant cells, show a nearly independent growth decrease to analog concentrations of ~100 μM, resulting in a shallow first phase. At high analog concentrations (> 100 μM), analogs became toxic to the *ΔbfrB* mutant cells, as indicated by the steep second phase. The rapid onset of toxicity at the high concentrations of analogs was only observed in

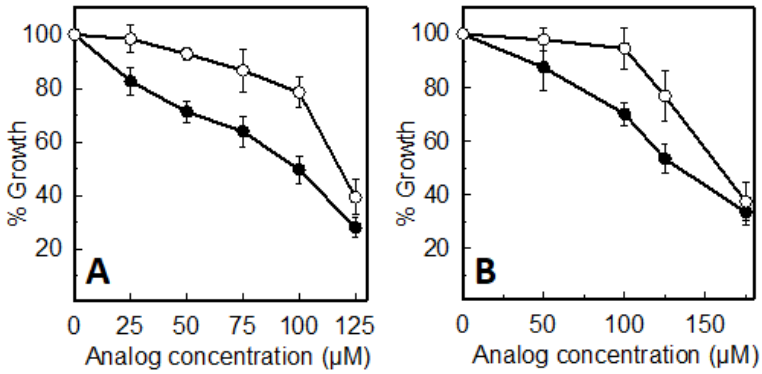

Figure 3-12: *P. aeruginosa* wild type and *ΔbfrB* cells were treated with different concentrations of (A) analog **16,** and (B) analog **11**. Open circles represent the *ΔbfrB* cells and closed circles represent the wild type cells. (Figures are reprinted from with permission Ref. 21 (https://pubs.acs.org/doi/10.1021/jacs.9b00394) and further permissions related to the material excerpted should be directed to the ACS)

the *ΔbfrB* mutant cells. This toxic effect may be due to the off-target consequences at high analog concentrations, which also emphasizes the low fitness of the *ΔbfrB* mutant cells caused by the absence of BfrB. Hence, the concentration-independent growth defect of the *ΔbfrB* cells and the concentration-dependent growth decrease of wild type cells is a clear indication of the target selectivity of analogs **11**, and **16** in *P. aeruginosa* cells.

3.3.4 Analogs elicit a pyoverdine hyper production phenotype in *P. aeruginosa* cells

As discussed in Chapter 2, disruption of the BfrB:Bfd interaction by genetic methods caused over-production of pyoverdine in the *P. aeruginosa Δbfd* and the *bfrB*(L68A/E81A) mutant cells. The unidirectional flux of iron into BfrB upon the blockade of the BfrB:Bfd interaction resulted in low free iron levels in the cytosol triggering the iron starvation responses. Consequently, during the chemical blockade

of the BfrB:Bfd interaction with the 4-aminoisoindoline-1,3-dione analogs, a similar phenotype may be observed in *P. aeruginosa.*

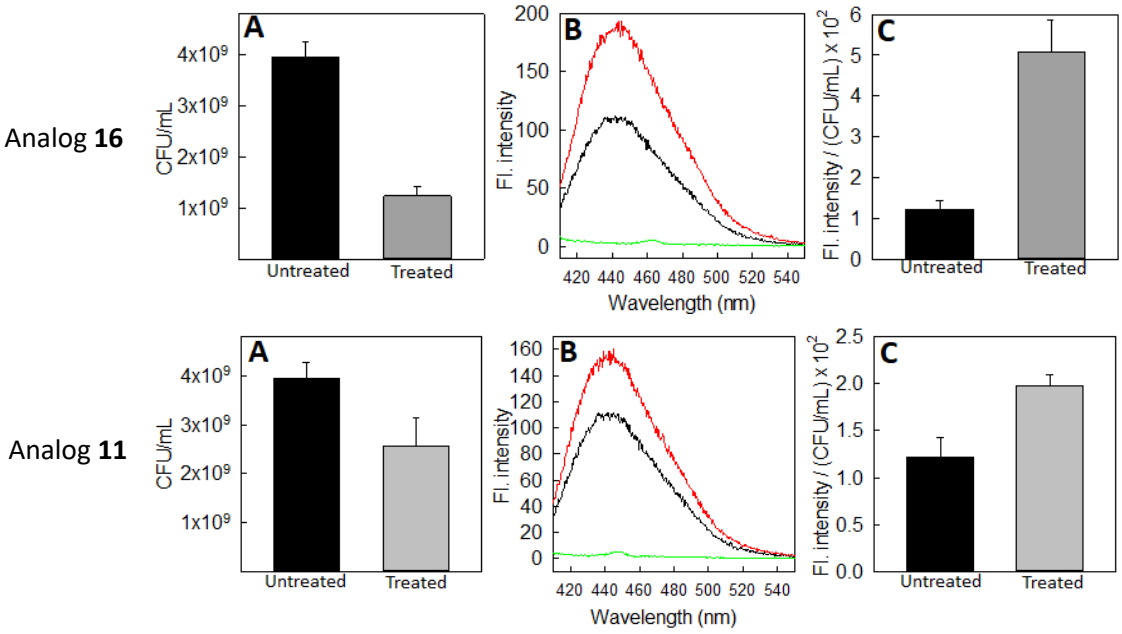

Figure 3-13: Analog **16** and **11** treated cultures over-produce pyoverdine. **Top panels:** *P. aeruginosa* cells treated with analog **16** (125 µM). **Bottom panels:** *P. aeruginosa* cells treated with analog **11** (125 µM). (A) Viable cell counts (CFU/mL) at 13-h post-inoculation. (B) Fluorescence emission spectra from the untreated (black trace), treated (red trace), and the diluted analog (green trace) acquired under same conditions. Diluted analog doesn't interfere with the pyoverdine fluorescence reading. (C) Fluorescence intensity normalized to the CFU/mL of the corresponding sample. (Figures are reprinted with permission from Ref. 21 (https://pubs.acs.org/doi/10.1021/jacs.9b00394) and further permissions related to the material excerpted should be directed to the ACS)

P. aeruginosa cells were treated with analog **16** and **11** in M63 media, as explained in the experimental section. Contents of the wells were collected at 13 h post-inoculation, and the viable cells were enumerated. Samples were centrifuged, and the supernatants were used to measure secreted pyoverdine levels by fluorescence spectroscopy. To reach this end, samples were diluted 500-fold in PBS. At this level of dilution, the residual compound fluorescence in the supernatants will not interfere with the strong fluorescence signal from pyoverdine. Samples were excited at 400 nm, and the emission at 455 nm

was recorded. The number of viable cells in the analog **16** (125 μM) treated sample was ~3 fold less related to the untreated control (**Top panel: Figure 3-13-A**). Fluorescence reading was normalized to the colony forming units/mL (CFU/mL). Analog **16** treated cells secrete about 3-4-fold excess pyoverdine compared to the untreated cells (**Top panel: Figure 3-13-C**).

A similar result was observed with the treatment of analog **11** (125 μM). As shown in the **bottom panels in Figure 3-13-A,** analog **11** treated cells had approximately two-fold less viable cells, and the level of secreted pyoverdine normalized to viable cells was two-fold higher than the untreated control. This observation agrees with the low binding affinity and high IC_{50} of analog **11** compared to analog **16**. The 4-aminoisoindoline-1,3-dione analogs elicited a pyoverdine hyper-production phenotype in *P. aeruginosa* cells, which is an indication of the low free iron levels in the cytosol due to the blockade of BfrB:Bfd interaction in *P. aeruginosa* by the analogs.

3.3.5 Analog treatment causes an irreversible accumulation of iron in BfrB and high total iron in *P. aeruginosa* cells

Disrupting the BfrB:Bfd interaction genetically caused irreversible accumulation of iron in BfrB and pyoverdine hyper-production in the *Δbfd* and *bfrB*(L68A/E81A) mutants. The small molecule inhibitors of the BfrB:Bfd interaction showed a similar pyoverdine hyper-production phenotype in *P. aeruginosa* cells. Consequently, it was important to explore the possibility of trapping iron irreversibly in BfrB in the presence of 4-aminoisoindoline-1,3-dione analogs. To reach this end, iron in BfrB was imaged using the

Native-Poly-acrylamide Gel Electrophoresis (PAGE). The development and optimization of this technique for imaging iron in BfrB is discussed in Chapter 2.

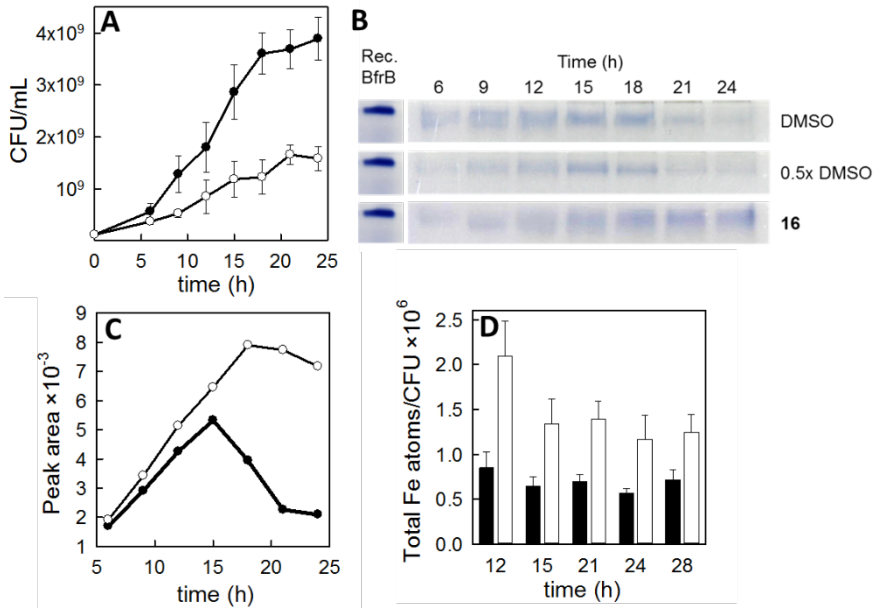

Figure 3-14: Analog **16** inhibits iron mobilization from BfrB in *P. aeruginosa* cells. *P.aeruginosa* untreated controls are presented in closed circles/bars and the analog **16** (125 µM) treatment is presented in open circles/bars. (A) *P. aeruginosa* growth curves constrcuted by enumerating viable cells. Cultures treated with analog **16** have ~ 2.5 fold fewer cells relative to untreated controls. (B) Lysates of *P.aeruginosa* were separated in a Native-PAGE and stained for iron in BfrB. Untreatd lysates were diluted 2-fold to account for the 2-fold excess of viable cells (0.5X DMSO). (C) Iron stained gels were analyzed using densitometry (using imageJ) and the peak areas in the plot corresponds to the iron stain intensity of each band in the gel.Untreated cells show the maximum accumulation of iron in BfrB ~ 15 h and mobilization during the stationary phase. The treated cells continued to accumulate iron and showed extremely slow mobilization during the stationary phase. (D) Analysis of total iron in the untreated and analog **16** treated cells revealed approximately 2-fold higher iron levels in the treated cells. The total iton measurments were normalized to the viable cell count. (Figures are reprinted with permission from Ref. 21 (https://pubs.acs.org/doi/10.1021/jacs.9b00394) and further permissions related to the material excerpted should be directed to the ACS)

P. aeruginosa cells were grown in M63 media supplemented with 4 µM in the presence of analog **16**. Cells were collected at 6, 9, 12, 15, 18, 21, and 24 h post-inoculation. Viable cells were enumerated,

and the cells were collected by centrifugation. The growth curve constructed by enumerating the viable cells is presented in **Figure 3-14-A**. The closed circles correspond to the untreated control, and the open circles correspond to the analog **16** treated cells. The number of the viable cells of the analog **16** treated sample is about 30 % relative to the untreated (DMSO only) control (except at 6 h). The cells were lysed and loaded into a Native-PAGE and stained with FereneS. Recombinant BfrB containing ~400 iron atoms was used as a control for the electrophoretic mobility. To normalize the 2-fold difference in the viable cells (CFU/mL) of the DMSO control, an additional Native-PAGE gel was run by diluting the DMSO control 2-fold (0.5X DMSO). As shown in **Figure 3-14-B**, DMSO control shows maximum iron accumulation in BfrB approximately at 15 h and is mobilized during the stationary phase. A similar trend was observed in the 0.5X DMSO control. Analog **16** treated cells show a gradual increment in the iron stain intensity, indicating continuous iron accumulation in BfrB. Iron stain intensities in the gels were further analyzed using ImageJ, gel intensity analysis tool. The color depth of each band was converted into a peak, and the peak areas between each group were compared. As presented in the densitometry analysis **Figure 3-14-C**, the 0.5X DMSO control shows the maximum accumulation of iron in BfrB during the log phase and mobilizes iron during the stationary phase (closed circles). Analog **16** treated samples show mostly iron accumulation with time and much slow mobilization of iron from BfrB. In this context, analog **16** blocks the BfrB:Bfd interaction causing irreversible accumulation of iron in the P. *aeruginosa* cells.

Two additional analog **16** concentrations (75 and 100 μM) were also tested in *P. aeruginosa* cells and imaged for iron in BfrB. As shown in **Figure 3-15**, the iron mobilization response was dose dependent. Analog **16** at 75 μM failed to inhibit the iron mobilization from BfrB (**Figure 3-15-B**), and the result was very similar to the DMSO control. Analog **16** at 100 μM was able to inhibit iron mobilization partially, an intense iron stain was visualized at 21 h, which was faded by 24 h (**Figure 3-15-C**). When the analog **16** concentration was further increased to 125 μM, iron mobilization from BfrB was entirely inhibited (**Figure 3-15-D** and **Figure 3-14-B**).

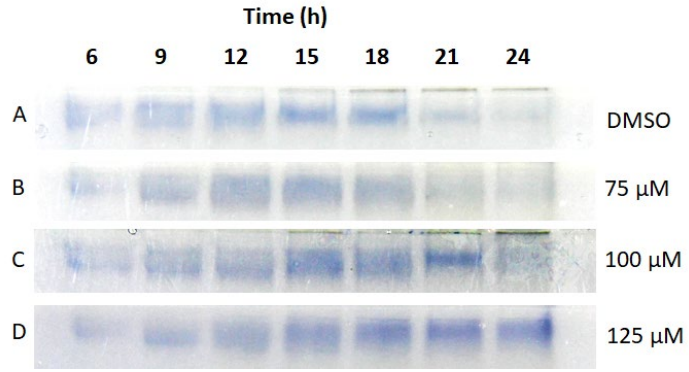

Figure 3-15: *P. aeruginosa* cells were treated with different concentrations of analog **16**. Mobilization of iron from BfrB was dose dependent.

Total intracellular iron levels were analyzed in the untreated control and in analog **16** (125 µM) treated cells (**Figure 3-14-D)**. The resultant iron concentrations were normalized to the Colony Forming Units. Analog **16** treated cells (open bars) had approximately 2-fold intracellular cellular iron levels than the untreated control. The majority of the total iron in the cell corresponds to the iron stored in BfrB. Despite the high levels of iron in BfrB, the treated cells elicited growth retardation and pyoverdine hyper-production; mainly because the iron reserves are not usable by the cells in the presence of BfrB:Bfd inhibitors. In this regard, it is clear that analog **16** acts on BfrB and inhibits iron mobilization by blocking the BfrB:Bfd interaction in *P. aeruginosa* cells.

3.3.6 4-aminoisoindoline-1,3-dione derivatives enhance the killing activity of fluoroquinolones

The 4-aminoisoindoline-1,3-dione derived analogs inhibit BfrB:Bfd interaction in *P. aeruginosa* cells, causing iron homeostasis dysregulation. In the presence of antibiotics, iron homeostasis dysregulation has been shown to boost oxidative stress the cells, causing cell death [30]. Therefore, iron homeostasis dysregulating probes may have the capability to potentiate the antibiotic activity. The efficacy of the existing antibiotics was studied in the presence of 4-aminoisoindoline-1,3-dione derivatives in *P. aeruginosa* cells.

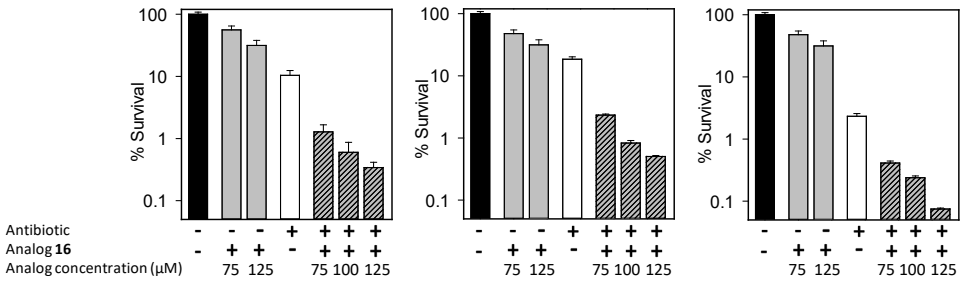

Figure 3-16: Analog **16** potentiates the activity of fluoroquinolones in *P. aeruginosa* cells. The plots present: untreated control (black), analog **16** alone (grey) fluoroquinolone alone (white) and analog **16** and fluoroquinolone combinations (shaded). The analog **16** concentrations are indicated at the bottom of each plot. The fluoroquinolones used are, (A) ciprofloxacin at 0.25 μg/mL (B) levofloxacin at 0.5 μg/mL, and (C) norfloxacin at 0.9 μg/mL. (Figures are reprinted with permission from Ref. 21 (https://pubs.acs.org/doi/10.1021/jacs.9b00394) and further permissions related to the material excerpted should be directed to the ACS)

Fluoroquinolones target DNA gyrase (topoisomerase II) and topoisomerase IV and interfere with the DNA strand rejoining after supercoil removal, leading to the accumulation of nicked DNA resulting in cell death [31]. The enhanced killing activity of fluoroquinolones was tested in the presence of 4-aminoisoindoline-1,3-dione derivatives. *P. aeruginosa* (PA01) cells were treated with (i) analog alone, (ii)antibiotic alone, (iii) analog and antibiotic combination, and (iv) DMSO control. At the end of an 18 h treatment, viable cells were enumerated, and the % survival was calculated compared to the untreated control (DMSO only).

All the fluoroquinolones in the study were tested at their MICs: ciprofloxacin (0.25 μg/mL), norfloxacin (0.9 μg/mL) and levofloxacin (0.5 μg/mL) [24]. Analog **16** was used at 75 and 125 μM concentrations for the analog alone treatments. For the antibiotic combination treatments, analog **16** was used at 75, 100, and 125 μM concentrations. As illustrated in **Figure 3-16-A**, analog **16** alone (125 μM) experienced about 30% survival, and ciprofloxacin alone experienced about 10 % survival relative to the untreated control. Interestingly, the cultures treated with the antibiotic and analog **16** (125 μM) combination experienced ~35-fold lower % survival than the ciprofloxacin alone. Similar results were observed when *P.*

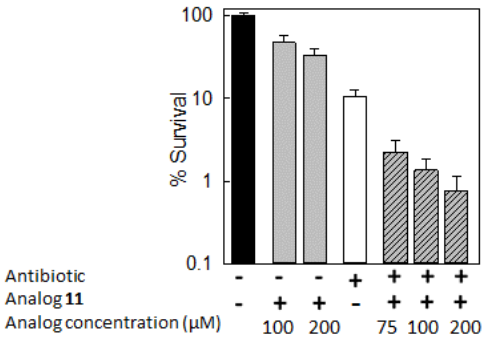

Figure 3-17: Analog **11** potentiates the activity of ciprofloxacin in *P. aeruginosa* cells. The plots present: untreated control (black), analog **11** alone (grey) ciprofloxacin alone (white) and analog **11** and ciprofloxacin combinations (shaded).

aeruginosa cells were treated with levofloxacin (**Figure 3-16-B**) and norfloxacin (**Figure 3-16-C**) in combination with analog **16** (125 μM).

A similar experiment was carried out with analog **11** and ciprofloxacin (**Figure 3-17**). *P. aeruginosa* cells treated with analog **11** alone (200 μM) resulted in approximately 30 % survival. Analog **11** (200 μM) and ciprofloxacin combination lowered the % survival by ~20-fold compared to the ciprofloxacin alone (**Figure 3-17**).

Analog and fluoroquinolone combination studies were further investigated with two clinical isolates of *P. aeruginosa*. The *P. aeruginosa* strains, MR3B, and MR60 are multidrug-resistant and are isolated from the cystic fibrosis lungs (these isolates were received from the Seattle Children's Research Foundation (NIH Grant P30DK089507)).

Both MR3B, and MR60 strains were treated with analog **16** at 125 μM concentration. In the analog **16** treatments, MR3B performed very similarly to the *P. aeruginosa* (PA01) strain. MR3B, treated with analog **16** alone experienced ~50 % survival, and ciprofloxacin (0.2 μg/mL) alone resulted in ~10 % survival, and analog, ciprofloxacin combination resulted in ~ 0.5 % survival. This % survival is approximately 20-fold lower than the ciprofloxacin alone (**Figure 3-18-A**).

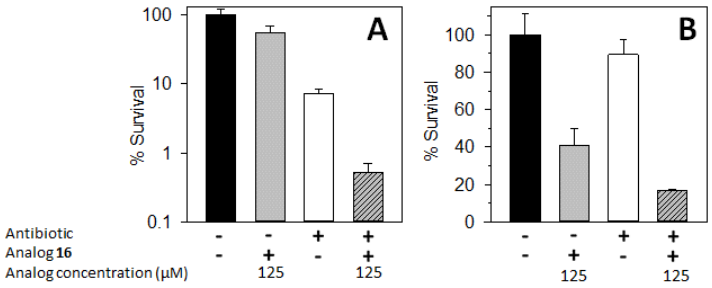

Figure 3-18: *P. aeruginosa* clinical isolates (A) MR3B and (B) MR60 were treated with analog **16** (125 μM) and/or ciprofloxacin. Ciprofloxacin concentration used for MR3B was 0.2 μg/mL and for MR60 was 1.0 μg/mL. The above plots present, untreated control (black), analog **16** alone (grey) ciprofloxacin alone (white) and analog **16** and ciprofloxacin combinations (shaded). (Figures are reprinted with permission from Ref. 21 (https://pubs.acs.org/doi/10.1021/jacs.9b00394) and further permissions related to the material excerpted should be directed to the ACS)

P. aeruginosa strain MR60 is more resistant to ciprofloxacin, and when used at 1 μg/mL, the dose is 4-5 times higher than what used for *P. aeruginosa* PA01 or MR3B. In MR60, ciprofloxacin alone resulted in ~90 % survival (**Figure 3-18-B**) compared to the untreated control. Interestingly, when MR60 was treated with analog **16** alone, the % survival dropped to ~40%, and the combination treatment lowered the % survival to ~10%. The treatment of analog **16** in a combination of fluoroquinolones reduced the % survival significantly.

The antibiotic, analog **16** (125 μM) combination effect was also explored with some other classes of antibiotics. Analog **16,** in combination with tobramycin, gentamycin, ceftazidime, and imipenem are discussed in **section 3.3.7**. Interestingly, the antibiotic potentiation effect was not as significant as the fluoroquinolones.

Peng and co-workers have analyzed the proteome of the low and high ciprofloxacin-resistant *P. aeruginosa* [32]. The low-level ciprofloxacin-resistant strains demonstrated the upregulation of heme iron uptake and TonB dependent siderophore uptake (12-fold). In the high-level ciprofloxacin-resistant strains,

only heme uptake was upregulated. Additionally, there was an upregulation in iron utilizing proteins, such as catalases and peroxidases [32]. The upregulation of iron acquisition proteins is evidence for the importance of iron when coping with the damages caused by ciprofloxacin.

As discussed in Chapter 4, analysis of the expression proteome of *P. aeruginosa* wild type and *Δbfd* mutant cells at 30 h post-inoculation revealed an under-representation of the MexE and MexF efflux pumps in the *Δbfd* mutant cells. MexE and MexF are the main fluoroquinolone efflux pumps expressed by *P. aeruginosa* [33]. Expression of efflux pumps helps to eliminate antibiotics from the cell cytosol, which reduces antibiotic accumulation and minimizes the damage caused by antibiotics. Under-representation of the MexE and MexF in *Δbfd* mutant cells suggests, more susceptibility to fluoroquinolones under iron homeostasis dysregulation.

In the presence of fluoroquinolones, there may be an additional nutritional requirement for iron by the *P. aeruginosa* cells [32]. The 4-aminoisoindoline-1,3-dione analogs (**11** and **16**) inhibit iron mobilization from BfrB, resulting in low free iron levels. At low cytosolic iron levels, cells fail to recover from damages caused by the fluoroquinolones (mainly repairing essential iron-containing proteins and enzymes). Additionally, low iron levels may result in fluoroquinolone accumulation in the cells due to the lower expression levels of MexE and MexF efflux pumps. In the absence of a functional BfrB:Bfd interaction, the *P. aeruginosa* cells become more susceptible to fluoroquinolones.

3.3.7 The activity of tobramycin, gentamycin, ceftazidime, and imipenem is not potentiated with the combination treatment

The 4-aminoisoindoline-1,3-dione derivatives, analog **16** and **11** were able to potentiate the action of fluoroquinolones. The adjuvant activity of analog **16** with other classes of antibiotics, such as aminoglycosides (tobramycin and gentamycin), cephalosporins (ceftazidime), and carbapenems (imipenem) was tested. Aminoglycosides, tobramycin, and gentamycin cause premature termination of translation of mRNA. They affect the 16S r-RNA of the 30S subunit by forming hydrogen bonds near the acceptor site [34]. Ceftazidime and imipenem are β-lactam antibiotics. The β-lactam ring mimics the D-

alanyl D-alanine portion of the peptide chain that binds to the penicillin-binding proteins (PBPs). Binding of the β-lactam ring to the PBPs inhibits the synthesis of new peptidoglycans, which is a central component of the cell wall [34].

P. aeruginosa cells were treated with (i) DMSO alone, (ii) analog **16** (125 µM), (iii) antibiotic alone, and (iv) analog **16** and antibiotic in combination. Viable cells were enumerated at 18 h post-inoculation. The % survival of each condition was calculated relative to the untreated control. Cultures treated with tobramycin (5 µg/mL) alone experienced ~ 6% survival, and the analog-tobramycin combination experienced ~0.8 % survival, which is about 7.5-fold lower survival relative to the tobramycin alone (**Figure 3-19-A**). As shown in **Figure 3-19-B,** gentamycin (5 µg/mL) alone resulted in ~15 % survival, and in the combination treatment, the % survival dropped to 3 %. The cultures treated with ceftazidime (1 µg/mL) alone experienced 15 % survival, and the combination treatment resulted in a 3-fold lower % survival relative to the ceftazidime alone (**Figure 3-19-C**). The imipenem treated (1.5 µg/mL)

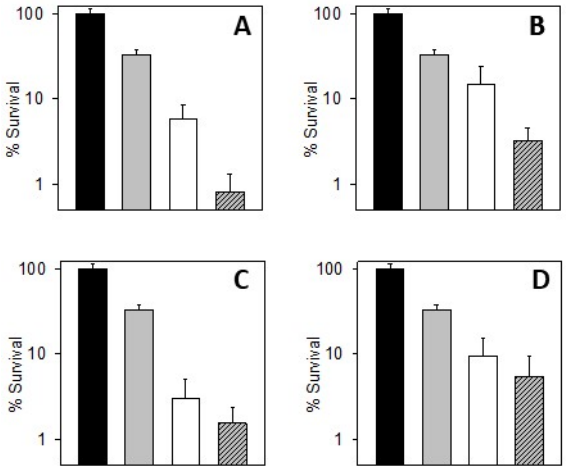

Figure 3-19: *P. aeruginosa* (PA01) cells were treated with (A) tobramycin (5 µg/mL), (B) gentamycin (5 µg/mL), (C) ceftazidime (1 µg/mL), and (D) imipenem (1.5 µg/mL) in combination with analog **16**. The plots present % survivals of: untreated control (black), analog **16** (grey), antibiotic (white) and antibiotic- analog combinations (shaded).

cultures resulted in about 9 % survival, and the combination treatment corresponded to about a 2- fold lower % survival (**Figure 3-19-D**).

Table 3-2: *P. aeruginosa* % survival fold changes between the antibiotic alone and antibiotic -analog **16** combination

Compound	Concentration (μg/mL)	% Survival			Fold change Antibiotic/Combination
		Analog	Antibiotic	Combination	
Analog **16**	125 μM	31.50			
Ciprofloxacin	0.25		10.39	0.34	30.4
Levofloxacin	0.5		18.46	0.50	36.7
Norfloxacin	0.5		2.32	0.07	31.1
Tobramycin	5		5.90	0.80	7.4
Gentamycin	5		15.05	3.29	4.6
Ceftazidime	1		3.01	1.56	1.9
Imipenem	1.5		9.48	5.53	1.7

The analog **16** and antibiotic combinations for tobramycin, gentamycin, ceftazidime, and imipenem did not result in significant changes in the experienced % survival relative to the antibiotic alone. Whereas in the analog **16** and fluoroquinolone combination treatment, the experienced % survival was 30-35-fold lower relative to the fluoroquinolone alone. The above-discussed results are summarized in **Table 3-2**.

3.3.8 Substituents on the hydroxyphenyl rings of 4-aminoisoindoline-1,3-dione analogs improve *P. aeruginosa* IC_{50}

Analog **16** is the most potent against *P. aeruginosa* (IC_{50} = 121 μM) among compounds listed in **Table 3-1**. Moreover, analog **16** acts on its target, BfrB, inhibiting the BfrB:Bfd interaction in the bacterial cell. To enhance the activity against *P. aeruginosa*, a group of halogenated hydroxyphenyl ring containing 4-aminoisoindoline-1,3-dione analogs was synthesized. The crystal structure of analog **11** with BfrB, illustrated two orientations for the *o*-hydroxyphenyl ring. One *o*-hydroxyphenyl is rotated by 180^0 from the other (**Figure 3-6-A** and **3-6-B**) [21]. Therefore, adding an additional substituent to the hydroxyphenyl ring

is expected to slow down or stop ring rotation when bound to BfrB and allow the analogs to bind more strongly. The hydroxyphenyl rings of the novel $-(CH_2)-$ linker and $-(CH_2)_3-$ linker analogs were substituted (Unpublished data from Dr. Richard A. Bunce, Department of Chemistry, Oklahoma State University). A bulkier substituent is also expected to weaken the π-π stacking interactions of the phenyl rings with its counterparts in other molecules. The advantages of lowering the π-π stacking interactions between analog molecules is expected to induce less analog aggregation and precipitation, and increased availability for the cells.

P. aeruginosa cells were grown in modified M63 media supplemented with 4 µM iron. Cells were diluted to 5×10^5 CFU/mL (OD_{600} = 5×10^{-3}) and grown in the presence analogs at 32, and 64 µM concentrations at 35 ^{0}C and 205 cpm in an Epoch 2 microplate reader. Viable cells were enumerated at 22 h post-inoculation. The % growth was calculated relative to the CFU/mL of the untreated cells. The analog

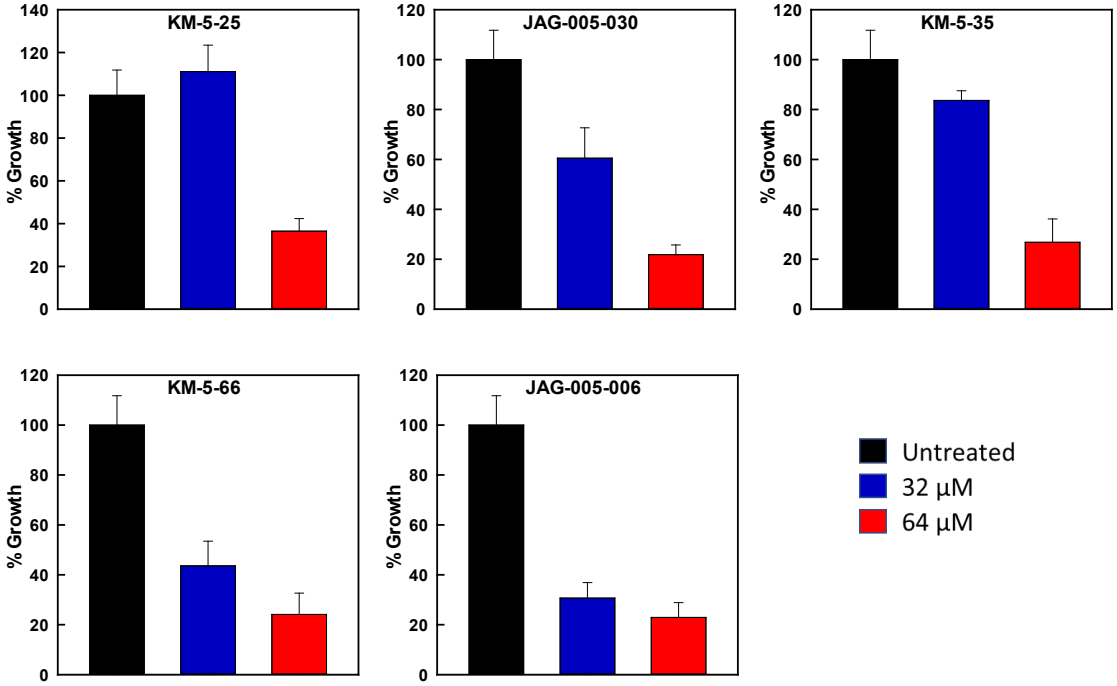

Figure 3-20: *P. aeruginosa* (PA01) cells were treated with the $-(CH_2)-$ linker analogs (**KM-5-25**, **KM-5-35** and **JAG-005-030**), and$-(CH_2)_3-$ linker analogs (**KM-5-66** and **JAG-005-006**) at 32 (blue), and 64 µM (red) concentrations. The % growth was calculated relative to the untreated control (black)

concertation resulting in 50 % growth inhibition was considered as the IC_{50}. **Figure 3-20** illustrates the % growth of *P. aeruginosa* (PA01) for each of the new analogs at 32 and 64 μM concentrations. All three $-(CH_2)-$ linker analogs (**KM-5-25**, **KM-5-35,** and **JAG-005-030**) exhibit an IC_{50} of ~48 μM (>32 - <64 μM), which is approximately 5-fold lower than the IC_{50} corresponding to the parent analog **11** (258 μM). The lower IC_{50} values (higher activity) of the new analogs correlate with the corresponding lower K_d values, as can be seen in **Table 3-1**.

The $-(CH_2)_3-$ linker analogs, **KM-5-66** and **JAG-005-006** resulted in an IC_{50} of ~32 μM. Comparing these values to that of the parent analog **16** (IC_{50} = 121 μM), indicates a 4-fold increase in activity, which is also in agreement with the lower K_d values exhibited by these new analogs (**Table 3-1**).

3.3.9 Analogs retard the growth of *P. aeruginosa* clinical isolates

The developed small molecule inhibitors of BfrB:Bfd acted on its target, BfrB, in *P. aeruginosa* (PA01) cells. Inhibition of the BfrB:Bfd interaction with 4-aminoisoindoline-1,3-dione analogs in *P. aeruginosa* cells resulted in impaired cell growth, pyoverdine hyper-production, and irreversible accumulation of iron in BfrB. In addition, two *P. aeruginosa* cystic fibrosis lung isolates, MR3B, and MR60, were affected by the analog **16** treatments. Testing 4-aminoisoindoline-1,3-dione analogs in different *P. aeruginosa* strains is useful to demonstrate the analogs are active against a number of *P. aeruginosa* strains, and to prove the suitability of the analogs to affect strains isolated from *P. aeruginosa* infections.

P. aeruginosa isolates from urinary tract infections were treated with analog **KM-5-35** from the−(CH_2)− linker category and analog **KM-5-66** from the −$(CH_2)_3$− linker category (**Figure 3-21**). Cells were grown in modified M63 media, starting with 5×10^5 CFU/mL. For the treatment, analog **KM-5-35** and **KM-5-66** were used at 64 μM concentration. At 24 h post-inoculation, viable cells were enumerated, and the % growth was calculated relative to the untreated control. All four JMI urinary tract clinical isolates experienced a growth defect in the presence of analog **KM-5-35** and **KM-5-66**. When treated with analog **KM-5-66** at 64 μM, the % growth of all the strains reached below 50% relative to the untreated control. The isolates U1, U2, U4, and U6 have an IC_{50} < 64 μM for **KM-5-66**. When treated with **KM-5-35** at 64 μM, a <50 % growth was only observed in U1, U2, and U4 strains. The U6 strain may require a higher to experience the ~50 % growth. The isolates U1, U2, and U4 have an IC_{50} <64 μM, and isolate U6 have an IC_{50} >64 μM for analog **KM-5-35**.

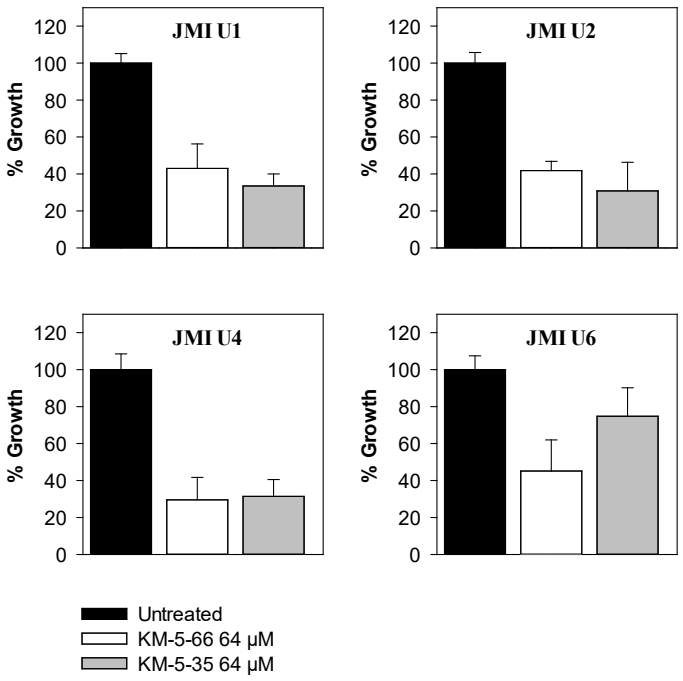

Figure 3-21: *P. aeruginosa* urinary tract JMI isolates U1, U2,U4, and U6 were treated with analogs, **KM-5-66** and **KM-5-35** at 64 μM concentration. Viable cells were enumerated at 24 h post- innoculation and the % growth was calculated relative to the untreated control.

The tested *P. aeruginosa* urinary tract isolates were able to uptake analogs and elicit a growth retardation phenotype. Undoubtedly, the developed 4-aminoisoindoline-1,3-dione analogs show potency in multiple strains of *P. aeruginosa*.

3.3.10 Small molecule inhibitors of the BfrB:Bfd interaction affect the fitness of *Acinetobacter baumannii* and elicit a hyper siderophore production phenotype

The World Health organization prioritization list recognizes *Acinetobacter baumannii* as a high healthcare burden and a critical priority pathogen for the development of new antibiotics [4]. *A. baumanii* strains are one of the leading causes of ventilator-associated pneumonia, bloodstream and wound infections. *A. baumannii* strains can acquire resistance readily, and they are intrinsically resistant to several classes of antibiotics. Especially, Carbapenem-resistant strains of *A. baumannii* show high mortality in invasive infections [35].

The *A. baumannii* (AB5075) strain was isolated in 2008 from a patient with osteomyelitis of the tibia. The genomic analysis revealed 133 genes that may cause resistance to aminoglycosides, quinolones, β-lactams, sulfonamides, and macrolides [36]. *A. baumannii* (AB5075) is a current clinical isolate model bacterium, which has shown to be virulent in animal models, multidrug-resistant, and genetically tractable. Therefore, this strain is commonly used in pathogenesis and antimicrobial studies [35]. To identify the suitability of this strain for testing inhibitors of the BfrB:Bfd interaction, sequences of *P. aeruginosa* (PA01) BfrB, and Bfd were aligned with the corresponding sequences of *A. baumannii* (AB5075).

```
                10         20         30         40         50         60
PA01     MKGDKKVIQH LNKILGNELI AINQYFLHSR MWNDWGLKRL GAHEYHESID EMKHADKLIE
AB5075   MKGNRDVINQ LNQVLYHHLT AINQYFLHSR MFNDWGIEQL GSAEYKESIR QMKHADKIIE
                70         80         90        100        110        120
PA01     RILFLEGLPN LQDLGKLLIG ENTQEMLQCD LNLELKATKD LREAIVHCEQ VHDYVSRDLL
AB5075   RILFLEGLPN LQHLGKLYIG QHTEEVLQCD IRKVKENIEA IQKAVALAET EQDYVTRDLV
               130        140        150        158
PA01     KDILESEEEH IDYLETQLGL IQKVGLENYL QSHMHEDD
AB5075   QEILEKEEEY WDWLDTQIDL IGSVGIENYI QSQM
```

Figure 3-22: The Bacterioferritin of *Acinetobacter baumannii* (AB5075); gene ID: A591_A0279, aligned with the BfrB of *P. aeruginosa* (PA01); gene ID: PA3531. The methionine required for the heme coordination is highlighted in cyan. The residues at the *P. aeruginosa*, BfrB:Bfd buried surface is highlighted in yellow and the mismatches in *A. baumannii* sequence are shown in red.

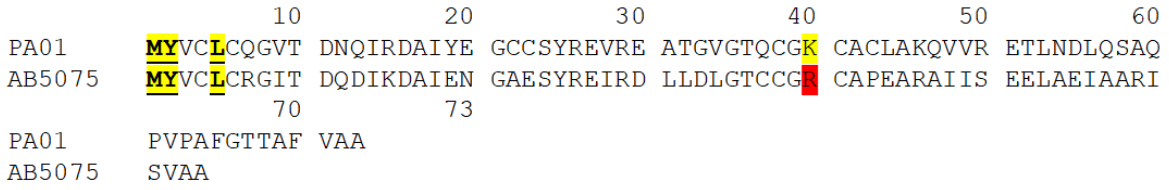

Figure 3-23: The putative bacterioferritin-associated ferredoxin of *Acinetobacter baumannii* (AB5075); gene ID: A591_A0280 aligned with the Bfd of *P. aeruginosa* (PA01); PA3530. The residues at the buried surface of the *P. aeruginosa* BfrB:Bfd interface are highlighted in yellow. The mismatched residues of *A. baumannii* are highlighted in red.

Figure 3-22 shows the alignment of *P. aeruginosa* (PA01) BfrB with *A. baumannii* AB5075 Bacterioferritin (Gene ID: A591_A0279), and **Figure 3-23** shows the alignment of *P. aeruginosa* (PA01) Bfd with putative bacterioferritin-associated ferredoxin (Gene ID: A591_A0280). Residues of the *P. aeruginosa* (PA01) BfrB:Bfd buried surface are highlighted in yellow, and the hot spot residues of the interaction are presented in underlined bold text. The M52 residue for heme coordination is conserved (highlighted in cyan). The mismatched residues in *A. baumanniii* are highlighted in red.

In *A. baumannii* (AB5075), *bfr* and *bacterioferritin-associated ferredoxin* genes are adjacent as is the case in *P. aeruginosa* (PA01). Having adjacent genes raises the occurrence of a similar functionality of *Ab* Bfr and the bacterioferritin-associated ferredoxin. Additionally, the hot spot residue E81 of *Pa* BfrB is conservatively replaced by a glutamine residue in *Ab* Bfr. In *Pa* BfrB, the side-chain carbons of E81 make hydrophobic contacts with the carbons in the Y2 phenyl ring of Bfd, hence, the conservative replacement of E81 to Q81 is not expected to interfere with this hydrophobic interaction. Consequently, the developed small molecule inhibitors of the *Pa* BfrB:Bfd interaction are expected to be active against *A. baumannii* (AB5075) cells.

In order to test the effects of developed of 4-aminoisoindoline-1,3-dione analogs, *A. baumannii*, cells were treated with analogs **KM-5-25**, **JAG-005-030**, **KM-5-35, KM-5-66** and **JAG-005-006** in the

modified M63 media. Analogs were tested at 32 and 64 µM concentrations. The starting CFU/mL of the cultures was kept at 5 × 10^5 CFU/mL. Cells were grown in 48 well plates at 35 ^{0}C, and 205 cpm. The % growth was calculated relative to the untreated control by enumerating viable cells at 24 h of post-inoculation. The resultant plots, presented in **Figure 3-24**, indicate that all of the 4-aminoisoindoline-1,3-dione analogs treated exhibit activity against *A. baumannii* comparable to activity against the *P.* aeruginosa PAO1. These findings strongly suggest that the 4-aminoisoindoline-1,3-dione analogs penetrate the *A. baumannii* cells, affect iron homeostasis and impair cell growth. Additional experiments were carried out to show that the analogs elicit an enhanced siderophore secretion phenotype as a result of low cytosolic iron levels upon blockade of the BfrB:Bfd interaction.

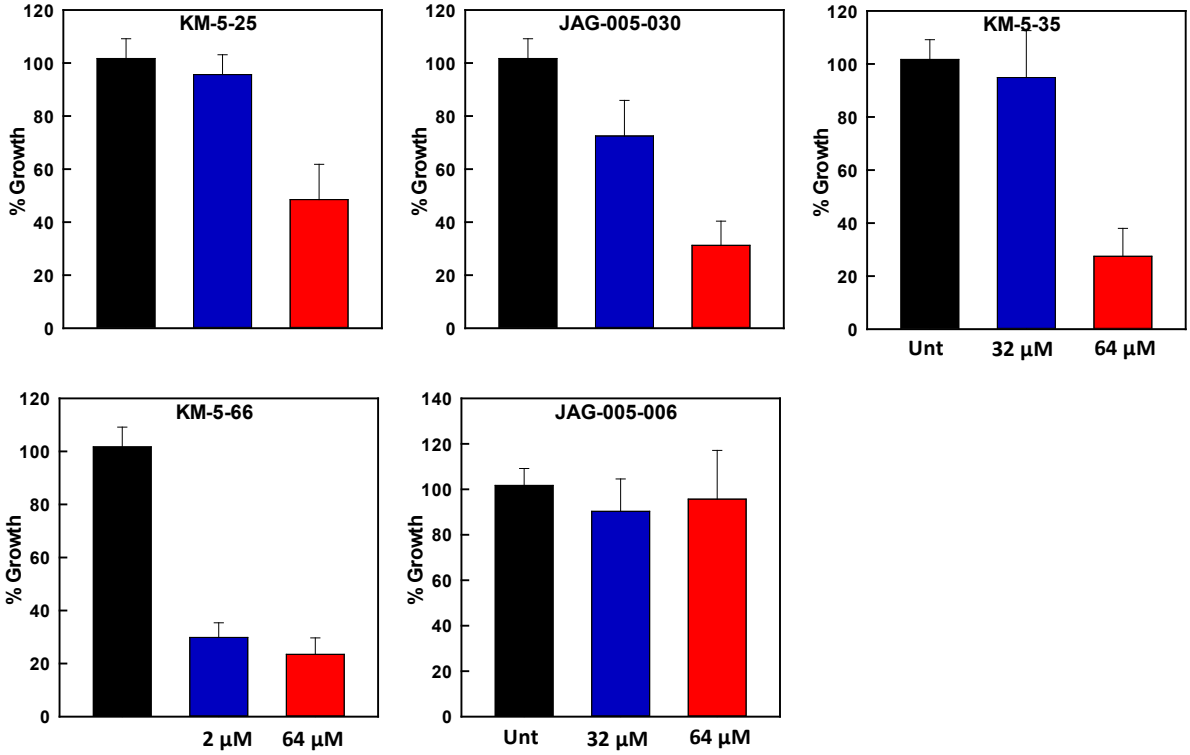

Figure 3-24: *A. baumanni* (AB5075) cultures were treated with analog **KM-5-25**, **JAG-005-030**, **KM-5-35**, **KM-5-66,** and **JAG-005-006** at 32, 64, and 128 µM. The % growth for each conditions was calculated relative to the untreated control.

A. baumannii cell supernatants at 24 h post-inoculation were analyzed for siderophore production. Siderophores are produced as a repercussion of blocking the Bfr:Bfd interaction. In the siderophore determination assay, iron is complexed with the chrome azurol S (CAS) and the counter ion hexadecyl

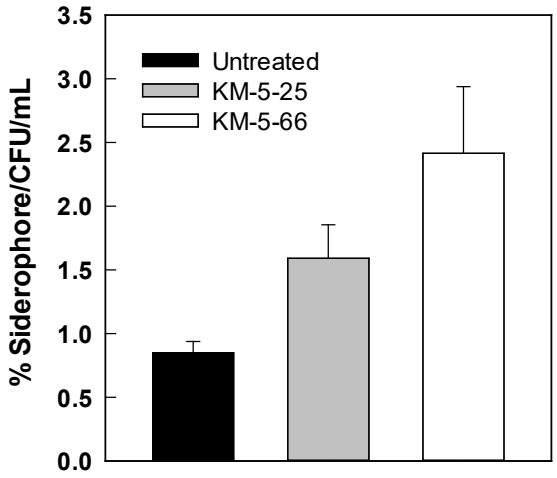

Figure 3-25: Siderophores produced by *A. baumannii* cells were quantified using CAS assay. The siderophore levels were normalized to the CFU/mL of each condition.

trimethyl ammonium bromide. In the presence of high-affinity siderophores iron from the Fe-CAS complex is scavenged. The release of iron from CAS will change the color from blue to yellow. This is measured by a decrease in absorbance at 630 nm. The decline in absorbance in the cell-free supernatants was used to calculate the % siderophore production units (PSU) using **equation 3** in the experimental section [29]. The calculated PSU was normalized to the viable cell counts of each sample. The resultant % siderophore/CFU/mL plot for analog **KM-5-25** and **KM-5-66** at 64 μM is presented in **Figure 3-25**. The *A. baumanni* cultures treated with 4-aminoisoindoline-1,3-dione analogs overproduced 2-3-fold siderophores relative to the untreated control. This is an indication of low free iron levels in the cytosol of *A. baumannii* cells when in the presence of 4-aminoisoindoline-1,3-dione analogs, suggesting that the analogs bind Bfr and inhibit the Bfr:Bfd interaction in *A. baumannii* cells. Consequently, the unidirectional flow of iron into Bfr results in low cytosolic free iron levels and stimulating siderophore synthesis and

secretion. Additional investigations on *A. baumannii* Bfr and bacterioferritin-associated ferredoxin are necessary to make definite conclusions on the effects of 4-aminoisoindoline-1,3-dione analogs in cells.

3.4 Conclusions

Iron is an essential nutrient for pathogens in the colonization of mammalian hosts, but the innate immune defenses restrict the iron availability *in-vivo*. The iron restriction presents challenges in establishing host colonization. Challenging iron metabolism in bacteria is being explored as a viable alternative target for anti-infective development.

BfrB is the main iron storage protein in *P. aeruginosa.* BfrB serves an iron reservoir and plays an essential role in sustaining the dynamic equilibrium between the free iron levels and iron stored in BfrB. As discussed in Chapter 2, the genetic intervention of the BfrB:Bfd interaction (*Δbfd* and *bfrB*(L68A/E81A) mutants) caused irreversible accumulation of iron in BfrB, which resulted in unusable intracellular iron in BfrB and a depletion of the free intracellular iron levels [7]. Despite normal intracellular total iron levels, the *Δbfd* and *bfrB*(L68A/E81A) mutants showed an acute iron starvation response by secreting pyoverdine. The genetic inhibition of the BfrB:Bfd interaction perturbed the dynamic equilibrium between Fe^{2+} in the cytosol and Fe^{3+} stored in BfrB, resulting in iron homeostasis dysregulation [7].

Inspired by these findings, a fragment screening and an iterative structure-based design approach were used to investigate potential inhibitors of the BfdB:Bfd interaction. The initial BfrB fragment hits were synthetically elaborated into 4-aminoisoindoline-1,3-dione analogs to enhance their binding affinity for BfrB. The X-ray crystallographic structures revealed analog binding to BfrB, engaging the pockets on BfrB where Y2 and L5 of Bfd bind [21]. The developed analogs were tested in *P. aeruginosa* cells to identify the potential of the analogs to perturb the BfrB:Bfd interaction *in-cell*. To reach this end, *P. aeruginosa* cells were treated with the 4-aminoisoindoline-1,3-dione derived analogs. Analog **16** was able to act on its target (BfrB) in the bacterial cytosol, causing a nearly irreversible accumulation of iron in BfrB. The analog-treated cells demonstrated concentration-dependent growth impairment and iron starvation response, despite the high intracellular iron levels in cells. Inhibiting the BfrB:Bfd interaction by chemical

probes establishes a unidirectional flow of iron into BfrB, limiting its use to the cells. The irreversible accumulation of iron is accompanied by the low cytosolic free iron levels, which is manifested in the hyper-production of pyoverdine, similar to observations made with the *Δbfd* mutant. The growth impairment observed in the treated cells may be due to the intracellular iron limitation as a repercussion of blocking the BfrB:Bfd interaction, which would exert an effect on crucial iron-dependent biosynthesis and repair mechanisms in the cell. Consequently, blocking the BfrB:Bfd interaction by 4-aminoisoindoline-1,3-dione derived analogs resulted in iron homeostasis dysregulation in *P. aeruginosa*.

The developed BfrB:Bfd inhibitors can also be used as synergistic or antagonistic probes. In the presence of antibiotics, iron homeostasis dysregulation has shown to exert an effect on bacterial survival [30]. The 4-aminoisoindoline-1,3-dione analogs act as probes to dysregulate iron homeostasis and have the possibility of potentiating the activity of existing antibiotics. *P. aeruginosa* cells were treated with the BfrB:Bfd Inhibitors in combination with different classes of antibiotics. Interestingly, when analogs were used in combination with fluoroquinolones, the activity of fluoroquinolones was enhanced by 30- fold. In the absence of intact iron homeostasis, the cells are incapable of restoring the damages caused by the antibiotics, primarily upon the treatment with fluoroquinolones [32]. Therefore, it is plausible to consider potential therapeutic strategies where the BfrB:Bfd inhibitors are used in combination with existing fluoroquinolones.

The 4-aminoisoindoline-1,3-dione analogs were experimented in different *P. aeruginosa* strains and in *A. baumannii* (AB5075) to rule out any stain specific effects. Importantly, the analogs exerted growth impairments in multiple *P. aeruginosa* strains (cystic fibrosis lung and urinary tract isolates) and A*cinetobactor baumannii* (AB5075). In an extended set of Gram-negative bacteria, the *bfrB* and *bfd* genes are adjacent, and the *Pa*-BfrB *Pa*-Bfd interface residues are highly conserved. Consequently, the developed small molecule BfrB:Bfd inhibitors could be of widespread application with a high significance.

3.5 References

1. Cornelis, P. and J. Dingemans, *Pseudomonas aeruginosa adapts its iron uptake strategies in function of the type of infections.* Front Cell Infect Microbiol, 2013. **3**: p. 75.
2. Zughaier, S.M. and P. Cornelis, *Editorial: Role of Iron in Bacterial Pathogenesis.* Front Cell Infect Microbiol, 2018. **8**: p. 344.
3. Smith, D.J., et al., *Targeting iron uptake to control Pseudomonas aeruginosa infections in cystic fibrosis.* Eur Respir J, 2013. **42**(6): p. 1723-36.
4. Organization, W.H., *Prioritization of pathogens to guide discovery, research and development of new antibiotics for drug-resistant bacterial infections, including tuberculosis*. 2017, World Health Organization.
5. Bassetti, M., et al., *How to manage Pseudomonas aeruginosa infections.* Drugs Context, 2018. **7**: p. 212527.
6. Ballouche, M., P. Cornelis, and C. Baysse, *Iron metabolism: a promising target for antibacterial strategies.* Recent Pat Antiinfect Drug Discov, 2009. **4**(3): p. 190-205.
7. Eshelman, K., et al., *Inhibiting the BfrB:Bfd interaction in Pseudomonas aeruginosa causes irreversible iron accumulation in bacterioferritin and iron deficiency in the bacterial cytosol.* Metallomics, 2017. **9**(6): p. 646-659.
8. Yao, H., et al., *The structure of the BfrB-Bfd complex reveals protein-protein interactions enabling iron release from bacterioferritin.* J Am Chem Soc, 2012. **134**(32): p. 13470-81.
9. Rivera, M., *Bacterioferritin: structure, dynamics, and protein–protein interactions at play in iron storage and mobilization.* Accounts of chemical research, 2017. **50**(2): p. 331-340 %@ 0001-4842.
10. Wang, Y., et al., *Characterization of the Bacterioferritin/Bacterioferritin Associated Ferredoxin Protein-Protein Interaction in Solution and Determination of Binding Energy Hot Spots.* Biochemistry, 2015. **54**(40): p. 6162-75.
11. Zgurskaya, H.I., C.A. Lopez, and S. Gnanakaran, *Permeability Barrier of Gram-Negative Cell Envelopes and Approaches To Bypass It.* ACS Infect Dis, 2015. **1**(11): p. 512-522.
12. Domalaon, R., et al., *Antibiotic Hybrids: the Next Generation of Agents and Adjuvants against Gram-Negative Pathogens?* Clin Microbiol Rev, 2018. **31**(2).
13. Hancock, R.E., G.M. Decad, and H. Nikaido, *Identification of the protein producing transmembrane diffusion pores in the outer membrane of Pseudomonas aeruginosa PA01.* Biochim Biophys Acta, 1979. **554**(2): p. 323-31.
14. Yoshimura, F., L.S. Zalman, and H. Nikaido, *Purification and properties of Pseudomonas aeruginosa porin.* J Biol Chem, 1983. **258**(4): p. 2308-14.
15. Richter, M.F., et al., *Predictive compound accumulation rules yield a broad-spectrum antibiotic.* Nature, 2017. **545**(7654): p. 299-304.
16. Mabonga, L. and A.P. Kappo, *Protein-protein interaction modulators: advances, successes and remaining challenges.* Biophys Rev, 2019. **11**(4): p. 559-581.
17. Erlanson, D.A., B.J. Davis, and W. Jahnke, *Fragment-Based Drug Discovery: Advancing Fragments in the Absence of Crystal Structures.* Cell Chem Biol, 2019. **26**(1): p. 9-15.
18. Zinzalla, G. and D.E. Thurston, *Targeting protein-protein interactions for therapeutic intervention: a challenge for the future.* Future Med Chem, 2009. **1**(1): p. 65-93.
19. Scott, D.E., et al., *Fragment-based approaches in drug discovery and chemical biology.* Biochemistry, 2012. **51**(25): p. 4990-5003.
20. Murray, C.W. and D.C. Rees, *The rise of fragment-based drug discovery.* Nat Chem, 2009. **1**(3): p. 187-92.
21. Punchi Hewage, A.N.D., et al., *Small Molecule Inhibitors of the BfrB–Bfd Interaction Decrease Pseudomonas aeruginosa Fitness and Potentiate Fluoroquinolone Activity.* Journal of the American Chemical Society, 2019. **141**(20): p. 8171-8184.

22. O'Toole, G.A. and R. Kolter, *Initiation of biofilm formation in Pseudomonas fluorescens WCS365 proceeds via multiple, convergent signalling pathways: a genetic analysis.* Mol Microbiol, 1998. **28**(3): p. 449-61.
23. Chen, Y., et al., *Initial Drug Dissolution from Amorphous Solid Dispersions Controlled by Polymer Dissolution and Drug-Polymer Interaction.* Pharm Res, 2016. **33**(10): p. 2445-58.
24. Andrews, J.M., *Determination of minimum inhibitory concentrations.* J Antimicrob Chemother, 2001. **48 Suppl 1**: p. 5-16.
25. Chung, M.C., *A specific iron stain for iron-binding proteins in polyacrylamide gels: application to transferrin and lactoferrin.* Anal Biochem, 1985. **148**(2): p. 498-502.
26. Fish, W.W., *Rapid colorimetric micromethod for the quantitation of complexed iron in biological samples.* Methods Enzymol, 1988. **158**: p. 357-64.
27. CLSI, *Methods for Dilution Antimicrobial Susceptibility Tests for Bacteria That Grow Aerobically;Approved Standard—Ninth Edition*, in *CLSI document M07-A9*. 2012, Clinical and Laboratory Standards Institute;: Wayne, PA.
28. Schwyn, B. and J.B. Neilands, *Universal chemical assay for the detection and determination of siderophores.* Anal Biochem, 1987. **160**(1): p. 47-56.
29. Arora, N.K. and M. Verma, *Modified microplate method for rapid and efficient estimation of siderophore produced by bacteria.* 3 Biotech, 2017. **7**(6): p. 381.
30. Yeom, J., J.A. Imlay, and W. Park, *Iron homeostasis affects antibiotic-mediated cell death in Pseudomonas species.* J Biol Chem, 2010. **285**(29): p. 22689-95.
31. Kohanski, M.A., D.J. Dwyer, and J.J. Collins, *How antibiotics kill bacteria: from targets to networks.* Nat Rev Microbiol, 2010. **8**(6): p. 423-35.
32. Peng, J., et al., *Pseudomonas aeruginosa develops Ciprofloxacin resistance from low to high level with distinctive proteome changes.* J Proteomics, 2017. **152**: p. 75-87.
33. Llanes, C., et al., *Role of the MexEF-OprN efflux system in low-level resistance of Pseudomonas aeruginosa to ciprofloxacin.* Antimicrob Agents Chemother, 2011. **55**(12): p. 5676-84.
34. Kapoor, G., S. Saigal, and A. Elongavan, *Action and resistance mechanisms of antibiotics: A guide for clinicians.* J Anaesthesiol Clin Pharmacol, 2017. **33**(3): p. 300-305.
35. Jacobs, A.C., et al., *AB5075, a Highly Virulent Isolate of Acinetobacter baumannii, as a Model Strain for the Evaluation of Pathogenesis and Antimicrobial Treatments.* mBio, 2014. **5**(3): p. e01076-14.
36. Cheng, Y.S., et al., *Repurposing Screen Identifies Unconventional Drugs With Activity Against Multidrug Resistant Acinetobacter baumannii.* Front Cell Infect Microbiol, 2018. **8**: p. 438.

Chapter 4 : Proteomics Profiling and Metabolic Pathway Mapping upon blockade of the BfrB:Bfd interaction in *P. aeruginosa* cells

4.1 Introduction

4.1.1 Significance of the BfrB:Bfd interaction in the iron metabolism of *P. aeruginosa.*

BfrB is the main iron storage protein in *P. aeruginosa* [1]. Mobilization of iron from BfrB requires interactions with its cognate partner protein, the Bacterioferritin Associated Ferredoxin (Bfd). In the absence of Bfd, very little, or no iron is mobilized from BfrB [2]. *P. aeruginosa* wild type and a *bfd* gene knockout mutant (*Δbfd*) were used to study the importance of the BfrB:Bfd interaction to the bacterial cells [1]. Under iron supplemented conditions, the growth of the wildtype and the *Δbfd* mutant are indistinguishable [1]. Wild type and the *Δbfd* mutant consume supplemented iron in the media at a similar rate (**Figure 4-1-B**) [1]. Iron-stained Native-PAGE was used to illustrate iron accumulation and mobilization in BfrB (Chapter 2). The wild type cells show maximum iron accumulation in BfrB during the log and the early stationary phases. Stored iron starts to mobilize from BfrB during the late stationary phase (when the iron concertation of media is ~ 1 μM). The *Δbfd* mutant cells show irreversible accumulation of iron in BfrB, as they failed to mobilize iron from BfrB in the absence of Bfd. These observations showed that in *P. aeruginosa* cells the BfrB:Bfd complex is the only mechanism available to mobilize iron from BfrB (**Figure 4-1-C**).

The genetic intervention of the BfrB:Bfd interaction resulted in an irreversible flux of iron into BfrB, low free iron levels in the cytosol, and high total iron to free iron ratio (**Figure 4-1-D-E-F**) [1]. Wild type cells carry a functional BfrB:Bfd interaction and maintain a total iron to free iron ratio of ~20 even under depleted extracellular iron levels. The low free iron levels in the *Δbfd* mutant cells caused dissociation of the Fe^{2+}- master iron regulator (Fur) complex activating iron acquisition genes. As a consequence, hyper-

production of pyoverdine was observed in the *Δbfd* mutant cells (**Figure 4-1-A**) [1]. Pyoverdine is the main Fe^{3+} chelating siderophore produced by *P. aeruginosa*.

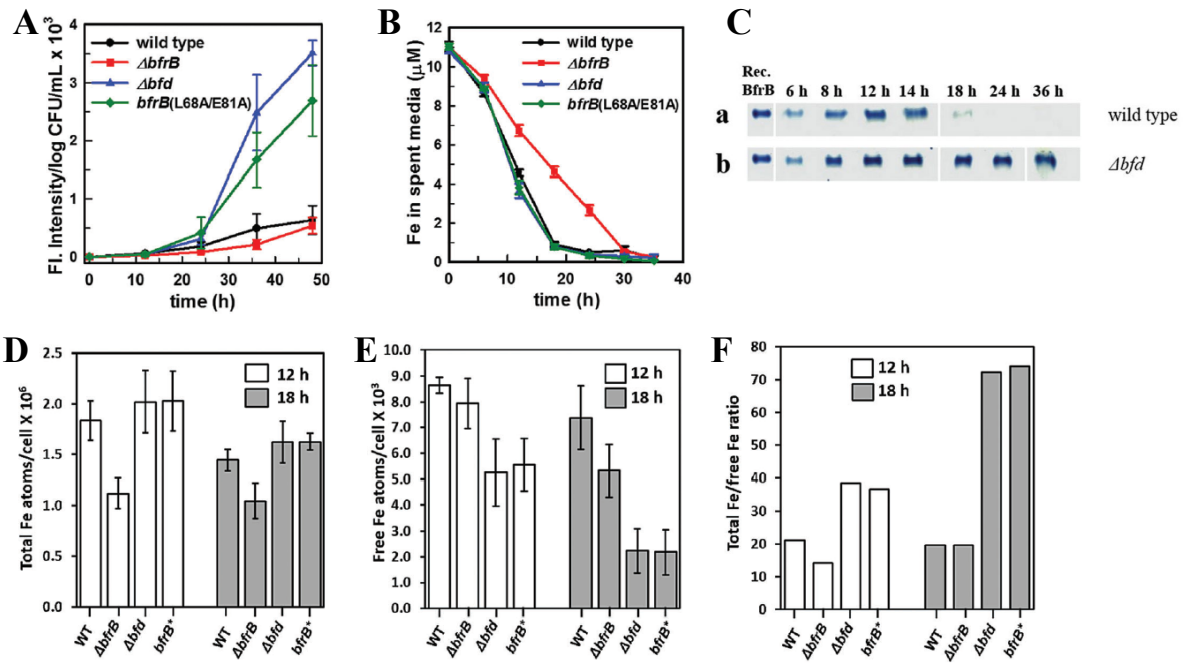

Figure 4-1: *P. aeruginsa* cells were grown in PI media supplemeted with 10 μM iron. (A) Secreted pyoverdine was analyzed and normalized to the viable cell count at each time point. (B) Iron concentration in the spent media was analyzed at different time points of post-innoculation. (C) Iron stained Native-PAGE illustrates irreversible accumulated in BfrB in the absence of *bfd*. (D) Total intracellular iron levels were analysed at 12 and 18 h post-innoculation using colorimetry. (E) Free iron in the cytosol was measured by EPR using a cell permeable iron chelator, deferoxamine. (F) The calculated total iron to free iron ratios of the wild type and the mutants at 12 and 18 h post-innoculation. (Figures are reprinted from Ref. 1 with permission from Royal Society of Chemistry)

Regulation of iron acquisition in response to iron availability is mediated through the actions of Fur. Under iron-replete conditions, Fur becomes ferrated and binds to the Fur box sequence in the promoters and prevents transcription of genes that are necessary for iron uptake. Fur directly or indirectly regulates the expression of a large number of genes and operons, which are involved in iron uptake and virulence.

The PrrF small regulatory RNAs (sRNAs) degrades mRNAs encoding iron-containing proteins to spare iron under limiting conditions. Moreover, Fur is involved in increased expression of genes by the repression of PrrF sRNAs [3, 4].

As has been shown in Chapter 2, disrupting the BfrB:Bfd interaction causes dysregulation of iron homeostasis in *P. aeruginosa* cells [1]. Work described in this Chapter was carried out to test a hypothesis that iron homeostasis dysregulation may create severe impact on other cellular functions, such that in addition to the phenotypic differences observed in the *P. aeruginosa Δbfd* mutant cells described in chapter 2, there may be an impact on the broader bacterial metabolism upon blockade of the BfrB:Bfd interaction. To test these ideas, the proteomes of wild type and *Δbfd P.aeruginosa* cells were compared, in order to study the intracellular biochemical repercussions of blocking the BfrB:Bfd interaction. The proteomics study revealed an over-representation of proteins functioning in iron acquisition, sulfur assimilation, and quorum sensing, and under-representation of several proteins in the TCA cycle, respiratory chain, amino acid biosynthesis, and oxidative stress response. The affected proteins fall into iron-dependent and iron-independent categories. Expression levels of the iron-containing proteins may directly or indirectly affect the expression of iron-independent proteins resulting in significant consequences to cell metabolism.

4.1.2 Protein expression proteomics

Proteomics involves the analysis of the entire protein complement of a tissue, cell, or an organism under a defined set of conditions. Proteomics is broadly used in protein expression profiling (medical microbiology, disease mechanisms, signal transduction), proteome mining (drug discovery, target identification/ validation), functional proteomics (affinity-purified protein complexes), and protein-protein interaction identifications.

Over the past years, transcriptomics has played an essential role in the identification of levels of biological processes and disease states. The mRNA analysis uses different methods such as serial analysis of gene expression (SAGE) and DNA microarray. However, the mRNA expression analysis doesn't directly correlate with the protein expression levels in the cells. In protein expression, mRNA synthesis is the first

step of a long sequence of steps. Cells regulate the protein expression levels by degradation or modification of the mRNA. Also, many different protein isoforms can be generated from a gene. Most importantly, proteins and not genes determine the phenotype of the cells [5].

Quantitatively studying protein expression among samples is known as expression proteomics. In this proteomics approach, the protein expression of the entire proteome or sub proteomes can be compared. Expression proteomics can give valuable insights into complex biological systems, mainly by analyzing expression, functions, modifications, and interactions. In the past 30-40 years, expression proteomics utilized methods such as 2-D Polyacrylamide Gel Electrophoresis (2-D PAGE), western blotting, and radioimmunoassay (RIA) [6]. One of the noteworthy developments in protein identification is the advancement of the Mass Spectroscopy (MS) based techniques. Over the past decade, the sensitivity and accuracy of protein identification by MS have increased. MS-based methods can accept protein mixtures and is amiable to high-throughput of proteomics approaches.

4.1.3 Proteomics study with Tandem Mass Tagged (TMT) peptides

Quantitative proteomics relies on the capability to detect changes in the proteins and peptide abundances. Protein quantitation can be absolute or relative. In absolute protein quantification approaches, the exact protein concentration is determined, whereas, in relative quantification methods, the abundance of particular proteins is determined relative to the corresponding control.

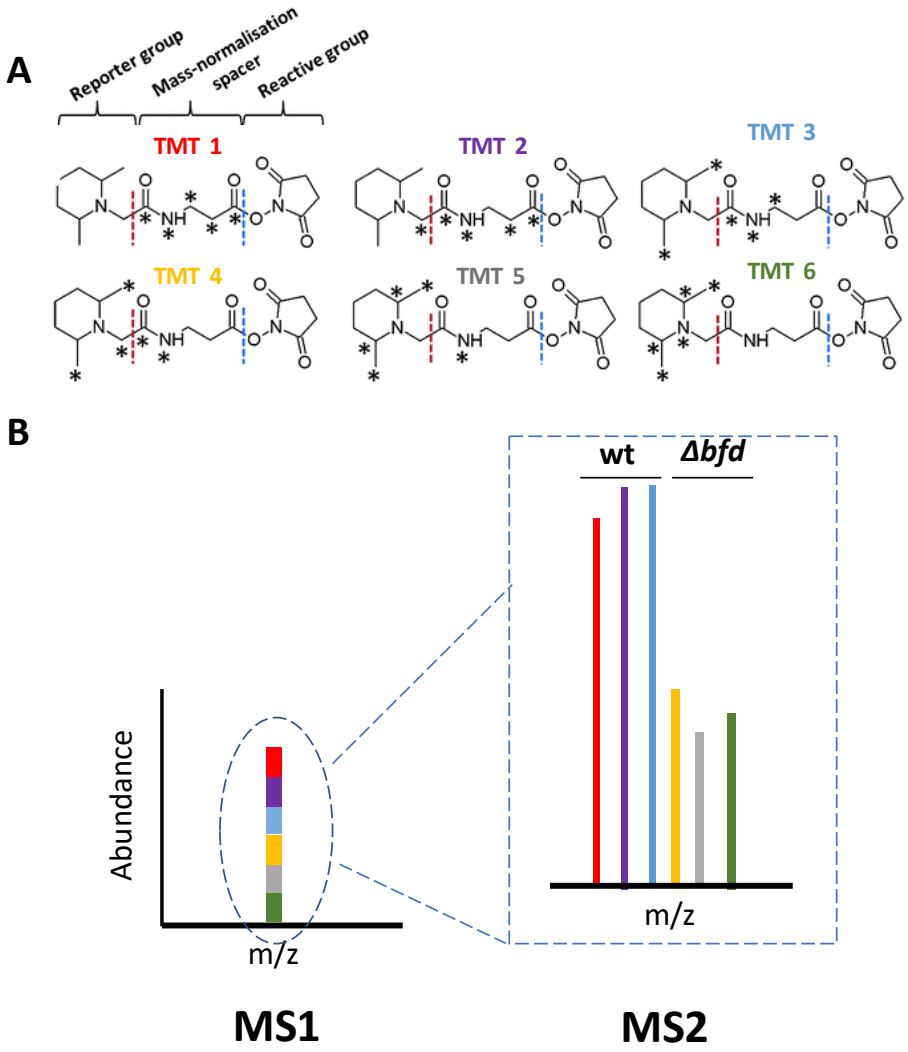

Figure 4-2: (A) Structures of the TMT-6plex tags. TMT tags are composed of a NH_2 reactive group, (separated by blue dotted line) a normalizer and a mass reporter (separated by red dotted line). The symbol * present isotopic labeling by ^{13}C or ^{15}N. (B) labeled identical peptides will show as a single peak in MS1. The labels are cleaved during peptide fragmentation (red dotted line), generating reporter irons with different masses. The reporter ion masses generated from the TMT-6plex are, m/z =126, m/z= 127, m/z =128, m/z =129, m/z= 130, and m/z =131. (Figures are adapted with permission from Springer Nature: Humana Press, Ref.7, 2012)

Quantitative proteomics approaches utilize labeled or non-labeled peptides. For labeled-proteomics, Tandem Mass Tags (TMT), or iTRAQ tags are commonly used, they allow parallel

multiplexing of quantitative experiments. The isobaric tags are isotopic tags that consist of an NH_2 reactive group, a normalizer, and a mass reporter (**Figure 4-2**) [7]. Stable isotopes ^{13}C or ^{15}N are incorporated into the reporter group and/or to the normalizer (isotopes are shown as * in **Figure 4-2-A**) [7]. Adding stable isotopes to the above groups allows designing a set of tags with identical chemical structures and identical mass but distinguishable in MS2 of an MS/MS (**Figure 4-2-B**).

All the peptides generated from a sample are labeled with a specific TMT tag (sample 1 is labeled with TMT 1, sample 2 is labeled with TMT 2 and sample 3 is labeled with TMT 3, *etc.*). The TMT tagged identical peptides (*e.g*., peptide A in all 6 samples) appear as a single peak in the mass spectrum (MS1) because of the identical mass of the tags (**Figure 4-2-B left**). Each tag has an MS2 variant known as the "mass reporter." The MS/MS fragmentation sites by higher energy collision dissociation (HCD) are shown in a red dashed line. Each reporter group is differentially labeled by ^{13}C or ^{15}N isotopes (shown by the * symbol in **Figure 4-2-A)**, TMT 1 is not labeled (*m/z*=126), TMT 2 is labeled with one ^{13}C (*m/z*=127), TMT 3 is labeled with two ^{13}C (*m/z*=128), *etc*., When a peptide is selected for fragmentation, the linker connected to the reporter ion is cleaved, generating 6 different reporter ions peaks in the low m/z region of MS2 (**Figure 4-2-B right**). As shown in the **Figure 4-2-B** (right) the intensities of the reporter ions correspond to the abundances of parent peptides (*e.g*., peptide A) in each sample (*e.g*., the intensities of reporter ions from TMT 1, 2, and 3 represent the abundance of peptide A in samples 1, 2 and 3, *etc*.) [8]. The peptide abundances are used for the relative quantification. Commercial TMT tags have up to 10 different tags, which allow running 10 samples simultaneously [9].

The goal of this study was to identify variations in the protein expression profiles upon blockade of the BfrB:Bfd interaction of *P. aeruginosa* by studying the expression proteome of the wild type and *Δbfd* cells, with the aim of identifying the implications of inducing cytosolic iron deprivation on protein expression and metabolic pathways.

4.2 Experimental

4.2.1 Strains, media and growth conditions

P. aeruginosa (PA01) and the *bfd* gene knock out mutant (*Δbfd)* were used for the experiments [1]. All strains were maintained on Pseudomonas Isolation Agar (PIA, BD Biosciences).

Pseudomonas aeruginosa isolation (PI) media was used to culture cells. PI media per 1L contains 20 g L^{-1} peptone, 1.4 g L^{-1} $MgCl_2.6H_2O$, 10 g L^{-1} K_2SO_4, 25 mg L^{-1} irgasan (Sigma-Aldrich), and 20 mL L^{-1} glycerol, pH 7.0. PI media was supplemented with 10 μM iron using a 10 mM stock of $(NH_4)_2Fe(SO_4)_2$ (pH ~2.0).

4.2.2 Cell growth and lysate preparation

P. aeruginosa pre-cultures were grown in 5 mL of PI media supplemented with 10 μM iron for 12 h at 37 ^{0}C and 220 rpm. Optical density at 600 nm (OD_{600}) was adjusted to 0.001 in PI media supplemented with 10 μM iron. *P. aeruginosa* wild type and *Δbfd* mutant cells were grown in 50 mL cultures (250 mL Erlenmeyer flasks), covered with an air-permeable membrane. Cells were incubated at 37 ^{0}C and 230 rpm. At 30 h post-inoculation, viable cells were enumerated. Cultures were divided into fractions and centrifuged at 4000 rpm for 15 min at 4 ^{0}C. Cell pellets were washed twice with 10 mL of Phosphate Buffered Saline (PBS) and stored at -20 ^{0}C. Cell-free supernatants were analyzed for pyoverdine using fluorescence spectroscopy [1].

A cell pellet from a 5 mL culture was re-suspended in 5 mL of 1 % SDS and sonicated for 90 s at a 20 % pulse amplitude with a 10 s ON and 10 s OFF pulses. The lysate was centrifuged, and the collected cell debris was lysed again by sonication using an additional 5 mL of 1% SDS. Lysates were kept frozen until proteomics sample preparation.

For the proteomics study, three technical replicates were prepared from a single biological replicate. Two additional biological replicates were collected but have not been analyzed at the time of writing (all biological replicates resulted in similar cell densities and pyoverdine secretion levels).

4.2.3 Sample preparation

Sample preparation and proteomics workflow were carried out by Dr. Jessie Guidry (Proteomics Core Facility, Louisiana State University Health Science Center, New Orleans) by following published protocols [10, 11].

A 100 µg of protein per sample was used for trypsin digestion. Proteins were reduced using tris(2-carboxyethyl)phosphine (TCEP) and alkylated with iodoacetamide. Proteins were subjected to chloroform-methanol precipitation, and the resultant pellet was digested with trypsin at 37 ^{0}C overnight. The digested proteins were labeled with TMT 6plex reagents set (Thermo Scientific) according to the manufacturer's recommended protocol. The tagged samples were stored at -80 ^{0}C.

An equal volume from each TMT tagged sample was pooled into a single tube and purified using acidic reverse phase conditions (SepPak -Waters, Ireland). Once the samples were dried, a fractionation step was carried out to lower the complexity of the sample. The sample volume was adjusted to 115 µL by 20 mM ammonium hydroxide (pH 10), and basic-pH reverse phase chromatography (Dionex U3000, Thermo Fisher) was carried out according to the parameters below. The injection volume was 100 µL, and the flow rate was 0.1 mL/min. A 90 min gradient was developed from 10 mM ammonium hydroxide (pH=10) to 100% acetonitrile (**AH** pH=10). A set of 48, 200 µL fractions were collected, and the fractions were combined in a checkerboard fashion (fraction 1, 12, 25, and 27 -super fraction 1; fractions 2, 14, 26, 38-super fraction 2, *etc*.) resulting in 12 super fractions. These fractions were run on a Dionex U3000 nanoflow coupled to Thermo Scientific™ Orbitrap Fusion™ Tribrid™ Mass Spectrometer. at a flow rate of 0.3 µL/min (Trap column: C18 PepMap 100, 5um, 100A, separation column: PicoChip REPROSIL-Pur C18-AQ, 3um, 120A, 105mm). A 90 min chromatographic method was employed. The gradient was as follows, 2-25 % ACN in 0.1 % Formic acid (FA) -65 min, 50 % ACN/FA-10 min, 90 % ACN/FA 5 min, and re-equilibration 2 % ACN/FA -10 min.

Electrospray ionization was performed at 2.6 kV. Data acquisition used an MS3 approach; survey scans were done in the Orbitrap, using a resolution of 120,000. MS2 scans were done in the linear ion trap,

using a collision-induced dissociation of 25 %. For the fragmentation of the reported ions, High energy Collision Dissociation (HCD) of 65 % was used and detected in the Orbitrap using a 30,000 resolution. Runs were done in triplicate for each super fraction.

TMT data was analyzed using Proteome Discoverer 2.2. The triplicate runs for the 12 super fractions were merged and searched against SEQUEST. The used parameters were as follows, TMT reagents on lysine and N-terminus (+229.163), carbamidomethyl on cysteines (=57.021), dynamic modification of methionine (=15.9949), two maximum trypsin mis-cleavages, parent ion tolerance - 10 ppm, and the fragment mass tolerance – 0.6 Da. High scoring peptides were considered using a false discovery rate of 1%. Data files were searched against the *Pseudomonas* genome database (www.Pseudomonas.com) [12].

4.2.4 Data analysis

A volcano plot was generated using the log_2(fold change), and the -log_{10}(abundance ratio *p*-values). Data were filtered based on the fold change, and the abundance ratio *p*-values. Proteins with (*Δbfd*) / (wild type) fold change of ≥ 1.4 and ≤ 0.7, and the abundance ratio *p*-value <0.05 were considered to be significant [13]. The filtered datasets were uploaded onto the Kyoto Encyclopedia of Genes and Genomes (KEGG) Pathway Mapper and searched against *P. aeruginosa* (PA01) organism-specific pathways [14]. Identified proteins in the KEGG mapper were also searched against the *Pseudomonas* genome database to get the functional predictions and classifications [12].

4.3 Results and Discussion

4.3.1 Overview of the consequences of inducing cytosolic iron deprivation by blocking the BfrB:Bfd complex

Mobilizing iron from BfrB requires specific interactions with its cognate partner protein, Bfd. The *bfd* gene knockout mutant cells (*Δbfd*) are unable to mobilize iron from BfrB. The irreversible flux of iron into BfrB lowered the free iron levels in the *Δbfd* mutant cells [1]. When the cytosolic free iron levels drop below the K_d of the Fe^{2+}- Master iron regulator complex (Fur), the iron acquisition genes get derepressed,

resulting in siderophore synthesis and secretion. Siderophore secretion (pyoverdine) is a reasonable indicator of cytosolic iron deprivation [1]. At 18-24 h of growth, iron in the media becomes scarce (~1 µM iron), and by 24 h pyoverdine becomes detectable in the *Δbfd* cells [1]. For the proteomics study, the wild type and the *Δbfd* mutant cells were grown for 30 h in PI media supplemented with 10 µM iron. At 30 h of growth, the *Δbfd* mutant showed cytosolic iron deprivation by secreting nearly 5-fold excess pyoverdine relative to the wild type cells.

The protein expression levels at 30 h post-inoculation were relatively quantified using Liquid Chromatography coupled Mass Spectroscopy. This method was able to quantify 3034 proteins, which is approximately 54 % of the total open reading frames in *P. aeruginosa* (PA01) [5570 open reading frames (ORFs)] [15]. All the quantified proteins were plotted against the $-log_{10}$ *p*-values and the log_2fold change in a volcano plot (**Figure 4-3**). Proteins with (*Δbfd*) / (wildtype) fold change of ≥ 1.4 (log_2fold change ≥0.5) are considered over-represented. Proteins with (*Δbfd*) / (wild type) fold change of ≤ 0.7 (log_2fold change ≤-0.5) are considered under-represented. The abundance ratio *p*-values < 0.05 ($-log_{10}$ *p*-value >1.3) are considered statistically significant. The blue lines in the plot represent log_2fold changes of 0.5 and -0.5, and $-log_{10}$ *p*-value =1.3 (*p* value = 0.05). As can be seen in the plot, the majority of the quantified proteins fall in the region between 0.5 and -0.5 region (no significant change). Among the 3034 identified proteins, 122

proteins are under-represented, and 126 proteins are over-represented in the *Δbfd* cells compared to the wild type cells.

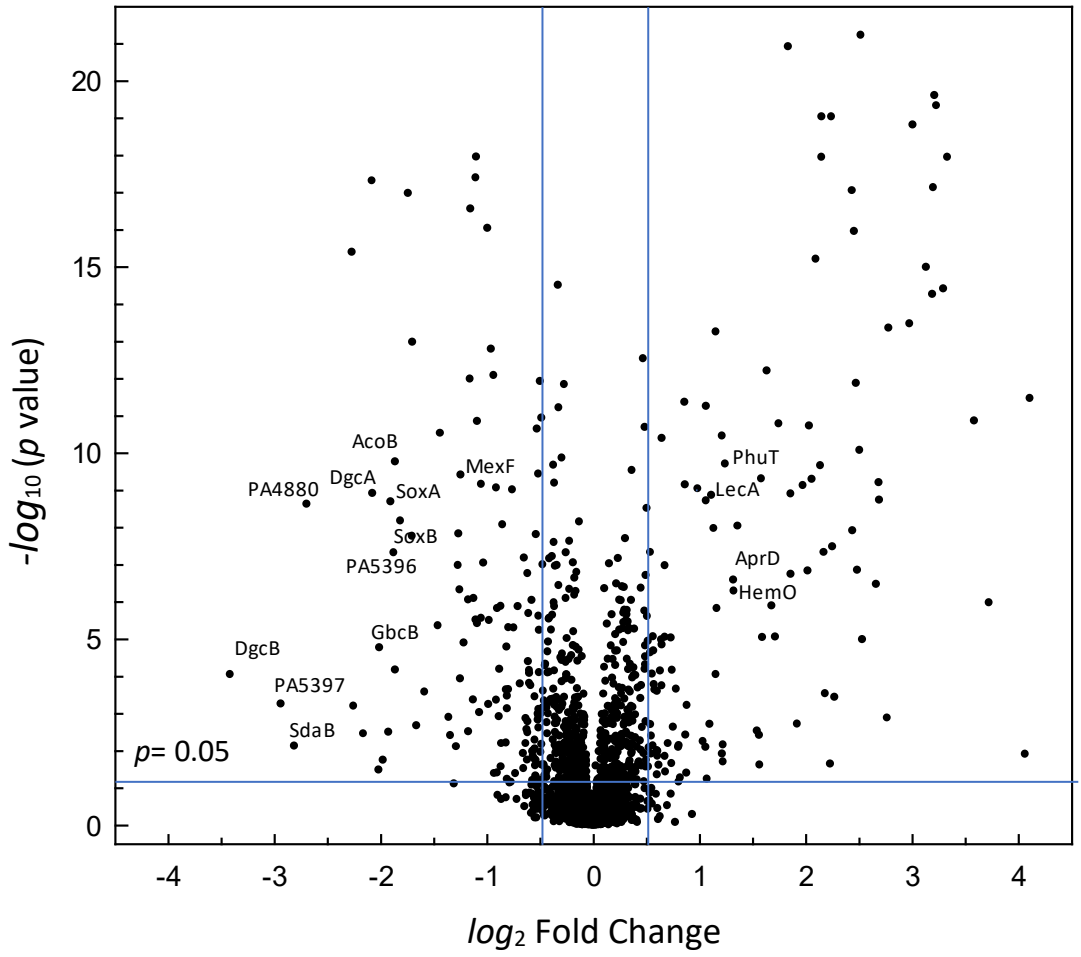

Figure 4-3: Identified *P. aeruginosa* proteins are placed in a volcano plot according to their relative abundance (log_2 fold change) and statistical significance (*-log p* value). Among the identified proteins, 122 were under-represented and 126 were over-represented in the *Δbfd* cells compared to the wild type cells.

The differentially expressed proteins were functionally categorized using the KEGG Orthology classification (**Figure 4-4**). This classification uses functional and sequence characteristics of experimentally characterized protein details to assign a functional category for a protein. Significant

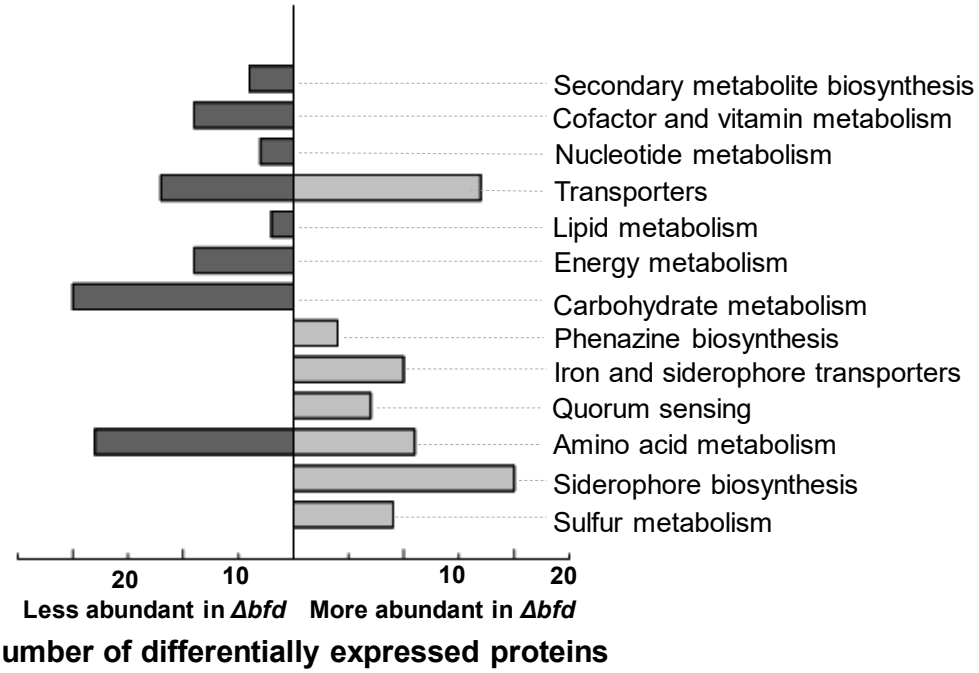

Figure 4-4: Functional classification of the proteins with significant fold changes and meaningful *p* values. The over-represented and under-represented proteins were categorized according to their function in *P. aeruginosa* cells using KEGG Orthology classification [14].

changes were observed in the proteins involved in siderophore biosynthesis, carbohydrate metabolism, amino acid metabolism, and cellular transport.

Among the under-represented proteins, 20 proteins were related to carbohydrate metabolism, which included several proteins from the citrate cycle (TCA cycle) [PATH:pae00020], glyoxylate and dicarboxylate metabolism [PATH:pae00630], butanoate metabolism [PATH:pae00650] and C5-Branched dibasic acid metabolism [PATH:pae00660]. In the amino acid metabolism, 18 proteins were under-represented, whereas 11 proteins were over-represented. The under-represented category included some proteins involving glycine, serine and threonine metabolism [PATH:pae00260], valine, leucine and isoleucine biosynthesis [PATH:pae00290], and tryptophan metabolism [PATH:pae00380]. Several over-represented amino acid metabolism proteins are involved in cysteine and methionine metabolism [PATH:pae00270], and tyrosine metabolism [PATH:pae00350] [14].

Nine proteins involved in energy metabolism are under-represented, and several of these proteins are involved in oxidative phosphorylation [PATH:pae00190], methane metabolism [PATH:pae00680], nitrogen metabolism [PATH:pae00910], and sulfur metabolism [PATH:pae00920]. The other under-represented proteins are involved in functions related to lipid, nucleotides, and cofactors, and vitamin metabolism [14].

Importantly, among the over-represented proteins, 30 proteins were related to iron metabolism, which includes siderophore biosynthesis, and siderophore and iron transport. The proteins involved in sulfur metabolism, quorum sensing, and phenazine biosynthesis are over-represented.

Differentially expressed proteins were matched with the existing pathways of *P. aeruginosa* using the KEGG mapper tool [14]. Identified proteins were searched against *Pseudomonas* genome database to identify functional and biochemical characteristics [12]. Among the 122 under-represented proteins, KEGG pathway tool identified proteins involved in the amino acid metabolism, carbohydrate metabolism, and butanoate metabolism. Among the identified 126 over-represented proteins, pathway tool identified proteins involved in the biosynthesis of siderophore group non-ribosomal peptides, sulfur metabolism, Quorum sensing, and biofilm formation.

4.3.2 Iron acquisition

(A) Pyoverdine biosynthesis

The *bfd* gene knockout mutant (*Δbfd*) cells of *P. aeruginosa* show low free iron levels in the cytosol and a high total iron to free iron ratio than the wild type cells [1]. When the cytosolic free iron levels drop below the K_d of the Fe^{2+}- Fur, Fur is no longer bound to Fe^{2+}. The apo-Fur derepresses the iron acquisition genes (*e.g*. pyoverdine, pyochelin, *etc*.). As shown in **Table 4-1,** proteins necessary for pyoverdine and pyochelin biosynthesis, and proteins involved in heme iron acquisition are over-represented in the *Δbfd* mutant cells.

Table 4-1: Proteins involved in iron and heme-iron acquisition are over-represented in the *Δbfd* mutant cells.

Protein ID	Name	Function	log_2Fold Change (Δbfd/Wt)
		Pyochelin biosynthesis	
PA4230	PchB	salicylate biosynthesis protein	2.46
PA4226	PchE	dihydroaeruginoic acid synthetase	2.52
PA4228	PchD	pyochelin biosynthesis protein	2.24
PA4225	PchF	pyochelin synthetase	2.15
PA4221	FptA	Fe(III)-pyochelin outer membrane receptor precursor	2.14
PA4224	PchG	pyochelin biosynthetic protein	2.10
PA4231	PchA	salicylate biosynthesis isochorismate synthase	1.64
PA4227	PchR	transcriptional regulator	0.81
PA4229	PchC	pyochelin biosynthetic protein	0.61
		Pyoverdine biosynthesis	
PA2394	PvdN		4.11
PA2397	PvdE	pyoverdine biosynthesis protein	3.73
PA2413	PvdH	L-2,4-diaminobutyrate:2-ketoglutarate 4-aminotransferase	3.59
PA2385	PvdQ	3-oxo-C12-homoserine lactone acylase	3.30
PA2386	PvdA	L-ornithine N5-oxygenase	3.22
PA2395	PvdO		3.14
PA2424	PvdL	Pyoverdine biosynthesis	3.01
PA2393	PvdM		2.67
PA2392	PvdP		2.54
PA2400	PvdJ		2.49
PA2396	PvdF	pyoverdine synthetase F	2.48
PA2399	PvdD	pyoverdine synthetase D	2.45
PA2402	PvdI		2.17
PA2391			1.68
PA2398	fpvA	ferripyoverdine receptor	1.17
		Heme iron acquisition	
PA4710	PhuR	Heme/Hemoglobin uptake outer membrane receptor PhuR precursor	2.15
PA0672	HemO	heme oxygenase	1.33
PA7408	PhuT	Heme-transport protein	1.24
PA4709	PhuS		1.16
PA3901	FecA	Fe(III) dicitrate transport protein FecA	0.61
PA4706	PhuV		0.55

Pyoverdine is a yellow-green fluorescent molecule. Pyoverdine I (PVD I) is the main siderophore secreted by *P. aeruginosa* for iron assimilation. PVD I biosynthesis is a complex biological process and involves at least 11 enzymes. The PVD I biosynthesis pathway is well characterized in P. aeruginosa PA01.

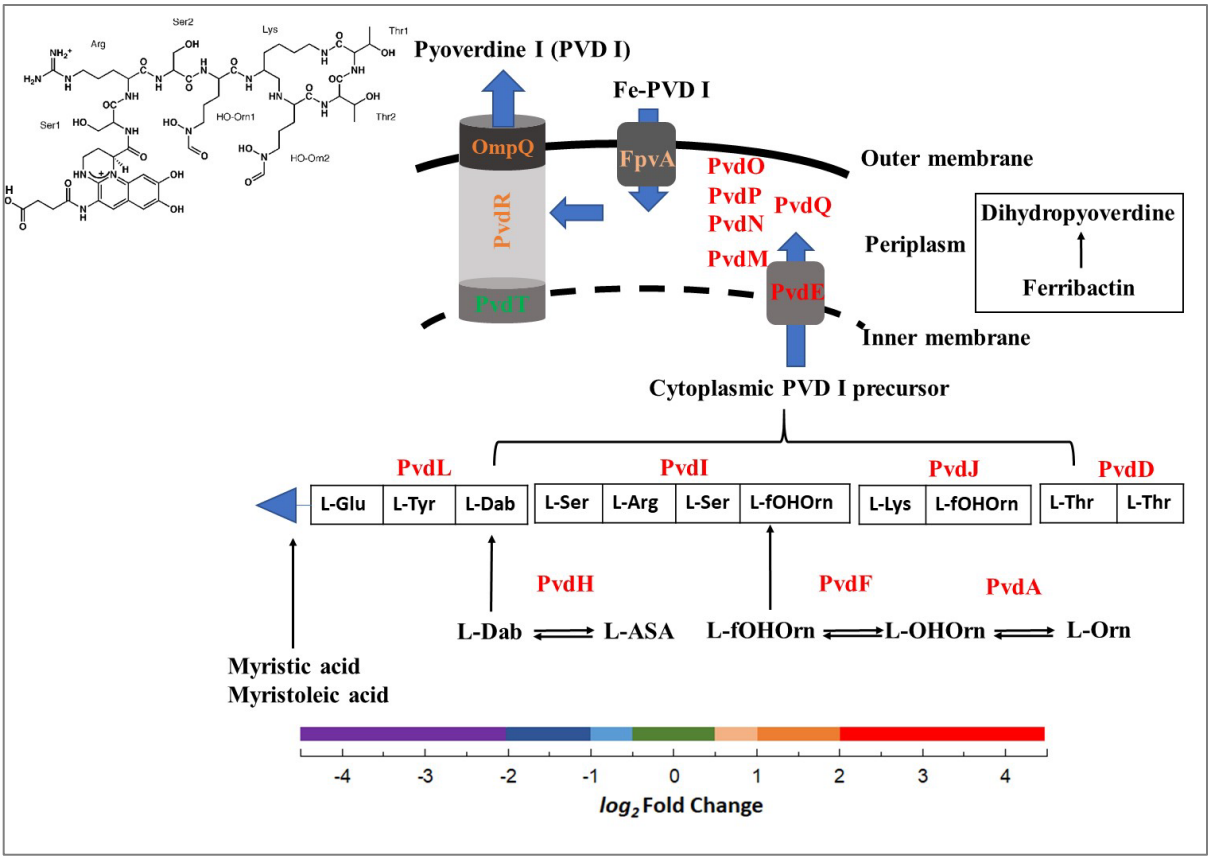

Figure 4-5: The pyoverdine I biosyntehsis pathway of *P.aeruginosa*. The color scale of protein abundance log_2fold change (*Δbfd*/ wt) is included, where green indicates no change. Proteins involved in pyoverdine synthesis are colored according to their fold change in color scale (Figure is adapted with permission from Ref. 17, 2012, John Wiley and Sons and re-formatted minorly)

Pyoverdine molecule consists of three portions, (i) dihydroquinoline type chromophore (fluorescent), (ii) strain-specific peptide with 6-12 amino acid, (iii) a side chain bound to the N at C-3. The PVD I synthesis begins in the cytoplasm, and the assembly is completed in the periplasm. Pyoverdine biosynthesis involves non-ribosomal peptide synthetases (NRPSs) and several other classes of enzymes. The NRPSs have a multi-module architecture, where each muddle contains about 1000 amino acids and corresponds to incorporating one specific amino acid substrate into the peptide chain [16, 17].

PVD I contains unusual amino acids, such as diamino butyric acid and ornithine. A variety of cytoplasmic enzymes (PvdH, PvdA, and PvdF) are involved in the synthesis of these unusual amino acids

that are necessary for NRPSs (PvdL, PvdI, PvdJ and PvdD) [17]. A schematic representation of the proverdine (PVD I) biosynthesis process with names of the involved proteins is shown in **Figure 4-5**. The expression levels of each protein are shown by color code. All the proteins necessary for the pyoverdine biosynthesis were over-represented by at least 2-fold. The most significant fold changes were observed in PvdN, PvdH, and PvdE (log_2 FC>3.5). The proteins PvdQ, PvdA, PvdO, and PvdL experienced a log_2 FC>3.0, while the PvdD, PvdF, PvdJ, and PvdP resulted in a log_2 FC>2.3 in the *Δbfd* mutants cells relative to the wild type cells.

The cytoplasmic protein, PvdH is one of the proteins with a high overrepresentation (log_2FC= 3.59). PvdH catalyzes the aminotransferase reaction by interconverting L-aspartate β-semialdehyde (L-ASA) and L-2,4-diaminobutyrate (L-Dab). The *pvdH* knockout mutant failed to synthesis pyoverdine under iron-depleted conditions. The pyoverdine production was restored when the media was supplemented with L-Dab [18]. PvdH is involved in the production of L-Dab, which is a crucial step in the PVD biosynthesis, and L-Dab is a substrate for PvdL (log_2 FC= 3.01) [18]. PvdL has a myristate binding site and contains a domain that is very similar to the acyl-coenzymeA ligases. The cytoplasmic precursor of PVD I contains a myristic or myristoleic acid. It has been proposed that the PvdL can join coenzyme A to a myristate in an ATP-dependent reaction and incorporate the complex to L-Glu followed by the addition of L-Tyr and L-Dab. The c-terminal domain of PvdL attaches the synthesized dihydroquinoline type chromophore to L-Ser, which is the first amino acid of the peptide moiety [16, 17].

The conversion of L-ornithine (L-Orn) to L-N^5-hydroxyornithine (L-OHOrn) is carried out by PvdA (log_2 FC= 3.22). The formylation of L-OH-Orn to produce L-N^5hydroxyornithine (L-fOHOrn) is catalyzed by PvdF (log_2 FC= 2.48). The biosynthesized amino acids are added into the peptide moiety by NRPSs, PvdI (log_2 FC= 2.17), PvdJ (log_2 FC= 2.49), and PvdD (log_2 FC= 2.45). Once all the peptides are assembled, the non-fluorescent precursor is transported across the inner membrane into the periplasm via ABC transporter PvdE, which is one of the significantly represented proteins in the *Δbfd* cells (log_2 FC=3.73) [17]. The *pvdE* knock out mutant (Δ*pvdE*) failed to secrete pyoverdine. Suzuki and the co-

workers used wild type *P. aeruginosa* (PA01) cells and the Δ*pvdE* mutant cells to determine the role of pyoverdine in bacterial survival in the cornea. The mice infected with the wild type cells resulted in severe disease (high corneal opacity), whereas the Δ*pvdE* unable to colonize because of their inability to secrete pyoverdine. Thus PvdE plays an important role in the pyoverdine biosynthesis and secretion machinery [19].

In the periplasm, PvdQ (log_2 FC= 3.3) cleaves the myristic or myristoleic chain that links the precursor with the cytoplasmic membrane. Removing the fatty acid chain allows the chromophore to diffuse freely into the periplasm. The product of PvdQ is the PVD I precursor, ferribactin, which is non- fluorescent. Removal of the fatty acid precedes chromophore cyclization. The PVD I precursor, ferribaction undergoes cyclization in the periplasm by a multistep oxidative process. A subsequent tautomerization step leads to the formation of dihydroxyquinoline ring. PVD I is identical to dihydopyoverdine except that there is one less unsaturation in PVD I [17, 20]. The periplasmic proteins PvdN (log_2 FC= 4.11), PvdM (log_2 FC= 2.67), PvdO (log_2 FC= 3.14), and PvdP (log_2 FC= 2.54), are predicted to be involved in either chromophore formation or in a step proceeding it [17].

PvdN is significantly over-represented in the *Δbfd* cells. The importance of PvdN was studied using a *pvdN* gene knockout mutant. PvdN is involved in adding a specific side-chain modification in the 3- amino group of the chromophore. The *pvdN* knockout mutation did not affect the overall pyoverdine production [21].

Gene *pvdRT-ompQ* codes for an efflux pump that is involved in the PVD I secretion. PvdT is an inner membrane protein, PvdR (log_2 FC= 1.92) is the periplasmic adaptor protein and OpmQ (log_2 FC= 1.68) is an outer membrane protein with a large periplasmic extension and a β-barrel domain inserted in the outer membrane [20].

The extracellular PVD I-Fe complex is transported back into the cell by FpvA (log_2 FC=1.17), and FpvB (No change). FpvA is the primary transporter of the PVD I-Fe complex. The PVD I-Fe complex uptake depends on the proton motive force, and the Fpva and FpvB are activated via TonB machinery [22].

Iron in the PVD I-Fe complex is released at the periplasm by a reduction mechanism. The apo-PVD I is recycled back to the extracellular environment by the PvdRT-OpmQ.

(B) Pyocheline biosynthesis

Under iron limitation conditions, pyochelin is synthesized first, and if the iron starvation is acute cells switch to the pyoverdine synthesis [23]. Pyochelin is a small, relatively low-affinity siderophore secreted by *P. aeruginosa*. At neutral pH pyochelin chelates Fe^{3+} with a 2:1 stoichiometry. The biosynthesis of pyochelin involves three NRPS. Pyochelin biosynthesis includes fewer number of proteins compared to the biosynthesis of pyoverdine. Pyochelin synthesis transcriptional activator, PchR, positively regulates the synthesis of pyochelin and pyochelin receptor, FptA [24]. The pyochelin biosynthesis pathway is illustrated in **Figure 4-6**, the proteins are color-coded according to the fold change color coded scale. All the proteins involved in pyochelin synthesis were at least 2-fold over-represented.

Pyochelin is made from three precursors, a salicylate, a hydroxyl acid, and two cysteine molecules. In the first step of pyochelin biosynthesis, chorismate is isomerized to isochorismate by PchA (isochorismate synthase, log_2 FC= 1.64). The produced isochorismate is converted into salicylate by

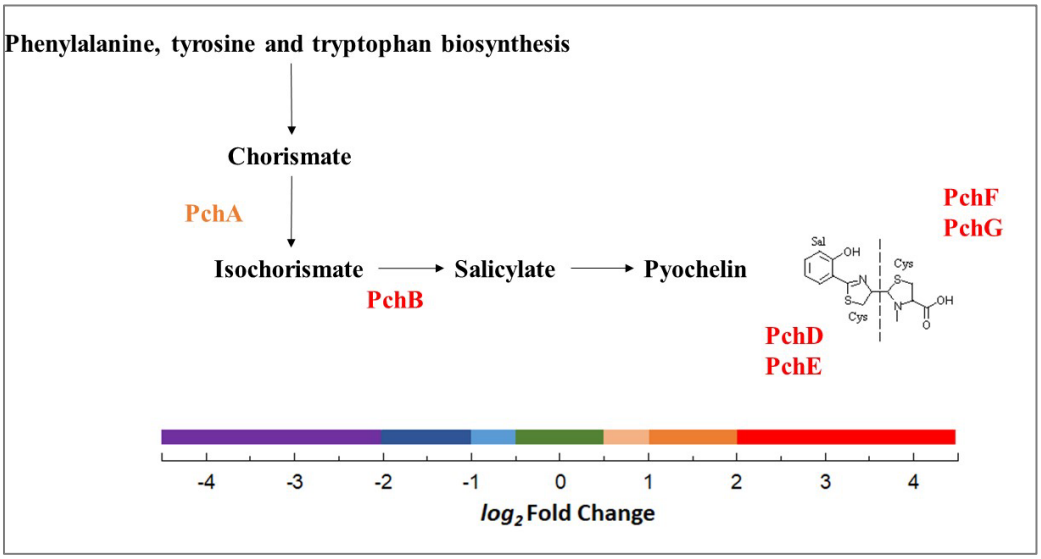

Figure 4-6: The pyochelin biosynthesis pathway of *P. aeruginosa*. The color scale of protein abundance log_2fold change (*Δbfd*/ wt), is included. (Modified from the KEGG pathway: pae01053, Ref. 14)

isochorismate pyruvate lyase, PchB (log_2 FC= 2.46). Salicylate is activated by the A-domain of PchD (log_2 FC= 2.24) and transferred to the P-domain of NRPs, PchE (initiation module, log_2 FC= 2.52). Next, the PchE elongation module incorporated a cysteine, and cyclize it, forming a thiazoline ring. The PchE termination module adds another cyclized L-cysteine generating a second thiazoline. PchG (log_2 FC= 2.10) acts as the tailoring domain, and reduces the thiazoline to thiazolidine. PchF (log_2 FC= 2.15) carries out a N-methylation of the thiazolidine, and the mature pyochelin is secreted by the T-domain of PchF [25].

(C) Heme iron acquisition

P. aeruginosa is equipped with strategies to extract heme iron from hemoproteins. The heme iron acquisition system, Phu (*Pseudomonas* heme utilization) consists of of PhuR, PhuS, PhuT, PhuV, and HemO [26]. Proteins in the Phu system are over-represented in the *Δbfd* mutant cells. The Phu system directly extracts heme using a TonB dependent receptor, PhuR (log_2 FC= 2.15), and transports it into the periplasm. The heme-binding transporter protein, PhuT (log_2 FC= 1.24) interacts with the ABC transporter, PhuUV (log_2 FC=0.55, PhuU=not detected), and transfers heme into the cytoplasmic heme-binding protein PhuS (log_2 FC=1.16). Heme in PhuS is transferred to HemO (heme oxygenase, log_2 FC=1.33). In *P.*

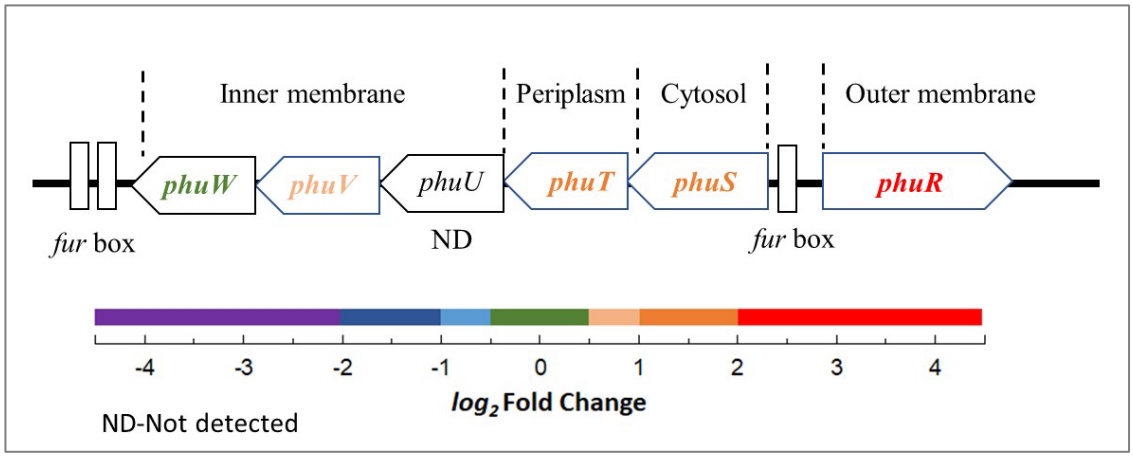

Figure 4-7: The *phu* operon of *P. aeruginsa*. The color scale of protein abundance log_2fold change (*Δbfd*/ wt), is included. (Figure is adopted with permission from Ref. 26, copyright 2008 Elsevier and modified minorly)

aeruginosa cells, the PhuS, along with HemO controls the heme flux into the cell [27]. In the cell, heme oxygenase degrades heme tetrrapyrrole ring into biliverdin, CO, and Fe^{2+} [28].

From the above, it is evident that the *Δbfd* mutant cells have over-representation of proteins involved in the primary iron acquisition mechanisms with significant fold changes compared to the rest of the protein pool. Fulfilling iron requirements is one of the foremost challenges faced by *Δbfd* mutant cells. Biosynthesis processes, such as pyoverdine synthesis, consume an enormous amount of the cell's resources, and forces the the *Δbfd* mutant cells to invest enormous resources to overcome the iron deficiency caused by the irreversible accumulation of iron in BfrB.

4.3.3 Carbon metabolism and energy production

(A) Tricarboxylic acid (TCA) cycle

Energy production in *P. aeruginosa* mainly relies on aerobic respiration. Therefore, the tricarboxylic acid cycle (TCA) is essential for the production of reducing equivalents for the respiratory chain. TCA cycle plays a dual role in the cell, (i) catabolism of acetyl-CoA into CO_2, producing reducing power to generate ATP via oxidative phosphorylation, (ii) synthesis of metabolite precursors for amino acid and fatty acid synthesis. A microarray study done under iron-limiting conditions demonstrated reduced expression levels in iron-containing enzymes in the TCA cycle [4]. The *Δbfd* mutant cells' proteome, experiences an under-representation of TCA cycle enzymes, aconitase, succinate dehydrogenase, and fumarase.

The key source of acetyl-CoA in the TCA cycle is pyruvate. Pyruvate dehydrogenase (AceE- no change) converts pyruvate into acetyl-CoA. Additionally, AcoA (probable dehydrogenase E1 component, log_2 FC=-2.16), AcoB (Acetoin catabolism protein, log_2 FC=-1.86), and AcoC (probable hydrolase, log_2 FC=-1.30) can covert pyruvate into Acetyl-CoA via the formation of acetoin. The AcoA, AcoB, and AcoC are enzymes of the acetoin cleaving system in the butanoate metabolism pathway (**Figure 4-8**).

Acetyl-CoA, transfers the acetyl group to oxaloacetate generating citrate. Citrate is isomerized to isocitrate through *cis*-aconitate, aconitases catalyze this reaction. Aconitases, AcnA (log_2 FC= -1.10), and

AcnB (log_2 FC= -0.53) are 4Fe-4S cluster containing proteins. The activity of the AcnB is considered essential for the TCA cycle, and the under-representation of aconitases in the *Δbfd* mutant cells produce breaks in the TCA cycle [29].

Table 4-2: Proteins involved in carbon metabolism are under-represented the *Δbfd* mutant cells

Protein ID	Name	Function	Iron-ion binding	log_2Fold Change (Δbfd/Wt)
		TCA cycle		
PA4150	AcoA	probable dehydrogenase E1 component	No	-2.16
PA4151	AcoB	acetoin catabolism protein	No	-1.86
PA4152	AcoC*	probable hydrolase	No	-1.30
PA0794		probable aconitate hydratase	No	-0.76
PA1787	AcnB	aconitate hydratase 2	Yes	-0.53
PA1562	AcnA	aconitate hydratase 1	Yes	-1.10
PA5445	PsecoA	probable coenzyme A transferase	No	-0.55
PA4333	FumA	probable fumarase	Yes	-2.08
PA1581	SdhC*	succinate dehydrogenase c subunit	Yes	-0.57
PA4470	FumC1	fumarate hydratase	No (Mn)	3.23
		Butanoate metabolism		
PA2035		Probable decarboxylase	No	-0.54
PA3506		Probable decarboxylase	No	-0.56
PA4148		Probable short-chain dehydrogenase	No	-2.25
PA4153		2,3-butanediol dehydrogenase	No	-1.58

* *p* value>0.05

Succinyl-CoA is converted into succinate by Probable Co-A transferase (PA5445, log_2 FC= -0.55), and succinyl-CoA synthetases, SucC (succinyl-CoA synthetase beta chain, no change), and SucD (succinyl-CoA synthetase alpha chain, no change). The produced succinate is converted into fumarate by succinate dehydrogenases (Sdhs). Sdhs are a part of the TCA cycle and the electron transport chain. The Sdhs catalyze the oxidation of succinate to fumarate while reducing ubiquinone to ubiquinol in the cytosolic membrane. SdhC is a cytosolic membrane protein, which participates in the TCA cycle and electron transport chain reactions. The SdhC inhibitor, promysalin prevented the SdhCs coupled reactions in *P. aeruginosa*. In the presence of promysalin, the utilization of glucose or succinate as the carbon source brought challenges to the *P. aeruginsa* growth [30]. The RNA-sequencing data corroborated this fact. In the attendance of

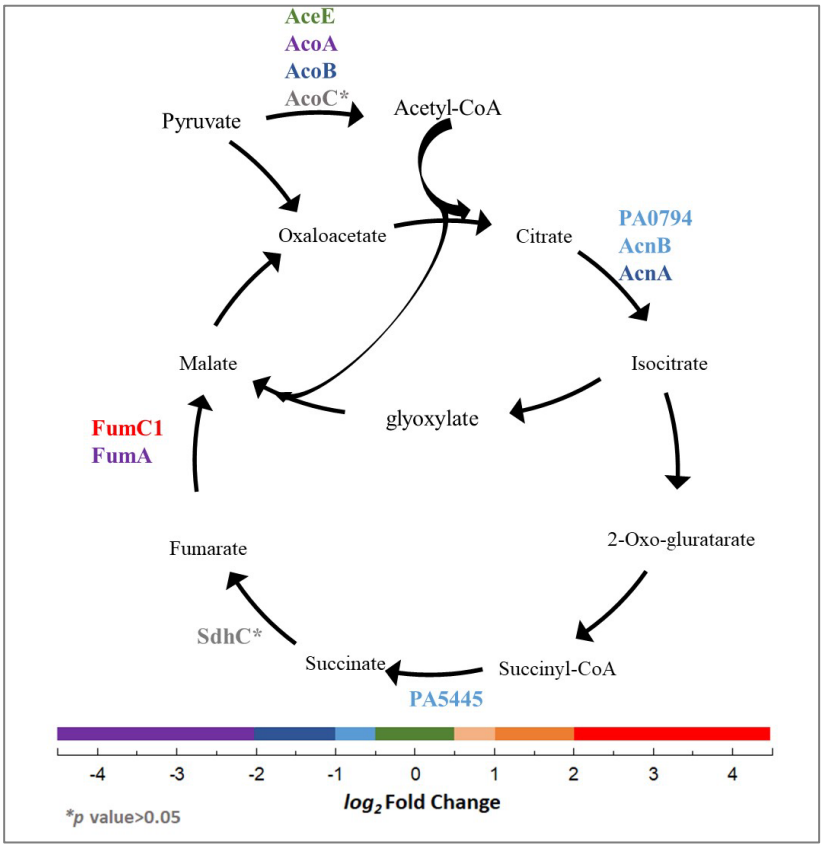

Figure 4-8: A schematic representation of the Tricarboxylic Acid cycle (TCA). The color scale of protein abundance log_2fold change (*Δbfd*/ wt), is included. (Figure is modified from the KEGG pathway: pae00020, Ref.14)

promysalin, some Entner–Doudoroff pathway genes were downregulated, indicating alterations in the carbon flux [30, 31]. SdhC (log_2 FC= -0.57, p>0.05) is under-represented in the *Δbfd* mutant cells, and this may create implications in the carbon flux and the electron transport chain.

Transposon sequencing data (Tn-seq) identified FumA (fumarase, PA4333, log_2FC= -2.08) as an essential enzyme for *P. aeruginosa* [29]. FumA is an iron-binding protein and is under the PrrF regulon, and one of the significantly under-represented proteins in the TCA cycle enzymes in the *Δbfd* mutant cells [32]. FumC1 (fumarase hydratase, PA4470, log_2FC= 3.23) is over-represented and may compensate for the low levels of FumA. FumC1 is known to over-express under iron-deprived conditions [33]. Fumarase convert fumarate to malate, and additional fumarate is produced in the cells by aromatic amino acid

degradation. Under low iron levels, iron independent, FumC1 allows the entry of the produced fumarate into the TCA cycle [32].

The glyoxylate shunt allows bypassing the oxidative decarboxylation when the lower part of the TCA cycle is affected. In the current study, no change in the expression levels of glyoxylate shunt enzymes, isocitrate lyase (AceA), and malate synthase G (GlcB) were observed in the *Δbfd* mutant cells.

(B) Butanone metabolism

P. aeruginosa cells can utilize the synthesized pyruvate from the EDP or PPP to produce 2,3-butanediol (**Figure 4-9**). 2,3-Butanediol (2,3-BD) is a commonly found primary metabolite in the microenvironments of the human lung during *P. aeruginosa* infections [34]. In the 2,3-butanediol synthesis, pyruvate is converted to α-acetolactate by two probable decarboxylases, PA2035 (log_2FC= -0.54) and PA3506 (log_2FC= -0.56). The produced α-acetolactate is converted to (*R*)-2- acetoin or (S)-2-acetoin via diacetyl by PA4148 (probable short-chain dehydrogenase, log_2FC=-2.25) and PA4151 (2,3-butanediol dehydrogenase, log_2FC=-1.58). The (*R*)-2- acetoin and (S)-2-acetoin are reduced to form three stereoisomeric forms of 2,3-BD (**Figure 4-9)**. The produced 2,3-BD is secreted or converted back to (*R*)-2- acetoin or (S)-2-acetoin to produce acetyl-CoA or aldehyde, which are subsequently converted into acetyl-CoA and introduced into the TCA cycle [34]. The conversion of acetoin to acetyl-CoA is catalyzed by, AcoA (probable dehydrogenase E1 component, log_2 FC=-2.16), AcoB (Acetoin catabolism protein, log_2 FC=-1.86), and AcoC (probable hydrolase, log_2 FC=-1.30) [34].

The isogenic mutants of *P. aeruginosa* (PA01), *PA4150*, *PA4151* or *PA4153* resulted in decreased biofilm formation and low competitiveness in the rhizosphere [34]. The 2,3-BD catabolism related genes are essential in *P. aeruginosa* fitness, virulence, and infection. Additionally, being able to utilize 2,3-BD is an advantage when growing in restrictive nutrient environments such as airways of cystic fibrosis patients [34].

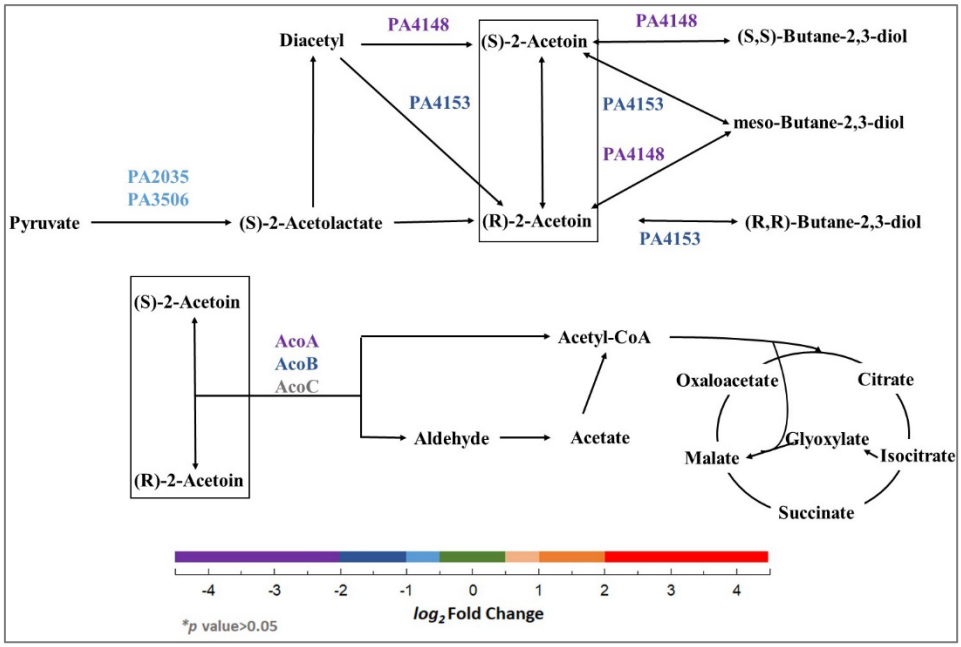

Figure 4-9: Butanone metabolism pathway of *P.aeruginsa*. The color scale of protein abundance log_2fold change (*Δbfd*/ wt), is included. (Top: Figure is modified from the KEGG pathway: pae00650, Ref.14. Bottom: adapted with permission from Ref. 34, copyright 2018 Society for Applied Microbiology and John Wiley & Sons Ltd.)

In the *Δbfd* mutant cells, the butanone metabolism pathway is compromised relative to the wild type cells. The enzymes involved in the 2,3-BD metabolism are not iron-harboring proteins. Therefore, the under-representation of the related enzymes may be a measure taken by the *Δbfd* mutant cells to preserve produced pyruvate for energy and amino acid production. Thus, the *Δbfd* mutant cells repress the other mechanism that uses pyruvate as a substrate. Consequently, the failure to secrete or use 2,3-BD may reduce the fitness and the virulence of the *Δbfd* mutant cells.

4.3.4 Amino acid biosynthesis

Amino acids are the primary building block of proteins as well as vital metabolic intermediates. In the *Δbfd* mutant cells, about 20 enzymes required in amino acid biosynthesis are under-represented; 8 of these are identified as iron-binding proteins. A reasonable fraction of the cells' energy is devoted to the biosynthesis of amino acids. The central carbon metabolism provides necessary precursors for the synthesis of 20 primary amino acids. Thereby cells lose some energy-producing intermediates due to this diversion.

Moreover, additional energy from the cells is required to convert the carbon metabolism precursors into amino acids [35]. Therefore, the *Δbfd* mutant cells appear to down-regulate or have a lower basal expression level in the amino acid biosynthesis-related genes to preserve resources for the essential cellular functions.

Table 4-3: Amino acid biosynthesis paths affected in the *Δbfd* mutant cells

Protein ID	Name	Function	Iron-ion binding	log_2Fold Change (Δbfd/Wt)
Glycine, Serine				
PA5379	SdaB	L-serine dehydratase	Yes	-2.81
PA5415	GlyA1	serine hydroxymethyltransferase	No	-1.06
PA5378	CbcX		No	-0.50
PA5376	CbcV		No	-1.09
PA5377	CbcW		No	-1.17
PA5410	GbcA	glycine betaine catabolism protein	Yes	-2.27
PA5411	GbcB	glycine betaine catabolism protein	Yes	-2.01
PA5398	DgcA	Dimethylglycine catabolism	No	-2.07
PA5399	DgcB	Dimethylglycine catabolism	Yes	-3.41
PA5416	SoxB	sarcosine oxidase beta subunit	No	-1.70
PA5417	SoxD	sarcosine oxidase delta subunit	No	-1.28
PA5418	SoxA	sarcosine oxidase alpha subunit	Yes	-1.90
Valine, Leucine, Isoleucine				
PA3121	LeuC	3-isopropylmalate dehydratase large subunit	Yes	-1.09
PA3120	LeuD	3-isopropylmalate dehydratase small subunit	No	-0.85
PA2035		probable decarboxylase	No	-0.54
PA3506		probable decarboxylase	No	-0.56
Lysine, Aspartate, Asparagine, Glutamate, Glutamine, Proline, Cysteine and Arginine				
PA1787	AcnB	aconitate hydratase 2	Yes	-0.53
PA1562	AcnA	aconitate hydratase 1	Yes	-1.10
PA0399		cystathionine beta-synthase	No	0.50
PA0051	PhzH	potential phenazine-modifying enzyme	No	0.61
PA2084		probable asparagine synthetase	No	0.87
PA3459		probable glutamine amidotransferase	No	-0.51
PA5172	arcB	ornithine carbamoyltransferase, catabolic	No	-0.51

(A) Glycine and serine biosynthesis

P. aeruginosa can use glycine betaine (GB) as carbon, nitrogen, and energy source. GB can also act as an important osmoprotectant. GB can be uptaken as a free molecule or can be derived from choline or carnitine. As illustrated in **Figure 4-10**, GB binds to CbcX (log_2 FC=-0.5) in the periplasm. GB in the periplasm is taken into the cell cytosol by the ABC family transporters, CbcV (log_2 FC= -1.09), and CbcW (log_2 FC= -1.17) [36].

The proteins, GbcA (glycine betaine catabolism A, log_2FC= -2.27) and GbcB (glycine betaine catabolism B, log_2FC= -2.01) are necessary to convert GB to dimethylglycine (DMG) in the cytosol. Both GbcA and GbcB are iron-containing proteins and are under-represented ~5-fold in the *Δbfd* mutant cells compared to the wild type cells. The knockout mutants of *gbcA* and *gbcB* failed to utilize GB or choline as a carbon source but were able to use dimethylglycine (DMG) [37]. The enzymes GbcA and GbcB are essential to convert GB to DMG in order to synthesize glycine.

Proteins involved in dimethylglycine catabolism, DgcA (log_2FC= -2.07) and DgcB (log_2FC= -3.41) are predicted to be a flavin mononucleotide oxidoreductase and a membrane associated ferredoxin Fe-S oxidoreductase respectively [37]. DMG is demethylated to sarcosine by DgcA and DgcB enzymes. The

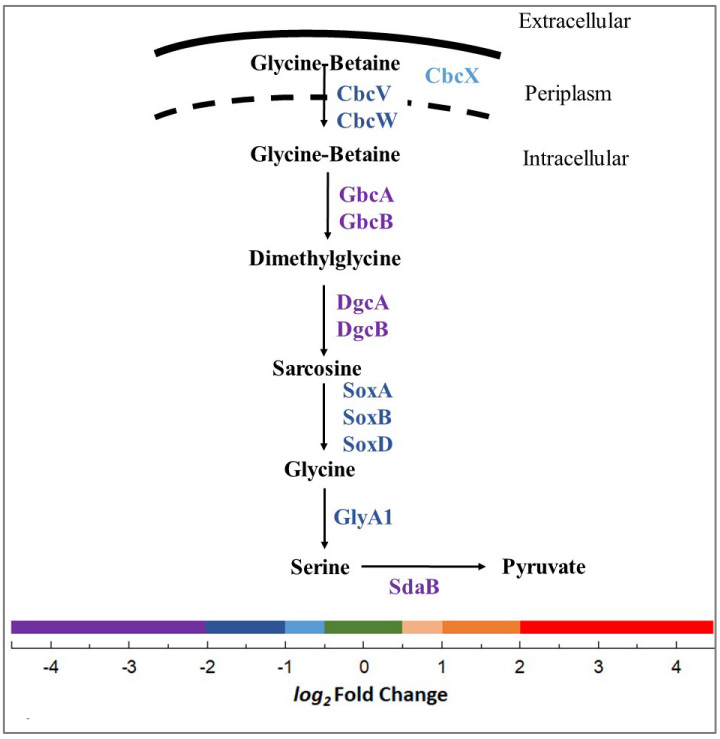

Figure 4-10:The glycine-betaine metabolism pathway in *P.aeruginosa* may be compromised in the Δ*bfd* mutant Glycine-betaine is converted into pyruvate by a series of biological reactions. Glycine and serine are produced as intermediates. The color scale of protein abundance log_2fold change (*Δbfd*/ wt), is included. (Figures are adapted from Ref. 36 and Ref. 38)

production of sarcosine stimulates the sarcosine oxidation and utilization regulator and thereby inducing the *soxBDAG* operon [38]. SoxB (log_2FC= -1.70), SoxD (log_2FC= -1.28) and SoxA ([2Fe-2S] enzyme, log_2FC= -1.90) enzymes are involved in the sarcosine catabolism to glycine. The SoxBDA enzymes are under-represented, while the SoxG presented no change in the *Δbfd* mutant cells relative to the wild type. The produced glycine is catabolized to serine via GlyA1 (serine hydroxymethyltransferase, log_2FC= -1.16). Serine is converted into pyruvate by SdaB (L-serine dehydratase, log_2FC= -2.81). The under-representation of the enzymes in the of the glycine betaine pathway proves the strain in the *Δbfd* cells in the catabolism of GB as a carbon source. Consequently, the synthesis of the amino acids, glycine, serine, and pyruvate appear to be compromised. Moreover, pyruvate acts as a precursor for the synthesis of 11 other amino acids (**Figure 4-11**), which are also be affected.

(B) Biosynthesis of other amino acids

The biosynthetic pathway of 11 other amino acids is illustrated in **Figure 4-11**. Pyruvate is converted to valine via 2-oxoisovalerate using the probable decarboxylase enzymes PA2035 (log_2FC= -0.54) and PA3506 (log_2FC= -0.56). The 2-oxoisovalerate can be converted into 2-oxoisocaproate by LeuC (3-isopropylmatate dehydrogenase large subunit, log_2FC= -1.09) and LeuD (3- isopropylmatate dehydrogenase small subunit, log_2FC= -0.85), with the subsequent production of leucine. The enzymes LeuCD are also involved in the conversion of pyruvate to 2-oxobutanoate for the successive production of isoleucine. LeuC is a [4Fe-4S] cluster harboring enzyme; both LeuCD are under-represented in the *Δbfd* cells, which may affect the biosynthesis of valine, leucine, and Isoleucine.

Pyruvate derived oxaloacetate is converted into 2-oxoglutarate using aconitases, AcnA (log_2FC= -1.10) and AcnB (log_2FC= -0.53). Both aconitases are iron-dependent and are under-represented in the *Δbfd* mutant cells. The 2-oxoglutarate or the derived product 2-oxoadipate is used for the synthesis of lysine, aspartate, asparagine, glutamate, glutamine, proline and arginine.

Additionally, aspartate is converted to asparagine using, PA3459 (probable glutamine amidotransferase, log_2FC= -0.51), PA2084 (probable asparagine synthetase, log_2FC= 0.87) and PhzH

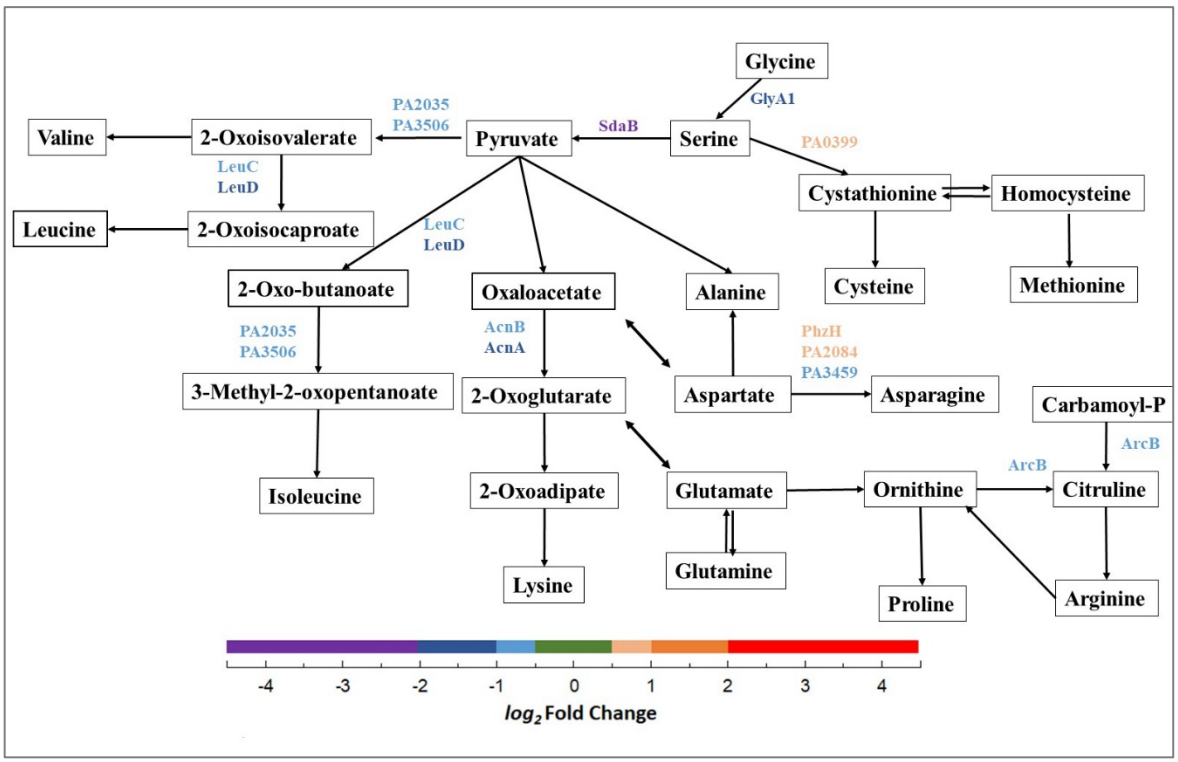

Figure 4-11: The biosynthesis of several amino acids in *P.aeruginosa* may be compromised in the Δ*bfd* mutant. Pyruvate acts as the precursor for the synthesis of several types of amino acids. The color scale of protein abundance log_2fold change (*Δbfd*/ wt), is included. (Figure modified from the KEGG pathway: pae01230, Ref.14)

(potential phenazine modifying enzyme, log_2FC= 0.61). There is an over-representation in PA2084 and PhzH; the over-representation of PhzH may not be related to the asparagine synthesis because it is also involved in quorum sensing.

The enzyme PA0399 (cystathione betasynthase, log_2FC= 0.50) is involved in the production of cystathionin from serine is over-represented. There may be an additional need for cysteine in the *Δbfd* cells, to repair damaged Fe-S cluster proteins and to synthesize pyochelin.

The under-representation of aconitase, LeuCD in the Δbfd mutant cells, may affect the biosynthesis of 9 amino acids. Besides, the levels of glycine, serine are also affected due to the under-representation glycine-betaine metabolism-related enzymes. The in-cell amino acid content analysis by NMR identified

low levels of glycine, leucine, valine, alanine, glutamate, and aspartate in the Δbfd mutant cells relative to the wild type cells (unpublished data).

4.3.5 Sulfur metabolism

Table 4-4: The sulfur assimilation pathway related proteins are over-represented in the *Δbfd* cells.

Protein ID	Name	Function	Iron binding	log_2Fold Change (Δbfd/Wt)
PA0280	CysA	Sulfate transport protein	No	0.87
PA0282	CysT	sulfate transport protein	No	0.57
PA0283	sbp	sulfate-binding protein precursor	No	1.75
PA3938	TauA	probable periplasmic taurine-binding protein	No	2.69
PA3445		conserved hypothetical protein	No	2.51
PA2594		conserved hypothetical protein	No	1.37
PA1838	CysI	sulfite reductase	Yes	0.54
PA4442	CysN	ATP sulfurylase GTP-binding subunit/APS kinase	No	0.65
PA4443	CysD	ATP sulfurylase small subunit	No	0.57
PA2566		conserved hypothetical protein	No	-1.12

Sulfur is an essential nutrient and is mainly found in cysteine, methionine, cofactors, and prosthetic groups such as Fe-S centers. Sulfate uptake and metabolism-related enzymes are over-represented in the *Δbfd* cells, suggesting a nutritional requirement for sulfur higher than the wild type cells. *P. aeruginosa* can utilize a broad range of sulfur sources, including cysteine, methionine, sulfate, thiocyanate, alkanesulfonates and organosulfate esters. The pathways for sulfate assimilation and cysteine biosynthesis proceeds by activating inorganic sulfate and reducing the intermediate 3'-phosphoadenosine-5'-phosphosulfate (PAPS) to sulfite (**Figure 4-12**). The produced sulfite is transferred into an organic backbone.

The extracellular sulfate transporter contains, a periplasmic sulfate binding protein (Sbp, (log_2FC= 1.75), permeases CysT (log_2FC= 0.57) and CysW (not detected), and a ATP binding domain CysA (log_2FC= 0.87). ATP sulfurylase activates sulfate *via* and ATP-dependent reaction resulting in the formation of adenylyl sulfate (APS) and pyrophosphate. This involves the catalytic subunit CysD (log_2FC= 0.57) and the GTP regulatory subunit CysN (log_2FC= 0.65). APS is converted into PAPS by ATP-

dependent phosphorylation. APS kinase, CysN consists a GTP-binding subunit and an adenosine 5'-phosphosulfate kinase subunit. e *P. aeruginosa* CysN shows the fusion activity of *E. coli* CysC and CysN proteins [39]. PAPS is converted to phosphoadenosine phosphate (PAP) and sulfite by PAPS sulfotransferase, CysH (No change).

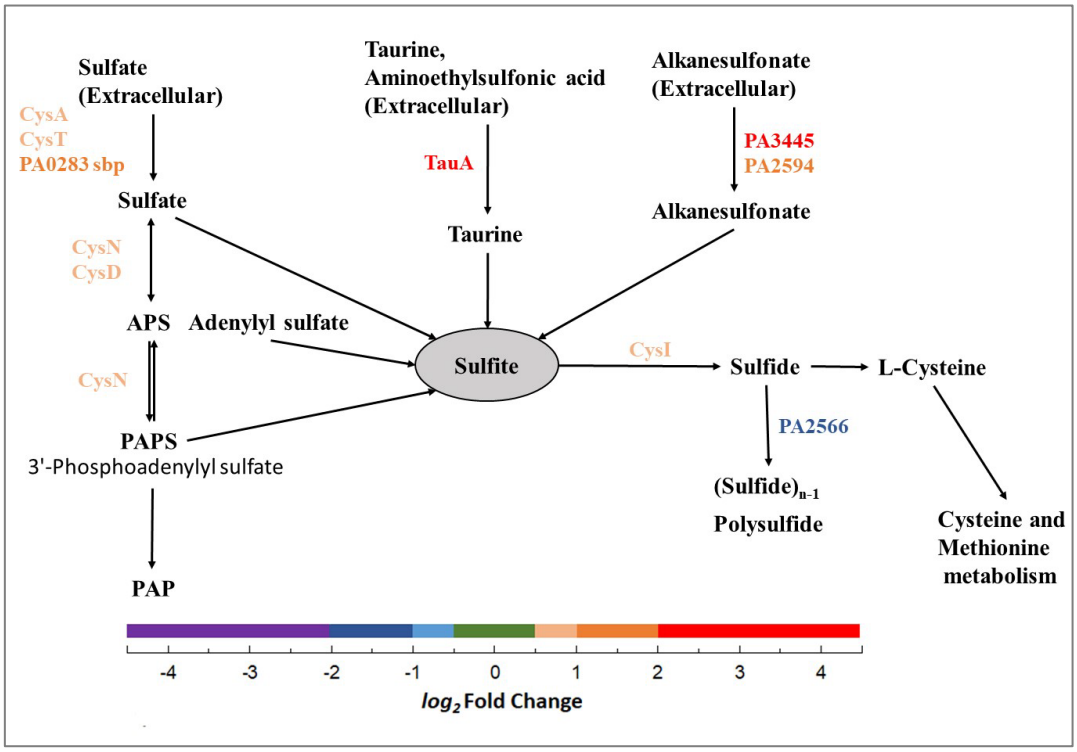

Figure 4-12: Sulfur assimilation pathway of *P. aeruginosa*. The color scale of protein abundance log_2fold change (*Δbfd*/ wt), is included. (Figure modified from the KEGG pathway: pae00920, Ref.14)

P. aeruginosa can uptake extracellular alkane sulfonates using the SsuA family ABC transporter, aliphatic sulfonates-binding proteins, PA3445 (log_2FC= 2.51) and PA2594 (log_2FC= 1.37). Taurine, aminoethylsufonic acid is transported into the cell via TauABC. Only TauA (probable periplasmic taurine binding protein, log_2FC= 2.69) was identified in the proteomics data set. In the preceding steps, taurine and the alkanesulfonates are converted into sulfite by TauD (not detected) and MsuDE (not detected), respectively.

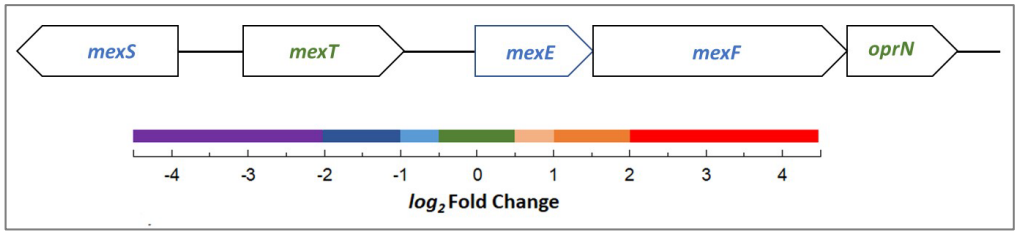

Figure 4-13: The mexEF-oprN operon of *P. aeruginosa*. Proteins MexS, MexE and MexF were under-represented in the *Δbfd* mutant cells. The color scale of protein abundance log_2fold change (*Δbfd*/ wt), is included.

Produced sulfite is reduced to sulfide by NADPH sulfite reductase, CysI (log_2FC= 0.54). CysI is a hemoprotein harboring a 4Fe-4S cluster and a siroheme binding motif typical of the sulfite and nitrite reductases family [39, 40]. Sulfite can be converted into polysulfide by PA2566 (log_2FC= -1.12), which is predicted to have a FAD/NAD(P) binding domain. In the sulfur assimilation pathway, this is the only under-represented enzyme. The produced sulfide can be used for the synthesis of cysteine, which is necessary for the Fe-S cluster proteins and pyochelin biosynthesis.

4.3.6 Selective Resistance-Nodulation-Cell Division (RND) efflux pumps

Quinolones, ciprofloxacin, and levofloxacin are widely used to treat *P. aeruginosa* infections. The mutations in the targets, GyrA, ParC, GyrB, and ParE can lower the effectiveness of the quinolones. Additionally, the over-expression of efflux pumps helps to avoid antibiotic accumulation in the cytosol and thereby to prevent damage caused by the antibiotics. Efflux pumps belong to the resistance nodulation cell division (RND) family of transporters includes, MexAB-OprM, MexXY-OprM, MexCD-OprJ, and MexEF-OprN. The m*exEF-oprN* operon confers resistance of *P. aeruginosa* to quinolones, chloramphenicol and trimethoprim [41].

The activity of MexS (log_2FC= -1.10) is postulated to be a putative upper regulator of the *mexEF-oprN* [42]. The *mexS* gene is located upstream of the *mexT* gene. The expression of MexEF-OprN is positively regulated by the transcriptional activator, MexT (No change), coded by *mexT* adjacent to the *mexEF-oprN.*

MexEF-OprN consists of an inner-membrane drug proton antiporter (RND component) MexF (log_2FC= -1.24), an outer membrane channel OprN (No change), and a periplasmic membrane fusion protein MexE (log_2FC= -1.15) [43].

Over-expression of MexEF-OprN in *P. aeruginosa* allows developing resistance to fluoroquinolones, where the Minimum Inhibitory Concentrations (MIC) are increased up to 8 µg/mL. Moreover, persisting in the presence of ciprofloxacin results in an additional requirement for iron. [44].

In the *Δbfd* mutant cells, the MexEF-OprN is under-represented, probably as an implication of iron homeostasis dysregulation. Iron homeostasis dysregulation by the small molecule inhibitors of the BfrB:Bfd interaction made *P. aeruginosa* cells more susceptible to fluoroquinolones [45]. Consequently, under iron homeostasis dysregulation the cells' inability to express the mexEF-OprN pumps at their optimum levels resulted in additional susceptibility to fluoroquinolones.

4.3.7 Other essential cellular functions affected

In *P. aeruginosa Δbfd* mutant cells, several other cellular functions were affected as a result of the iron homeostasis dysregulation. Most importantly, reactive oxygen species management, nitrogen metabolism, phenazine biosynthesis, biofilm formation and pyrimidine metabolism were affected.

(A) Oxidative stress

In aerobic bacteria, the majority of the metabolic energy is supplied via oxidative phosphorylation, which involves reducing molecular oxygen to water. Electrons from the electron transport chain or redox enzymes can reduce O_2 directly, which can progress into the production of reactive oxygen species (ROS), such as superoxide radical (O_2^-), hydrogen peroxide (H_2O_2), and hydroxyl radical. In addition to the ROS generated in the cells, bacteria could get exposed to exogenous ROS as well. ROS could damage the enzymes, DNA, and lipids. Antioxidant enzymes such as catalases, superoxide dismutase, and peroxidases

protect against the generated ROS in the cells. Superoxide dismutase (SOD) converts produced O_2^- radicals into H_2O_2 and O_2. Catalases and peroxidases, disproportionate H_2O_2 to water and O_2.

Table 4-5: Functional importance of other proteins differently affected in the *Δbfd* mutant cells

Protein ID	Name	Function	Iron binding	log_2Fold Change (Δbfd/Wt)
		Oxidative stress related		
PA4468	SodM	SodA Superoxide dismutase	No (Mn)	3.20
PA4366	SodB	Superoxide dismutase	Yes	-0.90
PA4236	KatA	Catalase	Yes	-1.15
PA2147	KatE	Catalase HPII	Yes	-0.91
		Quorum sensing and biofilm formation		
PA0999	PqsD	3-oxoacyl-ACP synthase	No	0.68
PA1000	PqsE	thioesterase PqsE	No	1.06
PA1899	PhzA2	phenazine biosynthesis protein PhzA	No	0.49
PA2587	PqsH	2-heptyl-3-hydroxy-4(1H)-quinolone synthase	No	1.22
PA4209	PhzM	phenazine-specific methyltransferase	No	-0.51
PA2570	LecA	PA-I galactophilic lectin	No	1.12
PA3478	RhlB	rhamnosyltransferase subunit B	No	0.49
		Alkaline protease secretion system		
PA1245	AprX		No	0.75
PA1246	AprD	Alkaline protease secretion protein	No	1.32
PA1247	AprE	Alkaline protease secretion protein	No	1.57
		Respiration		
PA1172	NapC	Cytochrome c-type protein	Yes	-1.34
PA1173	NapB	Cytochrome c-type protein	No	-1.05
PA1174	NapA	Periplasmic nitrate reductase protein	Yes	-1.26
PA1557	ccoN2	cbb3-type cytochrome C oxidase subunit I	Yes	-0.50
PA4133	CcoN	cbb3-type cytochrome C oxidase subunit I	Yes	-0.97
		Pyrimidine metabolism		
PA1155	NrdB*	Tyrosyl radical-harboring component of class IA ribonucleotide reductase	Yes	-0.53
PA1156	NrdA	catalytic component of class Ia ribonucleotide reductase	No	-0.95
		Others		
PA4031	Ppa	Inorganic pyrophosphatase	No	0.65

P. aeruginosa possesses two superoxide dismutases. SodB has iron as the cofactor and SodM has manganese as the co-factor. In the *Δbfd* cells, SodB (log_2FC= -0.90) is under-represented relative to the wild type. Interestingly, the Mn-binding SodM (log_2FC= 3.20) is significantly over-represented. The SodM-Mn containing enzyme's activity is elevated only under an iron starvation condition. A study done by Ghorbal and co-workers revealed the importance of Fe-SOD compared to the Mn-SOD. *P. aeruginosa* cells were exposed to UV-C radiation, and the activities of SodB vs SodM were compared. The overall results

suggest an important protective role played by SodB against the radiation generated ROS [46]. It is evident in the proteomics data that the cells express high levels of SodM to compensate for the loss in SodB.

P. aeruginosa contains three monofunctional heme-containing catalases, KatA, KatB, and KatE. Additionally, another non-heme pseudo catalase (KatN PA218) has also been discovered [47]. KatA is necessary to defend against H_2O_2, and important for virulence and osmoprotection. The activity of KatB cannot fully compensate for the absence of KatA [47]. In the *Δbfd* cells, heme-containing KatA (log_2FC= -1.15) and KatE (log_2FC= -0.91) were under-represented, but the levels of KatN, non-heme catalase (Mn catalase) were not changed. The low abundance of heme catalases generates difficulties in the cells in defending against H_2O_2. High levels of H_2O_2 cause damages to the proteins, lipids, and DNA in the cells.

(B) Quorum sensing and biofilm formation

P. aeruginosa cells contain regulatory networks for the production of secondary metabolites and virulence factors. The intracellular communication network is known as quorum sensing (QS). QS network regulates the gene expression relative to the growth phase, culture density, iron availability *etc*. The QS system consists of three main QS signaling pathways, *las*, *rhl*, and *pqs*. The *las* and *rhl* system uses N-acylhomoserine lactones, and the *pqs* system employs 2-alkyl-4-quinolones (AQs) as QS signal molecules. The QS system mainly depends on the synthesis, secretion, and recognition of the signal molecules, which allows bacteria to operate at the population level.

P. aeruginosa synthesizes more than 50 AQs. Among them, 2-heptyl-3-hydroxy-4-quinolone (*Pseudomonas* Quinolone Signal (PQS)) and its precursor 2-heptyl-4-hydroxyquinoline (HHQ), stand high significance [48]. Most AQs synthesis genes are in the *pqsABCDE* operon, and the operon is under the regulation of PqsR (a transcription factor). PqsR is also induced, in the presence of the sigma factor PvdS (under iron starvation conditions), and Fur-regulated sRNAs, PrrF1, and Prrf2 [49].

Chorismate is the precursor for aromatic amino acid and PQS biosynthesis. In the first step of PQS biosynthesis, chorismate is converted into anthranilate by anthranilate synthase (**Figure 4-14**). Anthranilate

is converted into anthaniloyl-CoA by PqsA (not detected). Next, anthaniloyl-CoA condenses with malonyl-CoA forming 2-aminobenzoylacetyl-CoA (2-ABA-CoA). This reaction is catalyzed by the condensing enzyme PqsD (log_2FC= 0.68).

The thioesterase activity of PqsEs (log_2FC= 1.06) converts 2-ABA-CoA to 2-aminobenzoylacetate (2-ABA). PqsE represses the 2-aminobenzoylacetate (DHQ) formation and supports 2-ABA formation. PqsE also enhances the production of 2,4-dihydroxyquinoline (2-AA). This enzyme plays an important role in balancing the levels of secondary metabolites derived from the AQ biosynthetic pathway [50]. PqsE is known as the "PQS response protein" and is also important in PQS –mediated synthesis of pyocyanin and rhamnolipids. PqsBC (no change) heterodimer condenses 2-ABA and octanoyl-coenzymeA forming HHQ. The produced HHQ is oxidized to PQS by the monooxygenase, PqsH (log_2FC= 1.22).

The enzymes PqsD, PqsE, and PqsH are over-represented in the *Δbfd* mutant cells. In a previous study done by Soldano and co-workers, the *Δbfd,* and the *bfrB*(L68A/E81A) mutant cells overproduced HHQ, PQS, and HQNO [49]. Low cytosolic free iron levels caused by the blockade of the BfrB:Bfd interaction elicited PQS and HHQ biosynthesis approximately ~ 10-fold more than the wild type cells.

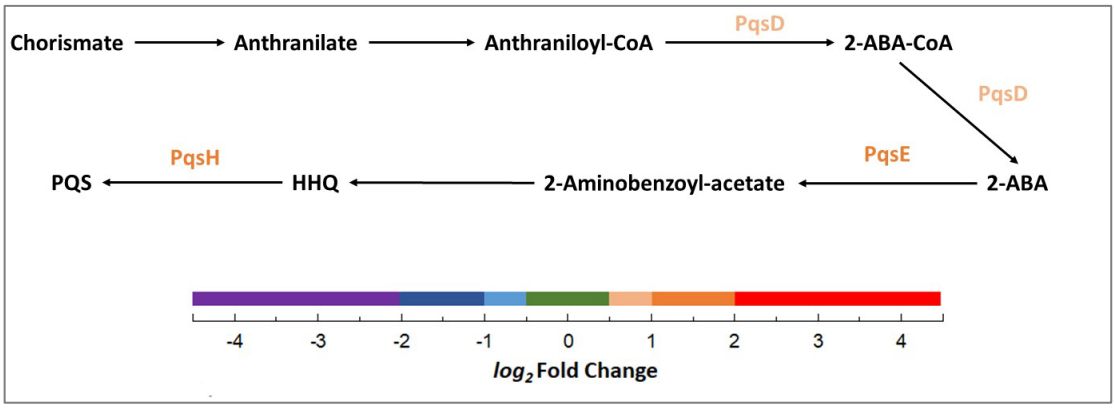

Figure 4-14: The PQS biosynthesis pathway of *P. aeruginosa*. The color scale of protein abundance log_2fold change (*Δbfd*/ wt), is included. (Figure modified from the KEGG pathway: pae02024, Ref.14 and Ref.48)

Which agrees with the over-representation of the PQS and HHQ biosynthesis enzymes in the *Δbfd* mutant cells.

Additionally, iron availability affects the swarming motility and biofilm formation. Rhamnolipid and lectin synthesis is regulated by the *rhl* QS system. Galactophilic lectins, LecA, and LecB are important in biofilm development and cell adhesion [51]. LecA (log_2FC= 1.12) is over-represented in the *Δbfd* mutant cells. In *P. aeruginosa,* rhamnolipids are considered important in defining the structure of biofilms and are normally produced during the late stages of biofilm formation. Under iron limiting conditions rhamnolipids synthesis operon *rhlAB* is induced, and the synthesis could shift to the early stages of biofilms formation, which results in high swarming motility and biofilm dispersal [49, 51]. The *Δbfd* mutant cells secrete about 5- fold more rphamnolipids relative to the wild type cells at 48 h (static growth in PI media supplemented with 20 μM iron) [49]. The *Δbfd* mutant cells exhibit over-represented RhlB (log_2FC= 0.49), which is one of the proteins coded by *rhlAB* operon (RhlA-no change). The proteomics analysis was done by collecting the cells at 30 h, and presumably, in the longer cultures, rhamnolipid synthesis enzymes in the *Δbfd* mutant cells may over-express significantly.

(C) Alkaline proteases

The ability of *P. aeruginosa* to secrete extracellular proteins is one of the major factors related to the virulence. Under iron-rich conditions, the expression of exotoxins and proteases are repressed. Several protein secretion pathways are present in *P. aeruginosa,* and each pathway is dedicated to a protein or a group of proteins. Type III pathway is used for the secretion of exoenzymeS and other regulated proteins. Secretion of degradative enzymes and toxins such as elastases, lipases and exotoxin A are carried out by the type II secretion system [52].

Alkaline proteases (AP) are secreted by a type I system. Membrane proteins AprD, AprE, and AprF are the members of this ABC exporter. AprD (log_2FC= 1.32) is the ATD binding cassette, and AprE (log_2FC= 1.57) and AprF (not detected) are the components in the membrane fusion protein and the outer

membrane protein respectively. The alkaline proteases AprA and AprX (log_2FC= 0.75) are secreted via the AprDEF exporter [52].

The alkaline protease AprA can degrade components in the host immune system, such as cytokines (IFN-ɣ and TNF-α) and complement C1q andC3 [53]. AP secretion is iron-responsive and is regulated by the master iron regulator (Fur). Also, the AP production is promoted in the presence of the iron starvation sigma factor PvdS. AP can proteolytically cleave proteins such as transferrin and released iron for the use of cells [54]. The over-representation of AP related proteins in the *Δbfd* mutant cells is an attempt to overcome the cell's nutritional requirement for iron, amino acids, C and N.

(D) Aerobic respiration

The primary energy production mechanism in *P. aeruginosa* is respiration. Respiration uses the proton motive force for ATP synthesis. About 17 respiration related dehydrogenases are responsible for feeding electrons from the respiratory substrates into the quinone pool. The dehydrogenases include three different types of NADH dehydrogenases and a succinate dehydrogenase (SdhC, log_2FC= -0.57, *p* value =0.15). Sdh is a part of the TCA cycle and the electron transport chain. Sdh catalyzes the oxidation of succinate to fumarate with concomitant reduction of cofactor ubiquinone (CoQ_{10}) to ubiquinol [30]. The heme binding enzyme, SdhC, is under-represented in the *Δbfd* mutant, which disrupts the TCA cycle affecting electron flow into the oxidative phosphorylation.

P. aeruginosa possess a highly branched respiratory chain, terminated via multiple terminal oxidases and denitrification enzymes. Five terminal oxidases catalyze the reduction of O_2 to water. Two of them are quinol oxidases that receive electrons from ubiquinol (cytochrome bo_3 oxidase (Cyo) and the cyanide-insensitive oxidase (CIO)). The other three, cbb_3-1 oxidase (Cbb3-1), cbb_3 -2 oxidase (Cbb3-2), and aa_3 oxidase (Aa3), are cytochrome c oxidases that receive electrons from cytochrome *bc1* and *c*-type cytochromes [55]. In the *Δbfd* mutant, heme-containing cbb_3 type cytochrome c oxidase enzymes $CcoN_2$ (log_2FC= -0.50) and CcoN (log_2FC= -0.97) were under-represented.

The CcoN is coded by the *ccoNOQP* tetracistronuic operon. CcoNs catalytic subunit comprises of a binuclear center, that contains a high spin heme b_3 and a Cu_B. Enzyme CcoN2 is a product of cbb_3 cytochrome oxidase (Cbb3-2) gene *ccoN2O2Q2P2* [55]. The *cco2* genes are over-expressed under low oxygen conditions or during the stationary phase when the oxygen levels are low. The expression of cbb_3 oxidases are critical for respiration under microaerobic conditions [55]. The under-representation of heme-containing respiratory enzymes brings in a disadvantage in energy production to the *Δbfd* mutant cell.

(E) Anaerobic respiration

Nitrate acts as a terminal electron acceptor under anaerobic respiratory conditions. Reducing nitrate to nitrite generates a transmembrane proton motive force that allows ATP synthesis during anaerobic growth. Nitrate reduction in respiration can be mediated by nitrate reductase complexes, NarGHI, and NapAB.

NarGHI (inner membrane-bound) is encoded by the *narK1K2GHJI* operon, and NapAB (periplasmic nitrate reductase) is encoded by the *napEFDABC* operon [56]. NapA (log_2FC= -1.34) is the large subunit in the complex which contains a molybdenum cofactor and a [4Fe-4S cluster]. NapB (log_2FC= -1.05) is a nitrate reductase cytochrome c-type subunit and NapC (log_2FC= -1.26) is a nitrate reductase c-type cytochrome with a heme [57]. The NapAB and NapC are under- resented in the *Δbfd* mutant cells. The low availability of iron reduced the expression levels of iron containing NapA and NapC. The low abundance of these proteins in the *Δbfd* mutant cells may result in difficulties to respire nitrate and nitrite under anaerobic conditions.

(E) Pyrimidine/purine metabolism

P. aeruginosa encodes for three Ribonucleotide Reductase (RNRs) classes (Ia, II and III). These enzymes catalyze the reduction of ribonucleotides to their corresponding deoxyribonucleotides. Deoxyribonucleotides are important for DNA synthesis and repair. Class I RNRs use oxygen to generate a tyrosyl radical with the help of a di-ferric iron or a di-manganese ion center [58]. Class Ia RNRs, NrdA

(log_2FC= -0.95) harbors the active site for substrate binding and iron-binding protein NrdB (log_2FC= -0.53, *p* value=0.052) contains a stable tyrosyl radical to initiate the catalysis [58]. Class Ib RNRs can substitute manganese for iron under iron-deplete conditions [59]. RNRs activity is highly regulated in the cells. An unbalanced level of dNTPs could increase the mutation rate and loose DNA replication reliability [60]. Under-representation of the NrdA and NrdB enzymes in the *Δbfd* mutant cells may affect the DNA synthesis and repair. Also, *Δbfd* mutant cells may face difficulties during cell proliferation, as there is a high requirement for dNTPs for daughter DNA synthesis.

4.4 Conclusions

BfrB is the main iron storage protein in *P. aeruginosa* [1]. Iron mobilization from BfrB requires specific interactions with a ferredoxin, Bfd [2]. I*n-cell* studies with *P. aeruginosa bfd* gene knockout mutant (*Δbfd*) discovered the BfrB:Bfd interaction as the sole mechanism to release iron from BfrB. Blocking the BfrB:Bfd interaction resulted in irreversible accumulation of iron in BfrB and cytosolic iron deprivation. Consequently, the *Δbfd* mutant shows iron starvation responses regardless of the high iron content in the cells [1].

Alterations in iron homeostasis by disrupting the BfrB:Bfd interaction resulted in significant changes in the protein expression and metabolism. When the free iron levels in the cytosol are low, the apo-Fur depresses the iron acquisition systems. Moreover, low iron conditions induce the expression of PrrF small regulatory RNAs that repress the expression of multiple iron-containing proteins. Analysis of the *P. aeruginosa* wild type cells and *Δbfd* mutant cells proteome allowed us to identify 3034 *P. aeruginosa* proteins. Among them, 250 proteins were differentially expressed in the *Δbfd* mutant cells. Metabolic pathway assignments for the differentially regulated proteins permitted to identify some critical changes in the *Δbfd* mutant metabolism.

Iron acquisition-related proteins were significantly over-represented in the *Δbfd* mutant cells. All the enzymes involved in the pyoverdine and pyochelin biosynthesis, and Phu heme iron acquisition were over-represented. Additionally, the *Δbfd* mutant cells secrete alkaline protease in search for extracellular

iron. Pyoverdine synthesis machinery involves about 14 proteins, and it's only triggered under severe iron limiting conditions. The majority of the cell resources are fluxed toward the pyoverdine synthesis. Despite the production cost, the *Δbfd* mutant cells continued to produce siderophores, as iron is a crucial cofactor to drive metabolic functions.

Essential cellular mechanisms, such as the Tricarboxylic acid cycle (TCA), respiratory cycle, amino acid synthesis, and oxidative stress tolerance, rely on iron availability. Iron-containing TCA cycle enzymes, aconitases (AcnA, AcnB, and a probable aconitase - PA0794) succinate dehydrogenase (SdhC), fumarase (FumA), were under-represented in the *Δbfd* mutant cells. The low levels of these essential enzymes disrupt the TCA cycle and affect the energy production. Interestingly, the activity of iron-dependent fumarase FumA is restored by an iron-independent FumC1.

Pyruvate is essential for the TCA cycle and amino acid biosynthesis and is generated by glycolysis and glycine-betaine metabolism. Pyruvate synthesis from the glycine-betaine metabolism was compromised as most of the enzymes in the metabolism path were under-represented. Therefore, *Δbfd* mutant cells block pyruvate consuming pathways such as 2,3-butanone synthesis by down-regulating the butanone metabolism-related proteins.

Glycine is synthesized through the glycine-betaine metabolism path, and 12 enzymes in this pathway were under-represented. Iron-independent CbcX, CbcV, CbcW, DgcA, SoxB, and SoxD enzymes and iron-dependent GbcA, GbcB, SoxA, and SdaB are among the under-represented proteins. The synthesized glycine can be converted into pyruvate, and subsequently used in the TCA cycle and amino acid biosynthesis. Consequently, the disruption of the glycine-betaine metabolism may affect the TCA cycle and amino acid biosynthesis.

Amino acid biosynthesis-related enzymes, LeuD, AcnA, AcnB, SdaB are affected by low iron levels. This results in reduced levels of amino acids, Val, Ile, Leu, Lys, Asp, Gln, Glu, Pro, and Arg in the cell, which affect the protein synthesis and amino acid-related functions. Iron-containing oxidative stress-

managing enzymes KatA, KatE, and SodB are under-represented. The inability to manage reactive oxygen species in the cells could result in damages to DNA, protein, and lipids. Interestingly, the low levels of iron-dependent superoxide dismutase, SodB is compensated by the Mn-dependent SodM.

In the *Δbfd* mutant, *Pseudomonas* Quorum Sensing (PQS) network-related enzymes are over-represented as a result of low cytosolic iron levels [49]. The over-representation of the sulfur assimilation pathway-related proteins indicate an additional need for sulfur in the *Δbfd* mutant. Sulfur is necessary for Fe-S cluster biogenesis and cysteine biosynthesis. The synthesized cysteines are used to produce pyochelin as well, which results in an additional requirement for sulfur in the cell. Moreover, in the *Δbfd* mutant, the fluoroquinolone efflux pump MexEF is under-represented. Reduced expression levels of the MexEF efflux pump under low iron conditions results in enhanced fluoroquinolone susceptibility. This agrees with the potentiation of fluoroquinolones in the presence of the BfrB:Bfd inhibitors [45].

Disrupting the BfrB:Bfd interaction in *P. aeruginosa* uncovered weaknesses in its broader metabolism. Low cytosolic iron levels repressed or maintained a basal expression level for iron harboring enzymes, which affected the iron-independent enzyme regulation as well. Under low iron conditions, cells adapt their metabolism to be driven under sub-optimal levels. These additional weaknesses generated by blocking the BfrB:Bfd interaction in *P. aeruginosa*, make BfrB:Bfd an ideal anti-infective target. Moreover, the sup-optimal metabolism under low cytosolic iron levels generates an additional susceptibility for antibiotics. Also, inhibiting BfrB:Bfd interaction by small molecules may cause similar weaknesses in *P. aeruginosa* cells. Further investigations are necessary to reach this end.

4.5 References

1. Eshelman, K., et al., *Inhibiting the BfrB:Bfd interaction in Pseudomonas aeruginosa causes irreversible iron accumulation in bacterioferritin and iron deficiency in the bacterial cytosol.* Metallomics, 2017. **9**(6): p. 646-659.
2. Yao, H., et al., *The structure of the BfrB-Bfd complex reveals protein-protein interactions enabling iron release from bacterioferritin.* J Am Chem Soc, 2012. **134**(32): p. 13470-81.
3. Reinhart, A.A., et al., *The prrF-encoded small regulatory RNAs are required for iron homeostasis and virulence of Pseudomonas aeruginosa.* Infect Immun, 2015. **83**(3): p. 863-75.
4. Oglesby, A.G., et al., *The influence of iron on Pseudomonas aeruginosa physiology: a regulatory link between iron and quorum sensing.* J Biol Chem, 2008. **283**(23): p. 15558-67.
5. Graves, P.R. and T.A. Haystead, *Molecular biologist's guide to proteomics.* Microbiol Mol Biol Rev, 2002. **66**(1): p. 39-63; table of contents.
6. Ashman, K., G. Rice, and M. Mitchell, *Proteomics Methods*, in *Molecular Pathology in Cancer Research*, S.R. Lakhani and S.B. Fox, Editors. 2016, Springer New York: New York, NY. p. 219-237.
7. Dayon, L. and J.-C. Sanchez, *Relative Protein Quantification by MS/MS Using the Tandem Mass Tag Technology*, in *Quantitative Methods in Proteomics*, K. Marcus, Editor. 2012, Humana Press: Totowa, NJ. p. 115-127.
8. Zhang, L. and J.E. Elias, *Relative Protein Quantification Using Tandem Mass Tag Mass Spectrometry.* Methods Mol Biol, 2017. **1550**: p. 185-198.
9. Pappireddi, N., L. Martin, and M. Wuhr, *A Review on Quantitative Multiplexed Proteomics.* Chembiochem, 2019. **20**(10): p. 1210-1224.
10. Yang, F., et al., *High-pH reversed-phase chromatography with fraction concatenation for 2D proteomic analysis.* Expert Rev Proteomics, 2012. **9**(2): p. 129-34.
11. Yue, X. and J.J. Guidry, *Differential Protein Expression Profiles of Bronchoalveolar Lavage Fluid Following Lipopolysaccharide-Induced Direct and Indirect Lung Injury in Mice.* Int J Mol Sci, 2019. **20**(14).
12. Winsor, G.L., et al., *Enhanced annotations and features for comparing thousands of Pseudomonas genomes in the Pseudomonas genome database.* Nucleic Acids Res, 2016. **44**(D1): p. D646-53.
13. King, C.D., et al., *Dataset of proteomics analysis of aging C. elegans exposed to Pseudomonas aeruginosa strain PA01.* Data Brief, 2017. **11**: p. 245-251.
14. Kanehisa, M. and Y. Sato, *KEGG Mapper for inferring cellular functions from protein sequences.* Protein Sci, 2020. **29**(1): p. 28-35.
15. Labaer, J., et al., *The Pseudomonas aeruginosa PA01 gene collection.* Genome Res, 2004. **14**(10B): p. 2190-200.
16. Hannauer, M., et al., *Biosynthesis of the pyoverdine siderophore of Pseudomonas aeruginosa involves precursors with a myristic or a myristoleic acid chain.* FEBS Lett, 2012. **586**(1): p. 96-101.
17. Schalk, I.J. and L. Guillon, *Pyoverdine biosynthesis and secretion in Pseudomonas aeruginosa: implications for metal homeostasis.* Environ Microbiol, 2013. **15**(6): p. 1661-73.
18. Vandenende, C.S., M. Vlasschaert, and S.Y. Seah, *Functional characterization of an aminotransferase required for pyoverdine siderophore biosynthesis in Pseudomonas aeruginosa PAO1.* J Bacteriol, 2004. **186**(17): p. 5596-602.
19. Suzuki, T., et al., *Role of pvdE Pyoverdine Synthesis in Pseudomonas aeruginosa Keratitis.* Cornea, 2018. **37 Suppl 1**: p. S99-S105.
20. Ringel, M.T. and T. Bruser, *The biosynthesis of pyoverdines.* Microb Cell, 2018. **5**(10): p. 424-437.
21. Ringel, M.T., G. Drager, and T. Bruser, *PvdN Enzyme Catalyzes a Periplasmic Pyoverdine Modification.* J Biol Chem, 2016. **291**(46): p. 23929-23938.
22. Adams, H., et al., *Interaction of TonB with the outer membrane receptor FpvA of Pseudomonas aeruginosa.* J Bacteriol, 2006. **188**(16): p. 5752-61.

23. Dumas, Z., A. Ross-Gillespie, and R. Kummerli, *Switching between apparently redundant iron-uptake mechanisms benefits bacteria in changeable environments.* Proc Biol Sci, 2013. **280**(1764): p. 20131055.
24. Serino, L., et al., *Biosynthesis of pyochelin and dihydroaeruginoic acid requires the iron-regulated pchDCBA operon in Pseudomonas aeruginosa.* J Bacteriol, 1997. **179**(1): p. 248-57.
25. Ronnebaum, T.A. and A.L. Lamb, *Nonribosomal peptides for iron acquisition: pyochelin biosynthesis as a case study.* Curr Opin Struct Biol, 2018. **53**: p. 1-11.
26. Tong, Y. and M. Guo, *Bacterial heme-transport proteins and their heme-coordination modes.* Arch Biochem Biophys, 2009. **481**(1): p. 1-15.
27. Mourino, S., et al., *Metabolite-driven Regulation of Heme Uptake by the Biliverdin IXbeta/delta-Selective Heme Oxygenase (HemO) of Pseudomonas aeruginosa.* J Biol Chem, 2016. **291**(39): p. 20503-15.
28. Cornelis, P. and J. Dingemans, *Pseudomonas aeruginosa adapts its iron uptake strategies in function of the type of infections.* Front Cell Infect Microbiol, 2013. **3**: p. 75.
29. Lee, S.A., et al., *General and condition-specific essential functions of Pseudomonas aeruginosa.* Proc Natl Acad Sci U S A, 2015. **112**(16): p. 5189-94.
30. Keohane, C.E., et al., *Promysalin Elicits Species-Selective Inhibition of Pseudomonas aeruginosa by Targeting Succinate Dehydrogenase.* J Am Chem Soc, 2018. **140**(5): p. 1774-1782.
31. Shapiro, J.A., A.R. Kaplan, and W.M. Wuest, *From General to Specific: Can Pseudomonas Primary Metabolism Be Exploited for Narrow-Spectrum Antibiotics?* Chembiochem, 2019. **20**(1): p. 34-39.
32. Nelson, C.E., et al., *Proteomic Analysis of the Pseudomonas aeruginosa Iron Starvation Response Reveals PrrF Small Regulatory RNA-Dependent Iron Regulation of Twitching Motility, Amino Acid Metabolism, and Zinc Homeostasis Proteins.* J Bacteriol, 2019. **201**(12).
33. Hassett, D.J., et al., *Fumarase C activity is elevated in response to iron deprivation and in mucoid, alginate-producing Pseudomonas aeruginosa: cloning and characterization of fumC and purification of native fumC.* J Bacteriol, 1997. **179**(5): p. 1442-51.
34. Liu, Q., et al., *2,3-Butanediol catabolism in Pseudomonas aeruginosa PAO1.* Environ Microbiol, 2018. **20**(11): p. 3927-3940.
35. Akashi, H. and T. Gojobori, *Metabolic efficiency and amino acid composition in the proteomes of Escherichia coli and Bacillus subtilis.* Proc Natl Acad Sci U S A, 2002. **99**(6): p. 3695-700.
36. Wargo, M.J., *Homeostasis and catabolism of choline and glycine betaine: lessons from Pseudomonas aeruginosa.* Appl Environ Microbiol, 2013. **79**(7): p. 2112-20.
37. Wargo, M.J., B.S. Szwergold, and D.A. Hogan, *Identification of two gene clusters and a transcriptional regulator required for Pseudomonas aeruginosa glycine betaine catabolism.* J Bacteriol, 2008. **190**(8): p. 2690-9.
38. Willsey, G.G. and M.J. Wargo, *Sarcosine Catabolism in Pseudomonas aeruginosa Is Transcriptionally Regulated by SouR.* J Bacteriol, 2016. **198**(2): p. 301-10.
39. Hummerjohann, J., et al., *Regulation of the sulfate starvation response in Pseudomonas aeruginosa: role of cysteine biosynthetic intermediates.* Microbiology, 1998. **144 (Pt 5)**: p. 1375-86.
40. Guédon, E. and I. Martin-Verstraete, *Cysteine Metabolism and Its Regulation in Bacteria*, in *Amino Acid Biosynthesis ~ Pathways, Regulation and Metabolic Engineering*, V.F. Wendisch, Editor. 2007, Springer Berlin Heidelberg: Berlin, Heidelberg. p. 195-218.
41. Llanes, C., et al., *Role of the MexEF-OprN efflux system in low-level resistance of Pseudomonas aeruginosa to ciprofloxacin.* Antimicrob Agents Chemother, 2011. **55**(12): p. 5676-84.
42. Uwate, M., et al., *Two routes of MexS-MexT-mediated regulation of MexEF-OprN and MexAB-OprM efflux pump expression in Pseudomonas aeruginosa.* Microbiol Immunol, 2013. **57**(4): p. 263-72.

43. Fetar, H., et al., *mexEF-oprN multidrug efflux operon of Pseudomonas aeruginosa: regulation by the MexT activator in response to nitrosative stress and chloramphenicol.* Antimicrob Agents Chemother, 2011. **55**(2): p. 508-14.
44. Peng, J., et al., *Pseudomonas aeruginosa develops Ciprofloxacin resistance from low to high level with distinctive proteome changes.* J Proteomics, 2017. **152**: p. 75-87.
45. Punchi Hewage, A.N.D., et al., *Small Molecule Inhibitors of the BfrB-Bfd Interaction Decrease Pseudomonas aeruginosa Fitness and Potentiate Fluoroquinolone Activity.* J Am Chem Soc, 2019. **141**(20): p. 8171-8184.
46. Ghorbal, S.K., et al., *Antioxidant Defense Mechanisms in Pseudomonas aeruginosa: Role of Iron-Cofactored Superoxide Dismutase in Response to UV-C Radiations.* Curr Microbiol, 2016. **73**(2): p. 159-64.
47. Lee, J.S., et al., *KatA, the major catalase, is critical for osmoprotection and virulence in Pseudomonas aeruginosa PA14.* Infect Immun, 2005. **73**(7): p. 4399-403.
48. Rampioni, G., et al., *Unravelling the Genome-Wide Contributions of Specific 2-Alkyl-4-Quinolones and PqsE to Quorum Sensing in Pseudomonas aeruginosa.* PLoS Pathog, 2016. **12**(11): p. e1006029.
49. Soldano, A., et al., *Inhibiting Iron Mobilization from Bacterioferritin in Pseudomonas aeruginosa Impairs Biofilm Formation Irrespective of Environmental Iron Availability.* ACS Infect Dis, 2020.
50. Drees, S.L. and S. Fetzner, *PqsE of Pseudomonas aeruginosa Acts as Pathway-Specific Thioesterase in the Biosynthesis of Alkylquinolone Signaling Molecules.* Chem Biol, 2015. **22**(5): p. 611-8.
51. Rasamiravaka, T., et al., *The formation of biofilms by Pseudomonas aeruginosa: a review of the natural and synthetic compounds interfering with control mechanisms.* Biomed Res Int, 2015. **2015**: p. 759348.
52. Duong, F., et al., *The AprX protein of Pseudomonas aeruginosa: a new substrate for the Apr type I secretion system.* Gene, 2001. **262**(1-2): p. 147-53.
53. Laarman, A.J., et al., *Pseudomonas aeruginosa alkaline protease blocks complement activation via the classical and lectin pathways.* J Immunol, 2012. **188**(1): p. 386-93.
54. Shigematsu, T., et al., *Iron-Mediated regulation of alkaline proteinase production in Pseudomonas aeruginosa.* Microbiol Immunol, 2001. **45**(8): p. 579-90.
55. Arai, H., *Regulation and Function of Versatile Aerobic and Anaerobic Respiratory Metabolism in Pseudomonas aeruginosa.* Front Microbiol, 2011. **2**: p. 103.
56. Van Alst, N.E., et al., *Compensatory periplasmic nitrate reductase activity supports anaerobic growth of Pseudomonas aeruginosa PAO1 in the absence of membrane nitrate reductase.* Can J Microbiol, 2009. **55**(10): p. 1133-44.
57. Bedzyk, L., T. Wang, and R.W. Ye, *The periplasmic nitrate reductase in Pseudomonas sp. strain G-179 catalyzes the first step of denitrification.* J Bacteriol, 1999. **181**(9): p. 2802-6.
58. Torrents, E., et al., *Ribonucleotide reductase modularity: Atypical duplication of the ATP-cone domain in Pseudomonas aeruginosa.* J Biol Chem, 2006. **281**(35): p. 25287-96.
59. Torrents, E., *Ribonucleotide reductases: essential enzymes for bacterial life.* Front Cell Infect Microbiol, 2014. **4**: p. 52.
60. Ahluwalia, D., R.J. Bienstock, and R.M. Schaaper, *Novel mutator mutants of E. coli nrdAB ribonucleotide reductase: insight into allosteric regulation and control of mutation rates.* DNA repair, 2012. **11**(5): p. 480-487.

Chapter 5 : Purification of recombinant topoisomerase IA from *P. aeruginosa*

5.1 Introduction

5.1.1 Topoisomerase IA enzymes

DNA topoisomerases are classical enzymes that help cells to solve DNA topological problems occurred during replication, transcription, and recombination. The importance of topoisomerase arises because of the double-helical structure of DNA. The double helices need to be unwound during transcription and replication, and topoisomerases introduce single or double strandard breaks into the DNA. Upon breaking a strand, a part of the broken strand forms a temporary covalent phosphodiester bond with the enzyme, and topology changes are introduced when the intact DNA strand passes through the break. This mechanism relieves intertwined parental DNA during replication, unlink catenated (interlocked) double strandard DNA, and introduce or remove knots to DNA [1].

DNA topoisomerases are divided into two categories, type I and type II. These two types can be further grouped into four subfamilies: IA, IB, IIA, and IIB. Type I enzymes break a single DNA strand at a time. On the other hand, in type II enzymes, a pair of DNA strands in the double helix is transiently broken [2]. The difference between type IA and IB is the binding position of protein to DNA; the type IA binds to the 5' phosphate, whereas type IB binds to the 3' phosphate. In *E. coli*, all four DNA topoisomerases are identified, type IA enzymes: DNA topoisomerase I and III, and the type IIA enzymes: DNA gyrase and topoisomerase IV. Each of these proteins carries out a function related to DNA topology [3].

DNA topoisomerase IA catalyzes the relaxation of negatively supercoiled DNA. The energy of enzyme binding is sufficient to melt the DNA duplex locally and to introduce a single strandard break. The majority of type IA proteins bind to a pre-existing single strandard DNA. The type IA enzymes can also facilitate catenation (linking) and decatenation (unlinking) reactions of double strandard DNA [3]. As explained above, the enzyme introduces a nick into one of the DNA strands, then adds a temporary break in the opposite strand to unknot the DNA.

5.1.2 Structure and function relationships in topoisomerase IA

When DNA topoisomerase IA nicks a single strand DNA, the 5' phosphate interacts covalently with the tyrosine residue at the active site, whereas the 3' end interacts with the protein non covalently. The activity of the topoisomerase IA requires the presence of Mg^{2+} ions for the positioning of the 3' end of the cleaved DNA in the catalytic site. Once the DNA is nicked and the complementary strand passed through the cleft, supercoils get relaxed, and the enzyme cavity moves to the closed position. The nicked DNA strand is ligated and released by opening the cavity again [3].

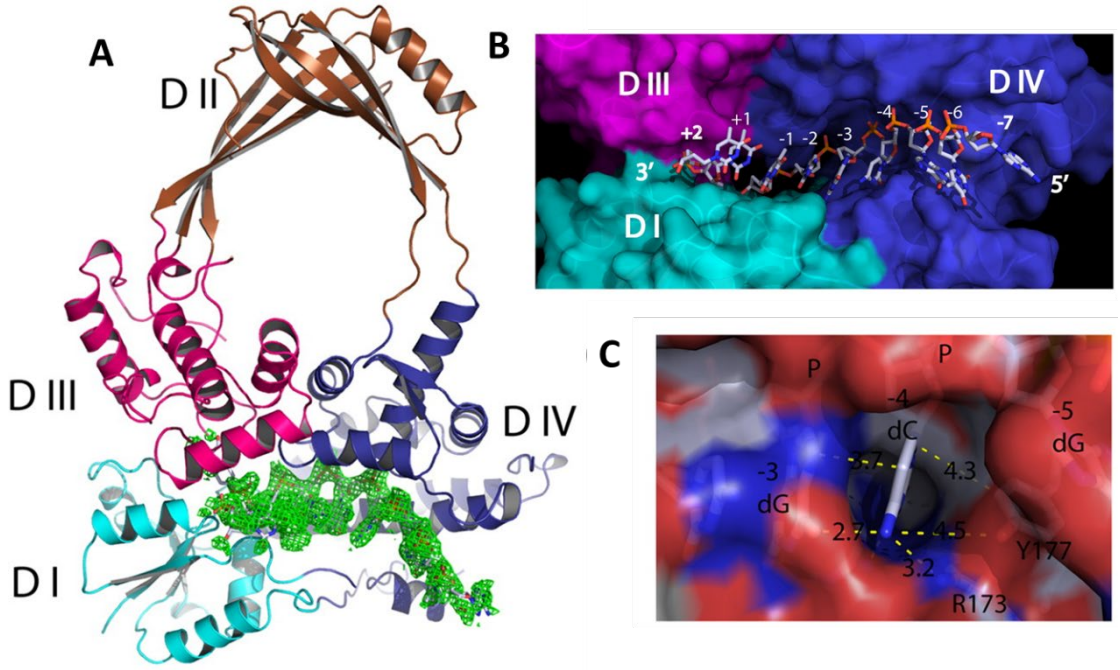

Figure 5-1: A) The structure of *E. coli* Top I 67 kDa N-transesterification domain (residues 1-695, mutant D111N, PDB ID: 3PX7). The four domains are represented in different colors. (B) A representation of the DNA binding groove in surface rendering mode. The cleavage site is on the border between domain III and IV. (C) The side chain of Y177 wedges between the -4 and -5 bases forming π interactions. (Figures are reprinted with permission from Ref. 4)

The X-ray crystal structure of *E. coli* topoisomerase IA catalytic domain (residues 2-695) with a covalent DNA intermediate **Figure 5-1** [4]. The catalytic residue, Tyr319, makes a covalent bond with the DNA fragment. The oligonucleotide 5' to the catalytic site is buried in a deep groove formed by domains

I, III, and IV. The phosphate groups bind toward the deep end of the groove *via* hydrogen bonds and salt bridges. The phosphate that interacts with the catalytic Tyr is defined as the +1 base, and the phosphate groups toward the 5' are defined as -1, -2, -3, *etc*. The phosphate groups toward the 3' from the catalytic (+1) site are defined as +2, +3, +4, *etc*. The phosphate groups, +1, -1, -2, and -4 are held in position by R321, R493, R195, and R507 [4]. The R195 and R321 have identified to be essential for DNA cleavage in *E. coli* by mutagenesis. The ionic and hydrogen bonds of E115, R168, and D172 with the deoxyribose oxygens hold the DNA strand in place [4].

Bacterial topoisomerase I and II have a specific DNA cleavage selectivity. Top I has been shown to cleave DNA when there is a cytosine 4 bases 5' the Tyr cleavage site. The X-ray crystal structure of *E. coli* catalytic domain with DNA shows a distinguishable twist between the -4 and -5 position in the DNA chain. The Y177 forms a wedge between the cytosine (-4) and guanine (-5). The specific twist and Y177 form a sterically restrictive cavity in the protein, where only a cytosine can be accommodated at the -4 position [4]. A similar observation was made in the X-ray crystal structure of *Mycobacterium tuberculosis*

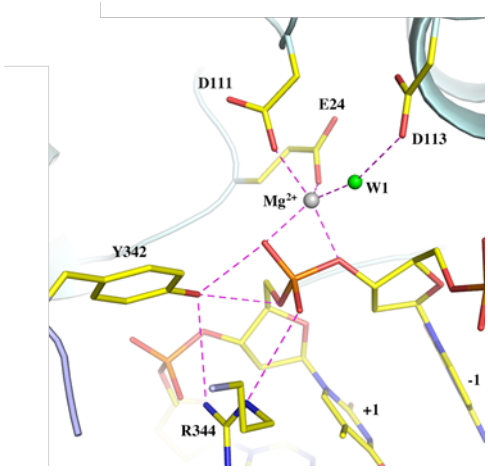

Figure 5-2: The Mg^{2+} binding site of the of *M. tuberculosis* Top I, TopMtTOP1-704t/MTS2-13/Mg (PDB code: 6CQ2). The Mg^{2+} is coordinated by two phosphate oxygens, E24, D111 and water (W1) forming a distorted octahedron with one ligand missing. (Figure is reprinted with permission from Ref.5)

topoisomerase I with single strand DNA. In this structure, the unique twist between the -4 and -5 positions and the side chain of Y176 generated the specificity for cytosine at the -4 position [5].

The acidic residues (acidic triad) DxDxE in the catalytic domain of the *E. coli* Top I is known to participate in the coordination of divalent metal ions to help hold the scissile bond in position for cleavage. The X-ray crystal structure of the *M. tuberculosis*, MTS2-13 (PDB ID:6CQ2) revealed Mg^{2+} binding at the active site of Top I. A Mg^{2+} ion is coordinated by E24, D111, a water molecule (W1), and two oxygens from phosphate. The Mg^{2+} coordination formed a distorted octahedral geometry with one ligand missing [5].

In addition to the N-terminal transesterification domain (residues 1-695), the C-terminal domain of the Top I is essential for the removal of the negative supercoils. Topoisomerases of *E. coli* and eukaryotes have three or more tetracysteine Zn-binding motifs in the C-terminal and is predicted to be a part of the 4-Cys zinc ribbon domains. Mutations in the Zn coordination cysteine residues or the removal of Zn(II) from the protein resulted in a loss of enzyme activity [6]. Also, the C-terminal domain is essential for interacting with RNA polymerase β-subunit during transcription elongation. The full-length *E. coli* Top I structure bound to single-stranded DNA (ssDNA) provides significant structural insights about the C-terminal domain [7]. Among the 4-Cys zinc ribbon domains, none of the three Zn(II) binding sites directly interact with ssDNA. The metal binding site at the top of each Zn ribbon domain supports the stabilization of the fold and help to maintain a suitable conformation for the association and dissociation of ssDNA [7].

P. aeruginosa is a Gram-negative pathogen and one of the significant causes of hospital-acquired infections. In World Health Organizations' (WHO) report on the prioritization of pathogens to guide new antibiotics development, *P. aeruginosa* is identified as a critical priority pathogen [8]. *P. aeruginosa* is intrinsically resistant to many antibiotics and expresses an array of efflux pumps limiting the access of antibiotics to their targets. Currently, a wide range of novel antibiotic targets is being studied. These potential targets are associated with vital functions for the survival of cells, such as essential amino acid biosynthesis, siderophore biosynthesis, quorum sensing metabolism, and cell wall lipid synthesis [9].

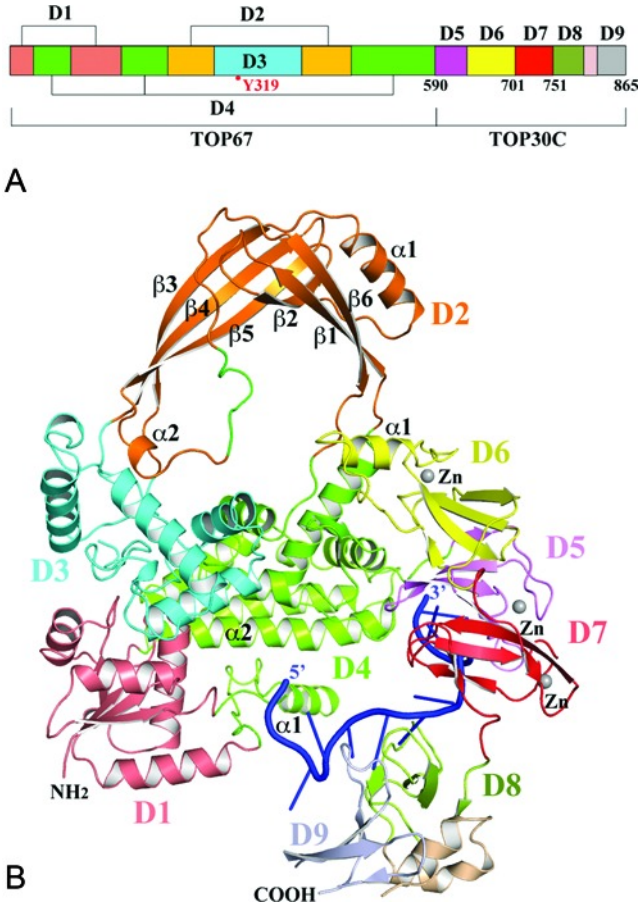

Figure 5-3: (A) The domain arrangement of Top I is represented in different colors. (B)*E. coli* topoisomerase I, full length structure complexed with single stranded DNA (ssDNA), PDB ID: 4RUL. (Figure is reprinted with permission from Ref.7)

Topoisomerase II (Gyrase) is an essential enzyme to maintain DNA topology during DNA replication, transcription, and recombination, and is the main target of fluoroquinolones. Topoisomerase IA is also involved in crucial DNA topology related functions. Several approaches are being taken so far to develop inhibitors for this protein, and Top I has been recently validated as a potential antitubercular target [10, 11]. Therefore, Top IA of *P. aeruginosa* may have potential therapeutic value for anti-infective development. The first step in inhibitor development is the structural and functional characterization of the target. In this chapter, the development of purification protocols, and biochemical characterization of Top IA of *P. aeruginosa* is discussed.

5.2 Experimental

5.2.1 Cloning and purification of His-tagged *P. aeruginosa* Top IA

The gene encoding *P. aeruginosa* Top IA (PA3011) was engineered, introducing codons favored by *E. coli,* and with *Nde I* and *BamH I* restriction sites at the 5' and 3' ends respectively (GeneScript Corp., Piscataway, NJ). Cloning the construct in *Nde I* and *BamH I* site of the pET-28a(+)-TEV vector adds a hexa-His tag coupled to the Tobacco Etch Virus (TEV) protease identification site to the N-terminus of the expressed protein. The subcloned pET-28a(+)-TEV vector was transformed into *E. coli* BL21-Gold (DE3) competent cells (Agilent).

A single colony from the BL21- Gold (DE3) cells harboring the recombinant pET11a/ *top IA* was cultured overnight at 37 ^{0}C in 50 mL LB medium supplemented with 100 µg/mL ampicillin. The pre-cultures were transferred to 1 L of LB media without antibiotic supplementation and grown at 37 ^{0}C. When the optical density, OD_{600} is 0.7, the protein expression was induced by the addition of 1 mM isopropyl 1-thiol-D-galactopyranose (IPTG). Cells were allowed to grow for 3 h at 37 ^{0}C, harvested by centrifugation (4500 rpm for 10 min at 10 ^{0}C), and stored at -80 ^{0}C.

The cell pellet was resuspended in 50 mL of buffer A. Buffer A contained 20 mM potassium phosphate pH 7.4, 300 mM NaCl, 10 % Glycerol, 5 mM tris(2-carboxyethyl)phosphine TCEP. Buffer A was supplemented with 1 mg/mL lysozyme and 1 protease inhibitor tablet (Pierce). The cell suspension was exposed to two freeze- thaw cycles, and the cells were lysed at room temperature for 60 min. Cell debris was removed by centrifugation (19,000 rpm, 1 h at 4 ^{0}C). Lysate was loaded into a Ni Sepharose 6 Fast Flow column (5 mL, GE Healthcare Life Sciences) equilibrated with buffer A. The column was washed with 10 column volumes of buffer A, 10 column volumes of buffer A supplemented with 20 mM imidazole and 4 column volumes of buffer A supplemented with 40 mM imidazole to remove non-specifically binding proteins. The affinity bound protein was eluted by 6 column volumes of buffer A supplemented with 350 mM imidazole. The eluant was concentrated and exchanged to buffer B (buffer A with 150 mM NaCl

instead of 300 mM NaCl) by Amicon Ultra centrifugal filter units (50 k cut-off). Pooled protein was mixed with TEV protease at a 1:10 protease to protein ratio and incubated at 4 ^{0}C for 16 h.

The protein TEV mixture was loaded again into the Ni Sepharose 6 Fast Flow column equilibrated with buffer B. The column was washed with 5 column volumes of buffer B. The eluted proteins were loaded into a Bio-Scale Mini CHT ceramic hydroxyapatite cartridges (5 mL, Bio-Rad). The column was washed with 10 column volumes of buffer B. Bound protein was eluted using a 20-400 mM potassium phosphate (pH 7.4) gradient in buffer B. Pure fractions were concentrated and buffer exchanged (buffer B) by Amicon Ultra centrifugal filter units (50 k cut-off). Proteins were aliquoted and frozen at -80 ^{0}C.

5.2.2 Cloning and purification of non-tagged *P. aeruginosa* Top IA

The gene encoding *P. aeruginosa* Top IA (PA3011) was engineered, introducing codons favored by *E. coli* and with the *Nde I* and *BamH I* restriction sites at the 5' and 3' ends respectively (GeneScript Corp., Piscataway, NJ). The engineered gene was subcloned into pET 11a vector and transformed into *E. coli* ArcticExpress (DE3) Competent Cells (Agilent).

A single colony from the ArcticExpress (DE3) competent cells harboring the recombinant pET11a/ *top IA* was cultured overnight at 37 ^{0}C in 50 mL LB medium supplemented with 100 µg/mL ampicillin and 20 µg/mL gentamycin. The pre-cultures were transferred into 1 L of LB media without antibiotic supplementation and grown at 37 ^{0}C until the optical density, OD_{600} is 0.7. The temperature was lowered to 10 ^{0}C, and the cultures were allowed to equilibrate for 1 h at low temperature before induction. Protein expression was induced by the addition of 1 mM IPTG. Cells were allowed to grow for 24 h at 10 ^{0}C, harvested by centrifugation (4500 rpm for 10 min at 10 ^{0}C), and stored at -80 ^{0}C.

The cell pellet was resuspended in 100 mL of buffer C. Buffer C contained 50 mM Tris-Base pH 7.5, 150 mM KCl, 10 % Glycerol, 20 mM β-mercaptoethanol, 1 mM phenylmethylsulfonyl fluoride (PMSF) and 1 mM Ethylenediaminetetraacetic acid (EDTA). Buffer C was supplemented with 1 mg/mL lysozyme for cell lysis. Cells were allowed to lyse at room temperature for 60 min. The cell suspension was

exposed to two freeze- thaw cycles to improve cell lysis. Cell debris was removed by centrifugation (19,000 rpm, 1 h at 4 ^{0}C). The lysate was subjected to the $(NH_4)_2SO_4$ precipitation. Lysate (100 mL) was mixed with $(NH_4)_2SO_4$ until 40 % (1 M) saturation is reached. The resultant supernatant was loaded into a phenyl sepharose column (20 mL, GE Healthcare Life Sciences) equilibrated with 50 mM Tris-Base pH 7.5, 1 M $(NH_4)_2SO_4$, 10 % Glycerol, 20 mM β-mercaptoethanol and 0.5 mM EDTA. The column was washed with 50 mL of the same buffer, and protein was eluted by a gradient made by lowering the $(NH_4)_2SO_4$ concentration to 500 mM (a 300 mL gradient).

Top IA containing fractions were pooled, and the buffer was exchanged to 50 mM Tris-Base pH 7.5, 175 mM KCl, 10 % Glycerol, 20 mM β-mercaptoethanol and 0.5 mM EDTA by Amicon centrifugal filters (50 k cut-off). Pooled protein samples were loaded to an SP-sepharose column (20 mL, Sigma-Aldrich) equilibrated with the same buffer. The column was washed with 50 mL of buffer, and proteins were eluted by a 300 mL of 175-500 mM KCl gradient. Selected fractions from the eluate were loaded into a Hydroxyapatite column (20 mL, Bio-Rad) equilibrated with 50 mM potassium phosphate pH 7.4, 150 mM KCl, and 10 % Glycerol. The column was washed with 50 mL of buffer, and the proteins were eluted by a 300 mL 50- 250 mM phosphate gradient. Pure protein-containing fractions were pooled, and the buffer was exchanged to 50 mM Tris-Base pH 7.5, 200 mM KCl, 10 % Glycerol, 5 mM TCEP. Concentrated protein was aliquoted and frozen at -80 ^{0}C.

5.2.3 DNA relaxation assay

The relaxation activity of the purified protein was measured as follows. The total volume of the reaction mixture was maintained at 15 µL. Reaction was carried out in the relaxation buffer, 10 mM Tris-HCl (pH 8.0), 50 mM NaCl, and 6 mM $MgCl_2$. Supercoiled, pUC 18 DNA ~600 ng was mixed with different concentrations of Top IA (5, 10, 20, 40, 80 nM). Samples were incubated at 37 ^{0}C for 30 min. The reaction was quenched by adding 1 µL of 2% SDS. Samples were mixed with 4 µL of DNA loading dye (30% (v/v) glycerol, 0.25% (w/v) bromophenol blue) and loaded into a 1 % agarose gel in 1X TAE buffer (1L of 50X TAE buffer contains: Tris base 242 g, disodium EDTA 18.61 g, glacial acetic acid 57.1 ml). Samples were

electrophoretically separated at 100 V. Once the run was complete, the gel was stained with 0.02 % ethidium bromide for 15 min and imaged under UV light.

5.2.4 Analysis of zinc in Top IA

The Zn content in Top IA was analyzed colorimetrically by using the metallochromic indicator 4-(2-pyridylazo) resorcinol (PAR). PAR solution (0.23 mM) was prepared by dissolving 2.5 mg of reagent in 20 mM Tris-Base pH 7.4 and 0.2 M NaCl. A 1 mM Zn^{2+} stock in Tris buffer was prepared using $ZnCl_2$. An appropriate volume (see **table 5-1**) from the Zn^{2+} stock was pipetted to make 1 mL of 6 different Zn^{2+} standards, 1, 2, 4, 6, and 8 µM. A volume of 0.5 mL of the PAR reagent was added to all the solutions. Finally, a volume of 0.25 mL H_2O_2 (30 % stock) was added, and the samples were incubated for 10 min at room temperature. The absorbance at 500 nm was measured. A similar procedure was used to determine Zn concentration in Top IA. Top IA and reagents were mixed following the volumes indicated in **table 5-1**. Four different protein concentrations were used. Upon the addition of H_2O_2, absorbance at 500 nm was read every 30 s. The stoichiometric ratio of the Top IA: Zn was calculated.

Table 5-1: The volumes required for the PAR assay for Zn analysis

Zn^{2+} concentration (µM)	Volume of the 100 µM $ZnCl_2$ stock (µL)	Volume of the 0.23 mM PAR solution (µL)	Volume of the 30 % H_2O_2 stock (µL)	Volume of the buffer (µL)
1	10	500	250	240
2	20	500	250	230
4	40	500	250	210
5	50	500	250	200
6	60	500	250	190
8	80	500	250	170
Protein concentration (µM)	**Volume of the protein (µL)**	**Volume of the 0.23 mM PAR solution (µL)**	**Volume of the 30 % H_2O_2 stock (µL)**	**Volume of the buffer (µL)**
0.54	100	500	250	150
0.68	125	500	250	125
0.81	150	500	250	100
1.0	200	500	250	50

5.2.5 Gel-shift assays

DNA sequence preference by Top IA was tested using a Native-polyacrylamide gel (Native-PAGE) shift assay. Single strandard DNA with varying lengths and sequences were mixed with protein in a DNA to protein mole ratio of 1:1, 1:2 and 2:1 in 10 mM Tris-HCl (pH 8.0), 50 mM NaCl, and 6 mM $MgCl_2$ buffer (Single strandard DNA (54 pmol) and protein (27 pmol or 54 pmol)). DNA- protein mixtures were incubated at room temperature for 1 h. The complexes were loaded into a 7% Native-PAGE and separated electrophoretically at 200 V. Gels were first stained with 0.02 % ethidium bromide to detect unbound DNA and DNA-protein complex. Gels were secondly stained with coomassie-brilliant blue to detect proteins.

5.3 Results and Discussion

5.3.1 Topoisomerase IA from *P. aeruginosa*

Topoisomerase IA (Top IA) of *P. aeruginosa* is coded by gene *topA* (locus tag: PA3011), and the protein contains 868 amino acids resulting in a molecular weight of 97.28 kDa. The calculated isoelectric point is 8.7, and the computed molar absorption coefficient (Ɛ) at 280 nm is 91680 M^{-1} cm^{-1} (Assuming all the cysteines are reduced). The measured molar absorption coefficient (Ɛ) of Top IA is 126.6 ± 1.8 M^{-1} cm^{-1}.

Structure of the *P. aeruginosa* Top IA was predicted using I-TASSER (Iterative Threading ASSEmbly Refinement). I-TASSER is a bioinformatic tool for predicting 3D models from the amino acid sequence. It identifies the templates from the Protein Data Bank (PDB) using a technique called threading, and the complete structures are modeled by re-assembling structural fragments from threading templates [12].

The predicted Top IA model with the highest C-score (1.21) is shown in **Figure 5-4**. C-score is given by I-TASSER as an estimate for the quality of the predicted model. The C-scores are in the range of -5 to 2.

Figure 5-4: The predicted model of *P. aeruginosa* Topoisomerase IA by I-TASSER (C-score 1.21). The N-terminal catalytic domain is presented in green, and the C-terminal domain is presented in orange.

5.3.2 Top IA expression and purification

Methods were developed to purify Top IA with a His-tag and without a tag. Purification of the Top IA without a tag involves a series of steps. Once the cell debris was removed, a $(NH_4)_2SO_4$ precipitation was carried out. The lysate was exposed to 40% $(NH_4)_2SO_4$ saturation; Top IA does not precipitate at this saturation level. Top IA containing supernatant was separated via an aromatic hydrophobic interaction chromatographic step (phenyl sepharose resin). The high salt concentration results in a "salting out" effect in the proteins, and the proteins are bound hydrophobically to the ligands on the resin. Proteins were eluted from the phenyl sepharose column by lowering the $(NH_4)_2SO_4$ concentration. Top IA collected from the eluate of phenyl sepharose still contained a significant amount of *E.coli* protein impurities. Selected Top IA containing fractions were loaded into a cation exchange column (SP-sepharose). The cation exchange step allowed us to collect proteins with 80% purity. Next, Top IA was further purified by a hydroxyapatite column. Hydroxyapatite (HA) contains two types of binding sites, positively charged calcium ions, and negatively charged phosphate groups. These sites are distributed homogenously on the HA matrix. Cation exchange occurs when the amino groups of the protein interact with the phosphate groups of the resign, and

at the same time, the amine groups are repelled by the calcium ions disturbing the ionic interaction. Therefore, binding into HA is a combined effect, and the binding can be weakened by adding neutral salts (NaCl) or buffering species (phosphate). The HA abound Top IA was eluted via a phosphate gradient. The eluant from the HA column contained 95 % pure Top IA.

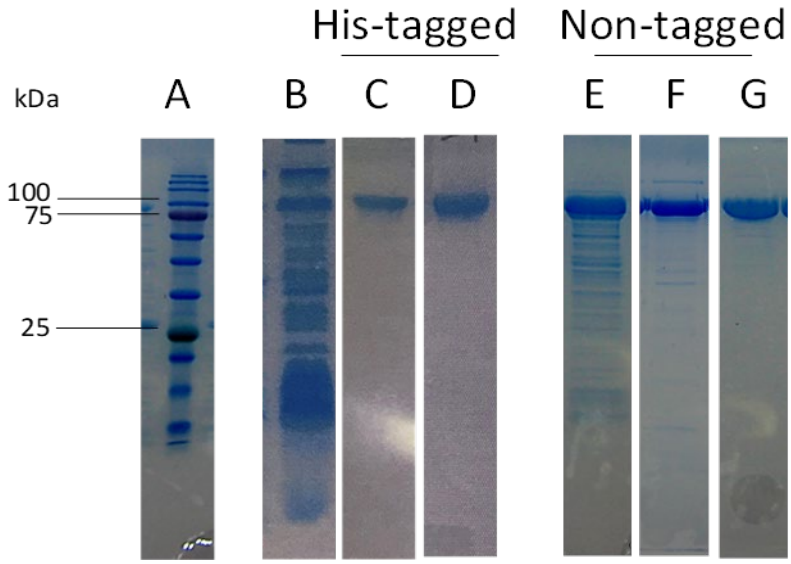

Figure 5-5: The purification processes of His-tagged and Non-tagged Top IA. (A) Protein molecular weight marker, (B) Proteins present in the lysate of *E. coli* BL21 Gold (DE3). Top IA (~100 kDa) is over expressed. (C) A representative Top IA fraction after Ni-NTA column. Top IA is further purified in a (D) hydroxyapatite column. In the non-tagged purification process proteins eluted from the, (E) phenyl sepharose column, (F) SP-sepharose column, and (G) hydroxyapatite column are increasingly pure.

Adding a Hexa-His tag to the N-terminus of the protein has not affected the function of the protein [7]. His-tagged purification was efficient and was able to purify Top IA with only two chromatographic steps, where a Ni-NTA column and an HA column was used. The proteins in the cell lysate were directly loaded onto a Ni-NTA column. The column was washed with two different concentrations of imidazole (20 and 40 mM) to remove all non-specifically bound proteins. Specifically- bound proteins were eluted using a high imidazole concentration (350 mM). Top IA collected from Ni-NTA column was 85% pure, and the

hexa-His tag of Top IA was cleaved by TEV protease. Top IA was mixed with TEV protease at a 1:10 enzyme to protein ratio, and the mixture was incubated for 16 h at 4 ^{0}C. TEV protease contains a Hexa-His tag; therefore, the TEV and Top IA protein mixture were separated by passing through the Ni-NTA column. The eluate, Top IA was further purified (95 %) using an HA column.

5.3.3 Relaxation activity of Top IA

The relaxation assay evaluates the enzymatic activity of the purified Top IA. This assay tests the operation of Top IA on supercoiled plasmid DNA. The active Top IA protein relaxes the supercoiled plasmids in a concentration-dependent manner. The relaxed and supercoiled DNA migrate differently in

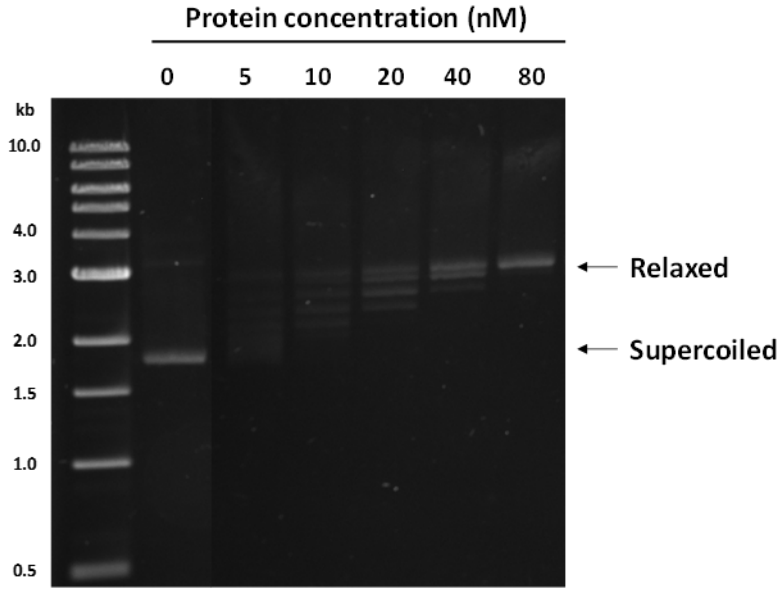

Figure 5-6: The activity of Top IA was tested in a relaxation assay. The plasmid DNA alone (2nd lane) exhibits a supercoiled DNA band at 1.8 kb. When the concentration of Top IA increases, the supercoiled DNA gradually gets to the relaxed state.

agarose gels. The supercoiled DNA is more compact and creates less frictional forces. Therefore, they migrate faster than the relaxed DNA. The relaxation assay buffer contains $Mg^{2+,}$ which is necessary for the optimum activity of the enzyme. In the absence of Mg^{2+}, the relaxation activity of Top IA is compromised [13]. The relaxation reaction can be terminated by adding sodium dodecyl sulfate (SDS) or a metal chelator such as EDTA. The resultant mixture is separated electrophoretically and stained with ethidium bromide.

It is not recommended to add ethidium bromide into the gel, as intercalation of the dye would alter the results.

The pUC18 supercoiled plasmid DNA (2.6 kb) was selected for the assay. About 600 ng of DNA was mixed with different concentrations of Top IA (**Figure 5-5**) in the relaxation buffer (see experimental). The mixture was incubated at 37 ^{0}C for 30 h, and the reaction was terminated by adding 2 % SDS. The plasmid DNA was electrophoretically separated in a 1 % agarose gel.

Supercoiled plasmids run faster (approximately at 1.8 kb) in the agarose gel. Relaxed DNA runs around 2.6 kb (pUC18). The DNA bands in between the relaxed and supercoiled DNA are partially relaxed DNA. A concentration of 80 nM Top IA was required to completely relax 600 ng of pUC18 DNA. The relaxation assay revealed the quality and activity of the purified protein.

5.3.4 Analysis of zinc in Top IA

One of the important structural characterizations of topoisomerase is the presence of Zn fingers, coordinated by four cysteines. The X-ray crystal structure of the *E.coli* full-length Top I (PDB ID: 4RUL) illustrated the importance of the Zn fingers in positioning the DNA binding. *P. aeruginosa* Top IA contains 15 cysteines, and 14 of the cysteines are located in the C-terminal domain of the protein. The structural alignment of the I-TASSER predicted model with the *E. coli* full-length Top IA revealed Zn binding sites in *P. aeruginosa* Top IA (**Figure 5-7**).

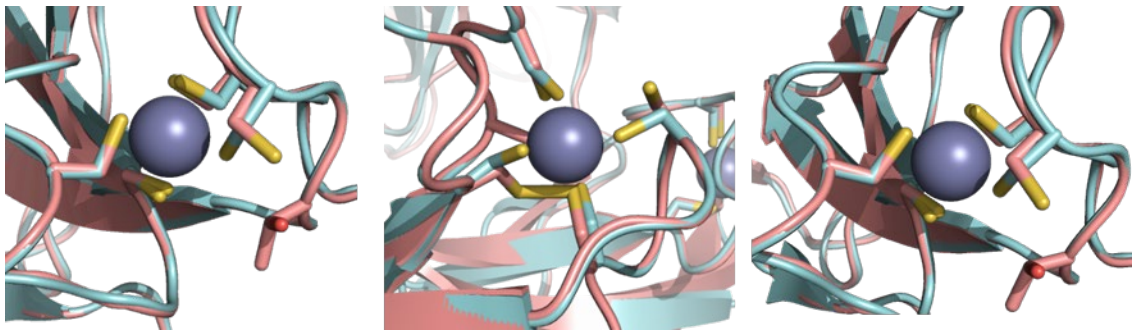

Figure 5-7: Structural alignment of the C-terminal Zn fingers of *E. coli* Top IA (PDB ID: 4RUL) with *P. aeruginosa* Top IA model (orange). Zn atoms are presented as grey spheres.

The stoichiometry between Zn and Top IA was analyzed by the metallochromic indicator 4-(2-pyridylazo) resorcinol (PAR). Different protein concentrations were treated with the denaturant, H_2O_2 in the presence of PAR. The change in the absorbance at 500 nm was monitored. When the absorbance reading was constant, zinc concentration in each condition was calculated using the standard curve. The calculated ratio between Zn and protein was 2.8 ± 0.38. This value agrees with the structural characteristics of Top IA, where one Top IA contains three possible Zn fingers.

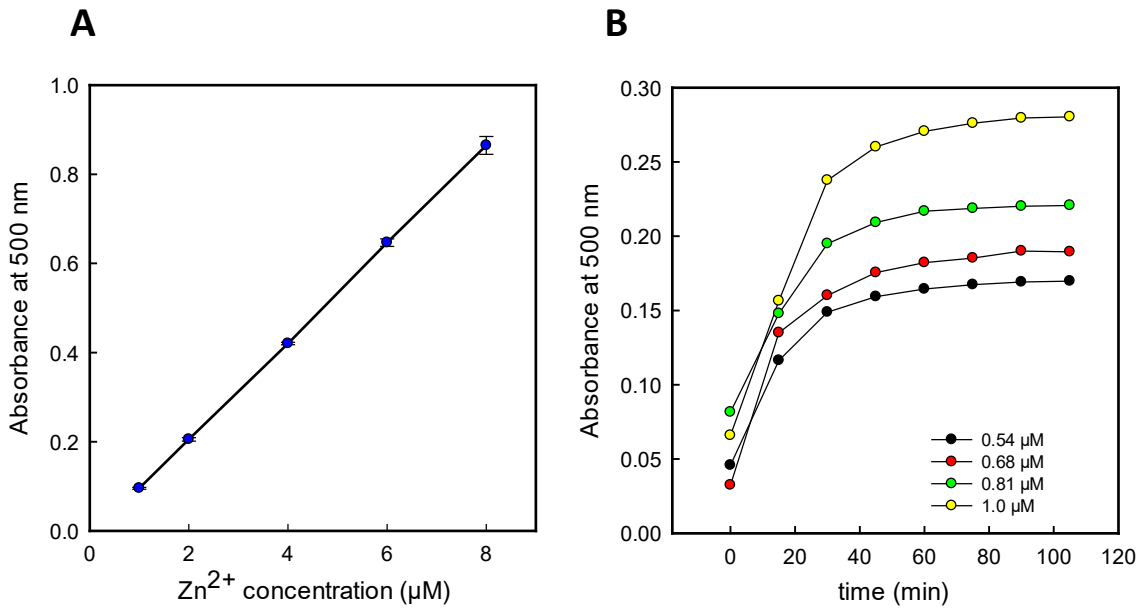

Figure 5-8: (A) The standard calibration curve for the Zn concentration determination. (B) The change in absorbance (500 nm) as a function of time. Four different Top IA concentrations were used for the analysis.

5.3.5 DNA-Top IA gel shift assays

Determining the protein X-ray crystallographic structure is essential to uncover the structural and functional characteristics of a novel protein. Therefore, the crystallization of *P. aeruginosa* topoisomerase IA full-length protein is necessary to discover insights of the enzyme function and activity. The C-terminal domain of the Topoisomerases are known to contain flexible regions, and many create difficulties in

growing protein crystals [7]. These flexible regions may get stabilized in the presence of DNA [5, 7]. Therefore, attempts are made to co-crystalize *P. aeruginosa* Top IA with its binding partner, DNA.

Different sequences and lengths of DNA were tested against Top IA to identify a suitable DNA fragment for crystallization studies. DNA sequences 1-6 (**Figure 5-9**) were mixed in two different DNA to protein mole ratios, 1:1 and 2:1, and incubated for 1 h. Mixtures were separated on a 7 % Native-PAGE.

At the end of the run, gels were stained with ethidium bromide and Coomassie-brilliant blue, respectively. The resultant gels are presented in **Figure 5-9**. Top IA is positively charged at pH 6.8 (pH of the stacking gel) and doesn't enter into the gel and was visualized at the top of the stacking gel. DNA only and unbound DNA containing samples show a fluorescence stain toward the bottom of the gel. Interestingly, the DNA: Top IA complexes show alternations in the electrophoretic mobility and get stained with both ethidium bromide and Coomassie.

When DNA and Top IA were mixed at a 1:1 mole ratio, the sequences 1, 2, 4, 5, 6 resulted in low levels unbound DNA, and DNA sequence 2 resulted in the least unbound DNA at this ratio. When DNA and Top IA were mixed at a 2:1 mole ratio, an additional increment in the DNA-Top IA intensity was not observed, and adding extra DNA resulted in high levels of unbound DNA. Therefore, the preferred mole ratio of single strandard DNA to Top IA may be 1:1.

One of the interesting observations from the gel shift assays was the differences in the ethidium bromide stains of DNA sequences 2 and 3. These two sequences have the same number of bases, but when mixed with protein at a 1:1 mole ratio, DNA sequence 2 resulted in almost complete binding by Top IA, and is evident in the low intensity ethidium bromide stain of unbound DNA. Whereas, DNA sequence 3-Top IA had a small change in the migration and a low concentration of DNA was bound to Top IA, presented by the faint ethidium bromide stain, but the resulting Coomassie-protein stain was as deep as

DNA seq 2-Top IA complex. Top IA has a very high affinity toward DNA, and a small DNA concentration may be sufficient to generate a migration shit.

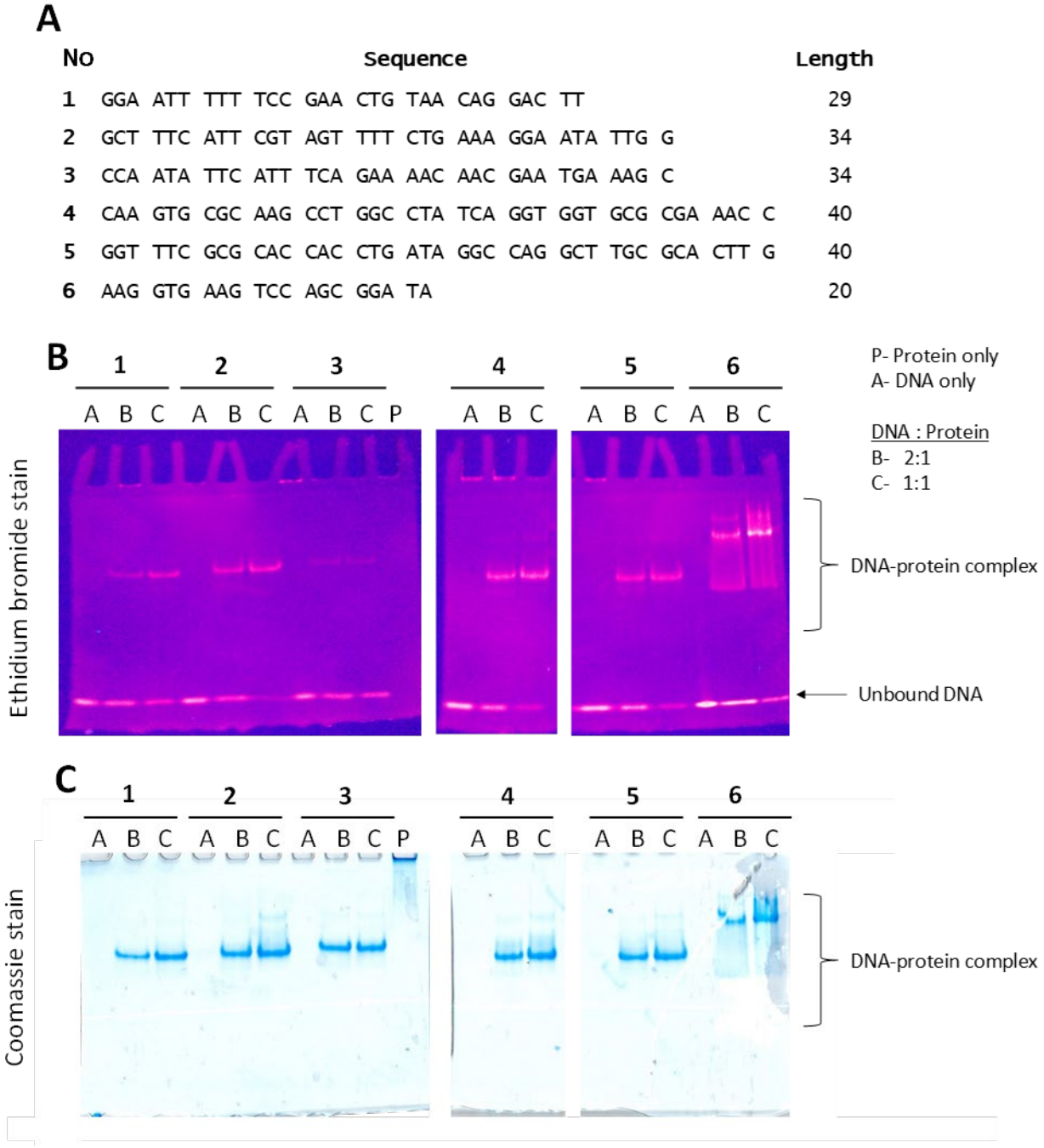

Figure 5-9: (A) Six different single strandard DNA sequences with different lengths were tested (sequences are presented 5' to 3'). DNA and Top IA were mixed at 1:1 and 2:1 mole ratio and the resultant complex was separated in a Native-PAGE and stained with (B) ethidium bromide to detect DNA, and (C) Coomassie brilliant blue to detect proteins.

The shortest DNA sequence, 6 (20 nucleotides) resulted in two possible migration shifts for the DNA-Top IA complex as visualized in the ethidium bromide stain, but the Coomassie stain suggested the presence of protein in the least shifted band. A short DNA fragment may not bind optimally to Top IA, and a shorter DNA sequence carries fewer negatively charged phosphates that may result smaller shifts in migration. On the other hand, DNA-Top IA complex with 29 and 40 bases had almost indistinguishable electrophoretic migration despite the difference in the negative charges. Therefore, the migration difference of the DNA sequence 6-Top IA complex may not be due to the negative charge difference but due to the preference of DNA length by Top IA.

The aforementioned results suggested DNA sequence 2 as a promising start point for the DNA: Top IA crystallization experiments. For crystallization trials, Top IA was concentrated up to 10 mg/mL, and mixed with DNA sequence 2 at a 1.2:1, DNA to Top IA mole ratio, and incubated for 1 h at 4 ^{0}C. A volume of 48 µL from the resultant DNA: Top IA solution was used per 96 well plate sitting drop screens.

It is essential to explore other DNA forms such as double stranded and partial duplex DNA combinations with Top IA. The *E. coli* Top IA was initially identified as protein ω and was first purified in 1971. *E. coli* Top IA was extensively studied over the past decades, but there was no X-ray crystallographic structure available for the full-length protein. Growing crystals to resolve *E. coli* Top IA full-length crystal structure was challenging because of the high flexibility in the C-terminal domain. Fortunately, in 2015 Kemin and co-workers resolved the X-ray crystallographic structure for the full-length *E. coli* Top IA in complex with a partial duplex [7]. Additional research may be necessary to identify correct screening conditions to reach this end, with *P. aeruginosa* Top IA.

5.4 Conclusions

Topoisomerases are essential to maintain the topological states of DNA in the cells. Topoisomerase IA (Top IA) relaxes negatively supercoiled DNA and resolves DNA twisting-related problems associated with replication, transcription, and recombination. This enzyme introduces a nick in one strand allowing

the other strand to pass through by relaxing DNA. Top IA is an essential enzyme for the cells. Top IA has also been shown to be of clinical importance in developing antitubercular targets [10, 11].

P. aeruginosa is an opportunistic pathogen with a critical priority for new anti-infective development. Given the potential clinical significance of Top IA in developing antitubercular targets, the Top IA of *P. aeruginosa* may carry potential therapeutic values. The initial stage in developing a possible therapeutic strategy is the structural and biochemical characterization of the target.

A series of purification methods were developed to purify *P. aeruginosa* Top IA in 95 % purity. The developed methods can be used to purify non-tagged and his-tagged Top IA. The purified protein was active and successfully relaxed negatively supercoiled DNA. One of the essential structural characteristics of topoisomerases is the presence of Zn-fingers. *P. aeruginosa* Top IA can bind 3 Zn ions, which is characterized by the sequence alignment of the *E. coli* Top IA (PDB ID: 4RUL), and by the PAR colorimetric assay. Other than the discussed biochemical characterization, structural characterization helps enormously in understanding the functional insights of the protein. Therefore, attempts were made to grow Top IA protein crystals in the presence of DNA. DNA sequence and length preferences of Top IA were studied to identify a reasonably stable binding DNA fragment for crystallization. The single stranded DNA sequence 2 had a sufficiently good binding compared to the rest of the sequences. This DNA sequence was selected for the *P. aeruginosa* Top IA-DNA crystallization studies. Additional exploration is necessary to identify the correct crystallization screening condition and the right DNA sequence to stabilize the C-terminal domain for Top IA- DNA co-crystallization.

5.5 References

1. Wang, J.C., *Cellular roles of DNA topoisomerases: a molecular perspective.* Nat Rev Mol Cell Biol, 2002. **3**(6): p. 430-40.
2. Champoux, J.J., *DNA Topoisomerases: Structure, Function, and Mechanism.* Annual Review of Biochemistry, 2001. **70**(1): p. 369-413.
3. Ghilarov, D.A. and I.S. Shkundina, *DNA topoisomerases and their functions in a cell.* Molecular Biology, 2012. **46**(1): p. 47-57.
4. Zhang, Z., B. Cheng, and Y.-C. Tse-Dinh, *Crystal structure of a covalent intermediate in DNA cleavage and rejoining by Escherichia coli DNA topoisomerase I.* Proceedings of the National Academy of Sciences, 2011. **108**(17): p. 6939-6944.
5. Cao, N., et al., *Investigating mycobacterial topoisomerase I mechanism from the analysis of metal and DNA substrate interactions at the active site.* Nucleic Acids Research, 2018. **46**(14): p. 7296-7308.
6. Ahumada, A. and Y.-C. Tse-Dinh, *The role of the Zn(II) binding domain in the mechanism of E. coli DNA topoisomerase I.* BMC biochemistry, 2002. **3**: p. 13-13.
7. Tan, K., et al., *Structural basis for suppression of hypernegative DNA supercoiling by E. coli topoisomerase I.* Nucleic acids research, 2015. **43**(22): p. 11031-11046.
8. Organization, W.H., *Prioritization of pathogens to guide discovery, research and development of new antibiotics for drug-resistant bacterial infections, including tuberculosis*. 2017, World Health Organization.
9. Mantravadi, P.K., et al., *The Quest for Novel Antimicrobial Compounds: Emerging Trends in Research, Development, and Technologies.* Antibiotics (Basel), 2019. **8**(1).
10. Sandhaus, S., et al., *Small-Molecule Inhibitors Targeting Topoisomerase I as Novel Antituberculosis Agents.* Antimicrobial Agents and Chemotherapy, 2016. **60**(7): p. 4028-4036.
11. Leelaram, M.N., et al., *Inhibition of type IA topoisomerase by a monoclonal antibody through perturbation of DNA cleavage-religation equilibrium.* FEBS J, 2012. **279**(1): p. 55-65.
12. Roy, A., A. Kucukural, and Y. Zhang, *I-TASSER: a unified platform for automated protein structure and function prediction.* Nat Protoc, 2010. **5**(4): p. 725-38.
13. Annamalai, T., et al., *Analysis of DNA relaxation and cleavage activities of recombinant Mycobacterium tuberculosis DNA topoisomerase I from a new expression and purification protocol.* BMC biochemistry, 2009. **10**: p. 18-18.